https://doi.org/10.15388/vu.thesis.518
https://orcid.org/0000-0002-5633-9623

VILNIUS UNIVERSITY
CENTER FOR PHYSICAL SCIENCES AND TECHNOLOGY

Rusnė Ivaškevičiūtė-Povilauskienė

# Optical engineering in terahertz imaging and 2D materials inspection

**DOCTORAL DISSERTATION**

Natural Sciences,
Physics (N 002)

VILNIUS 2023

The dissertation was prepared between 2018 and 2023 at the Center for Physical Sciences and Technology. The research was supported by the Research Council of Lithuania:
Mobility funding – P-DAK-19-121
Publication funding – P-PUB-19-80

**Academic supervisor –** Prof. Dr. Gintaras Valušis (Center for Physical Sciences and Technology, Natural Sciences, Physics – N002).

This doctoral dissertation will be defended in a public/closed meeting of the Dissertation Defence Panel:

**Chairman** – Prof. Habil. Dr. Gintautas Tamulaitis (Vilnius University, Natural Sciences, Physics, N 002).
**Members:**
Dr. Ignas Nevinskas (Center for Physical Sciences and Technology, Natural Sciences, Physics, N 002),
Dr. Evaldas Stankevičius (Center for Physical Sciences and Technology, Natural Sciences, Physics, N 002),
Prof. Dr. Kęstutis Staliūnas (Universitat Politècnica de Catalunya (UPC), Natural Sciences, Physics, N 002),
Assoc. Prof. Dr. Virgilijus Vaičaitis (Vilnius University, Natural Sciences, Physics, N 002).

The dissertation shall be defended at a public meeting of the Dissertation Defence Panel at 2 p.m. on 29th September 2023 in room A101 of the Center for Physical Sciences and Technology.
Address: Saulėtekio av., 3, Vilnius, Lithuania
Tel. +37052648884; e-mail: office@ftmc.lt
The text of this dissertation can be accessed at the libraries of the Center for Physical Sciences and Technology and Vilnius University, as well as on the website of Vilnius University:
*www.vu.lt/lt/naujienos/ivykiu-kalendorius*

https://doi.org/10.15388/vu.thesis.518
https://orcid.org/0000-0002-5633-9623

VILNIAUS UNIVERSITETAS
FIZINIŲ IR TECHNOLOGIJOS MOKSLŲ CENTRAS

Rusnė Ivaškevičiūtė-Povilauskienė

# Optinė inžinerija teraherciniame vaizdinime ir dvimačių medžiagų tyrimuose

**DAKTARO DISERTACIJA**

Gamtos mokslai,
Fizika (N 002)

VILNIUS 2023

Disertacija rengta 2018–2023 metais Fizinių ir technologijos mokslų centre.
Mokslinius tyrimus rėmė Lietuvos mokslo taryba:
Parama akademinėms išvykoms – P-DAK-19-121
Parama paskelbti mokslinį straipsnį – P-PUB-19-80

**Mokslinis vadovas –** prof. dr. Gintaras Valušis (Fizinių ir technologijos mokslų centras, gamtos mokslai, fizika – N002).

Gynimo taryba:
**Pirmininkas –** prof. habil. dr. Gintautas Tamulaitis (Vilniaus universitetas, gamtos mokslai, fizika, N 002).
**Nariai:**
dr. Ignas Nevinskas (Fizinių ir technologijos mokslų centras, gamtos mokslai, fizika, N 002),
dr. Evaldas Stankevičius (Fizinių ir technologijos mokslų centras, gamtos mokslai, fizika, N 002),
prof. dr. Kęstutis Staliūnas (Katalonijos politechnikos universitetas (UPC), gamtos mokslai, fizika, N 002),
doc. dr. Virgilijus Vaičaitis (Vilniaus universitetas, gamtos mokslai, fizika, N 002).

Disertacija ginama viešame Gynimo tarybos posėdyje 2023 m. rugsėjo mėn. 29 d. 14 val. Fizinių ir technologijos mokslų centro A101 auditorijoje.
Adresas: (Saulėtekio al., 3, Vilnius, Lietuva), tel. +37052648884; el. paštas: office@ftmc.lt.

Disertaciją galima peržiūrėti Fizinių ir technologijos mokslų centro bei VU bibliotekose ir VU interneto svetainėje adresu:
*https://www.vu.lt/naujienos/ivykiu-kalendorius*

TABLE OF CONTENTS

## LIST OF ABBREVIATIONS

| | |
|---|---|
| 0D | Zero dimensional |
| 1D | One dimensional |
| 2D | Two dimensional |
| 3D | Three dimensional |
| BWO | Backward Wave Oscillator |
| CVD | Chemical Vapor Deposition |
| CSRR | Complementary Split Ring Resonator |
| DOE | Diffractive Optical Element |
| DOF | Depth of Field |
| FWHM | Full Width at Half Maximum |
| FZP | Fresnel Zone Plate |
| GZP | Graphene-based Zone Plate |
| HDPE | High-density Polyethylene |
| LDW | Laser Direct Writing Technique |
| PMMA | Poly(methyl methacrylate) |
| PS | Phase Shifting |
| QCL | Quantum Cascade Laser |
| Si | Silicon |
| SRR | Split Ring Resonator |
| THz | Terahertz |
| THz-CW | Terahertz Continuous Wave System |
| THz-FDS | Terahertz Frequency Domain Spectroscopy System |
| THz-TDS | Terahertz Time Domain Spectroscopy System |
| TZP | Terahertz Zone Plate |
| ZP | Zone Plate |

# INTRODUCTION

Terahertz (THz) (1 THz=$10^{12}$ Hz) radiation, also called submillimeter radiation, refers to electromagnetic waves that are positioned between infrared and microwaves in the electromagnetic spectrum. THz extends from 0.1 THz to 10 THz (3 mm to 30 μm), corresponding to energies from 0.4 meV to 40 meV [1] [2]. Microwaves, which occupy the lower end of the THz band, employ electronic principles, however, further increase in device operational frequency is limited by specific transient times. On the other end, THz quantum energy is very low (1 THz corresponds to 4.1 meV), therefore, population inversion at room temperature is hard to achieve, thus, this circumstance induces limitations for device design from the optical side of the electromagnetic spectrum. Consequently, the THz range can be assumed as a bridge between electronic and photonic devices [3], whose operation should include different physical principles. Regarding applications, many materials, such as paper, clothing, or plastic, that are opaque to visible and infrared light are transparent to THz radiation. Due to this feature, THz radiation can offer non-destructive imaging, which is used in security systems, for packaging inspection, examination of paintings, etc [4]–[6]. Furthermore, its low energy and nonionizing nature, unlike X-rays, make THz radiation safe for the

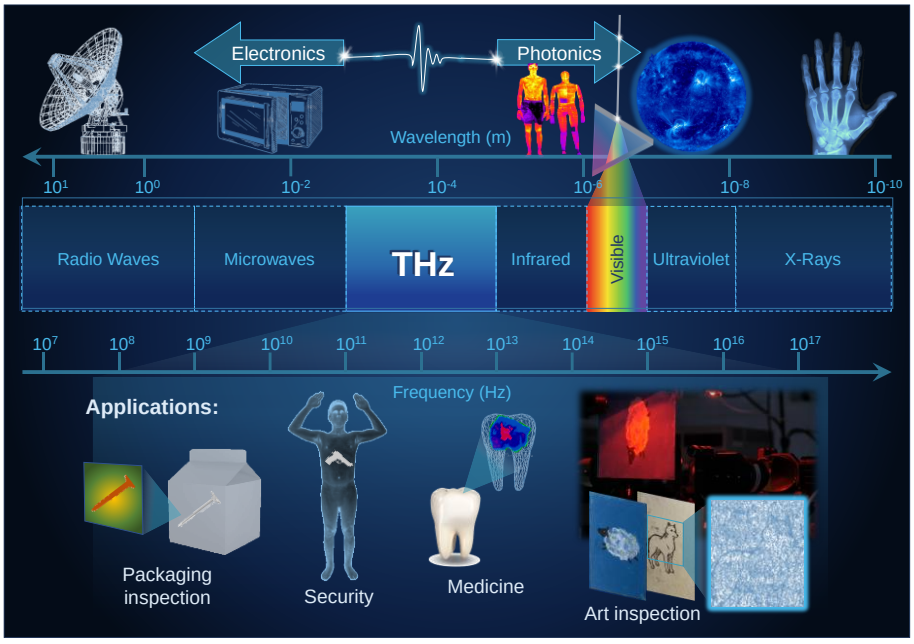


Figure 1: Electromagnetic spectrum. THz radiation range is positioned between the infrared and microwaves region. Applications of THz radiation find their place in many areas, such as packaging inspection, security systems, medicine, or art inspection.

human body and thus can be applied for medical aims [7], [8].

There are a few different types of THz systems that are usually divided into two different approaches: the first one uses pulsed coherent sources (such as THz time-domain spectroscopy (THz-TDS)) and the second one – continuous wave sources (such as direct THz continuous-wave (THz-CW) systems)[9].

THz-TDS is the most commonly used spectroscopic technique, where the imaged sample is probed with short THz pulses. Pulsed THz radiation is generated by femtosecond lasers when semiconducting materials exhibiting short carrier lifetimes are illuminated [10]. This method provides information about the amplitude and phase of the THz radiation that passed through (or was reflected from) the sample. The obtained data can give a better understanding of the sample's structure, composition, or optical properties [11], [12].

Arguably, the primary driving force behind the growing popularity of THz radiation is the THz imaging systems. The THz-CW system is capable of capturing real-time two-dimensional (2D) images of a sample. This method uses a single frequency source and records only the amplitude of the transmitted or reflected beam. Although, in homodyne or heterodyne detection, the CW system can also provide phase information. Moreover, THz-CW systems are known for their simplicity compared to the aforementioned THz systems. Moreover, they are relatively low-cost and fast in recording images. THz-CW imaging systems primarily comprise a continuous wave source, optical components for focusing the THz beam onto the sample, and a detector to record the transmitted or reflected signal [9]. CW THz sources enclose a variety of options, including Gunn diodes [13], quantum cascade lasers (QCLs) [14], optically pumped THz gas lasers [15], and backward wave oscillators (BWOs) [16]. There is a wide range of detector options available for THz-CW systems, including pyroelectrics [17], microbolometers [18], Golay cells [19], bow-tie diodes [20] and Schottky diodes [21].

To broaden the scope of THz imaging systems and enhance their applicability, design must achieve maximum compactness and convenience in use. The focus of attention in achieving miniaturization for THz imaging systems lies predominantly on active components, such as sources and detectors, rather than passive components like lenses and mirrors, even though these components are bulky and often necessitate precise optical alignment [1]. Fortunately, the large optical components can be replaced by thin and more compact diffractive elements. For instance, high-density polyethylene (HDPE) lenses or bulky parabolic mirrors can be replaced by high-resistivity

silicon-based diffractive optical elements, produced by using laser ablation technology [22], [23]. Meanwhile, there are several flexible approaches that can be employed for beam shaping purposes [24]. Metasurfaces [25], which consist of precisely shaped arrays of sub-wavelength-sized resonators, provide an ability of THz beamforming and manipulation of its characteristics through control of amplitude, phase, and polarization.

**Major goal**

To develop and explore solutions for compact and flexible optics suitable for THz imaging, enabling to replace conventional bulky optical components.

**Tasks of this Work**

1. To extend a collection of diffractive optical elements for THz imaging systems by finding and adapting efficient new flexible materials and designs.
2. To develop a lensless THz imaging system utilizing only flat silicon-based optical elements and explore their suitability for generation and collection of the engineered light in THz imaging.
3. To implement THz digital holography technique enabling a better quality of recorded images.

**Scientific Novelty**

1. For the first time, graphite-based thin and flexible film was used to fabricate a terahertz zone plate, which resulted in transmittance spectra almost identical to that of a metallic terahertz zone plate. The focusing performance of graphite-based zone plate was evaluated, resulting in an 8-fold signal value increase, demonstrating the suitability of graphite-based substrate for thin and flexible terahertz zone plate fabrication.
2. Optical modulation of charge carrier concentration was applied for multiple graphene layers transferred on a silicon substrate, resulting in modulation depth values of 42 % and 45 % for single and double graphene layers, respectively. A combination of optical modulation and terahertz imaging technique was conducted for the first time – it exhibited a pronounced change in contrast: 0.16 for single layer and 0.23 for double layer graphene indicating that the simultaneous operation of both techniques can help to distinguish between different graphene layers.
3. Graphene-based zone plate was fabricated and its focusing performance was demonstrated by simultaneously applying the optical modulation of charge carrier concentration.

4. Metasurfaces with complementary split-ring resonators were fabricated from 25 μm thin and flexible stainless steel. The focusing performance under the mechanical deformation, i.e. bending, was shown, resulting in the decrease of beam intensity only by 30 %. Furthermore, even under mechanical deformation of the metasurface, the shape of the Gaussian beam remains unaltered.

5. It was demonstrated that the metasurfaces composed of complementary split-ring resonators in flexible stainless steel foil can be used for polarization-resolved terahertz imaging.

6. It was shown that the combination of silicon-based Airy lens and zone plate generates a nondiffracting nonparaxial Airy beam with a parabolic trajectory and can significantly improve the signal-to-noise ratio from 570 to 1180, moreover, resulting in twice better spatial resolution (1.6λ), when compared to the performance of a single Airy lens, that produces the expanding Airy beam with the reciprocal trajectory.

7. The capability to perform terahertz imaging in the presence of an opaque beam block was demonstrated. It was shown that even when the 60 % area of the illuminating Airy lens was covered, the obtained image was still clear, exhibiting a rational contrast of about 30 (a.u.) and a spatial resolution of 3.2λ. Meanwhile, when the combination of Airy lens and zone plate was employed, the spatial resolution was significantly better – reaching 1.6λ.

8. It was shown that the structured nonparaxial Airy beam provides a possibility for evaluation of optical properties of graphene layers when the combination of Airy lens and a zone plate exhibits a three times higher signal-to-noise ratio of 300 compared to the Gaussian illumination.

9. It was demonstrated that the 2-step and 4-step phase-shifting methods can improve the quality of holographic images by eliminating undesired background noise levels and provide more accurate phase mapping.

10. Coloured terahertz digital holography was demonstrated at four different - 1.39 THz, 2.52 THz, 3.11 THz, and 4.25 THz – frequencies for the first time, extending thus boundaries of thin materials inspection using THz light illumination.

**Statements for Defence**

1. Optical modulation of charge carrier concentration in graphene on silicon structures simultaneously applied with terahertz imaging increases the contrast by an order of magnitude, thereby indicating the technique as a convenient contactless tool for the characterization of graphene deposited on high-resistivity silicon substrates.

2. Metasurface composed from complementary split-ring resonators in flexible stainless steel foil is suitable for polarization-resolved terahertz imaging and focusing even under mechanical bending.

3. The nonparaxial structured light in the shape of THz Airy beam can be generated using silicon-only based diffractive optics and its accelerating nature can be applied for imaging of partially obscured objects.

4. The structured THz light illumination outperforms conventional Gaussian one in terms of resolution and contrast in THz imaging of thin graphene layers.

5. Digital terahertz holography with two- and four-step phase-shifting techniques enable a better quality of the recorded images and their reconstructions than a single terahertz hologram due to unwanted background subtraction.

**Author Contribution**

In [P1] publication author participated in preparing the investigated diffractive elements and experimental setup. Conducted terahertz imaging experiments and analyzed the obtained data. Participated in the preparation of this paper and was responsible for the representation of results (graphs and figures).

In [P2] author prepared all investigated samples. Conducted terahertz imaging and spectroscopy experiments and analysis of the data. Participated in the preparation of this publication and was responsible for the representation of results.

In [P3] author conducted a major part of experimental measurements and analyzed the obtained data. Participated in the preparation of this publication and was responsible for the representation of results.

In [P4] author conducted all experimental terahertz imaging measurements and analysis of the obtained data. Prepared investigated samples with different number of graphene layers. Participated in the preparation of this publication and was responsible for the representation of results.

In [P5] author participated in experimental measurements and later analysis of the obtained data. Was involved in the preparation or this article and the representation of results.

## LIST OF PUBLICATIONS

On the dissertation topic:

[P1] **R. Ivaškevičiūtė-Povilauskienė**, L. Minkevičius, D. Jokubauskis, A. Urbanowicz, S. Indrišiūnas, G. Valušis, "Flexible materials for terahertz optics: advantages of graphite-based structures", *Optical Materials Express* **9**, 4438-4446 (2019). DOI: 10.1364/OME.9.004438

[P2] **R. Ivaškevičiūtė-Povilauskienė**, A. Paddubskaya, D. Seliuta, D. Jokubauskis, L. Minkevičius, A. Urbanowicz, I. Matulaitienė, L. Mikoliūnaitė, P. Kuzhir, G. Valušis, "Advantages of optical modulation in terahertz imaging for study of graphene layers", *Journal of Applied Physics* **131**, 033101 (2022). DOI: 10.1063/5.0074772

[P3] **R. Ivaškevičiūtė-Povilauskienė**, V. Čižas, E. Nacius, I. Grigelionis, K. Redeckas, M. Bernatonis, S. Orlov, G. Valušis, L. Minkevičius, "Flexible terahertz optics: light beam profile engineering via C-shaped metallic metasurface", *Frontiers in Physics* **11**, 1196726 (2023).
DOI: 10.3389/fphy.2023.1196726

[P4] **R. Ivaškevičiūtė-Povilauskienė**, P. Kizevičius, E. Nacius, D. Jokubauskis, K. Ikamas, A. Lisauskas, N. Alexeeva, I. Matulaitienė, V. Jukna, S. Orlov, L. Minkevičius, G. Valušis, "Terahertz structured light: nonparaxial Airy imaging using silicon diffractive optics", *Light: Science and Applications* **11**, 326 (2022). DOI: 10.1038/s41377-022-01007-z

[P5] A. Semion, L. Minkevičius, D. Jokubauskis, **R. Ivaškevičiūtė-Povilauskienė**, G. Valušis, "Terahertz digital holography: Two- and four-step phase shifting technique in two plane image recording", *AIP Advances* **11**, 105212 (2021). DOI: 10.1063/5.0062330

Other publications:

[P6] M. L. Seol, **R. Ivaškevičiūtė**, M. A. Ciappesoni, F. V. Thompson, D. I. Moon, S. J. Kim, S. J. Kim, J. W. Han, M. Meyyappan, "All 3D printed energy harvester for autonomous and sustainable resource utilization", *Nano Energy* **52**, 271-278 (2018). DOI: 10.1016/j.nanoen.2018.07.061

## LIST OF CONFERENCE PRESENTATIONS

[C1] **R. Ivaškevičiūtė-Povilauskienė**, P. Kizevičius, E. Nacius, D. Jokubauskis, K. Ikamas, A. Lisauskas, N. Alexeeva, S. Orlov, L. Minkevičius, G. Valušis, Terahertz imaging using diffractive Airy lens, Apropos'18, Vilnius, Lithuania, 2022.

[C2] **R. Ivaškevičiūtė-Povilauskienė**, D. Seliuta, D. Jokubauskis, L. Minkevičius, A. Urbanowicz, I. Matulaitienė, L. Mikoliūnaitė, N. Alexeeva, G. Valušis, Terahertz imaging of optically modulated graphene layers, 47th International Conference on Infrared, Millimeter, and Terahertz Waves, Delft, Netherlands, 2022.

[C3] **R. Ivaškevičiūtė-Povilauskienė**, A. Paddubskaya, D. Seliuta, D. Jokubauskis, L. Minkevičius, A. Urbanowicz, I. Matulaitienė, L. Mikoliūnaitė, P. Kuzhir, Natalia Alexeeva, G. Valušis, Terahertz imaging of optically modulated graphene layers, 8th Workshop on Nanocarbon Photonics and Optoelectronics (NPO), Polvijärvi, Finland, 2022.

[C4] **R. Ivaškevičiūtė-Povilauskienė**, L. Minkevičius, D. Jokubauskis, P. Gotovski, E. Nacius, P. Kizevičius, S. Orlovas, G. Valušis, Terahercinis Airy vaizdinimas naudojant silicio optiką, FizTech, Vilnius, Lithuania, 2021.

[C5] B. Bužinskas, **R. Ivaškevičiūtė-Povilauskienė**, D. Jokubauskis, L. Minkevičius, Terahercinis spalvotas struktūrinių defektų vaizdinimas mene ir pramonėje, LNFK, Vilnius, Lithuania, 2021.

[C6] **R. Ivaškevičiūtė-Povilauskienė**, D. Seliuta, A. Paddubskaya, D. Jokubauskis, L. Minkevičius, A. Urbanowicz, I. Matulaitienė, L. Mikoliūnaitė, G. Valušis, Optical modulation of mono and bi-layer graphene, Open Readings, Vilnius, Lithuania, 2021.

[C7] **R. Ivaškevičiūtė-Povilauskienė**, D. Seliuta, D. Jokubauskis, L. Minkevičius, I. Matulaitienė, Ž. A. Kancleris, A. Urbanowicz, G. Valušis, Optinė grafeno sluoksnių moduliacija, FizTech, Vilnius, Lithuania, 2020.

[C8] **R. Ivaškevičiūtė-Povilauskienė**, D. Seliuta, D. Jokubauskis, L. Minkevičius, I. Matulaitienė, Ž. A. Kancleris, N. Alexeeva, G. Valušis, All-optical modulation of graphene layers, Apropos'17, Vilnius, Lithuania, 2020.

[C9] **R. Ivaškevičiūtė-Povilauskienė**, L. Minkevičius, A. Urbanovič, L. Laurinavičius, R. Pauliukaitė, G. Valušis, Grafitinės terahercinės zoninės plokštelės, FizTech, Vilnius, Lithuania, 2019.

[C10] **R. Ivaškevičiūtė**, L. Minkevičius, A. Urbanovič, L. Laurinavičius, R. Pauliukaitė, A. Paddubskaya, G. Valušis, Anglies pagrindo difrakciniai optiniai elementai terahercinės spinduliuotės sričiai, LNFK, Kaunas, Lithuania, 2019.

[C11] **R. Ivaškevičiūtė**, L. Minkevičius, A. Urbanovič, L. Laurinavičius, R. Pauliukaitė, G. Valušis, Carbon-based terahertz zone plates, 44$^{th}$ International Conference on Infrared, Millimeter, and Terahertz Waves, Paris, France, 2019.

[C12] **R. Ivaškevičiūtė**, L. Minkevičius, A. Urbanovič, L. Laurinavičius, R. Pauliukaitė, G. Valušis, Graphite based diffractive optical elements for terahertz frequency range, Advanced materials and technologies, Palanga, Lithuania, 2019.

[C13] **R. Ivaškevičiūtė**, J. Zinkevičius, L. Laurinavičius, R. Pauliukaitė, J. Macutkevič, G. Valušis, Study of graphite composites for diffractive terahertz optics needs, Open Readings, Vilnius, Lithuania, 2019.

[C14] **R. Ivaškevičiūtė**, A. Lukša, L. Minkevičius, D. Jokubauskis, A. Urbanovič, A. Sakavičius, A. Šetkus, G. Valušis, Carbon nanolayers for diffractive terahertz optics, Apropos'16, Vilnius, Lithuania, 2018.

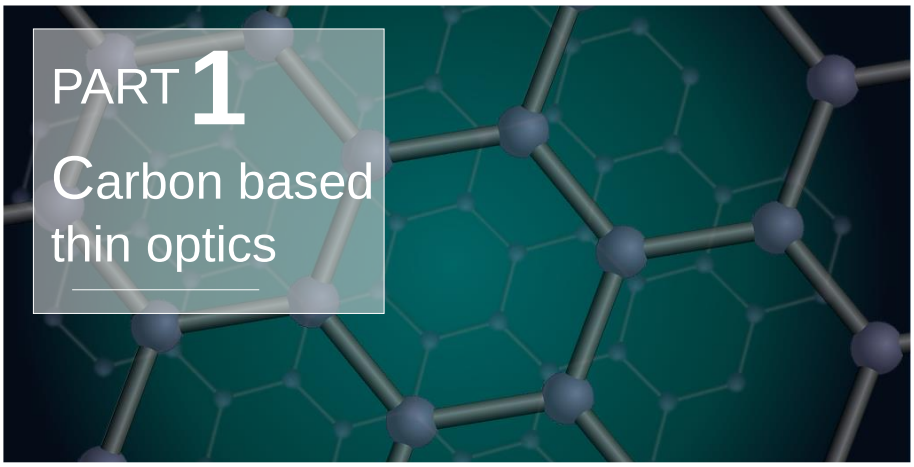

# PART 1
# Carbon based thin optics

The advancement of THz imaging systems is propelling the progress of both THz emitters and detectors, nonetheless, it also drives the search for novel approaches to enhance the efficiency and compactness of passive optical components. In the process of miniaturizing THz imaging systems, optical elements must be also compact without losing their properties and ability to manipulate a THz beam. Furthermore, it is desirable that these components could be easily integrated and aligned. Diffractive optical elements (DOE) offer a potential solution by utilizing the principle of light diffraction to create thin and planar components that can serve as a substitute for bulky conventional optical lenses, parabolic mirrors, or polyethylene lenses.

However, relying solely on DOE may not be enough to achieve the desired compactness, reliability, and flexibility of optical elements. In this case, the DOE design can be enriched by the use of metamaterials, which make it possible to transform thick optical lenses into thin and flat components with a diverse range of beam shaping options. The combination of both DOE and metamaterials provide the efficiency of such optical components to a higher level. Moreover, to develop compact THz imaging systems, using on-chip solutions, it is also necessary to find alternative materials suitable for such optical elements. An optimal solution would be the employment of carbon-based materials, such as graphite or graphene, that are distinguished by remarkable properties. Consequently, this part focuses on the application of carbon-based optical elements in THz imaging systems.

### 1.1. Diffractive Optical Elements: Fresnel Zone Plates

One of the most commonly used DOE in THz imaging systems is the Fresnel zone plate (FZP) [26]. Unlike conventional lenses, instead of refraction, zone plate uses diffraction. Moreover, zone plates are superior to conventional lenses in terms of design because they offer a wider range of material options and the flexibility to vary their constructions [22], [27], [28].

A Fresnel zone plate is composed of a series of concentric rings (half-wave zones) with radial symmetry, where each ring alternates between being opaque and transparent. Binary Fresnel zone plates can be divided into two types: negative FZPs when odd zones are opaque and positive FZPs when even zones are opaque (see Figure 2 (a)). As the axially incident spherical wave approaches the FZP it diffracts around the opaque zones into multiple spherical waves that converge at a focal point [29], [30]. This effect is illustrated in Figure 2 (b). More precisely, the focusing occurs at multiple focal points located at distances:

$$z = \frac{F}{n} \tag{1}$$

where $F$ is the distance from the FZP to the main focal point and $n$ is an odd number (1, 3, 5…). The feature of multiple foci is observed in binary zone plates. In this case, only two values of zone variation are possible, i. e., a value of "0" for a completely opaque zone and a value of "1" for a completely transparent zone. Meanwhile, the occurrence of multiple foci can be avoided by using a sinusoidal (or continuous) phase zone plate, in which zones are characterized by gradually varying transmittance [31].

In the case where the incident light has plane wavefronts, such as a collimated Gaussian beam, designing a binary zone plate can be based on the formula:

$$r_m = \sqrt{m\lambda F + \frac{m^2\lambda^2}{4}} \tag{2}$$

where $r_m$ is the radius of the $m$-th zone, $m$ is the number of zone, $\lambda$ is the wavelength and $F$ is the focal length.

If the FZP radius is small, compared to the focal length, $m\lambda F >> \frac{m^2\lambda^2}{4}$, the second part of the equation can be neglected, therefore the following approximation is typically considered valid:

$$r_m = \sqrt{m\lambda F} \tag{3}$$

In this case, all zones possess identical areas, therefore, as the diameter of successive zones increases, their width decreases, hence from the center outwards zones become narrower [31].

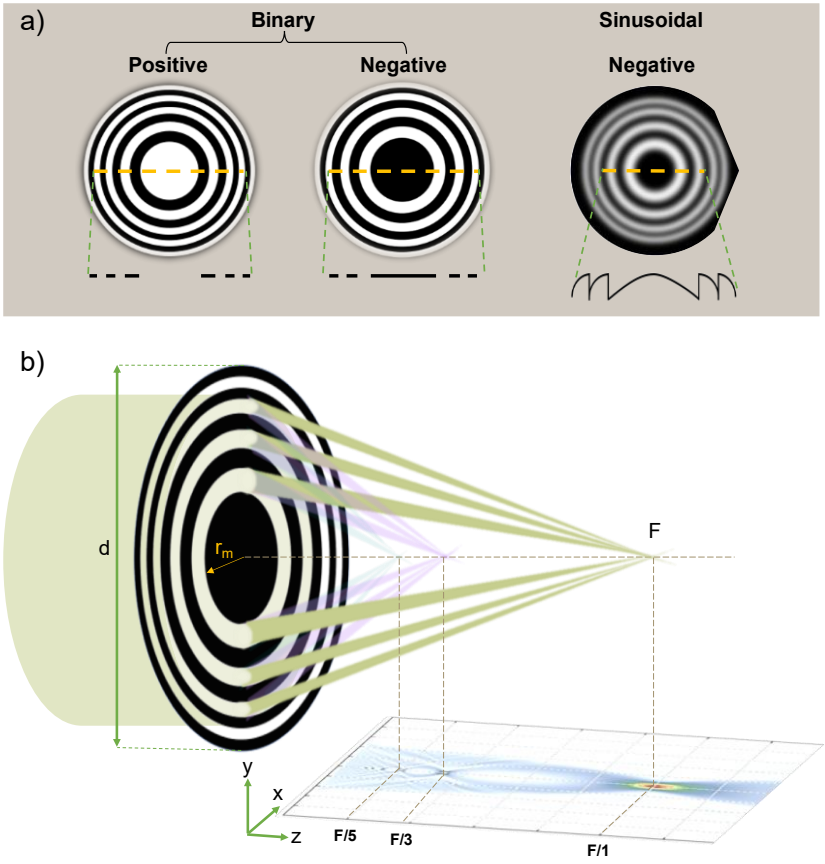


Figure 2: Structure and principle of Fresnel zone plates. Positive and negative binary zone plates are depicted on the left side and sinusoidal negative zone plate on the right side (a). Insets at the bottom of each zone plate depict their profiles. Beam focusing using FZP (b). Inset at the bottom depicts the intensity distribution along the optical axis, showing multiple focal points, located at $z=F/1$, $F/3$, and $F/5$.

As far as it concerns the resolution, it is expressed by the resolving angle $\varphi$, meaning that the smaller the angle, the higher the resolution is:

$$\varphi = \chi \frac{\lambda}{d} \tag{4}$$

where $d$ is the diameter of the aperture and $\chi$ is the constant for open apertures. Typically, it is assumed to be $\chi$=1.22, however, for binary zone plates, this constant depends on the number of zones [31].

The aforementioned value is valid only when the number of zones exceeds 200. For positive FZPs with a smaller number of zones, this constant will exceed 1.22 value, meanwhile, for negative FZPs with a smaller number of zones it will be less than 1.22. Using the same parameters, the negative FZP has a smaller resolving angle, therefore a higher resolution [31].

### 1.2. Metamaterials in THz Optics: Band-pass Filters

To enhance the optical components of THz imaging systems, and improve their performance, new artificial metamaterials, capable to manipulate THz beam in extraordinary ways, can be employed. Their structure is composed of various shapes elements arranged in periodic pattern. By resonantly coupling with magnetic or electric components of incident electromagnetic wave, metamaterials can develop unique properties, such as sub-wavelength focusing, anomalous refraction or reflection, perfect absorption, etc, that can not be found in natural materials. For this reason, the prefix „meta“ entails „beyond“ materials [32], [33]. Metamaterials can be applied to diverse types of THz devices, such as metamaterial absorbers, optical modulators, THz band-pass filters, or frequency resonators.

In spectroscopic (multispectral) imaging narrow THz spectrum is usually required for sample imaging and characterization. Band-pass metamaterials or band-pass filters are an ideal choice in this case, as they can filter a particular range of frequencies and improve the detected signal by eliminating undesirable frequency components [34]. Moreover, aforesaid filters display exceptional transmission performance, with a high peak transmission (higher than 80 %) at the central frequency. The transmittance frequency depends on illumination absorbed by electrons in the metal and the re-emission of radiation at certain wavelengths. Therewith the transmission properties comprise not only the intensity of the transmitted signal and the position of

resonant frequency but also the full width at half maximum (FWHM) bandwidth [35].

Conventional band-pass filters are considered as metal meshes that are fabricated from a thin metal film containing a matrix of apertures of any geometry from simple circular or square holes to complex patterns [36]. Such metal mesh filters can serve as low-pass, high-pass, or band-pass filters [37].

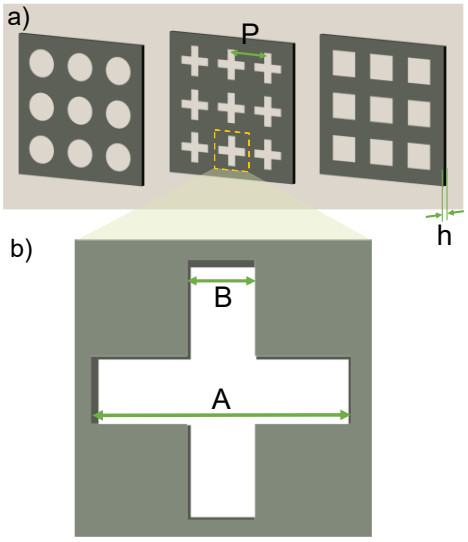


Figure 3: Band-pass filters of different geometries (a). Cross-shaped band-pass filter and its characteristic geometrical parameters (b).

The resonant frequency is specified by the design of the apertures. For long wavelengths, i.e. THz radiation, an analytical method can be used to find the resonant wavelength ($\lambda_r$) of a standard hole array aperture [38]:

$$\lambda_r = \frac{P}{\sqrt{i^2+j^2}} n_{sp} = \frac{P}{\sqrt{i^2+j^2}} \sqrt{\varepsilon_d} \tag{5}$$

where $P$ is the periodicity of metamaterial elements, $n_{sp}$ is the refractive index of the surface propagating wave, $\varepsilon_d$ is the dielectric constant of the interfacial dielectric media, and $i$ and $j$ are indices corresponding to the resonance order.

In the work of Cao and Nahata (2004) circular, square, and rectangular aperture arrays, perforated in thin steel film, were compared. It was demonstrated that the THz transmission is affected by the geometry of the aperture as it influences the waveforms. The absolute amplitude transmission

coefficient of 0.8 was obtained using square shape apertures that exhibited the best results [38].

Another common type of band-pass filters are cross-shaped apertures that were proposed by Nolte et al. [39] and Moller et al. [40]. The symmetrical shape of the cross ensures that the filter is independent of polarization. Their frequency profile can be modified by altering their geometrical parameters, such as cross length, width, and periodicity, as shown in Figure 3. The resonant frequency ($f_r$) of this filter can be determined by the empirical formula [41], [42]:

$$f_r = \frac{c}{1.8A - 1.35B + 0.2P} \tag{6}$$

where $c$ is the speed of light, $A$ is the length and $B$ is the width of the cross-shaped aperture, while $P$ labels periodicity.

This implies that with the increase in aperture length ($A$), resonant frequency decreases, meanwhile increasing width ($B$) results in increased bandwidth, therefore slightly increased frequency. Furthermore, the transmission performance is resolved not only by the geometrical parameters of the aperture but also by the thickness of the metal film ($h$) or any other material in which these apertures are engraved. With increasing thickness, resonant frequency slightly decreases. Besides, it is highly significant to achieve a precise perforation of apertures, because rounding of cross-shapes increases the resonant frequency [37]. In this instance there are many possible ways to fabricate band-pass metamaterials, for example, using micro- and nanofabrication, mechanical perforation, laser micromachining, or 3D printing [43], [44]. Moreover, commonly used laser direct writing (LDW) is an excellent technique for manufacturing metallic filters with explicit geometries [35].

### 1.3. Graphite-based Terahertz Zone Plates

Previously discussed metamaterials can be spatially arranged to form specific patterns, such as concentric rings that resemble zone plate, thus obtaining compact optical elements – metasurfaces - that not only have the ability to focus THz radiation but also filter the required resonant frequency or otherwise manipulate the radiation. Comparing conventional optical components with metalenses, the latter are much thinner, more flexible, and more compact. Additionally, their numerical aperture exhibits a wider variation scope. Thanks to its ability to control the amplitude and phase at

subwavelength scales, the metasurface can achieve a high-efficiency diffraction-limited focusing [45]. Such novel multifunctional optical elements can improve THz imaging systems by making them more compact and effective.

In order to create a compact optical element suitable for THz imaging, the cross-shaped filters discussed above can be integrated into a conventional zone plate, making a THz zone plate (TZP) that is capable of focusing and shaping THz beam for imaging at only certain frequencies. This type of TZPs were proposed and investigated in several articles by L. Minkevičius et al. [24][46].

In the TZP design, the open areas of the Fresnel zone plate have been replaced by cross-shaped band-pass filters. These filters were ablated in flexible 30 μm thickness steel foil, using an LDW system. As a reference, a regular zone plate from the same steel foil was produced. In the first work, it was demonstrated that the incorporation of cross-shaped filters resulted in a slightly smaller signal enhancement, although it increased the frequency selectivity [24].

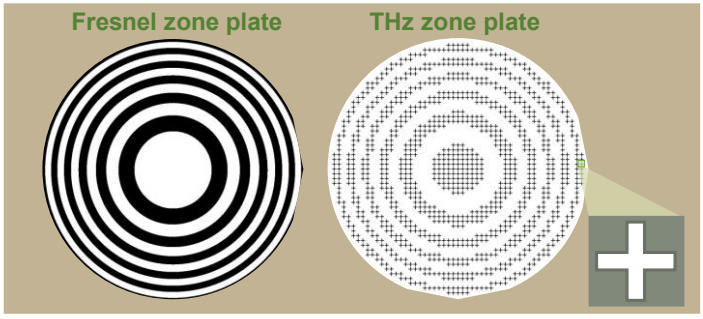


Figure 4: Design of conventional Fresnel zone plate on the left and a THz zone plate with integrated cross-shaped band-pass filters (depicted in the enlarged part) on the right.

In the second study [46], conventional zone plates with 5 and 15 zones and TZP with 5 zones were compared. For regular zone plates, the bandwidth decreases with an increasing number of zones, although focused beam signal intensity remains about the same. This means that to achieve a smaller bandwidth, a larger number of zones is required, nevertheless, the larger number of zones reduces the compactness and efficiency of the TZP. Results showed that in the case of TZP, the focused THz beam profile was smoother and the bandwidth was proportional to the beam, focused with conventional ZP with 15 zones and almost twice as smaller than in the case of ZP with 5

zones. Thus, the integration of band-pass filters makes zone plates more efficient [46].

**In this work, the potential of thin and flexible TZPs was extended by exploring the possibilities of using carbon-based materials.** For this purpose, our group conducted a study [P1] where graphite-based ZPs with integrated cross-shaped filters were produced and investigated. When trying to find a replacement for metal, it is required that an alternative material would also be electrically conductive and at the same time thin, flexible, and reliable. An excellent solution would be a carbon-based substrate such as graphite – the most stable form of carbon. As required, it exhibits a high electrical conductivity, it is ecofriendly and inexpensive. Moreover, the graphite film that was used for the fabrication of TZP in [P1] was produced of only a 10 μm thick graphite layer deposited on 75 μm thick plastic polyester film, making it thin and flexible. The graphite foil was acquired from industrial manufacturer.

The spectral properties of TZP were studied by employing the THz-TDS system. Meanwhile, the focusing performance was investigated using the THz-CW system at 0.6 THz frequency. Metallic TZP that was used in previous [24][46] studies served here as a reference for the graphite-based TZP. Transmittance spectra, depicted in Figure 5 (c), showed that metallic and graphite TZPs resulted in very similar spectral shapes. The maximum transmittance value of graphite TZP was only 18 % smaller than the metallic one.

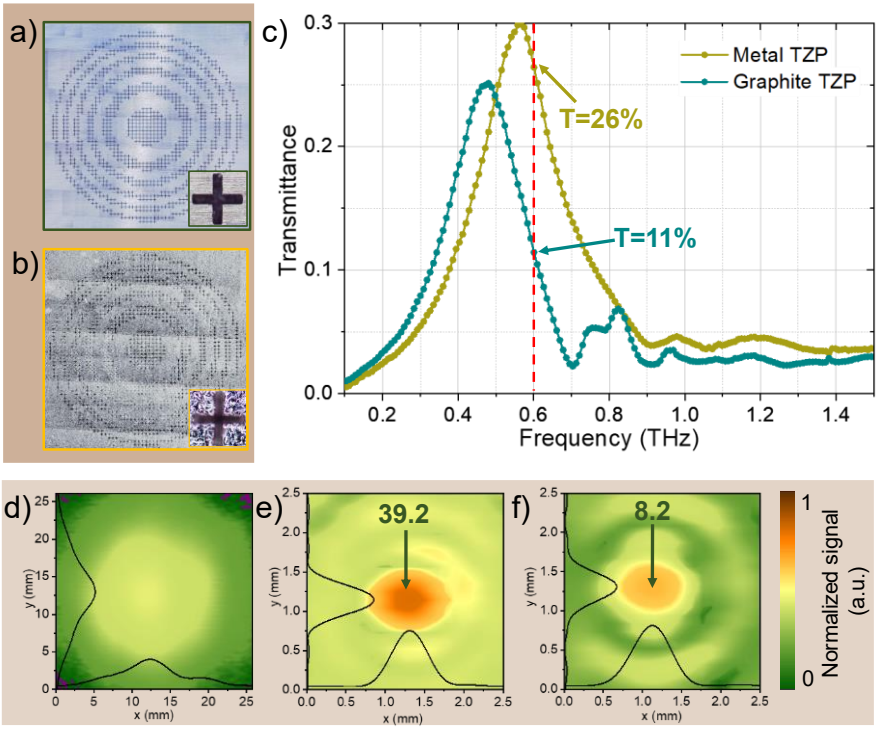


Figure 5: Pictures of metallic (a) and graphite (b) TZPs. Insets depict cross-shaped bandpass filters. Transmittance spectra of metallic and graphite TZPs (c). Two-dimensional THz beam profiles of the unfocused beam (d) and focused with metallic TZP (e) and graphite TZP (f). Solid black lines represent beam cross-sections at the maximum intensity. Adapted from [P1].

Two-dimensional THz beam profiles of the unfocused beam are given in Figure 5 (d), the beam focused with metallic TZP is shown in Figure 5 (e) and with graphite TZP is displayed in Figure 5 (f). Measurements were performed using 0.6 THz frequency radiation. Solid black lines represent beam cross-sections at the maximum intensity. By comparing with the unfocused beam, graphite TZP demonstrated focusing by increasing signal value by 8 times.

Moreover, this study examined not only graphite foil-based TZP but also investigated a flexible TZP made of a thin graphite layer deposited by an HB graphite pencil on a 100 μm paper sheet. A broader overview of obtained results is provided in [P1].

These findings showed that graphite-based TZPs could serve as an inexpensive, flexible, and compact alternative to metal-based elements in THz imaging systems.

## 1.4. Graphene in Terahertz Optics

As compact THz imaging systems are rapidly improving [1], it causes a growing demand for novel alternative materials that not only possess the properties suitable for THz optics but also are as thin as possible. The vast majority of optical components employed in THz systems are static and lack a variability of their characteristics [47]. The ability for optical elements to be dynamically tuned in real-time would be a significant benefit in modern imaging systems, enabling diverse modifications of the THz beam to be achieved using the same components. A perfect solution for this requirement could be graphene, which today is one of the most popular and highly promising materials. Whereas the primary reason that has gained graphene popularity and recognition is its outstanding features. First of all, it is the thinnest known material with a thickness of only 0.3 nm, however, graphene is also the strongest material ever measured. Furthermore, it displays excellent electrical conductivity, conducts heat better than all other materials, and is transparent, although so dense that it is impermeable to gases [48]. Moreover, due to its unique energy band structure, graphene can be modulated, thus enabling the conception of dynamically tunable optical elements. These amazing properties and their multifunctionality make graphene suitable for a wide spectrum of applications, including THz imaging.

Graphene is a single layer of carbon atoms, arranged in a two-dimensional hexagonal lattice. Essentially, it serves as a fundamental building block for other carbon-based materials as it is shown in Figure 6. For example, the wrapped graphene would make a 0D fullerene, rolled graphene can be transformed into a 1D nanotube and a number of 2D graphene layers stacked on each other gives a 3D graphite that was discussed in Chapter 1.3., and as was demonstrated in [P1], can serve as an excellent flexible material for THz optics. Although for graphene to become a 3D material (graphite), it is commonly understood that at least 10 layers of graphene are necessary [49].

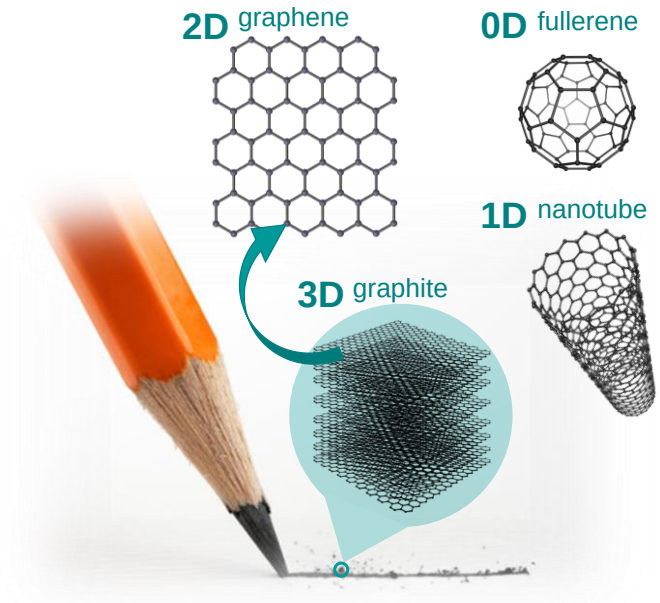


Figure 6: Carbon allotropes: 3D graphite, 2D graphene, 1D nanotube, and 0D fullerene.

The isolation of a single graphene layer was initially accomplished by A. Geim and K. Novoselov [50]. In recognition of their groundbreaking study, both scientists were later awarded the Nobel Prize in Physics.

### 1.4.1. Graphene Sample Preparation

There are several techniques for graphene production, such as:

- Simple mechanical exfoliation, which involves peeling off graphene layers from graphite using adhesive tape.
- Epitaxial growth when due to heating in a vacuum, the graphene grows on a single-crystal substrate.
- Liquid-phase exfoliation, which involves dispersing graphite powder in a solvent and using mechanical disturbance to separate the graphite into individual graphene layers.
- Chemical or thermal treatments that can remove the oxygen-containing groups from the graphene oxide also produce the graphene.
- Chemical vapor deposition (CVD) is the most commonly used method for producing graphene. This process involves depositing carbon atoms onto a metal catalyst surface, generally copper, at high temperatures.

Carbon atoms rearrange in the typical hexagonal lattice and form graphene. This method allows producing large-area graphene sheets.

All samples, investigated in [P2] and [P4] articles were fabricated by transferring the sheets of CVD graphene on the Si substrates. In all cases, the commercially available CVD graphene (from "Graphenea") grown on a copper substrate and covered with ~60 nm thick PMMA polymer, was utilized. The PMMA layer protects graphene and allows one to see its position on the surface of water during the transferring process. To transfer graphene on the Si substrate, a "classical" wet transferring technique was employed.

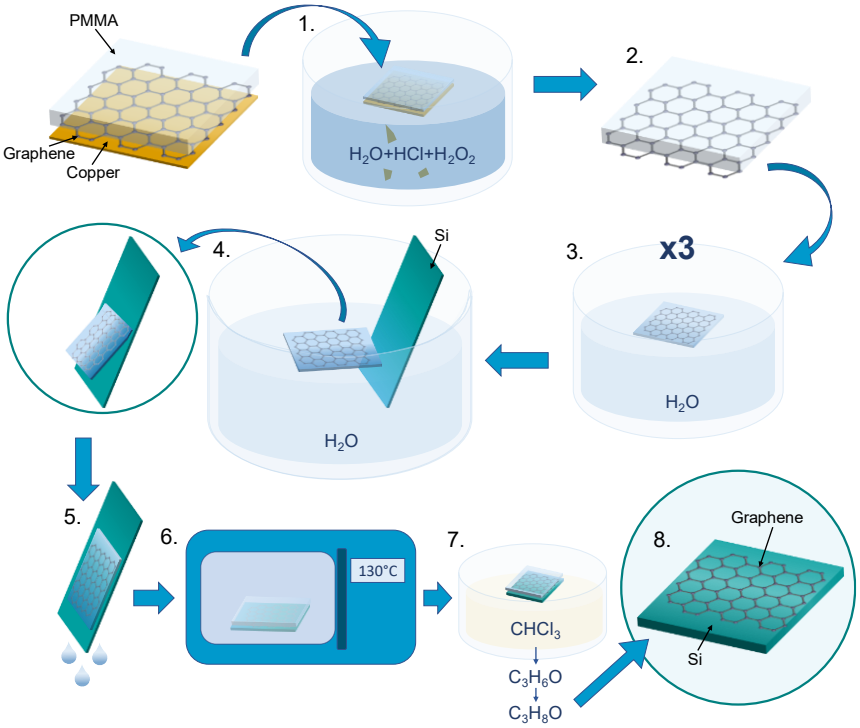


Figure 7: Principal scheme of wet graphene transferring technique.

The procedure of the wet graphene transferring technique is illustrated in Figure 7. As the graphene is grown on copper film and covered with the PMMA film, the initial step involves removing the metallic substrate. For copper etching solution, containing $30H_2O$:$2.5HCl$:$1H_2O_2$, is prepared and left to sit for 30 min. Then the graphene is placed copper-side down on the surface of this solution and left for about 30 min. until the copper is completely etched. Subsequently, graphene, with graphene side down and PMMA film on top is transferred to the surface of distilled water and left to sit for 10 min. This step

is repeated 3 times. After this, the substrate (in this case Si) on which the graphene is to be placed is submerged in the water where the graphene is floating. The substrate is tilted at a right angle and placed next to the edge of the graphene. As the edge of the graphene makes contact with the substrate at the water surface, it sticks to the Si. The substrate is then slowly and perpendicularly pulled out of the water until the entire graphene sheet sticks to it. Si with graphene and PMMA on top is placed vertically and left for the water to run down. When the sample dries out, to improve the adhesion between the graphene and Si, the sample is placed in a heating chamber at room temperature. Then the sample is heated for 30 min. at a temperature of 130°C. After that, in order to remove the PMMA layer, the sample is placed in chloroform and left overnight. For the final step, the sample is removed from chloroform and washed with acetone and isopropanol. As a result, the graphene is transferred on a Si substrate.

### 1.4.2. Graphene Sample Characterization using Raman Spectroscopy

Graphene is both extremely thin and completely transparent for visible light, therefore, a visual inspection of graphene is not possible through the conventional optics. Meanwhile, Raman spectroscopy is a widely used method for the characterization and quality evaluation of graphene. It is a highly sensitive vibrational technique that can detect geometric structure and bonding within molecules [51]. A Raman spectrometer is composed of a monochromatic laser that interacts with the molecular vibrational modes and phonons of the investigated material, resulting in inelastic scattering that shifts the laser energy either down (Stokes) or up (anti-Stokes). When graphene is excited by a laser, it causes the Stokes phonon energy shift that generates three characteristical peaks in the Raman spectrum (Figure 8). G peak at 1580 $cm^{-1}$ corresponds to in-plane vibrational mode. A 2D peak at 2690 $cm^{-1}$ is an overtone of the D band that results from two phonon lattice vibrational processes [52]. The D peak at 1350 $cm^{-1}$ is caused by a disordered structure of graphene. The ratio of D and G peak intensities implies the degree of structural order and quality of graphene. The smaller this ratio, the better the quality [53].

Moreover, an increasing number of graphene layers, due to interactions between them, causes changes in the Raman spectrum. First of all, the 2D peak splits into several modes and therefore becomes wider. Generally, for a single graphene layer, FWHM is ~30 $cm^{-1}$ and it increases with increasing number of layers. Moreover, the G peak red-shifts, and its intensity increases linearly

with the increasing number of graphene layers. Furthermore, it is considered that for a single graphene layer, the ratio of 2D and G peak intensities is equal to 2.

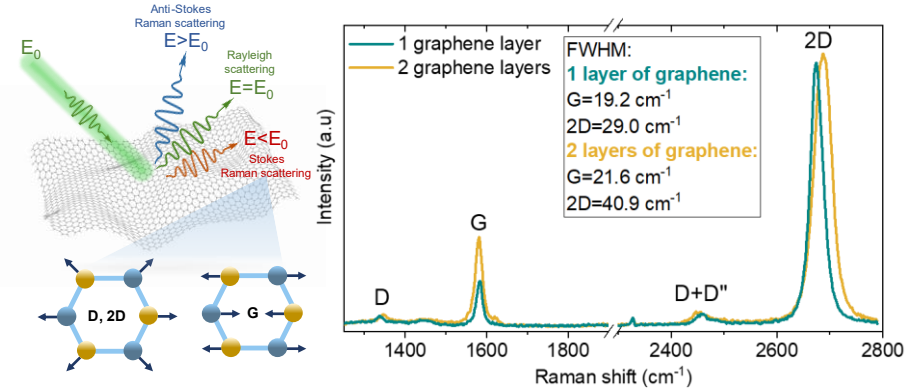


Figure 8: Raman spectra of single and double graphene layers. The illustration on the left side depicts the principle of Raman measurement, where laser excitation in graphene causes Stokes energy shift, which results in main peaks of D, 2D, and G in the Raman spectrum. The illustration on the bottom left side represents the lattice vibrations that cause these peaks.

The graphene samples described in [P2] were also measured with a Raman spectrometer. As one can see, the very weak intensity D peak indicates the lack of defects and good quality of graphene. Moreover, the aforementioned variations in the Raman spectra depending on the number of graphene layers were confirmed experimentally. In this case, double-layered graphene exhibits a wider 2D peak, compared to a single graphene layer. Its FWHM increases by 12 $cm^{-1}$ which indicates 2D peak splitting into overlapping modes. Furthermore, the G peak intensity increased by 2 times with an additional graphene layer. In this case, additional D+D“ bands appear at 2450 $cm^{-1}$, due to the emission of two phonons in the structure. These results confirmed that Raman spectroscopy not only can allow to observe graphene and evaluate its quality but also discriminate the number of graphene layers.

### 1.4.3. Optical Modulation of Graphene in Terahertz Imaging

As it was mentioned, the carbon atoms in graphene are arranged in a 2D hexagonal lattice, which is considered to be comprised of two triangular sublattices (marked in yellow and blue colours in Figure 9 (a)). The distance between two neighbour carbon atoms is 1.42 Å and each of these adjacent atoms pairs form a σ bond, which determines the strength of graphene (Figure

9 (b)). Moreover, each carbon atom forms a π bond, which is orientated perpendicularly to the graphene plane and determines the electrical conduction in graphene. When hybridized together they form a π and π* bands. The unique electronic properties of graphene are primarily attributed to these bands [54].

Graphene is distinguished from other materials by its unique electronic band structure. Its 2D structure results in the first Brillouin zone as a hexagon with six corner points, where two equivalent sets of points marked as K and K‘ are called the Dirac points and indicate two sublattices (see Figure 9 (c)) [54]. This represents the relation between energy and momentum of the graphene structure with six linearly dispersing Dirac cones. Figure 9 (d) shows the enlarged part of cone-like energy bands. As one can see, its valence and conduction bands meet at the Dirac point and therefore graphene is considered a zero-gap semiconductor or a zero-overlap semimetal. The maximum energy state that can be occupied by an electron at absolute zero temperature is called a Fermi level. In the case of neutral graphene, its Fermi level is at the Dirac point. Electrons with an energy of ~1 eV exhibit a linear dispersion. The fact that charge carrier behaviour in this material mimics that of relativistic particles moving at the speed of light, leads to one of the most appealing features of graphene – simple charge carrier modulation [55].

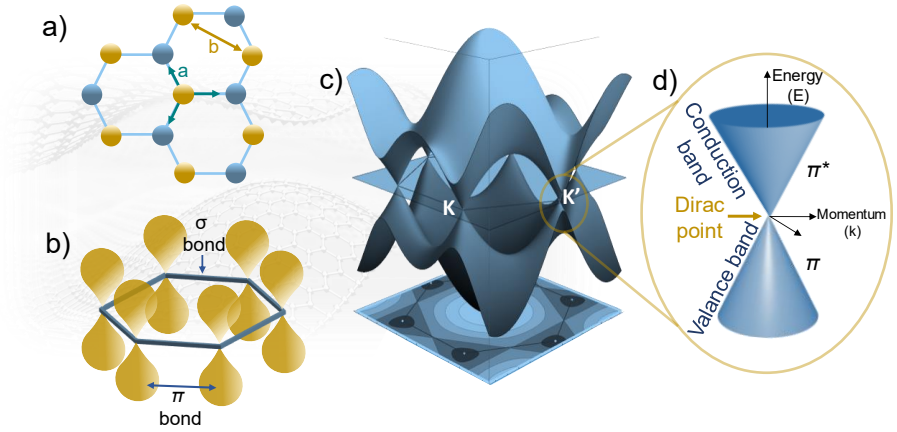


Figure 9: Hexagonal lattice of graphene, consisting of two triangular sublattices (marked in yellow and blue) (a). The distance between nearest neighbours is a=1.42 Å and the distance between the nearest neighbours of the same triangular sublattice is b=2.46 Å. Binding between the carbon atoms in graphene structure (b). Energy momentum spectrum of the graphene band structure (c). Graphene energy band structure near Dirac point (d).

Since graphene is almost completely transparent to THz radiation its transmission must be reduced to utilize it effectively in diffractive optical components. Fortunately, due to graphene's unique cone-like band structure, its transmittance can be modulated by tuning the Fermi level by doping graphene chemically, electrically, or optically. Depending on the doping type (*n* or *p*), Fermi energy decreases or increases when charge carriers are generated (see Figure 10 (b)) [56], [57].

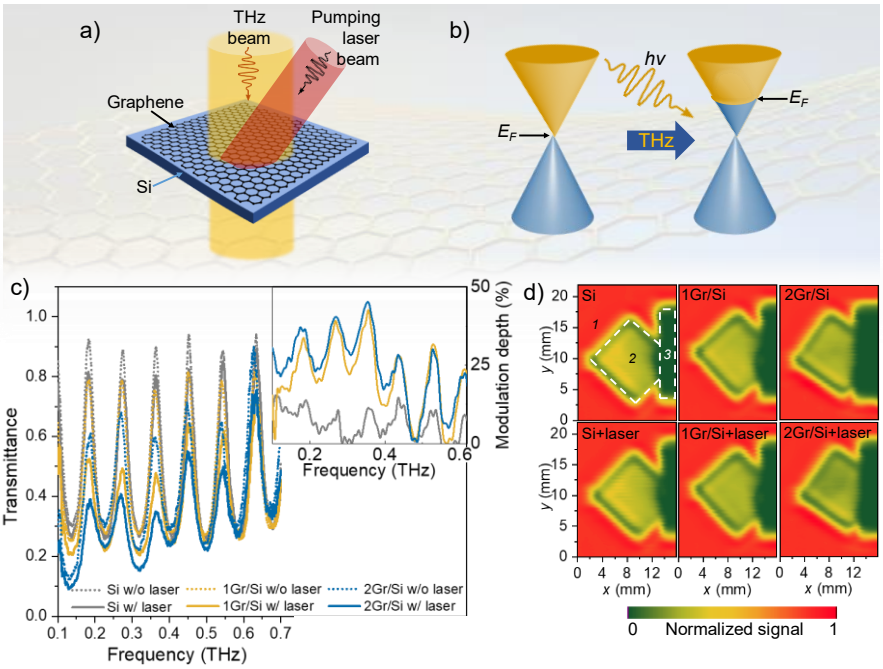


Figure 10: Principal scheme of the experiment with a photoexcitation (a). Graphene energy band structure before (left) and after (right) photoexcitation (b). Transmittance spectra of the investigated samples (c). Dotted lines indicate transmittance without photoexcitation and solid lines – with photoexcitation. Inset depicts the modulation depth spectrum. 2D THz imaging under 0.3 THz frequency illumination: top row represents results without photoexcitation and the bottom row – with photoexcitation (d). The coloured scale is normalized to the maximum signal value. Adapted from [P2].

**In this part of the research, the transmittance tuning of different graphene layers was investigated to validate its potential for implementation in THz imaging systems.** In the study [P2] conducted by our group, optical modulation was chosen due to its simplicity and contactless nature. Two types of samples were fabricated with one and two graphene layers transferred on a high resistivity 460 μm Si substrate. Moreover, the bare Si substrate served as a reference sample. The optical modulation was

induced using a continuous wave laser with a wavelength of 666 nm. The electromagnetic radiation with this precise wavelength can penetrate up to 8 μm into the Si substrate, which absorption coefficient is ~$2.5 \cdot 10^3$ $cm^{-1}$. This relatively shallow penetration depth guarantees easy transfer of the carriers generated in Si to the graphene layers. The optical charge carrier modulation in graphene was investigated by measuring its transmission spectra two times: with and without photoexcitation. The principal scheme of this experiment is shown in Figure 10 (a). Transmission spectra were obtained using the THz spectroscopy system, described in [P2]. Results are shown in Figure 10 (c). As one can see, the transmittance varies due to Fabry-Perot interferration. The modulation depth was evaluated using the equation:

$$M = \frac{T_{w/o} - T_{w/}}{T_{w/o}} \cdot 100\% \quad (7)$$

where $T_{w/o}$ is transmittance without laser illumination and $T_{w/}$ marks a transmittance with laser illumination.

The sample without graphene exhibited the weakest modulation depth, with a maximum value reaching only 14 % at 0.43 THz. As expected, samples with graphene resulted in higher modulation depth: at 0.36 THz modulation depth value reached 42 % for the sample with a single graphene layer and 45 % for the sample with two graphene layers. The reason why samples with graphene exhibit higher optical modulation is the optical injection of carriers. When light is absorbed in the Si layer, free carriers are generated and transferred to the graphene layer to balance the carrier concentration between the two layers. Since graphene has higher carrier mobility, it exhibits increased electrical conductivity, resulting in reduced transmittance. Furthermore, the addition of the second layer of graphene further increases the mobility of transferred free carriers, leading to even greater conductivity and a subsequent higher reduction of transmittance. Based on the findings, optical modulation offers the potential for graphene to be utilized in the creation of optical components that are well-suited for the THz frequency range.

Moreover, samples were investigated using the THz-CW imaging system at the 0.3 THz frequency. Once again, measurements were repeated twice – with and without photoexcitation. Results are depicted in Figure 10 (d). In this case, a single layer of graphene reduces transmittance by 5 %, meanwhile, the double layer of graphene reaches a 12 % reduction. These results enabled the estimation of the contrast for all the samples, which was determined by:

$$C = \left| \frac{T_{w/} - T_{w/o}}{T_{w/}} \right| \quad (8)$$

For samples with single and double graphene layers, the contrast value was 0.16 and 0.23 accordingly. In the meantime, the contrast of the bare Si sample was only 0.05.

Subsequently, in the [P2] study our group attempted to find out whether it is possible to produce a graphene-based diffractive optical element capable of focusing THz radiation. To do this, graphene was transferred on a silicon substrate and patterned as a binary ZP so that only Si was left in the "open" zones and the areas with graphene would correspond to the "opaque" zones. The produced binary graphene-based zone plate (GZP) with a focal length of 10 mm was designed for 0.58 THz radiation and it is shown in Figure 11 (a).

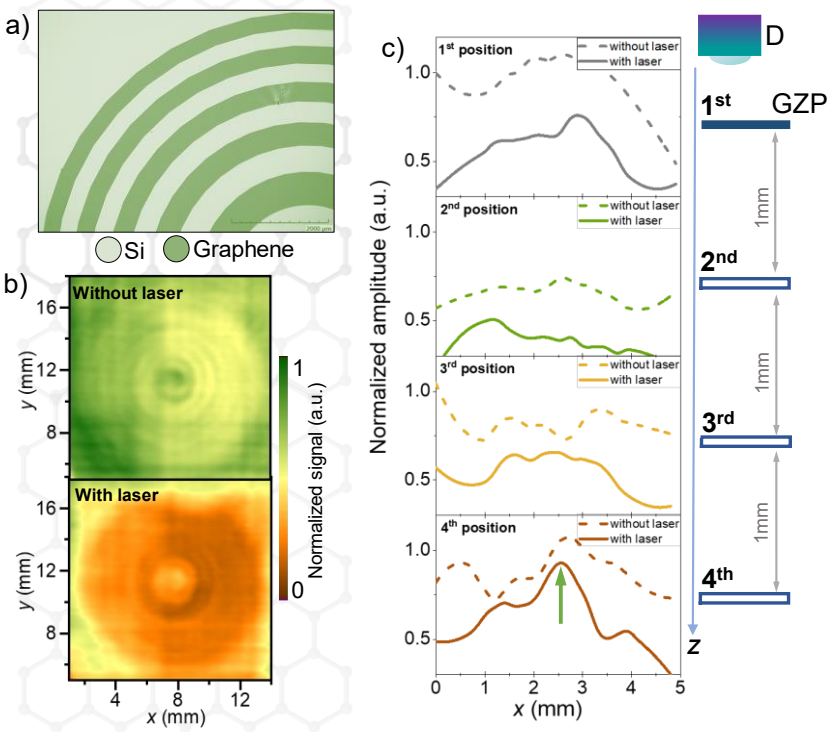


Figure 11: A photo of graphene-based ZP (a). Lighter coloured area indicates silicon and a darker green area indicates graphene. 2D imaging of graphene-based ZP without (top picture) and with (bottom picture) laser illumination (b). The coloured scale is normalized to the maximum value of the signal. Cross-sections of transmitted THz radiation through the graphene-based ZP (c) when it was placed in four different positions, moving GZP further away from the detector (D) with a 1 mm step. Green arrow indicating the focal spot. Adapted from [P2].

The focusing performance of such GZP was investigated using the THz-CW system. 2D imaging of GZP without and with laser illumination is depicted in Figure 11 (b). As one can see, photoexcitation significantly reduced the transmittance of the GZP, increasing the contrast from 0.44 to 4.17, thereby enhancing the element's geometrical structure, i.e., its constituent zones. This implies that optical modulation of GZP decreases the transmittance of the graphene regions, leading to the diffraction of light and consequently, GZP could function as a focusing element. It was examined by scanning the GZP repeatedly, gradually moving it away from the detector with the 1 mm step. The cross-sections of the transmitted signal in all positions are shown in Figure 11 (c). By placing the GZP in the first three positions, the transmittance profile is quite smooth and flat, with values of 0.15 mV, 0.09 mV, and 0.12 mV, respectively. Meanwhile, at the fourth position, the transmittance profile exhibits an expressed narrow peak (marked with a green arrow) which also displays the increase in signal of 0.19 mV, compared to the first three positions.

To conclude, the observed changes, in contrast, indicate that together with optical modulation of graphene charge carrier concentrations, THz imaging systems could potentially be used as a contactless tool for the characterization and discrimination of graphene layers on silicon substrates. This technique could be used as an alternative to Raman spectroscopy to determine the location of graphene on a sample. Additionally, the ability to alter the graphene transmittance provides a potential for a graphene-based dynamically tunable optical element.

The obtained results of the discussed studies allowed to underline the following findings:

- Graphite-based thin terahertz zone plate was produced and its transmittance spectra exhibited an almost identical shape to the metallic terahertz zone plate. Moreover, its focusing performance was evaluated and compared to the unfocused beam, the graphite-based terahertz zone plate demonstrated an increase in signal value by 8.
- Single and double graphene layers transferred on a silicon substrate under laser illumination displayed optical modulation of charge carrier concentrations, resulting in modulation depth values of 42 % and 45 %, respectively.
- By applying the combination of terahertz imaging technique and optical modulation of charge carrier concentration, single and double

graphene layers transferred on silicon substrate exhibited a pronounced change in contrast: 0.16 for single layer and 0.23 for double layer graphene.

- The graphene-based zone plate was produced and its focusing performance was evaluated by employing the optical modulation of charge carrier concentration.

Relying on the presented findings, one can formulate the following statement for defence:

**Optical modulation of charge carrier concentration in graphene on silicon structures simultaneously applied with terahertz imaging increases the contrast by an order of magnitude, thereby indicating the technique as a convenient contactless tool for the characterization of graphene deposited on high-resistivity silicon substrates.**


As it was discussed in PART 1, metamaterial incorporation into DOEs can offer an interesting choice for producing novel and tunable optical elements. Nonetheless, to accomplish this objective, it is necessary to not only select the rational design but also to choose materials that possess the necessary properties for the manipulation of the THz beam. The adjustable geometry of optical components can provide the possibility of altering the focal length of the focused beam, while the tuning of this property can be accomplished through mechanical deformation. Moreover, a proper design of metamaterial geometry provides an opportunity not only to focus the THz beam but also to control the polarization of the incident radiation as well as a selection of the resonant frequency. The following section will discuss flexible metasurfaces with integrated split-ring resonators.

### 2.1. Split-ring Resonators

Another type of metamaterial enriching the functionality of compact THz optical elements are single split ring resonators (SRRs) proposed by Pendry et al. [58] SRR is a conductive ring with a small gap, illustrated in Figure 12 (a). This type of metaatom is designed to be much smaller than the wavelength of incident THz radiation.

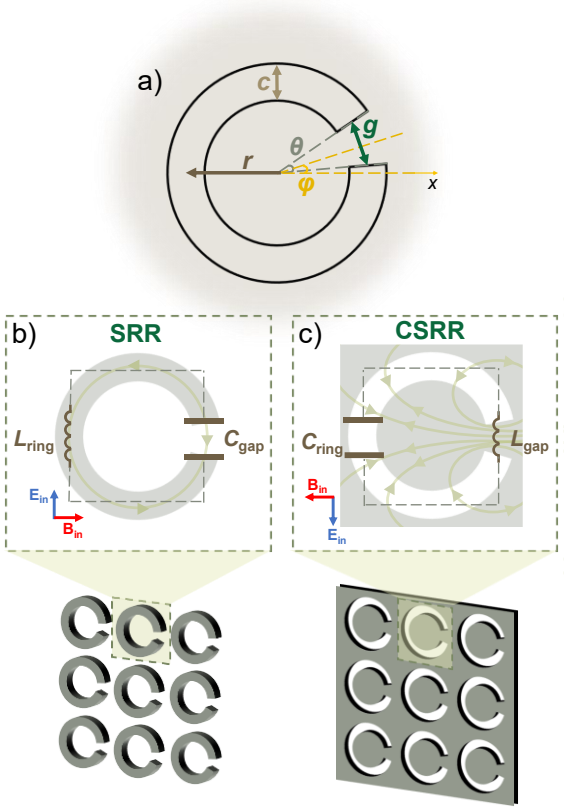


Figure 12: Structure of SRR element and its geometrical parameters: $c$ is the ring thickness, $g$ denotes the gap size, $r$ is the radius, $\theta$ is the cutout angle and $\varphi$ is the position of the gap (a). SRR and CSRR arrays and their equivalent LC circuits (b) and (c), accordingly.

As the electromagnetic wave interacts with the SRR element, an electric current is induced and it begins to circulate through the ring. Charge accumulates across the gap, forming an electric field. The circulating current generates a magnetic field that has a maximum value at the opposite side of the gap. Moreover, the magnetic field is in phase with the electric field of the incident THz wave, thus causing a resonance effect [59].

To simplify the understanding of the SRR principle, it can be depicted as an equivalent LC circuit, where the gap serves as a parallel plate capacitor (with a capacitance $C_{gap}$) and the metal ring acts as a selenoid with one turn or an inductor (with an inductance $L_{ring}$).

The resonant frequency can be calculated [60]:

$$f_0 = \frac{1}{2\pi\sqrt{L_{ring}C_{gap}}} \tag{9}$$

While inductance can be found as:

$$L_{ring} = \mu_0 R_m \left( log \frac{8R_m}{h+c} - \frac{1}{2} \right) \quad (10)$$

where the $\mu_0$ is a free space permeability, $R_m$ is the outer radius ($r+c/2$), $c$ is the width of the ring and $h$ is the thickness of the ring.

Meanwhile, the capacitance of the gap can be obtained by [61]:

$$C_{gap} = \varepsilon_0 \frac{hc}{g} \quad (11)$$

where $\varepsilon_0$ is the metal permittivity and g is the width of the gap.

As one can see, the geometrical parameters of the SRR element play an important role in defining the resonant frequency, which value increases with increasing thickness of the ring and gap width and decreasing radius.

Furthermore, the inverse SRR element, by inverting the roles of the object and background, gives the complementary split-ring resonator (CSRR) [62]. This implies that the ring is non-conductive and is surrounded by a conductive material. The CSRR operates based on the Babinet principle, which states that the diffraction pattern produced by an opaque element (SRR) is equal to the diffraction pattern produced by a transparent element with the same shape and size (CSRR) [63].

In this case, the capacitor is formed in the open area of the ring, giving a larger capacitance than the SRR [61]:

$$C_{ring} = \varepsilon_0 \frac{h(2\pi r - g)}{c} \quad (12)$$

Meanwhile, the metallic gap operates as an inductor.

It is interesting to notice that CSRR produces two - low ($\upsilon_L$) and high ($\upsilon_H$) - frequency modes. When the incident THz wave is perpendicular to the CSRR array and the electrical field component is perpendicular to the gap, the symmetric axis of the current coincides with the gap. Currents flow in mirrored directions at the lower and upper halves of the ring. Since currents are circulating due to the LC resonance, it is influencing the $\upsilon_L$ mode. Meanwhile, for the $\upsilon_H$, the dipole oscillation takes over [59].

In the CSRR case, the width of the metal gap has an impact on the teeter-totter effect in the transmission spectra. With increasing gap width, the transmission at lower frequency mode increases, meanwhile the transmission of higher frequency mode decreases. By selecting the right gap width, both

modes can become equivalent, thus providing a dual band-pass filter that could be well-suited for THz applications [59].

## 2.2. Metasurfaces with Split-ring Resonators

Split-ring resonators can be applied for the fabrication of novel metalenses, which nowadays are successfully paving the way to THz technology and especially - THz imaging. So far, such SRRs employment for metasurfaces that are capable of manipulating THz light, e.g. by focusing the beam or re-emitting the THz wave with different polarisation in comparison with the incident wave, is relatively new. Nevertheless, some outstanding articles demonstrate the diversity and potential of such metasurfaces for applications in the THz range optics [64]–[68].

The main principle behind the use of SRRs in metasurfaces involves arranging these elements in a specific manner and adjusting geometrical parameters such as the cutout angle, radius, or the angular position of the gap that was discussed in Chapter 2.1. In this way, SRRs with distinct geometrical characteristics provide diverse phase changes at different positions, resulting in the convergence of the transmitted beam at the focus.

There is a wide variety of lens designs and materials. For instance, Hashemi et al. [68] proposed an SRRs silicon-based multifocal metalens. In this case, not a usual two-dimensional, but one-dimensional layout was used, where SRRs with divergent cutout angles and angular gap positions were arranged in one row in a way that each adjacent SRR shifts the phase by $\pi/4$. In the work of Gan et al. [64] the employed all-metallic SRRs antennas exhibited wavelength-multiplexed dynamic metalens with high modulation depths that operated at different wavelengths. Despite most research was based on metallic SRRs, it is not always necessary. This was demonstrated by Cheng et al. [67], that proposed an all-silicon-based achromatic metalens with SRRs and CSRRs arrays. By combining the resonant and geometrical phases, the team succeeded in creating an achromatic metalens that has the potential to be used in THz bio-imaging systems.

**In this part of the research, we developed compact, reliable, and flexible metasurfaces containing CSRR elements, perforated into 25 μm thin and flexible stainless steel foil well-suitable for compact and reliable THz imaging aims [P3].**

There were two types of CSRRs elements, distinguished by their cutout angles, which were systematically arranged to operate as a Fresnel zone plate. The initial aim was to find the most optimal geometric parameters of these

elements, that would allow to achieve the most effective operation of such metasurface. The performance of such metasurfaces was theoretically simulated using the FDTD method (Figure 13 (a-c)) and experimentally (Figure 13 (c)) at 0.1 THz frequency, by altering the CSRR radius ($R$), cutout angles ($\theta_1$ and $\theta_2$) and the width of the opening ($c$). Simulations showed that the best results can be obtained when the CSRRs cutout angles are $\theta_1$=40° and $\theta_2$=135°. Moreover, the best value of element radius is $R$=240 μm and the most efficient width of the CSRR is $c$=75 μm. Furthermore, metasurfaces with parameters specified in Figure 13 (c) were studied experimentally and results (marked as symbols) were in good agreement with the theoretical calculations.

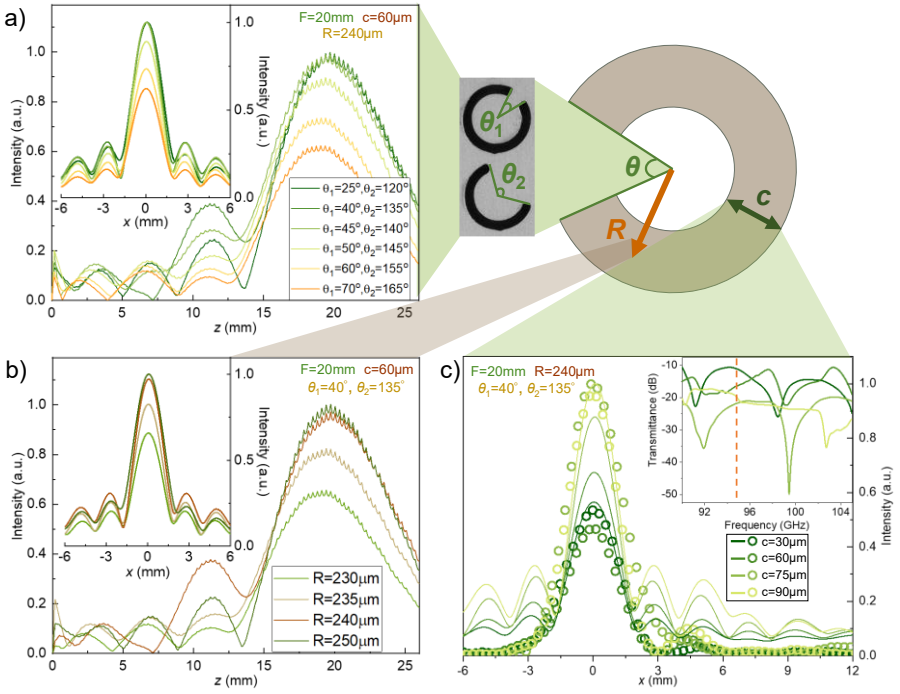


Figure 13: Dependence of CSRR metasurface focusing performance at 0.1 THz frequency on different geometrical parameters: cutout angles $\theta_1$ and $\theta_2$ (a), CSRR radius $R$ (b), and opening width $c$ (c). CSRR element scheme and it's geometrical parameters are depicted in the top right corner. Simulations of the intensity distribution along the optical axis (a) and (b). Insets denote intensities along the $x$-axis at the focal plane. Experimental results (symbols) and simulations (lines) of intensities along the $x$-axis at the focal plane (c). Inset depicts simulated transmission spectra at the focal point and the orange dashed line marks the frequency that was used in the experiment. The polarization of the incident component of the electric field is vertical. Adapted from [P3].

After determining the optimal geometrical parameters of the CSRR elements, four metasurfaces with different focal lengths (F=10, 20, 30, and 40 mm) were fabricated and a detailed investigation of these elements is represented in [P3]. As the metasurface with a focal length of 20 mm demonstrated the most substantial intensity enhancement, it was selected for further experiments.

The investigated CSRR-based metallic metasurface not only displayed remarkable beam focusing but also demonstrated its performance under mechanical deformation, i.e. bending. Experimentally obtained beam intensity distribution along the optical axis is shown in Figure 14 (a), where the top half represents the results of a flat metasurface, while the bottom half depicts a beam focused with a mechanically deformed metasurface. The bending is represented by the $d/L$ ratio, where $L$ is the diameter of the undeformed plate, meanwhile, $d$ is the distance between the opposite ends of the deformed metasurface. Moreover, the inset on the right side illustrates the beam intensity distribution at the focal plane. As one can see, the intensity of the beam, when the metasurface is bent ($d/L \approx 0.72$), decreases to ~30 % maximum signal value with respect to the undeformed plate, although it maintains its focusing ability. Furthermore, even when the metasurface is bent, the shape of the Gaussian beam remains. Its robustness under mechanical deformation can improve the development of THz imaging systems that involves compact and flexible optical elements.

Furthermore, a study [P3] showed that investigated metasurfaces not only can focus the THz beam, but also control the polarization. The polarization-resolved THz imaging was performed using an opaque sample – the metallic target with different widths (1.5, 2, and 3 mm) and period cutout bars. These hollow bars were orientated horizontally and vertically. It is important to notice that the incident electric field component was orientated vertically (marked with a green arrow). The imaging experiment was conducted in several ways. Figure 14 (b) shows the imaging results when the detector recorded horizontal polarization and the metasurface was rotated by 45º. In this particular geometry, the dominant radiation is perpendicularly-polarized, resulting in horizontal bars being more distinctly resolved than vertical bars. However, since the incident wavelength was 3 mm, the largest vertical bars of 3 mm are almost equally distinguishable as the horizontal ones. Moreover, it was estimated that the investigated metasurface exhibited an excellent $0.5\lambda$ spatial resolution.

As it is shown in Figure 14 (c), the metasurface was rotated by an additional 45º into 0º position, while still the perpendicular radiation was recorded. The metasurface that is orientated this way almost does not generate

perpendicularly-polarized radiation, which is why the image of the target is not visible. Figure 14 (d) demonstrates the recording of parallel-polarized radiation when the sample is again rotated by 45º. In this case, the generated parallel-polarized component is very weak, resulting in a blurry image of the target. Subsequently, Figure 14 (e) shows the result of parallel-polarized radiation recording while the metasurface was rotated into 0º position. In this orientation, the metasurface generates parallel-polarized radiation, although it's component is weaker than the perpendicularly-polarized component as in Figure 14 (b) case. In this scenario, polarization-resolved imaging is obtained once again, but with the vertical bars being more distinctly visible than the horizontal bars.

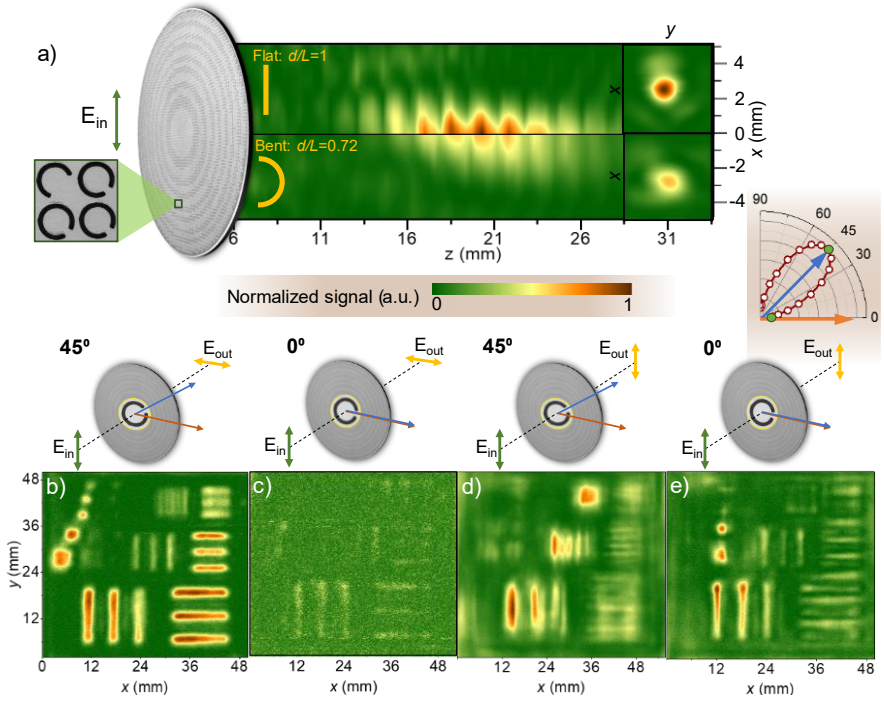


Figure 14: Focusing and imaging performance of metasurface. On the left side of panel (a) – a photo of the metallic CSRRs metasurface, where the enlarged part depicts CSRRs with different cutout angles. On the right side – beam intensity distribution along the optical axis: top half – when the metasurface is flat, bottom half – when the metasurface is bent. The insets on the right depict intensity distributions in the focal plane. The bottom panels (b-e) represents polarization-resolved imaging, obtained by recording different polarizations and by rotating the metasurface by 0 or 45 degrees, which is also indicated by blue and orange arrows. The inset on the right side illustrates the angular intensity dependence, where the green dots represent the metasurface angle during this experiment. The coloured scale is normalized to the maximum value of the signal. Adapted from [P3].

To conclude, the implementation of CSRRs into the Fresnel zone plate extends the capabilities of optical lenses beyond conventional beam focusing by changing the polarisation of the incident radiation and dynamical tuning of the focal point when it is under mechanical deformation. Moreover, by choosing the appropriate materials, such as steel foil, the produced metasurface can be thin and flexible. All these features could significantly improve THz imaging systems.

The obtained results allowed to underline the following findings:

- The flexibility of metasurface with complementary split-ring resonators, fabricated from 25 μm thin and flexible stainless steel foil, allowed it to demonstrate the focusing performance under mechanical deformation, i.e. bending. The intensity of the beam, when the metasurface is bent ($d/L \approx 0.72$), decreases to ~30 % maximum signal value with respect to the undeformed plate, although it maintains its focusing ability. Although the metasurface is mechanically deformed, the shape of the Gaussian beam remains.
- The polarization-resolved terahertz imaging was performed and the results confirmed that the metasurfaces with complementary split-ring resonators not only can focus the terahertz beam, but also control its polarization.

Relying on the presented findings, one can formulate the following statement for defence:

**Metasurface composed from complementary split-ring resonators in flexible stainless steel foil is suitable for polarization-resolved terahertz imaging and focusing even under mechanical bending.**

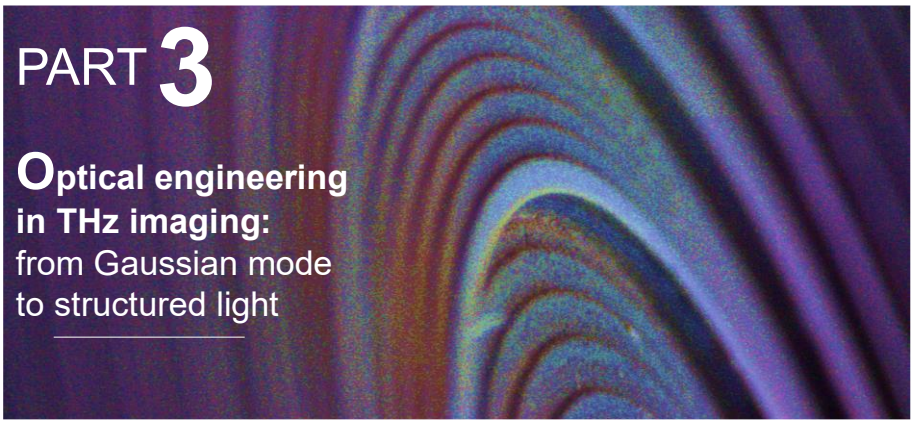


The flat diffractive optics were introduced in PART 1 via Fresnel zone plates. It is worth noting that zone plates of different designs can not only focus or filter the light but also via phase management provide a flexible platform to design optical elements that can manipulate light in different ways, such as forming bifocal focusing (Fibonacci zone plates), beam needle (Bessel zone plate) or bending the beam (Airy zone plate), etc. Depending on the imaged sample or the application requirements, each of these manipulations can enhance the THz imaging capabilities by leading to better contrast, resolution, and sharpness of the obtained images.

**This part of the research represents a comprehensive study of DOEs, such as Fresnel, Fibonacci, Bessel, and Airy zone plates, intended to achieve novel entirely silicon-based lensless THz imaging setup configurations.** The reliability of this systematic study was ensured by implementing consistent fabrication conditions as all investigated optical elements were fabricated from high-resistance silicon substrate with a thickness of 500 μm, using the same femtosecond laser ablation technology [69]. The fabricated DOEs are represented at the bottom of Figure 15. Furthermore, a new approach to optical beam engineering was demonstrated by introducing structured nonparaxial THz illumination in the form of an Airy beam, which improved the quality of THz imaging due to its self-accelerating and non-diffractive nature.

### 3.1. All Silicon-based Terahertz Imaging Setups

Before proceeding to the detailed analysis of beam engineering, the THz imaging setup will be discussed first. In order to evaluate the performance of produced DOEs, a THz-CW imaging setup was employed.

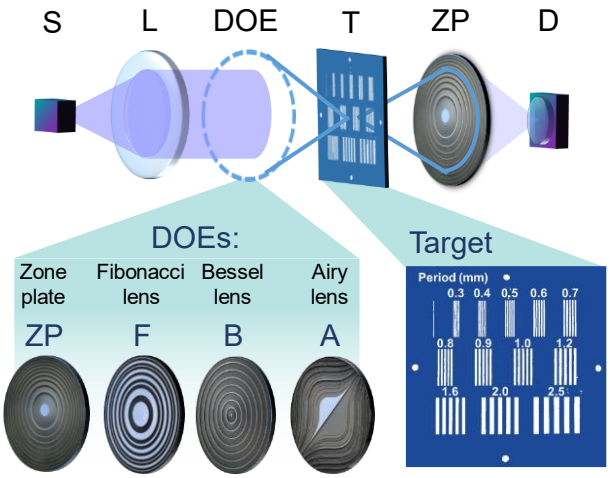


Figure 15: THz imaging setup. S denotes the THz source with a frequency of 0.6 THz. L is a converging lens. A DOE represents a location that may contain any of the diffractive optical elements shown below: zone plate (ZP), Fibonacci zone plate (F), Bessel zone plate (B), or Airy zone plate (A). T is the imaged opaque target, produced from thin metallic foil with cutout different period bars which are more clearly represented in the enlarged illustration of the target ar the bottom right. ZP stands for a collecting zone plate. D is the detector.

The experimental setup consisted of a continuous wave electronic multiplier chain-based emitter (*Virginia Diodes, Inc.*) (marked as S in Figure *15*) that emitted 0.6 THz frequency radiation. After passing the collimating high-density polyethylene (HDPE) lens (L), the beam goes through the investigated DOE that produces structured light and illuminates the imaged target (T). The target is an opaque metallic plate with cut-out different period bars. During the experiment, the target is raster scanned in the transverse direction. This type of imaged sample enables to determine the spatial resolution of the obtained image and evaluate the performance of the investigated DOE. Finally, after passing through the target, the beam is collected by the second DOE - Fresnel zone plate (ZP) and subsequently focused on the detector based on the antenna-coupled nanometric field effect transistor (D).

The focusing performance was investigated using the same setup, only without the target and the second DOE.

### 3.2. Fresnel Zone Plate

The main principle and fundamental concept of Fresnel zone plates were explained in PART 1, Chapter 1.1. This is the most widely used DOE, which

was also utilized in this systematic study by investigating FZP alone and in combination with the other Si-based diffractive optical elements.

Initially, the focusing performance of such FZP was investigated using the setup (its description is given in the previous chapter). The experimentally obtained intensity distribution of the beam passing through the ZP was measured along the optical axis (*xz*) and in the focal plane (*xy*), results are represented in Figure 16. It has been evaluated that the full width at half maximum (FWHM) of the beam at the focal point was 0.27 mm, i.e. almost 98 % narrower than the FWHM of the unfocused beam. In addition, a 65-fold increase in signal intensity was observed, confirming that the Si-based ZP can offer excellent focusing performance and serve as an alternative to bulky conventional optical lenses.

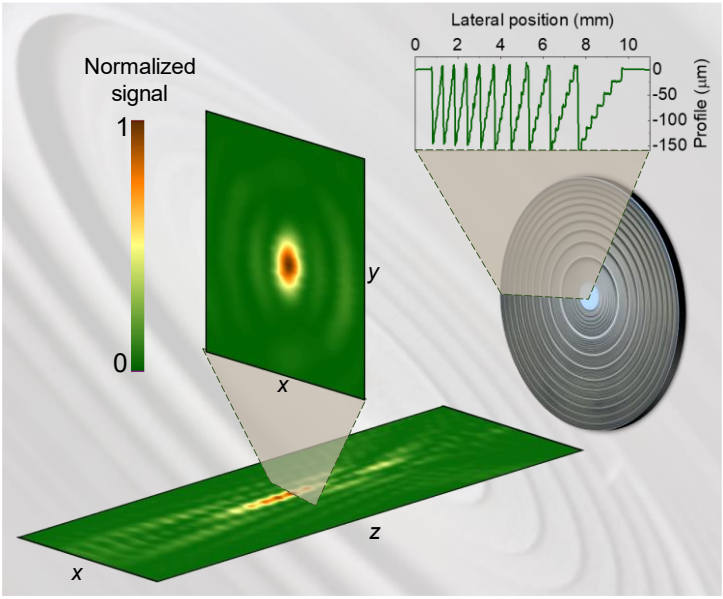


Figure 16: Silicon-based Fresnel zone plate for 0.6 THz frequency. A picture of investigated zone plate and its lateral profile is depicted on the right side. Two-dimensional signal intensity distribution along the optical axis (*xz*) and the beam intensity distribution in the focal plane (*xy*). The coloured scale is normalized to the maximum signal value.

These Si-based FZPs were employed in lensless THz imaging. Experimental setup and imaging results are shown in Figure 17. The intensity cross-sections (see Figure 17 (c)), obtained from this experimental transmittance intensity distribution of the imaged target, allowed to determine the spatial resolution. Since it is known that the wavelength of the beam is 0.5 mm and the individual slits of 0.6 mm period can be distinguished, the evaluated spatial resolution is in the range of wavelength. In addition, an

excellent signal-to-noise ratio (SNR) value of more than 3000 was recorded. These results lead to the conclusion that silicon-based ZP can serve as a useful focusing element in the THz imaging systems.

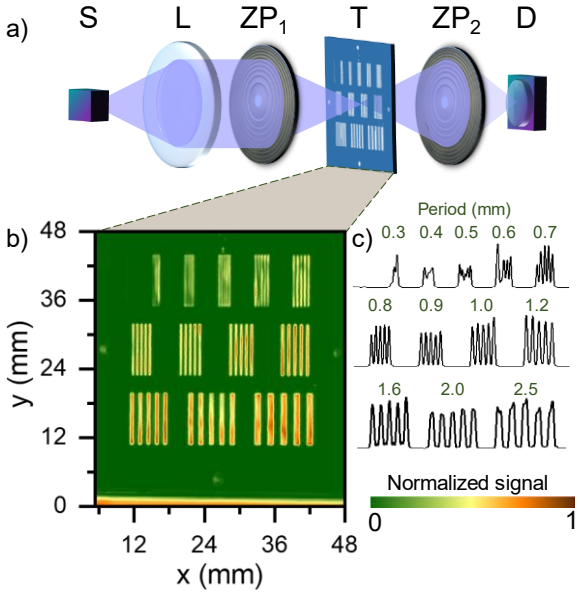


Figure 17: Imaging performance of Fresnel zone plate. Experimental THz-CW imaging setup (a). S marks the monochromatic source of 0.6 THz, L is a conventional converging HDPE lens, $ZP_1$ and $ZP_2$ are identical silicon-based Fresnel zone plates, T denotes the imaged target and D stands for the detector. THz image of the target (b). The colour scale is normalized to the maximum signal value. Signal intensity cross-sections of different period target slits (c).

### 3.3. Fibonacci Zone Plate

Normally conventional zone plates are composed of an equal proportion of opaque and transparent rings. Whereas a Fibonacci zone plate is capable of generating two focal points due to its unique arrangement of rings, which is aperiodic. The advantage of a bifocal lens is that it could allow simultaneous imaging of the contents of bulky objects in two different planes.

The initial step in constructing a Fibonacci plate involves determining its sequence pattern. In the Fibonacci sequence, each number is the sum of the two preceding numbers. Starting from seed values of $F_0=0$ and $F_1=1$, the Fibonacci sequence is defined as $F_{j+1}=F_j+F_{j-1}$, (where j=1, 2...) leading to $F_j=\{0, 1, 1, 2, 3, 5, 8, 13, 21, 34...\}$.

Meanwhile, the golden ratio, i.e. the ratio of the second and the first focal distances, is determined as [70]:

$$\varphi = \lim_{j\to\infty} \frac{F_j}{F_{j-1}} = \frac{1+\sqrt{5}}{2} \approx 1.618 \qquad (13)$$

Considering that the Fibonacci zone plate is binary, its sequence can be obtained using two seed elements $S_0$=0 and $S_1$=1 which are represented in Figure 18, where "0" could correspond to transparent areas and "1" would mark opaque areas. Starting from this, each sequence element can be found using $S_{j+1}=\{S_jS_{j-1}\}$. This gives the element sequence: $S_2=S_1S_0$=10, $S_3=S_2S_1$=101, $S_4$=10110, etc. Here, "0's" are never side by side and are always separated by at least one "1" [71].

Since the Fibonacci zone plate consists of concentric rings, the normalized radial coordinate can be obtained from $\zeta=(r/a)^2$, where $r$ is the radial coordinate, $a$ is the external radius of the Fibonacci plate and $\zeta_{n,j}=(|(\varphi+1)n|-1)$ is the position of the $n^{th}$ "0" element [72].

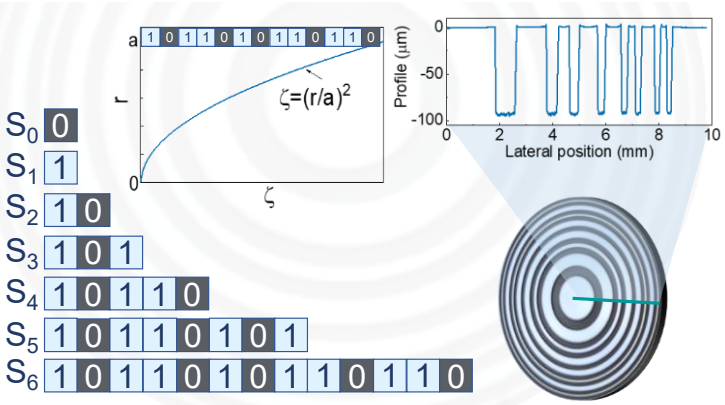


Figure 18: Fibonacci sequence elements ("0" stands for the transparent area and "1" is an opaque area) are depicted on the left side. The top left graph depicts the radial profile of the Fibonacci zone plate. A photo of the silicon-based Fibonacci zone plate is shown on the right side. The inset at the top right side depicts the profile of this element.

As well as the elements discussed in the preceding part of this thesis, the Fibonacci zone plate can also have a complimentary version, where opaque and transparent areas are interchanged. They differ from each other in a way that for conventional Fibonacci zone plates, transparent areas are of different widths, whereas these areas are equal for the complimentary version. Both, the conventional and complimentary Fibonacci zone plates were investigated by R. Verma et al. [70], where it was concluded that the conventional element

is superior to its compliment and that transmitted intensities through these elements were 61.8 % and 38.2 %, accordingly [70]–[73].

**The systematic study was extended by producing a THz Si-based Fibonacci zone plate and enhancing the lensless THz imaging system by adding an option of two foci.** Its focusing performance was evaluated once again using the discussed setup and the obtained results are depicted in Figure *19*. As one can see, the Fibonacci zone plate produced two focal points, where the second one exhibited 25 % higher intensity than the first one. Furthermore, as anticipated, the distance between both foci coincides with the golden ratio.

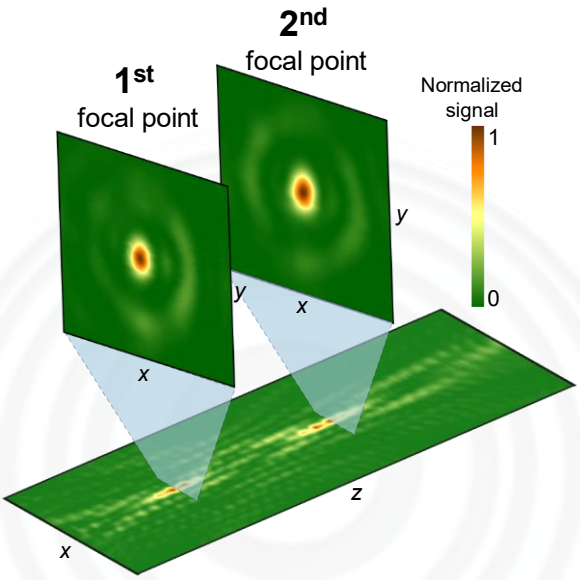


Figure 19: Two-dimensional Fibonacci beam intensity distribution along the optical axis and at the first and second focal planes. The coloured scale is normalized to the maximum signal value.

Subsequently, the Si-based Fibonacci zone plate was combined with the previously discussed FZP, thus enhancing the lensless THz imaging system. The target was raster scanned at both focal points and the results are depicted in Figure 20 (b). Due to the higher intensity of the second focal point, the resulting image exhibits a better resolution, estimated at 1.6λ. Moreover, the estimated SNR at the first focal point is 595 and the value is almost twice at the second focus 1000.

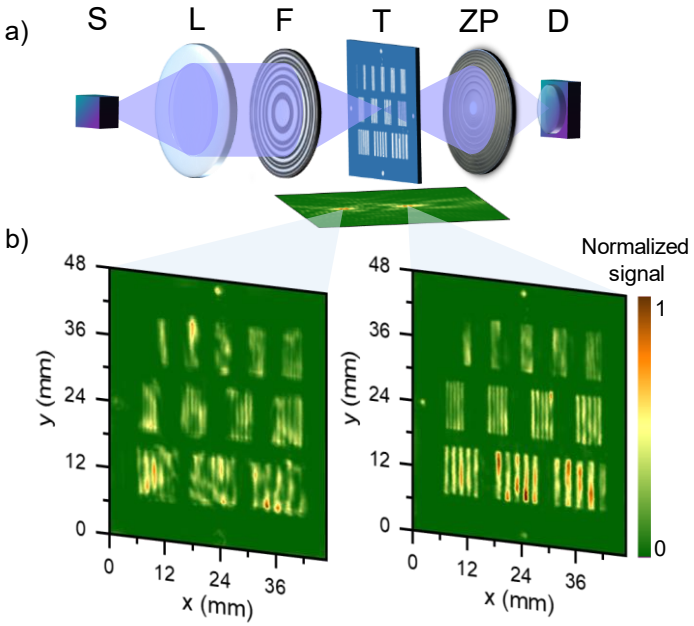


Figure 20: THz imaging setup (a). S is the THz source, L is a collimating lens, F denotes the Fibonacci zone plate, T stands for imaged target, ZP is a zone plate and D is the detector. Inset at the bottom depicts the two-dimensional beam intensity distribution along the optical axis. It indicated the two generated focal points. The experimentally obtained image at the first focal point is depicted on the left side and the image obtained at the second focal point is shown on the right side (b). The coloured scale is normalized to the maximum signal value.

The results obtained endorsed the use of the Si-based Fibonacci zone plate as a highly effective optical element that, when combined with the ZP, could enrich THz imaging systems by producing a bifocal beam, that would allow the imaging in two separate focal planes.

### 3.4. Bessel Zone Plate

Non-diffractive Besel beam derived from its radial transverse profile, which mathematically is described by the Bessel function of the zero-order [74]:

$$I(r,z) = \frac{4k_r P}{w_c}\frac{z}{z_{max}} J_0^2(k_r r) exp\left\{-\frac{2z^2}{z_{max}^2}\right\} \qquad (14)$$

where $k_r = k \sin\alpha$, $k$ is the incident beam wavenumber and $\alpha$ external cone angle, $P$ is the incident beam power, $w_c$ is the beam waist of the incident beam, $z$ is the displacement along the propagation direction, $z_{max} = w_c/\tan\alpha$, and $J_0$ is the first kind zero-order Bessel function.

Bessel functions were first proposed in 1987 as solutions to the Helmholtz equation [75]. These functions describe classical Bessel beams, which are not only non-diffracting but also self-healing and have a remarkable depth-of-field (*DOF*). Bessel beam modes are characterized by the order of the beam – $n$. The zero-order beam exhibits a peak intensity on the optical axis, meanwhile, if $n \geq 1$, the mode has a minimum intensity at the center [76] (see Figure 21). As one can see, when $n=0$, the beam cross-section contains concentric rings and has a bright center. The power in the Bessel beam is equally distributed between the rings. This means that with the increasing number of rings, the power at the center of the axis decreases. However, the more rings it has, the longer the propagation distance.

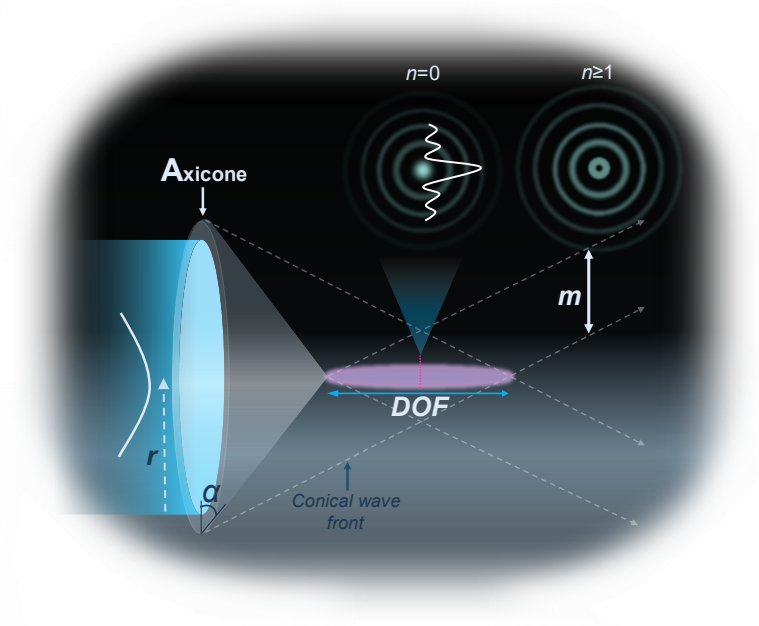


Figure 21: The Bessel beam formation from Gaussian beam, using axicon. The radius of the incident beam is marked as $r$, $\alpha$ is an external cone angle, *DOF* is Depth-of-field and $m$ is the ring thickness. Insets on the top depict a transverse Bessel beam intensity profile, where the $0^{th}$-order beam is shown on the left side, and the beam that has an order, equal to or greater than 1, is depicted on the right side.

In theory, the Bessel beam can consist of an infinite number of rings, carry infinite power, and have an infinite propagation. In reality, such a beam can not exist. J. Durnin and his colleagues [77] suggested a Bessel beam approximation that still acquires characteristics of a theoretical Bessel beam. There are a few options to obtain the approximation of the Bessel beam experimentally by applying a ring-shaped slit or an axicon. Comparing these two methods, the latter is more effective because it employs the whole incident Gaussian beam [78]. Axicon is a conical prism, made of a transparent substrate. When the plane wave reaches the axicon, it forms a beam that propagates very close to the optical axis and is very similar to the theoretical Bessel beam [79]. The axicon converts the incident plane wave into a conical light front, which begins to interact with itself at the axis of symmetry, forming the characteristic needle-shaped Bessel beam, defined by the *DOF* [76]:

$$DOF = \frac{r\sqrt{1-n^2 sin^2\alpha}}{sin\alpha \cdot cos\alpha\left(n\, cos\alpha - \sqrt{1-n^2 sin^2\alpha}\right)} \approx \frac{r}{(n-1)\alpha} \tag{15}$$

where *r* is the radius of an incident beam, *n* is the index of refraction of an axicon, and $\alpha$ is an external axicon angle.

Moreover, the light ring with a constant thickness, *m*, is generated ahead of *DOF*:

$$m = \frac{r\sqrt{1-n^2 sin^2\alpha}}{cos\alpha\left(nsin^2\alpha + cos\alpha\sqrt{1-n^2 sin^2\alpha}\right)} \approx r \tag{16}$$

As one can see, the thickness of the generated light ring is proportionate to the radius of the incident Gaussian beam [76].

However, if the aim is to create compact THz imaging systems, the discussed axicons are too bulky. The best solution to solve this problem is to design a binary axicon, whose performance is identical to the bulky axicon. The binary axicon with a continuous profile can be designed using the equation [80]:

$$h(\rho) = \frac{[\varphi(\rho) mod 2\pi]}{(n-n_0)k} \tag{17}$$

where the $\varphi(\rho)$ is the phase retardation, $h(\rho)$ is the surface height, *n* is the refractive index of the axicon, $n_0$ is the refractive index of air and *k* is the free space wave number.

To obtain the binary axicon, one must compute the continuous profile and then remove the undesired region from the bulky axicon as it is shown in Figure 22 (b). Moreover, such a binary axicon profile can be quantized with equal steps Δ [80]:

$$h_q(\rho) = int\left[\frac{h(\rho)}{\Delta}\right]\Delta \tag{18}$$

where $\Delta = \frac{\lambda}{(n-n_0)M}$ and $M$ defines the number of levels.

With an increasing number of levels, the efficiency of diffraction increases. Although, when considering the production of such multilevel lenses, the more levels there are, the greater the challenges of fabrication. For this reason, it is always necessary to find the optimum number of levels [80].

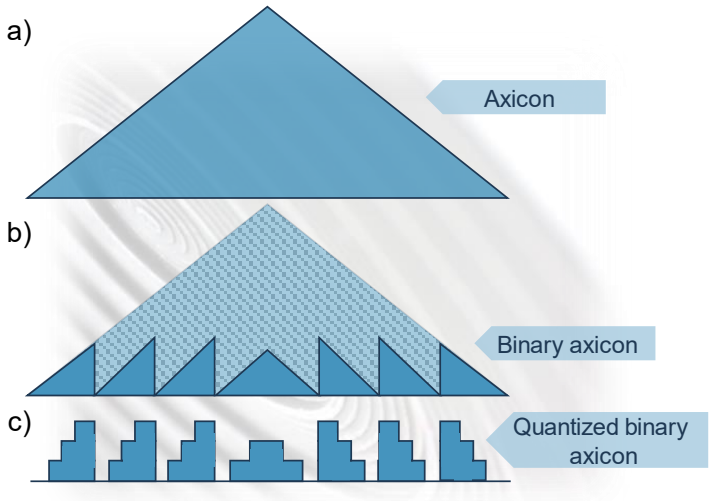


Figure 22: Bulky axicon (a). Darker blue parts depict binary axicon, while the lighter colour area illustrates the removed part from a bulky axicon (b). Binary axicon with quantized four levels (c). Adapted from [80].

Such multilevel zone plates were also investigated by L. Minkevičius et al. [81], [82]. These studies demonstrated excellent performance of silicon-based multi-phase optical elements that generate a Bessel beam and can be adapted to THz imaging systems.

**In this part of the research, we fabricated a Si-based Bessel zone plate, which was also incorporated into a lensless THz imaging system, this time enriching it with a non-diffractive illumination approach.** The focusing performance of the investigated zone plate and the obtained Bessel beam is shown in Figure 23. After the Gaussian beam passes through the

Bessel zone plate, radiation is focused into a 10 mm length “needle“ shaped beam that consists of 5 focal points. As one can see, the distance between these foci increases from 0.2 to 1.5 mm. Moreover, each focal point exhibits a wider FWHM: 1 mm, 1.1 mm, 1.9 mm, 2.2 mm, and 3.7 mm, accordingly.

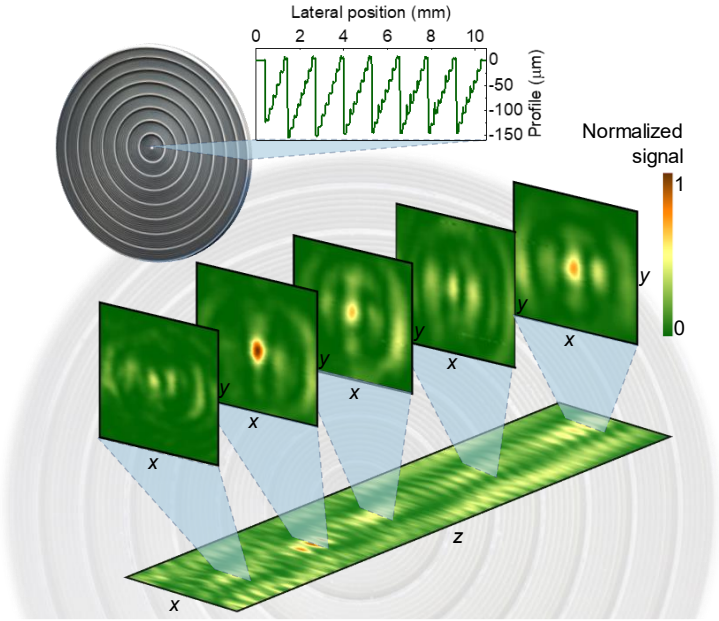


Figure 23: A photo of the Bessel zone plate. Inset depicts the lateral profile of this element. The image below shows an experimentally obtained two-dimensional beam intensity distribution along the optical axis and at the focal planes of five major foci. The coloured scale is normalized to the maximum signal value.

Bessel zone plate imaging performance was also experimentally investigated, and the obtained results are depicted in Figure 24. The target was imaged in all five focal planes and the estimated spatial resolution varied between 2.4λ and 1.6λ. As one can see in Figure 24 (b), the image of the target is vivid in a wide focal range. This feature can improve THz imaging by providing the benefit of scanning thick samples or evading the requirement of placing objects in a very specific spot in order to get a sufficient quality of image.

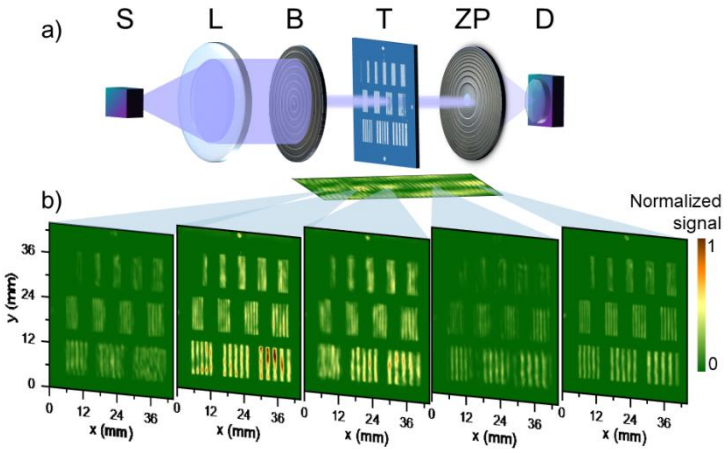


Figure 24: THz imaging setup (a). S denotes the THz source, L is a collimating lens, B stands for Bessel zone plate, T is imaged target, ZP is a zone plate and D is the detector. The inset below depicts the two-dimensional beam intensity distribution along the optical axis with expressed five major focal points. Experimentally obtained images of a target at the corresponding focal points (b). The coloured scale is normalized to the maximum signal value.

Until now, there has been only a brief mention of another very important and distinctive Bessel beam characteristic. Given that the Bessel beam can be considered as a set of waves propagating on a cone, it acquires a self-healing feature. If the beam encounters an obstacle, that is smaller than the Bessel zone plate, it will not diffract, however, the structured Bessel illumination will reappear behind the obstacle and continue to propagate. This feature was investigated in [P3] by imaging the same metallic target, only additionally placing an opaque metallic plate as an obstacle between the Bessel zone plate and the target. In this case, as the radiation passes through the Bessel zone plate, it generates a conical wavefront and when the obstacle is placed in front of the Bessel zone plate, it covers only a part of that conical wavefront. The uncovered part of structured light propagates further and reaches the target.As it is shown in Figure 25 (b), the obstacle was covered by a gradually increasing area of the Bessel beam (10 %, 30 %, and 50 %). An evaluated spatial resolution was 1.6λ for both 10 % and 30 % cases and it decreases to 3.2λ when the obstacle covered 50 % of the area. Although with the increasing coverage of the element, contrast drops from 35 (a.u.) to 3 (a.u.).

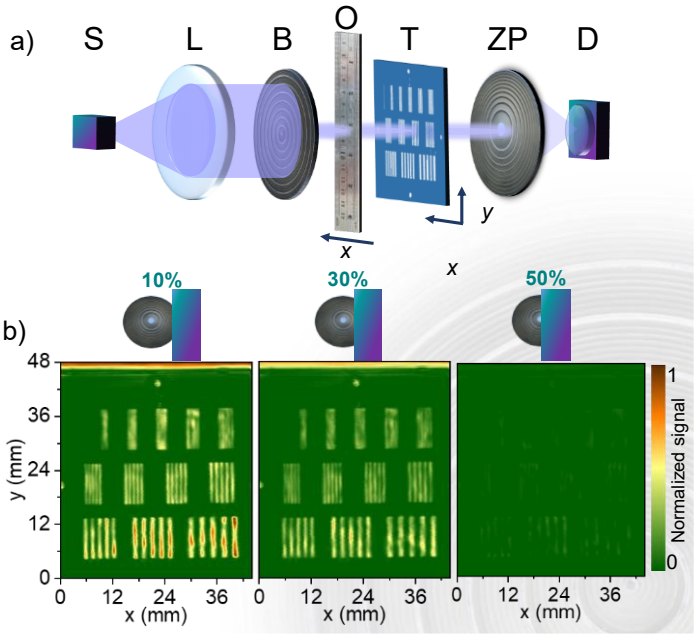


Figure 25: Imaging setup with an obstacle (O) impermeable for THz radiation (a). Experimentally obtained images of the scanned target, with the obstacle covering (from left to right) a 10 %, 30 %, and 50 % area of the Bessel zone plate (b). The coloured scale is normalized to the maximum signal value.

These results show that by employing the non-diffractive feature of the Bessel beam, the THz imaging system is improved by acquiring the ability of imaging samples even in the presence of an opaque obstacle.

### 3.5. Airy Zone Plate

The study of Bessel beams has created opportunities for the discovery and development of other non-diffracting solutions. One of the examples could be the Airy beam [83]. Similar to Bessel, Airy beams are also non-diffracting and exhibit a self-healing feature. However, Airy has another remarkable and unique characteristic of self-acceleration. Its concept is derived from quantum mechanics. In the study by Berry and Balazs (1979) [83] it was demonstrated that the Airy function is an eigenmode of the linear Schrödinger equation, and it is the only non-trivial solution that does not spread with time, but instead accelerates as it propagates through space [84].

To experimentally generate the Airy beam, Siviloglou et al. [85] proposed to modulate a Gaussian beam with a cubic phase. To accomplish this, they utilized a spatial light modulator (SLM) to apply the cubic phase modulation. The Gaussian beam was directed through the SLM and a

cylindrical converging lens. The Fourier transform of the modulated Gaussian beam was obtained at a specific distance behind the lens, resulting in the generation of an Airy beam.

**In this study, our group proposed and demonstrated a flat Si-based Airy zone plate enabling the generation and application of THz structured light in the form of an Airy beam [P4].** At this point, the structured THz illumination acquires a new supplemental feature of self-acceleration, which enables imaging of objects partially covered by an opaque beam block. Contradictory to conventional paraxial methods, a combination of Fresnel and Airy zone plates generates a nondiffracting Airy beam that can be employed in lensless THz imaging systems.

Structured light is electromagnetic radiation that exhibits a spatial variation in amplitude, phase, or polarization across the transverse plane. The initial objective was to experimentally generate structured nonparaxial Airy beams. To achieve this, experiments were performed using two setups, shown in Figure 26 (b,c).

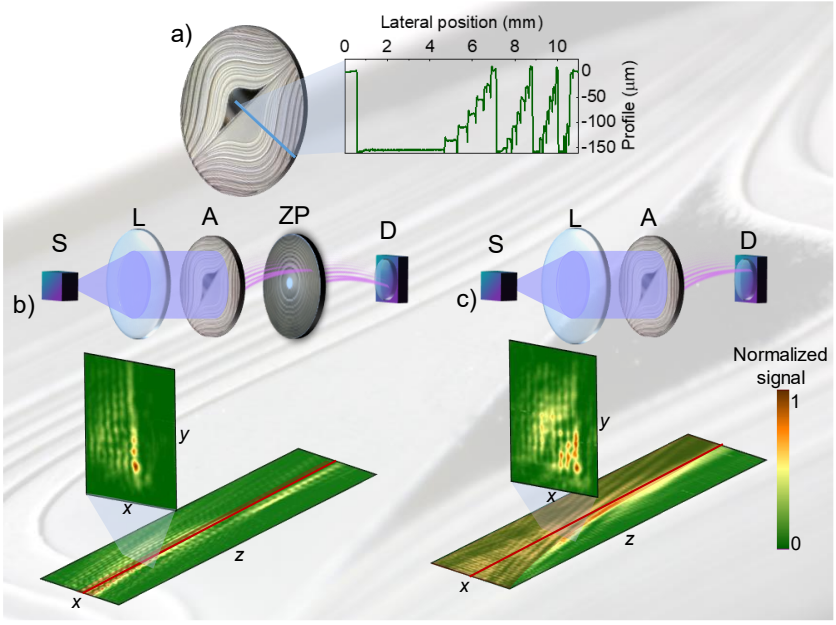


Figure 26: A photo of Airy zone plate (a). Inset depicts the lateral profile of this element. 2D beam intensity distribution in optical axis and focal plane, obtained using setup with combination of Airy and Fresnel zone plates (b) and only Airy zone plate (c). Red lines are guides for an eye to highlight the Airy beam which exhibits parabolic trajectory. The light red-shaded area emphasizes the reciprocal trajectories. Setups are depicted at the top of each segment. Coloured scale is normalized to the maximum signal value.

The initial setup configuration incorporates both - Airy and Fresnel zone plates, whereas the second setup only utilizes the Airy zone plate. The implementation of both Airy and Fresnel zone plates generate a beam with a consistent shape of longitudinal intensity distribution along the optical axis throughout the range of 0 to 10 mm, see Figure 26 (b). The obtained Airy beam exhibits a parabolic trajectory. The intensity distribution in the focal plane (transverse plane) displays some distortion due to the nonparaxial focusing via the zone plate. Moreover, the SNR reaches the value of 1180.

In contrast, the results achieved with the single Airy zone plate illustrate that the Airy beam establishes a reciprocal self-bending as it propagates through free space, maintaining its form over a distance of 6-16 mm. Meanwhile, the beam intensity distribution in the focal plane remains undistorted, and both "arms" are perpendicular to each other. Although, as the beam propagates along the optical axis, its dimensions increase proportionally to $z^2$. In this case, the SNR is 570. Both scenarios showed that due to the nonparaxiality of the Airy zone plate, it can generate a nonparaxial structured light either with or without the additional zone plate.

As it was shown in Chapter 3.4., the self-healing feature of the beam can be exploited for THz imaging behind the obstacle. The same experiment was replicated using the Airy zone plate in both ways: with (Figure 27 (a)) and without (Figure 27 (b)) the supplementary zone plate. The opaque metal plate was used as an obstacle, and it was positioned between the illuminating element and the imaged target. The imaging process was reruned several times with the obstacle gradually covering a greater area (10 %, 30 %, 50 %, and 60 %) of the illuminating element.

In the case where a single Airy zone plate was employed (Figure 27 (a)), even with the greatest coverage of the element, the image of the sample is still clear. Although the intensity is reduced, the bars with a period of 1.6 mm can be resolved, resulting in a spatial resolution of 3.2λ and a contrast value of 26 (a.u.). Nonetheless, employing the combination of an Airy and Fresnel zone plates (Figure 27 (b)) shows better results. After the obstacle covering 60 % of the illuminating element, the detected image is still clear and the bars with the period of 0.8 mm can be resolved, offering an improved spatial resolution of 1.6λ. Meanwhile, the contrast value slightly decreases to 21 (a.u.).

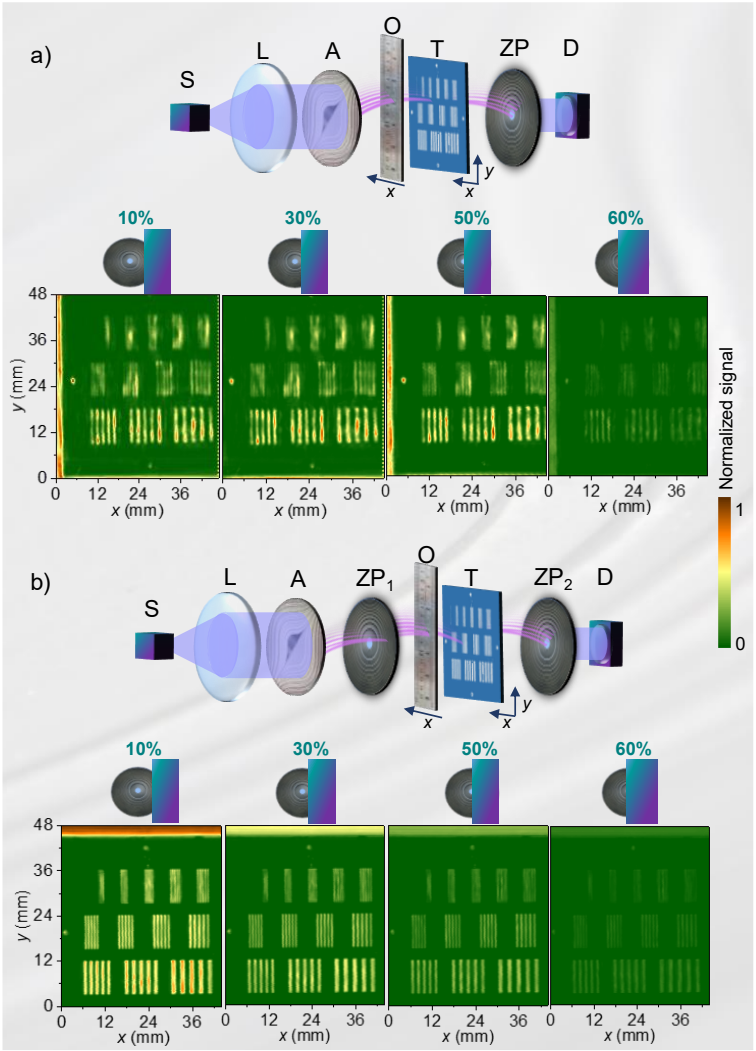


Figure 27: Imaging behind the obstacle, using setups where the target was illuminated with only Airy zone plate (a) and with a combination of Airy and Fresnel zone plates (b) when the obstacle covered 10 %, 30 %, 50 % and 60 % of the illuminating element area. Setups are depicted at the top of each segment. The coloured scale is normalized to the maximum signal value.

These results showed that the combination of the structured THz illumination generating elements plays an important role in the quality of THz imaging. With respect to the results, when the Bessel zone plate was used, at more than 50 % coverage no image of the sample was obtained. Meanwhile, when the Airy zone plate was employed, even with the reduced contrast, the obtained images were clear and exhibited sufficient spatial resolution.

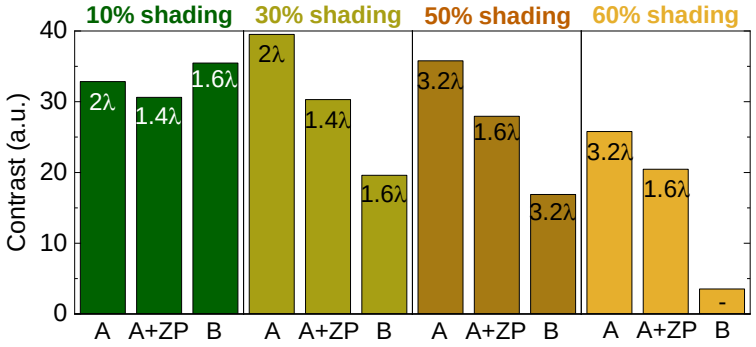


Figure 28: Spatial resolution and contrast obtained using different combinations of diffractive zone plates, with varying coverage (10, 30, 50, 60 %) of the illuminating element. The values of spatial resolution are marked inside the coloured bars. A denotes the setup with only the Airy zone plate as an illuminating element, A+ZP is the setup with a combination of Airy and Fresnel zone plates and B marks the setup with the Bessel zone plate. Adapted from [P4].

For better clarity, the dependence of contrast and spatial resolution on the varying coverage (10, 30, 50, and 60 %) of the illuminating element is shown in Figure 28. These values are obtained from the imaging results, shown in Figure 27. The contrast is defined as the ratio between the maximum and minimum intensity and its values are given on the *y*-axis. The spatial resolution values are marked inside the coloured bars. A denotes the setup with only the Airy zone plate as an illuminating element, A+ZP is the combination of Airy and Fresnel zone plates and B marks the setup with the Bessel zone plate. The performance of a single Airy zone plate decreases with increasing coverage, the spatial resolution reduces from 2λ to 3.2λ. The combination of Airy and Fresnel zone plates exhibits better performance – there is only a slight change in spatial resolution from 1.4λ to 1.6λ. Meanwhile, in the case of the Bessel zone plate, the spatial resolution decreases from 1.6λ to 3.2λ. Furthermore, when more than half of the element is covered, it is no longer possible to distinguish the resulting image. In all cases contrast decreased with the increasing coverage.

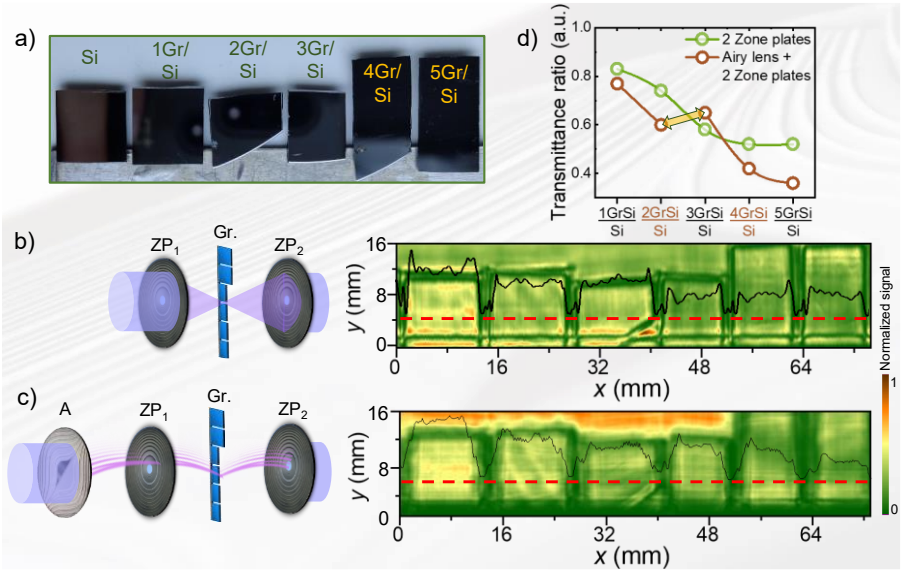


Figure 29: A photo of imaged sample, consisting of Si and various numbers of graphene layers (a). Imaging of graphene samples using only Gaussian illumination (b) and the illumination of nonparaxial Airy beam (c). The coloured scale is normalized to the maximum signal value. Black lines represent the intensity profile of imaged samples and the red dashed line marks the position of this cross-section. Setups are depicted on the left side of each segment. Transmittance ratio of graphene samples for both setup configurations (d).

The encouraging outcomes from the previous experiments sparked the interest in structured nonparaxial Airy THz illumination capabilities in the imaging of 2D materials. In this experiment, we chose graphene as a material of high interest for THz research. Despite the fact that graphene is very thin and exhibits low absorption, phase changes can be expected in the structured light illumination of graphene layers. Due to this, in the [P4] research 5 samples with 1, 2, 3, 4, and 5 graphene layers, were transferred on the Si substrate, while another sample of bare Si served as a reference (see Figure *29* (a)). The samples were investigated using THz-CW imaging system. The employed experimental setups were of two different configurations: the first one consisted of only two zone plates and produced Gaussian illumination while the second one contained a combination of the Airy and Fresnel zone plates resulting in nonparaxial Airy beam illumination. For the first setup that employed only the Gaussian illumination (Figure *29* (b)), it was noticed that with an increasing number of the graphene layers the intensity of the signal slightly decreases, although this dependence was weaker for samples with more graphene layers (4-5). In this case, the SNR value was 118. However,

for the second setup, delivering the structured illumination of the nonparaxial Airy beam, the intensity dependence on the number of graphene layers is no longer monotonical. It was noticed that the transmittance of the sample with 3 graphene layers increased in comparison with the results, obtained using Gaussian illumination. Moreover, these 4 and 5 graphene layers exhibit a greater difference of ~40 % in intensity. Furthermore, the combination of the Airy and Fresnel zone plates results in SNR=326, which is almost triple than for the setup without the Airy zone plate. This can be explained by taking into account the effects associated with the light polarization. Slight variations in the thickness of the sample or refractive indices of both the graphene and Si substrate can impact the transmissivity. For a better understanding of this effect, in the supplementary material [S1] of the [P4] publication the 2D plot of the transmission through the layered graphene structure was simulated.

The transmission of the *s*-polarized Gaussian beam $T_s^{Gauss}$ is depicted in Figure 30 (a). For comparison, to illustrate the difference caused by the structured illumination, the plot of the $T_s^{Airy}/T_s^{Gauss}$ ratio is presented in Figure *30* (b). The results suggest that the sample containing 3 graphene layers might behave differently due to the interaction of the graphene layer and the Si substrate, which leads to changes in the refractive index (*n*) of the Si or graphene conductivity. When the graphene becomes metallic, i. e. its refractive index (*n*) strongly changes, the difference in transmission of the light with varying polarizations is observed. When the incident angles of light are larger, graphene exhibits enhanced transmission of *p*-polarized light. However, at smaller incident angles, *s*-polarised light is transmitted better.

Whereas, the Gaussian beam propagates near the optical axis, the graphene displays a similar effect on *s* and *p*-polarized THz light. As can be seen from Figure 30 (a), the presence of variations in the real part of the refractive index results in an interferometric oscillatory pattern in the transmission for both *s* and *p* polarizations. However, in the case of the structured light illumination, the Airy beam spreads out leading to diverse incident angles and resulting in the more pronounced difference between polarizations. This can be seen in Figure 30 (b), where the oscillatory pattern differs from the case with the Gaussian illumination.

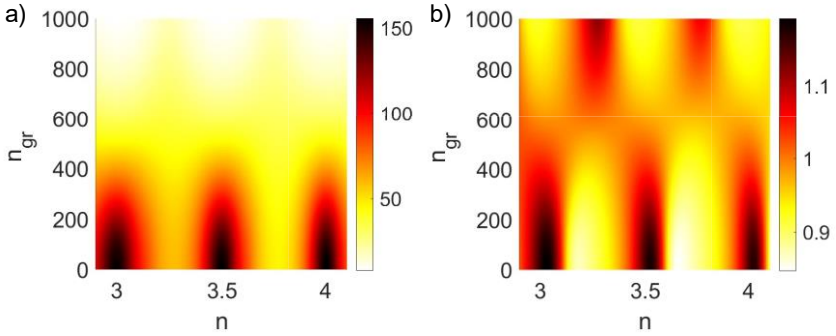


Figure 30: The transmittance distribution of the s polarized Gaussian beam passed through the 3 graphene layers placed on Silicon on the effective refractive index *n* of the Si and the normalized conductivity of graphene (a). Transmittance distribution of the ratio between the *s*-polarized Gaussian beam and the *s*-polarized Airy beam ($T_s^{Airy}/T_s^{Gauss}$) (b). Adapted from [S1].

The obtained results allowed to underline the following findings:

- It was shown that the combination of silicon-based Airy lens and zone plate generates a nondiffracting nonparaxial Airy beam with the parabolic trajectory and can significantly improve the signal-to-noise ratio from 570 to 1180, moreover, resulting in twice better spatial resolution (1.6λ), when compared to the performance of the single Airy lens, that produces the expanding Airy beam with the reciprocal trajectory.
- It was demonstrated that the Airy zone plate provides the capability to perform terahertz imaging in the presence of an opaque beam block. It was shown that even when the 60 % area of the illuminating Airy zone plate was covered, the obtained image was still clear, exhibiting a contrast of about 30 (a.u.) and a spatial resolution of 3.2λ. Meanwhile, when the combination of Airy and Fresnel zone plates was employed, the spatial resolution was significantly better - 1.6λ.
- The structured nonparaxial Airy beam provides a possibility for the evaluation of the optical properties of graphene layers. It was demonstrated that imaging of 2D samples with conventional Gaussian illumination gives a signal-to-noise ratio value of 118. The combination of Airy and Fresnel zone plates exhibits a three times higher signal-to-noise ratio with a value of 326.

Relying on the presented findings, one can formulate the following statements for defence:

**The nonparaxial structured light in the shape of THz Airy beam can be generated using silicon-only based diffractive optics and its accelerating nature can be applied for imaging of partially obscured objects.**

**The structured THz light illumination outperforms conventional Gaussian one in terms of resolution and contrast in THz imaging of thin graphene layers.**

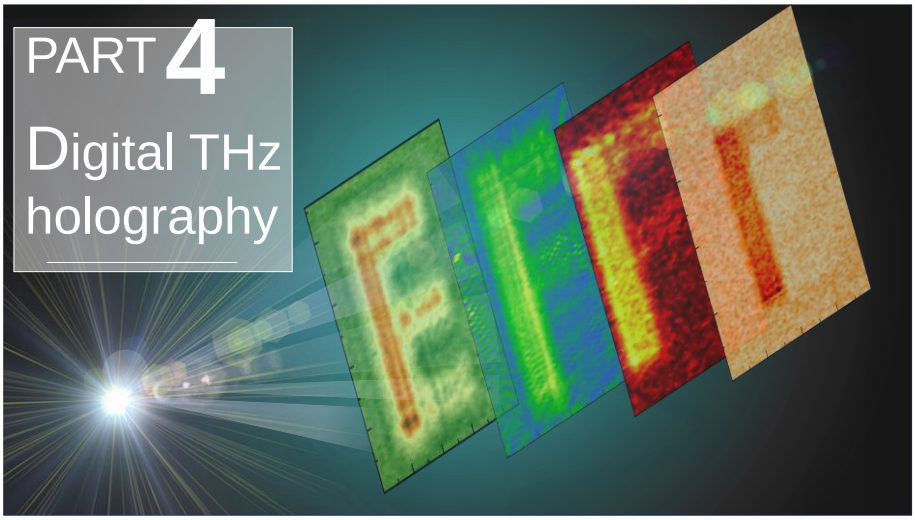


The distinctive properties of THz radiation make it a favorable option for imaging applications, including cases when imaged objects exhibit low absorption. It relies on phase shifts related effects rather than change in the intensity. As a rule, this approach requires a coherent way of image recording employing either heterodyning or homodyning techniques. In contrast to aforesaid methods, it is capable to reconstruct 3D images enabling thus obtaining the whole information on intensity and phase distribution in the object under test. This feature provides holography an advantage in discriminating transparent and low-absorbing materials.

### 4.1. Introduction to Holography

Holography is the best-known technique for reproducing 3D images. This method was invented by Dennis Gabor in 1947 [86], who later was awarded the Nobel Prize in Physics. Unlike conventional photography which captures only the intensity of the light, the holography registers both the intensity and the phase information of light.

To record a holographic image, the laser beam is split into two parts (see Figure 31). The first beam (the object beam) is reflected from (or transferred through) the sample and reaches the hologram plane. This beam contains information about the imaged object. The second beam (reference beam) goes straight to the hologram plane. Both – object and reference – beams meet at the hologram plane and create an interference pattern. This pattern encodes the specific 3D information about the imaged object. Hence, the object beam (A) and the reference beam (B) give the interference pattern (C): A+B=C. In order to reconstruct the hologram and obtain the real 3D image of the object

(A), the recorded interference pattern (C) needs to be illuminated with the reconstruction beam, which is identical to the reference beam (B): A=C-B. The reconstructed beam (A) is identical to the object beam, thus it recreates a 3D image of the object.

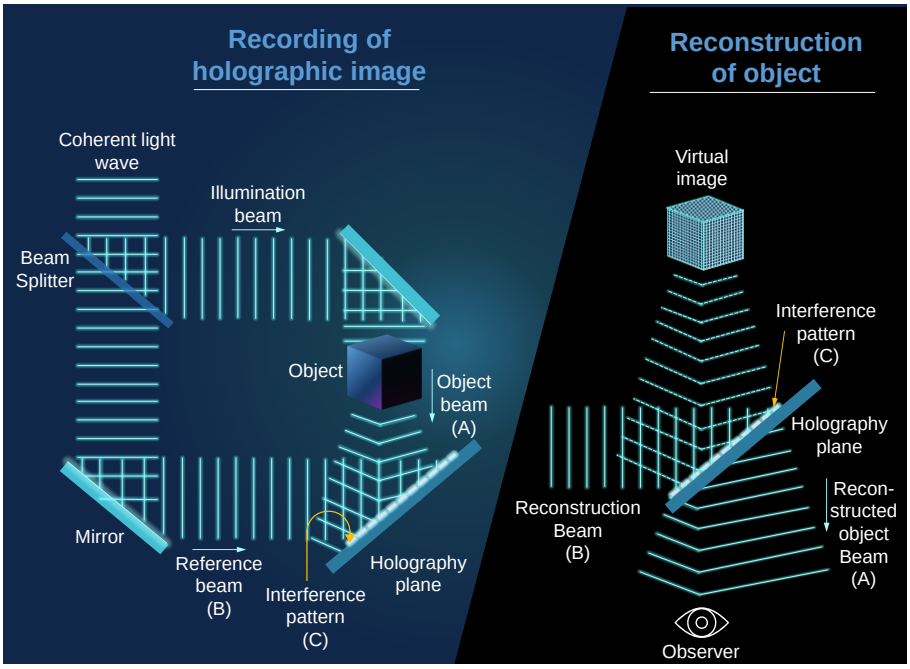


Figure 31: The principal of holographic image recording on the left side and the principal of object reconstruction on the right side.

In contrast to conventional photos, each part of the hologram, due to the phase, contains information about the whole image. Therefore, if the hologram plane would be split into many fragments, the complete image can be reconstructed from each separate piece of the hologram.

THz holographic images can be recorded and reconstructed using a wide range of techniques [87]. Among the most common techniques is the Fresnel hologram, which is based on the interferometer principle. However, THz holography still faces many challenges because of the need for reliable, sensitive detectors that can operate at room temperature and the limitations of low power of THz radiation sources. Numerous intriguing approaches have been explored to enhance THz holography, including near-field holography [88], time-reversal [89], off-axis [90], [91] and in-line [92] holography of hidden objects. Furthermore, the quality of recorded holographic images can be significantly enhanced by using contemporary THz holography solutions such as the step phase shifting technique, which is investigated and discussed in the following chapter.

**In this part of the research, our group conducted a [P5] study where a novel two- and four-step phase-shifting technique in THz digital holography was introduced.** By shifting the phase of the reference beam, this approach enables the reconstruction of 3D objects. By utilizing a setup based on the Mach-Zehnder interferometer, two- and four-step phase shifting (PS) methods were implemented. It was shown that phase shifts in Fresnel holograms can subtract the unwanted background, resulting in an enhancement in the overall quality of the holographic images.

In what follows, we propose a step PS technique to resolve the issue of noise subtraction and proper determination of phase distribution in the sample.

## 4.2. Two- and Four-step Phase-Shifting Techniques in Digital Terahertz Holography

When the hologram is recorded, the registered intensity interference pattern produces four components, however, in digital holography three of these components generate noise in reconstruction and therefore reduce quality and only real image can be observed and reconstructed. To eliminate the noise, produced by three unwanted components, the phase shifting (PS) technique can be employed [93], [94]. In this approach, the imaging process is repeated between two to five times, each time changing the phase of the reference beam [95]. This procedure enables the reconstruction of the image by employing a specific algorithm [96].

For the four-step PS the reconstructed complex transmittance, which describes the distribution of the light field propagating back to the real image plane, can be expressed using the equation:

$$T_{holoPS4}(x,y) = \sum_{j=1}^{j=4} I_j(x,y) U_{ref\_j}(x,y) \tag{19}$$

where $I_j$ is the intensity, obtained at each measurement. $j$ corresponds to phase shifts introduced at each measurement, i.e. $j$=1, 2, 3, 4 coincides with 0, $\pi/2$, $\pi$, and $3\pi/2$, respectively. $U_{ref\_j}$ is the reference beam in the hologram plane ($x$,$y$).

Subsequently, this equation can be simplified, when all four exposures are multiplied by the PS value:

$$T_{holoPS4}(x,y) = 4U_{obj}(x,y) \tag{20}$$

where the $U_{obj}$ is the light field distribution in the hologram plane.

This equation states that after the back propagation only the light field distribution of the real image will be reconstructed, thus removing the unwanted components, which reduces the hologram quality.

In the case of two-step PS, the simplified hologram transmittance is:

$$T_{holoPS2}(x,y) = 2U_{obj}(x,y) + 2U^{*}_{obj}(x,y) \qquad (21)$$

where $U^{*}_{obj}$ corresponds to the light field distribution forming a virtual image.

In this case, the unwanted component remains, although it is hardly noticeable whereas it forms a divergent beam.

Following that, the experimental measurements of THz holography were conducted using two-step and four-step PS methods, using the setup depicted in Figure 32 (a). The phase shift was achieved by placing paper sheets in the reference beam between $M_3$ and $BS_2$. The two-step PS matched phase shifts in the reference beam by 0 and π. Meanwhile, for four-step PS it corresponded to 0, π/2, π, and 3π/2. The THz holograms were recorded at 0.6 THz using a specific sample, shown in Figure 32 (b), that was employed to illustrate the advantages of using the PS method. The phase changes introducing sample was produced of opaque aluminum foil with cutout "E" shaped elements, where one of them was completely hollow and another one consisted of five areas with 0, 1, 2, 3, and 4 paper sheets that under 0.6 THz frequency illumination produced phase shifts of 0, π/4, π/2, 3π/4 and π, respectively. The experiment was conducted by holography without any paper sheets in the reference beam and again by adding 2, 4, and 6 paper sheets between $M_3$ and $BS_2$, which resulted in phase shift by 0, π/2, π, and 3 π/2. After obtaining the experimental results, the phase distributions were reconstructed using both two-step and four-step PS techniques, and the results are depicted in Figure *32* (c). For better comparison, the phase reconstruction using a single hologram (one-step) was also performed and shown in Figure 32 (c).

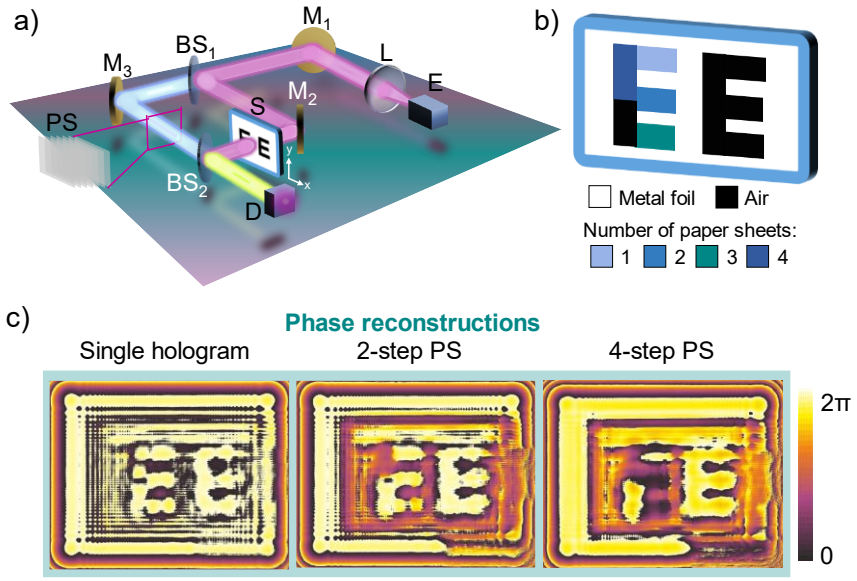


Figure 32: Optical setup used to record a THz digital hologram at 0.6 THz frequency (a). E labels the electronic THz emitter, generating radiation with 0.6 THz frequency; L is the collimating lens; $M_1$, $M_2$, and $M_3$ denote gold-coated flat mirrors; $BS_1$ and $BS_2$ are Si beam splitters; S labels the sample; PS is a phase shifting element; D is the microbolometer detector. Imaged sample made of aluminum foil with cutout "E" shaped elements (b). Coloured areas mark parts, covered with a different number of paper sheets. Phase distributions of the reconstructed holograms using one, two, and four-step phase shifting techniques (c). Coloured scales are normalized to the maximum value of the signal. Adapted from [P5].

As one can see, the phase distribution derived from the single hologram does not reveal the distinct phase variations in sample areas with different numbers of papers. However, phase changes are clearly distinguishable using two- and four-step PS techniques. When it comes to the two-step PS method, it offers a notable advantage of being twice as fast compared to the four-step PS technique. Additionally, this method can yield satisfactory results, particularly for objects that are absorbing and not transparent. Consequently, the two-step technique proves to be sufficient in eliminating undesired background noise levels from 0.034 to 0.017. Although, there was no distinction made between areas with the phase changes within the range of 0-$3\pi/4$, only the area exhibiting a phase change of $\pi$ were distinguished.

However, as one can see, the four-step PS technique provides the more accurate mapping of different phase level areas, as parts with different numbers of paper sheets, corresponding to the phase changes in a range of 0-$\pi$, are distinguishable from each other.

Therefore, the two-step PS method proves to be advantageous when measuring the absorbing objects, where the primary focus is on capturing intensity changes. On the other hand, the four-step PS technique is more favorable for investigating low-absorbing or transparent samples, as it effectively records phase changes in the holographic images.

### 4.3. Comparison of Imaging Techniques for Recording Phase Objects

As already highlighted in this section, holography enables the reconstruction of not only the intensity but also the phase distribution. A great way to demonstrate the potential of phase imaging is to compare the results obtained from various imaging techniques. This was established in the [P5] study, where the holography technique was compared to point-to-point, plane-to-plane, and dark field filtering methods. A consistent sample, which is depicted in Figure 33 (a), was used for all cases, which contains diverse components with varying levels of transmittance and therefore introducing different phase changes.

If the phase object exhibits an almost uniform intensity distribution in the object plane, it will lead to an almost uniform intensity distribution in the image plane. For instance, areas in the sample containing different numbers of papers will exhibit identical intensity levels, making them indistinguishable from each other. This is observed when the sample is imaged using the plane-to-plane technique. Obtained intensity distribution and a setup scheme are depicted in Figure 33 (b). Nevertheless, this imaging method possesses the advantage of capturing the entire plane instantly.

To address this issue and enhance the differentiation of these distinct phase objects, alternative setups such as point-to-point, spatial filtering, and holography were employed. The point-to-point imaging, shown in Figure *33* (c), provides improved resolution by focusing the THz radiation onto the detector. The resolution increases with the decreasing focal spot. As one can see, the image obtained using this technique exhibits good quality and reveals some phase changes by also highlighting the edges of individual components. However, this technique requires raster scanning of the sample, resulting in a longer acquisition time compared to the first case where the entire sample is captured in a single image.

Conventional direct THz imaging (bright field imaging) is well-suited for imaging of strongly absorbing objects. Although, in the case of weakly absorbing objects better contrast is needed. To tackle the problem, the spatial filtering technique can be employed [97]. The imaging results and a relevant setup of dark field filtering are depicted in Figure 33 (d). In this case, the filter

is placed in the plane-to-plane setup at the Fourier plane. The filter removes the direct light or low-frequency components from the spectrum and transmits only light scattered by the sample. Finally, the image with the dark background around the sample is obtained and the objects with different phase shifts can be distinguished.

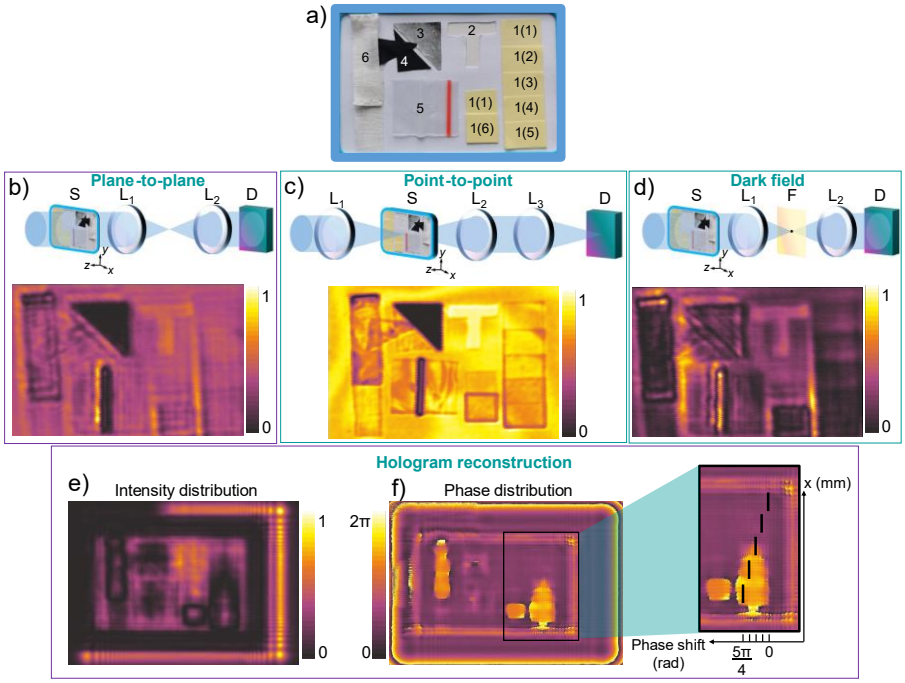


Figure 33: Imaged sample, consisting of diverse components exhibiting varying levels of transmittance (a). 1 marks paper sheets and the number in the brackets indicates the number of paper sheets. 2 denotes the T-shaped aperture. 3 marks a component made of aluminum foil. 4 is a rubber glove. 5 is a low-density polyethylene bag and 6 is a multilayered gauze cloth. Direct THz image obtained using the plane-to-plane technique (b). The top part illustrates the experimental setup scheme, where $L_1$ and $L_2$ are lenses, S denotes the sample and D is the detector. Direct THz image obtained using the point-to-point technique (c). Direct THz image obtained using dark field filtering technique (d). In the experimental setup above component F marks the spatial filter. Intensity (e) and phase (f) distribution reconstructions were obtained from registered holograms at 0.6 THz using the PS technique. The inset on the right side shows the enlarged part of the sample with a different number of paper sheets causing different phase levels, where the black lines indicate the phase change caused by papers. Colour scales are normalized to the maximum values.

Nonetheless, the dark field technique can be employed for imaging objects that introduce only the phase shifts within the range of 0 to $\pi/2$. However, the holography technique can extract phase values from the 0-$2\pi$ range, although it requires further phase retrieval techniques. Moreover, the holography method allows the recording of a complex light field distribution, containing information about both amplitude and phase, at different planes, starting from the hologram plane. This enables the reproduction of a 3D image.

The reconstructions of intensity and phase distributions obtained from registered holograms using the PS technique are depicted in Figure 33 (e) and (f), respectively. The reconstructed intensity distribution is not uniform and it exhibits dark edges of different phase shift objects. Although, techniques that enable visualization of the phase are more suitable because they allow for mapping different phase values from the object as distinct phase levels in the image plane. The enlarged inset in Figure 33 (f) that the phase levels of different number of paper sheets can be distinguished with phase shift reaching up to $5\pi/4$. Furthermore, the edges of different areas also can be observed.

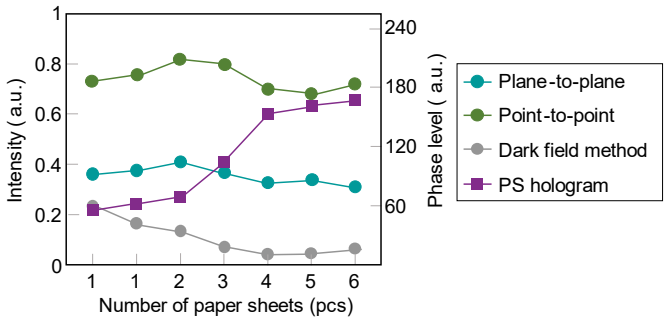


Figure 34: The comparison of different phase level mapping using various techniques: plane-to-plane, point-to-point, dark field method, and PS holography. The intensity distributions were recorded at 300 GHz, while the hologram was registered at 600 GHz.

The plane-to-plane, point-to-point, and dark field methods are employed to visualize phase variations within the recorded intensity pattern, meanwhile, the PS hologram method allowed to reconstruct the phase distribution. The comparison of different phase level mapping using various techniques is depicted in Figure 34. It is evident that the plane-to-plane and point-to-point methods provide completely different outcomes when compared to the holography method. The first two methods exhibit only a slight, less than 10 %, variation in intensity dependence to the introduced phase shift. Moving

forward, the dark field method generates an intensity image for the phase changes that do not surpass π/2. However, for higher phase change values, this method shows a reduction in intensity, which becomes apparent after introducing more than four paper sheets. It is important to notice that all intensity distributions, using the first three methods were recorded at 300 GHz, where the 2π phase shift is achieved by adding 16 paper sheets.

In contrast, the holography was registered at 600 GHz, where the 2π phase shift is achieved by adding 8 paper sheets. This method uncovered the capability to accurately map all introduced phase shifts ranging from 0 to 5π/4. The distinctive areas of each of the six paper sheets can be distinguished by comparing the average values in the reconstructed phase distribution.

To conclude, the plane-to-plane and point-to-point imaging techniques provide only information about the amplitude. The spatial filtering technique (dark field method) implements the mapping of phase values introduced by the sample into an intensity pattern within the image plane. Although this method can be employed only for objects that exhibit phase changes in the range of 0-π/2. The holography technique provides both – amplitude and phase – information and can be applied for imaging objects with phase changes in the range of 0-2π. The results of the phase level mapping demonstrate that holography outperforms other techniques in accurately discriminating objects with varying phase shifts.

### 4.4. Coloured Terahertz Digital Holography

As a general practice, holographic images are typically recorded using a single wavelength, resulting in monochromatic images. Although, by using different frequency illumination, coloured holography can be accomplished. To achieve this, for the first time our research group conducted digital holography [87], [98] [99] at four different frequencies: 1.39 THz, 2.52 THz, 3.11 THz, and 4.25 THz by employing an optically-pumped molecular THz laser and a broadband nanometric field effect transistor [100], [101].

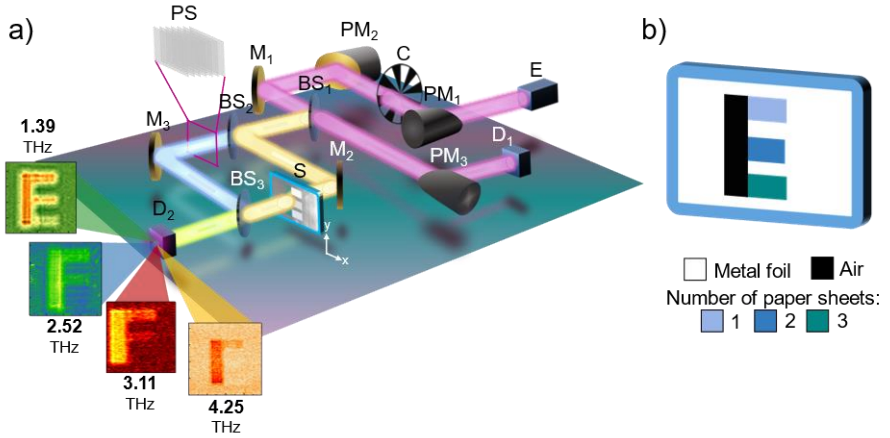


Figure 35: Optical setup used to record THz digital holograms at four different frequencies: 1.39 THz, 2.52 THz, 3.11 THz, and 4.25 THz (a). E labels the source – optically pumped molecular THz laser; $PM_1$, $PM_2$, and $PM_3$ denote parabolic mirrors; C is a chopper; $M_1$, $M_2$, and $M_3$ are gold-coated flat mirrors; $BS_1$, $BS_2$, and $BS_3$ label Si beam splitters; S is the imaged sample; PS denotes phase shift element; $D_1$ and $D_2$ are detectors. Imaged sample made of aluminum foil with cutout "E" shaped element (b). Coloured areas mark parts, covered with a different number of papers.

In this case, a sample produced of aluminum foil with a cut-out "E" shaped element was investigated. The element consisted of four areas with 0, 1, 2, and 3 paper sheets that induced a phase shift that is different under various illumination frequencies and is presented in Table 1.

Table 1: The phase shift dependence on a number of papers for different frequencies.

| | 1.39 THz | 2.52 THz | 3.11 THz | 4.25 THz |
|---|---|---|---|---|
| 1 paper sheet shifts phase by: | $\pi/7$ | $\pi/3$ | $2\pi/5$ | $\pi/2$ |
| The number of papers to reach $2\pi$ PS: | 14 | 6 | 5 | 4 |

Once again, the obtained experimental results were used for phase reconstructions using one-step, two-step, and four-step PS techniques that are depicted in Figure 36.

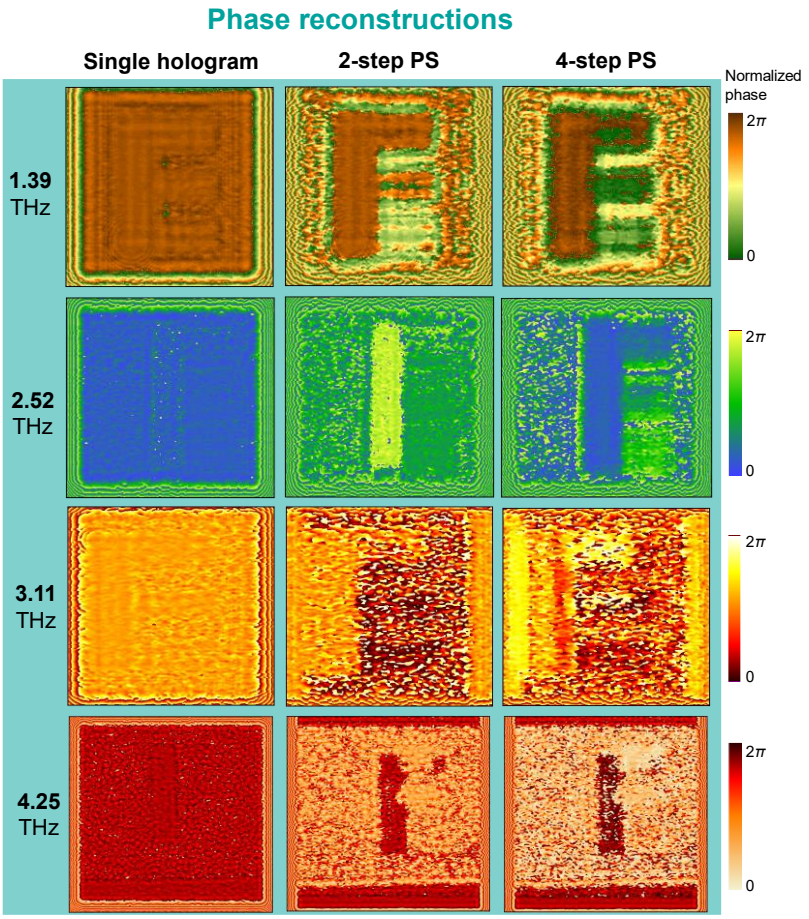


Figure 36: Phase distributions of the reconstructed holograms at four different frequencies: 1.39 THz, 2.52 THz, 3.11 THz, and 4.25 THz, using one, two, and four-step phase shifting techniques.

As one can see, for 1.39 THz and 2.52 THz frequencies, the four-step PS technique provides the accurate mapping of areas with different phase shifts, as the areas of the “E“ element containing a different number of paper sheets exhibit different phase shift values. Meanwhile for higher frequencies – 3.11 THz and 4.25 THz – the phase reconstructions using the four-step PS technique can also provide a mapping of phase changes. However, it is important to note that the accuracy of these reconstructions may be somewhat compromised. The potential reason behind this phenomenon could be attributed to the fact that the 3.11 THz and 4.25 THz radiation wavelengths correspond to 90 μm and 70 μm, respectively, while the areas comprising the 'E' element of the sample are filled with papers with a roughness of 80 μm. Consequently, at higher frequencies, the sample scatters the radiation more

significantly, leading to less accurate imaging results. This, in turn, affects the accuracy of the phase reconstructions. By chosing a proper phase object with reduced scattering characteristics one can enhance the potential of quality and precision of phase reconstructions.

In summary, colour digital THz holography is a promising technique in imaging and discrimination of materials exhibiting different spectral fingerprints at different frequencies.

The obtained results allowed to underline the following findings:

- A two- and four-step phase shifting technique is developed and this approach has been successfully employed to reconstruct the phase distribution of phase objects. The two-step technique proves to be sufficient in eliminating undesired background noise levels from 0.034 to 0.017. Although the four-step phase-shifting technique provides more accurate phase mapping.
- It was shown that the holography technique outperforms other imaging techniques, such as plane-to-plane, point-to-point, or spatial filtering, due to its ability to perform accurate phase shift mapping and accurately distinguish the objects with varying phase shifts within the range of 0-2$\pi$.
- The coloured digital terahertz holography was demonstrated for the first time by using different 1.39 THz, 2.52 THz, 3.11 THz, and 4.25 THz frequency illumination. The two- and four-step PS technique was applied, where the four-step PS method resulted in a more accurate mapping of phase changes.

Relying on the presented findings, one can formulate the following statements for defence:

**Digital terahertz holography with two- and four-step phase-shifting techniques enable a better quality of the recorded images and their reconstructions than a single terahertz hologram due to an unwanted background subtraction.**

## CONCLUSIONS

1. It was shown that graphite-based terahertz zone plate exhibited an almost identical transmittance spectra to the conventional metallic terahertz zone plate. Moreover, its focusing performance was evaluated and compared to the unfocused beam, the graphite-based terahertz zone plate demonstrated an increase in signal value by 8.

2. Single and double graphene layers transferred on a silicon substrate under the laser illumination displayed optical charge carrier modulation in grapehene, resulting in modulation depth values of 42 % and 45 %, respectively.

3. By applying the combination of terahertz imaging technique and optical charge carrier modulation, single and double graphene layers transferred on silicon substrate exhibited a pronounced change in contrast: 0.16 for single layer and 0.23 for double layer graphene.

4. Metasurfaces with complementary split-ring resonators were fabricated from 25 μm thin and flexible stainless steel foil. The flexibility of this metasurface allowed it to demonstrate the focusing performance under mechanical deformation, i.e. bending. The intensity of the beam, when the metasurface is bent ($d/L \approx 0.72$), decreases to ~30 % maximum signal value with respect to the undeformed plate, although it maintains its focusing ability. Although the metasurface is mechanically deformed, the shape of the Gaussian beam remains.

5. The polarization-resolved terahertz imaging was performed and the results confirmed that the metasurfaces with complementary split-ring resonators not only can focus the terahertz beam, but also control its polarization.

6. The generation of nonparaxial structured light in the shape of THz Airy beam was demonstrated using exclusively silicon diffractive optics. When using a single Airy zone plate the signal-to-noise ratio value of 570 was achieved. The additional introduction of the Fresnel zone plate together with Airy zone plate significantly improved the signal-to-noise ratio reaching the value of 1180. Furthermore, the combination of Airy and Fresnel zone plates results in twice better spatial resolution (1.6 λ) when compared to a single Airy zone plate. It implies that the proper selection of light-collecting optics can have an essential effect on the quality of the image.

7. It was demonstrated that the Airy zone plate provides the capability to perform terahertz imaging in the presence of an opaque beam block. It was shown that even when the 60 % area of the illuminating Airy zone plate was covered, the obtained image was still clear, exhibiting a contrast of about

30 (a.u.) and a spatial resolution of 3.2λ. Meanwhile, when the combination of Airy and Fresnel zone plates was employed, the spatial resolution was significantly better - 1.6λ.

8. The structured nonparaxial Airy beam provides a possibility for the evaluation of the optical properties of graphene layers. It was demonstrated that imaging of 2D samples with conventional Gaussian illumination gives a signal-to-noise ratio value of 118. The combination of Airy and Fresnel zone plates exhibits a three times higher signal-to-noise ratio with a value of 326.

9. A two- and four-step phase shifting technique is developed and this approach has been successfully employed to reconstruct the phase distribution of phase objects. The two-step technique proves to be sufficient in eliminating undesired background noise levels from 0.034 to 0.017. Although the four-step phase-shifting technique provides more accurate phase mapping.

10. The coloured digital holography was demonstrated by using different 1.39 THz, 2.52 THz, 3.11 THz, and 4.25 THz frequency illumination. The two- and four-step PS technique was applied, where the four-step PS method resulted in a more accurate mapping of phase changes.

# SANTRAUKA

## Įvadas

Terahercinė (THz) spinduliuotė (1 THz = $10^{12}$ Hz), dar vadinama submilimetrine spinduliuote, elektromagnetinių bangų skalėje priskiriama spektriniam ruožui nuo 0,1 THz iki 10 THz (atitinkamai, bangos ilgiams nuo 3 mm iki 30 μm bei energijoms nuo 0.4 meV iki 40 meV) [1][2]. Mikrobangų ruože, užimančiame žemesnių THz dažnių juostos dalį, taikomi elektroniniai principai, tačiau tolesnį darbinio dažnio didinimą riboja dreifinis greitis. Kita vertus, THz kvantinė energija yra labai maža (1 THz atitinka 4.1 meV), o tai reiškia, jog kambario temperatūroje sunku pasiekti krūvininkų inversiją, todėl ši aplinkybė lemia apribojimus optinėje elektromagnetinio spektro pusėje. Todėl THz diapazonas gali būti laikomas jungtimi tarp elektroninių ir fotoninių prietaisų [3], kurių veikimas turėtų apimti skirtingus fizikinius principus. THz spinduliuotės taikymų atveju, daugelis regimajai ir infraraudonajai šviesai neskaidrių medžiagų, pavyzdžiui, popierius, drabužiai ar plastikas, yra pralaidžios THz spinduliuotei. Dėl šios savybės THz spinduliuotė gali užtikrinti nedestruktyvų vaizdų atkūrimą, kuris yra taikomas apsaugos sistemose, pakuočių tikrinime, paveikslų tyrimuose ir t. t. [4]-[6]. Be to, skirtingai nei Rentgeno spinduliotė, THz spinduliuotė pasižymi maža energija, todėl yra nejonizuojanti bei saugi žmogaus organizmui ir dėl šios savybės taikoma medicinoje [7], [8].

Yra keletas pagrindinių THz sistemų tipų, kurie yra skirstomi pagal naudojamus šaltinius: THz spektroskopija su laikine skyra (THz-TDS) ir THz nuostoviosios veikos (THz-CW) matavimo metodas [9].

Dažniausiai naudojama THz-TDS sistema yra spektroskopijos metodas, kuomet vaizdinamas bandinys yra skenuojamas trumpais THz impulsais. THz impulsai generuojami puslaidininkinių darinių paviršiuje, apšviečiant juos femtosekundiniu lazeriu [10]. Šis metodas leidžia išmatuoti pro bandinį praėjusios (ar nuo jos atsispindėjusios) THz spinduliuotės spektrą, jo komponenčių amplitudę ir fazę. Gauti duomenys leidžia surinkti daugiau informacijos apie tiriamos medžiagos struktūrą, sudėtį ar optines savybes [11], [12].

Tačiau labiausiai THz spinduliuotė išpopuliarėjo pradėjus taikyti THz vaizdinimo sistemas. Naudojantis THz-CW vaizdinimo sistema, galima realiuoju laiku užfiksuoti dvimatį (2D) bandinio vaizdą. Taikant šį metodą naudojamas vienadažnis šaltinis ir fiksuojama tik pro bandinį praėjusios arba nuo jo atsispindėjusios THz šviesos amplitudė. Tačiau homodininėse ir heterodininėse CW vaizdinimo sistemose gali būti gaunama ne tik amplitudės,

bet ir fazės informacija, įgalinanti gauti fazinius vaizdus ir tuo būdu tyrinėti mažai absorbuojančius bandinius. Lyginant su pirmiau minėtomis THz-TDS sistemomis, THz-CW yra gana nebrangi ir pasižymi gana dideliu vaizdų užrašymo greičiu. THz-CW vaizdinimo sistemas įprastai sudaro nuostoviosios veikos šaltinis, optiniai komponentai, skirti sufokusuoti THz pluoštą į bandinį, ir detektorius, registruojantis pro bandinį praėjusį arba nuo jo atsispindėjusį signalą [9]. Nuostoviosios veikos THz šaltiniai gali būti įvairūs: elektronų pernašos (Gano) diodai [13], kvantiniai kaskadiniai lazeriai [14], optiškai žadinami THz dujų lazeriai [15] ir atgalinės bangos osciliatoriai [16]. Taip pat, THz-CW sistemose galimas platus detektorių, tokių kaip piroelektriniai detektoriai [17], mikrobolometrų masyvai [18], Golajaus celės (*angl.* Golay cells) [19], „peteliškės“ tipo antenos [20] ir Šotki diodai [21], pasirinkimas.

Siekiant patobulinti ir išplėsti THz vaizdinimo sistemų taikymą, jos turi tapti kaip įmanoma kompaktiškesnės ir patogios naudoti. Mažinant THz vaizdinimo sistemas, daugiausia dėmesio skiriama aktyviesiems komponentams, pavyzdžiui, šaltiniams ir detektoriams, o ne pasyviesiems, tokiems kaip lęšiai ir veidrodžiai, nepaisant to, kad pastarieji yra didelių gabaritų ir dažnai reikalauja tikslaus optinio suderinimo [1]. Laimei, didelius optinius komponentus galima pakeisti plonais ir kompaktiškais difrakciniais elementais. Pavyzdžiui, iš didelio tankio polietileno (HDPE) pagamintus storus lęšius ar stambius parabolinius veidrodžius galima pakeisti plonais difrakciniais optiniais elementais, pagamintais iš didžiavaržio silicio, naudojant lazerinės abliacijos technologiją [22], [23]. Tuo tarpu, pluošto formavimui galima pasitelkti ir kitas lanksčias bei plonas medžiagas [24]. Metapaviršiai [25], sudaryti iš mažesnių nei bangos ilgio rezonatorių masyvų, suteikia galimybę formuoti THz pluoštą ir keisti jo charakteristikas valdant amplitudę, fazę ir poliarizaciją.

**Darbo tikslas**

Sukurti ir ištirti terahercinėms vaizdinimo sistemoms tinkamus kompaktiškos ir lanksčios optikos elementus, galinčius pakeisti įprastus didelių gabaritų optinius komponentus.

**Darbo uždaviniai**

1. Išplėsti difrakcinių optinių elementų, skirtų THz vaizdinimo sistemoms, pasirinkimą, randant ir pritaikant tinkamas ir naujas lanksčias medžiagas bei dizainus.

2. Sukurti THz vaizdinimo sistemą, kurioje įprasti lęšiai ar veidrodžiai būtų pakeičiami plokščiais ir tik iš silicio pagamintais difrakciniais optiniais elementais ir ištirti jų galimybes terahercinės šviesos pluošto formavimui ir surinkimui.

3. Patobulinti THz skaitmeninės holografijos metodą, leidžiantį užtikrinti geresnę įrašytų vaizdų kokybę lyginant su įprastu vieno žingsnio holografijos metodu.

**Darbo naujumas**

1. Pirmą kartą terahercinių zoninių plokštelių gamybai buvo panaudota plona ir lanksti grafitinė plėvelė, o gauto optinio pralaidumo spektro forma yra beveik identiška metalinės terahercinės zoninės plokštelės spektro formai. Įvertintas grafito zoninės plokštelės fokusavimo efektyvumas ir nustatytas 8 kartus didesnis signalas, lyginant su nefokusuoto pluošto signalo verte, o tai rodo, jog grafitinė plėvelė yra tinkama plonų ir lanksčių terahercinių zoninių plokštelių gamybai.

2. Optinė krūvininkų koncentracijos moduliacija pritaikyta ant silicio užkeltiems grafeno sluoksniams, o gautos moduliacijos gylio vertės siekia 42 % ir 45 % atitinkamai vienam ir dviems grafeno sluoksniams. Pirmą kartą optinė moduliacija buvo taikoma kartu su terahercinio vaizdinimo metodu, taip sukuriant didesnį kontrasto pokytį: 0,16 vieno grafeno sluoksnio ir 0,23 dviejų grafeno sluoksnių atveju. Toks abiejų metodų naudojimas gali padėti atskirti sritis su skirtingu grafeno sluoksnių skaičiumi.

3. Pirmą kartą pagaminta grafeno pagrindo zoninė plokštelė ir pademonstruotos jos fokusavimo galimybės, kuomet kartu yra taikoma ir optinė grafeno krūvininkų koncentracijos moduliacija.

4. Iš 25 μm storio lanksčios nerūdijančio plieno folijos buvo pagaminti metapaviršiai su invertuotais padalinto žiedo rezonatoriais. Pademonstruotos šio metapaviršiaus fokusavimo galimybės esant mechaninei deformacijai, t.y. lankstant metapaviršių, dėl kurio fokusuojamo pluošto intensyvumas nukrito vos 30 %. Be to, nustatyta, jog lankstant metapaviršių, Gauso pluošto forma nekinta.

5. Pademonstruota, jog iš lanksčios nerūdijančio plieno folijos pagaminti metapaviršiai su invertuotais padalinto žiedo rezonatoriais yra tinkami naudoti poliarizuotam teraherciniam vaizdinimui.

6. Parodyta, jog iš silicio pagamintų Airy lęšio ir zoninės plokštelės derinys suformuoja nedifrakcinį ir neparaksialinį Airy pluoštą, sklindantį paraboline trajektorija, ir gali gerokai pagerinti signalo ir triukšmo santykį nuo

570 iki 1180, bei dvigubai padidinti erdvinę skiriamąją gebą (1,6λ), lyginant su vienu Airy lęšiu, generuojančiu besiplečiantį ir užsilenkiantį Airy pluoštą.

7. Pademonstruota, kad Airy pluoštas suteikia galimybę vaizdinti, kai vaizdinimo sistemoje yra dalinai blokuojamas krintanti spinduliuotė. Parodyta, jog net ir uždengus 60 % Airy lęšio ploto, gautas ryškus ir aiškus vaizdas, kurio kontrastas siekia iki 30 (s.v.), o erdvinė skiriamoji geba yra 3,2λ. Tuo tarpu Airy lęšio ir zoninės plokštelės derinys smarkiai pagerina skiriamąją gebą, kurios vertė siekia 1,6λ.

8. Parodyta, jog struktūrinės šviesos Airy pluoštas suteikia galimybę įvertinti optines grafeno sluoksnių savybes. Įvertinta, jog Airy lęšio ir zoninės plokštelės derinys leido pasiekti tris kartus didesnį signalo ir triukšmo santykį (300), lyginant su Gauso pluoštu.

9. Parodyta, kad taikant dviejų ir keturių žingsnių fazės poslinkio metodus galima pagerinti holografinių vaizdų kokybę sumažinant nepageidaujamo foninio triukšmo lygį ir gaunat tikslesnį fazės atvaizdavimą.

10. Pirmą kartą pademonstruota spalvota skaitmeninė terahercinė holografija, naudojant keturis skirtingus - 1,39 THz, 2,52 THz, 3,11 THz ir 4,25 THz – dažnius, taip išplečiant plonų medžiagų tyrimų, naudojant terahercinę spinduliuotę, ribas.

**Ginamieji teiginiai**

1. Kartu su terahercinių vaizdinimo metodu taikoma optinė krūvininkų koncentracijos moduliacija leidžia pagerinti gaunamo vaizdo kontrastą, todėl šis metodas gali būti taikomas kaip bekontaktis būdas ant didžiavaržio silicio perkeltų grafeno sluoksnių charakterizavimui.

2. Iš lanksčios nerūdijančio plieno folijos pagaminti metapaviršiai su su invertuotais padalinto žiedo rezonatoriais gali būti naudojami poliarizaciniam terahercinių vaizdinimui bei pluošto fokusavimui net ir esant mechaninei deformacijai.

3. Silicio pagrindo difrakciniai optiniai elementai gali būti pritaikyti generuojant Airy pluošto pavidalo struktūrinę neparaksialinę šviesą, kurios savybė sklisti erdvėje paraboline trajektorija gali būti taikoma vaizdinant objektus, esančius už terahercinei spinduliuotei neskaidrios kliūties.

4. Terahercinėse vaizdinimo sistemose atliekant plonų grafeno sluoksnių vaizdinimą, struktūrinė terahercinė šviesa kontrasto ir erdvinės skiriamosios gebos atžvilgiu yra pranašesnė už įprastą Gauso pluoštą.

5. Skaitmeninė terahercinė holografija, naudojanti dviejų ir keturių žingsnių fazės poslinkio metodus, leidžia sumažinti nepageidaujamą foninį

triukšmą ir tokiu būdu pagerinti vaizdų ir jų rekonstrukcijų kokybę, lyginant su vieno žingsnio terahercinės holografijos metodu.

**Autorės indėlis**

Autorė dalyvavo [P1] straipsnyje tirtų optinių elementų kūrime. Atliko visus terahercinio vaizdinimo eksperimentus bei visų gautų duomenų analizę. Taip pat dalyvavo publikacijos rašymo procese ir atliko visų rezultatų apipavidalinimą (grafikai ir paveikslėliai).

Autorė paruošė visus [P2] straipsnyje tirtus bandinius. Atliko visus terahercinio vaizdinimo eksperimentus bei gautų rezultatų analizę. Ruošė publikacijos tekstą bei apipavidalino visus rezultatus.

Autorė atliko [P3] straipsnyje aprašytus terahercinio vaizdinimo eksperimentus bei gautų duomenų analizę. Dalyvavo straipsnio rašyme bei apipavidalino gautus rezultatus.

Autorė atliko visus [P4] straipsnyje aprašytus terahercinio vaizdinimo eksperimentus, bei gautų duomenų analizę. Paruošė bandinius su skirtingais grafeno sluoksniais. Dalyvavo publikacijos rašyme bei apipavidalino gautus rezultatus.

Autorė dalyvavo atliekant [P5] straipsnyje aprašytus terahercinio vaizdinimo eksperimentus bei analizavo gautus duomenis. Dalyvavo publikacijos rašymo procese bei apipavidalino rezultatus.

**Rezultatų apžvalga**

Siekiant THz vaizdinimo sistemų kompaktiškumo, ieškoma alternatyvų stambiems optiniams lęšiams ar paraboliniams veidrodžiams. Puikus šios problemos sprendimas yra difrakciniai optiniai elementai (DOE), kurie savo efektyvumu nenusileidžia įprastiems optiniams komponentams, negana to, yra ploni ir kompaktiški. Tačiau siekiant, jog sistema tilptų ant vieno lusto, dėl mažėjančių matmenų metalizacija tampa nebetinkama, todėl privalu rasti alternatyvias medžiagas, tinkančias DOE gamybai. Viena iš siūlomų galimybių yra anglies nanomedžiagos, tokios kaip grafitas. Be to, DOE dizainą galima papildyti integruotomis metamedžiagomis, tokiomis kaip kryžiaus formos rezonansiniai filtrai, praleidžiantis tik tam tikro dažnio spinduliuotę. Šiame darbe pristatyta iš plonos grafito plėvelės pagaminta terahercinė zoninė plokštelė (TZP) su integruotais kryžiaus formos rezonansiniais filtrais. Išmatuotas grafito pagrindo TZP optinio pralaidumo spektras yra beveik identiškas etaloniniam metalinės TZP spektrui. Taip pat,

patikrintos grafito TZP pluošto fokusavimo galimybės ir gauta, jog, lyginant su nefokusuotu pluoštu, grafito TZP signalą pastiprino 8 kartus.

Kita anglies nanomedžiaga – grafenas – taip pat gali būti naudojama kaip alternatyva THz optinių komponentų kūrimui. Nors grafenas THz spinduliuotei yra beveik visiškai pralaidus, siekiant sukurti grafeno pagrindo difrakcinį optinį elementą, jo pralaidumas turėtų būti mažesnis. Tai galima pasiekti naudojantis optine moduliacija, kuomet apšvietus grafeną lazeriu, pakinta jo krūvininkų koncentracija, todėl sumažėja ir optinis pralaidumas. Šiame darbe tiriant optinę grafeno krūvininkų koncentracijos moduliaciją pagaminti du bandiniai, kuomet ant didžiavaržio silicio padėklo buvo atitinkamai užkelti vienas ir du grafeno sluoksniai. Įvertintas moduliacijos gylis siekė 42 % bandiniui su grafeno monosluoksniu ir 45 % bandiniui su dviem grafeno sluoksniais. Taip pat, nustatyta, jog apjungiant THz vaizdinimo metodą kartu su optine grafeno krūvininkų koncentracijos moduliacija, išryškėja kontrastas tarp skirtingo grafeno sluoksnių skaičiaus, t.y. bandinio su grafeno monosluoksniu kontrasto vertė siekė 0.16, tuo tarpu bandinio su dviem grafeno sluoksniais atveju kontrastas išaugo iki 0.23. Tai leidžia teigti, jog optinės krūvininkų koncentracijos moduliacijos metodo kombinavimas kartu su THz vaizdinimo sistema gali būti naudojamas kaip bekontaktis įrankis grafeno, užkelto ant didžiavaržio silicio, charakterizavimui.

Įvairių formų metamedžiagų naudojimas gali padėti praturtinti difrakcinių optinių elementų panaudojimo galimybes. Šiame darbe buvo tirti iš 25 μm storio nerūdijančio plieno folijos pagaminti metalęšiai su lazeriu išpjautais invertuotais padalinto žiedo rezonatoriais. Pastarieji suteikia galimybę sukurti ne tik pluoštą fokusuojantį, tačiau ir poliarizaciją sukantį elementą. Būtent tai buvo patvirtinta atlikus poliarizacinį THz vaizdinimą. Negana to, pademonstruota, jog dėl metalinės folijos plonumo ir patvarumo, metalęšiai gali puikiai veikti ir taikant mechaninę deformaciją, t.y. lankstant metalęšį. Gauta, jog sulenkus metalęšį, kai lenkimas atitinka $d/L \approx 0.72$, pluošto intensyvumas sumažėja vos 30 %. Negana to, gauta, jog deformuojant metalęšį, Gauso pluošto forma nepakinta.

Taip pat šiame darbe pademonstruota, jog THz vaizdinimo sistemoje įprasti optiniai lęšiai ar paraboliniai veidrodžiai gali būti pakeisti plonais iš didžiavaržio silicio lazerinės abliacijos metodu pagamintais difrakciniais elementais. Vienas svarbiausių parametrų THz vaizdinimo sistemose yra pluošto forma. Įprastai vaizdinimo eksperimentuose naudojamas Gauso pluoštas, tačiau pastaruoju metu vis daugiau dėmesio sulaukia nedifraguojantys, tokie kaip Besselio ar Airy, pluoštai. Šiame darbe parodyta, jog ant didžiavaržio silicio padėklo lazerinės abliacijos metodu pagaminus fazinę kaukę gaunamas optinis elementas gali suformuoti Airy pluoštą,

sklindantį išlenkta paraboline trajektorija. Kombinuojant pastarąjį elementą su taip pat iš didžiavaržio silicio pagaminta difrakcine zonine plokštele, galima lengvai valdyti THz spinduliuotę. Nemažiau svarbu tai, jog Airy pluoštas yra savaime atsistatantis, todėl susidūręs su kliūtimi, už jos pluoštas vėl atkuria savo formą išilgai sklidimo ašies. Pademonstruota, jog ši Airy pluošto savybė, kartu su paraboline sklidimo trajektorija gali būti pritaikomos atliekant bandinio vaizdinimą, tarp jo ir difrakcinio elemento esant THz spinduliuotei neskaidriai kliūčiai. Parodyta, jog uždengus net 60 % Airy lęšio, gautas aiškus bandinio vaizdas, kurio kontrastas siekė iki 30 (a.u.), o erdvinė skyra 3.2λ. Tuo tarpu naudojant Airy lęšio ir zoninės plokštelės kombinaciją ir esant tokiam pat optinio elemento uždengimui, gautas vaizdas pasižymėjo dvigubai geresne erdvine rezoliucija – 1.6λ. Taip pat, pademonstruota, jog gautas Airy pluoštas gali būti taikomas dvimačių medžiagių, tokių kaip grafenas, vaizdinimui ir charakterizavimui. Bandiniai su skirtingu (1, 2, 3, 4 ir 5) grafeno sluoksnių skaičiumi buvo vaizdinami naudojant įprastą Gauso pluoštą bei Airy ir zoninės plokštelės kombinaciją, kurios dėka buvo sukurtas neparaksialinis Airy pluoštas. Pastaruoju atveju gautas beveik tris kartus didesnis (300) signalo ir triukšmo santykis, lyginant su rezultatu, gautu vaizdinant bandinius Gauso pluoštu. Taigi, struktūrinė Airy šviesa gali būti naudojama mažą sugertį turinčių objektų vaizdinimui ir bekontakčiam grafeno sluoksnių įvertinimui.

Vaizdinant maža sugertimi pasižyminčias medžiagas, pranašumą turi skaitmeninės THz holografijos metodas, leidžiantis įrašyti ne tik amplitudės, bet ir fazės pasiskirstymo informaciją ir tokiu būdu atkurti trimačius vaizdus. Šiame darbe pademonstruota, jog atkuriamo vaizdo kokybė gali būti pagerinta THz holografijoje taikant dviejų ir keturių žingsnių fazės poslinkio (PS) metodus, kurie pašalina nereikalingus foninį triukšmą sukeliančius komponentus. Parodyta, jog keturių žingsnių PS metodas gali padėti tiksliausiai nustatyti fazės pokyčius ir yra tinkamesnis tiriant maža sugertimi ar dideliu pralaidumu pasižyminčius objektus.

**ACKNOWLEDGEMENTS**

Firstly, I would like to thank my academic supervisor, Gintaras Valušis, for all the support, guidance, kindness, help, and most of all – for elevating me from Kėdainių "Nevėžis" level and always reminding me to push the tempo.

Moreover, I am very grateful to Linas Minkevičius for the help, support, and for teaching me a million things. I would also like to express my gratitude to Domas Jokubauskis for all the help I received with experimental measurements and guidance. Additionally, I would like to thank Sergej Orlov for his wild ideas and collaborations, and Agnieszka Siemion for being a master of holography.

I would like to thank our gang: Ignas Grigelionis, Justinas Jorudas, Karolis Redeckas, Mindaugas Karaliūnas, Vladislovas Čižas, and once again, Linas Minkevičius and Domas Jokubauskis, for the laughs, friendship, and for always lightening the mood. You are the main reason why I look forward to going to work every day.

I am very grateful to all the members of the THz Atelier laboratory for inspiring discussions and for setting a wonderful example.

I am grateful to Algimantas Lukša for teaching me how to transfer graphene and Natalia Alexeeva for teaching me the graphene patterning technique. I would also like to thank Ernestas Nacius, Paulius Kizevičius and Karolis Mudrys for collaborations. Alesia Paddubskaya, thank you for your extensive knowledge about graphene and for sharing it with me. I thank Andžej Urbanovič and Dalius Seliuta for conducting THz spectroscopic measurements. Vytautas Jakštas, thank you for your expertise in lithography and for collaborating with me on conference preparations. It is always a pleasure to work with you all.

I would also like to thank Renata Butkutė for always being supportive, inspiring and spreading the good mood around FTMC.

Furthermore, I am incredibly grateful to my parents, Inga and Valdas, for their unconditional love, constant encouragement and the opportunities they have provided. I am also deeply grateful to my lovely husband, Eligijus, for his patience, comfort, being my best friend and for unwavering support in everything I do, it truly means the world to me. I would like to express my gratitude to my high school physics teacher, Renaldas Klimavičius, who, by the way, is the best teacher in the world, for inspiration and encouragement.

I am sure that my colleagues, who have read this far, are shocked that I have not thanked my cat. So here it goes – thank you, Phoebe, for always bringing me sunshine!

## REFERENCES


[1] G. Valušis, A. Lisauskas, H. Yuan, W. Knap, and H. G. Roskos, "Roadmap of Terahertz Imaging 2021," *Sensors*, vol. 21, no. 12, p. 4092, Jun. 2021, doi: 10.3390/s21124092.

[2] F. S. S. Y. P.-M. E. Yu C, "The potential of terahertz imaging for cancer diagnosis: A review of investigations to date," *Quant Imaging Med Surg.*, vol. 2, no. 1, pp. 33–45, 2012.

[3] A. Leitenstorfer *et al.*, "The 2023 terahertz science and technology roadmap," *J Phys D Appl Phys*, vol. 56, no. 22, p. 223001, Jun. 2023, doi: 10.1088/1361-6463/acbe4c.

[4] M. Tonouchi, "Cutting-edge terahertz technology," *Nat Photonics*, vol. 1, no. 2, pp. 97–105, Feb. 2007, doi: 10.1038/nphoton.2007.3.

[5] S. S. Dhillon *et al.*, "The 2017 terahertz science and technology roadmap," *J Phys D Appl Phys*, vol. 50, no. 4, p. 043001, Feb. 2017, doi: 10.1088/1361-6463/50/4/043001.

[6] C. L. Koch Dandolo, M. Picollo, C. Cucci, and P. U. Jepsen, "Fra Angelico's painting technique revealed by terahertz time-domain imaging (THz-TDI)," *Applied Physics A*, vol. 122, no. 10, p. 898, Oct. 2016, doi: 10.1007/s00339-016-0396-x.

[7] J.-H. Son, S. J. Oh, and H. Cheon, "Potential clinical applications of terahertz radiation," *J Appl Phys*, vol. 125, no. 19, p. 190901, May 2019, doi: 10.1063/1.5080205.

[8] Q. Sun, Y. He, K. Liu, S. Fan, E. P. J. Parrott, and E. Pickwell-MacPherson, "Recent advances in terahertz technology for biomedical applications," *Quant Imaging Med Surg*, vol. 7, no. 3, pp. 345–355, Jun. 2017, doi: 10.21037/qims.2017.06.02.

[9] N. Karpowicz, H. Zhong, J. Xu, K.-I. Lin, J.-S. Hwang, and X.-C. Zhang, "Comparison between pulsed terahertz time-domain imaging and continuous wave terahertz imaging," *Semicond Sci Technol*, vol. 20, no. 7, pp. S293–S299, Jul. 2005, doi: 10.1088/0268-1242/20/7/021.

[10] A. Krotkus, "Semiconductors for terahertz photonics applications," *J Phys D Appl Phys*, vol. 43, no. 27, p. 273001, Jul. 2010, doi: 10.1088/0022-3727/43/27/273001.

[11] J. Neu and C. A. Schmuttenmaer, "Tutorial: An introduction to terahertz time domain spectroscopy (THz-TDS)," *J Appl Phys*, vol. 124, no. 23, p. 231101, Dec. 2018, doi: 10.1063/1.5047659.

[12] D. M. Mittleman, M. Gupta, R. Neelamani, R. G. Baraniuk, J. V. Rudd, and M. Koch, "Recent advances in terahertz imaging," *Appl Phys B*,

vol. 68, no. 6, pp. 1085–1094, Jun. 1999, doi: 10.1007/s003400050750.

[13] K. Ahi, "Review of GaN-based devices for terahertz operation," *Optical Engineering*, vol. 56, no. 09, p. 1, Sep. 2017, doi: 10.1117/1.OE.56.9.090901.

[14] J. Darmo *et al.*, "Imaging with a Terahertz quantum cascade laser," *Opt Express*, vol. 12, no. 9, p. 1879, 2004, doi: 10.1364/OPEX.12.001879.

[15] K. Zhong *et al.*, "Optically pumped terahertz sources," *Sci China Technol Sci*, vol. 60, no. 12, pp. 1801–1818, Dec. 2017, doi: 10.1007/s11431-017-9057-3.

[16] A. Dobroiu, M. Yamashita, Y. N. Ohshima, Y. Morita, C. Otani, and K. Kawase, "Terahertz imaging system based on a backward-wave oscillator," *Appl Opt*, vol. 43, no. 30, p. 5637, Oct. 2004, doi: 10.1364/AO.43.005637.

[17] H. Huang *et al.*, "Continuous-wave terahertz high-resolution imaging via synthetic hologram extrapolation method using pyroelectric detector," *Opt Laser Technol*, vol. 120, p. 105683, Dec. 2019, doi: 10.1016/j.optlastec.2019.105683.

[18] N. Oda *et al.*, "Microbolometer Terahertz Focal Plane Array and Camera with Improved Sensitivity in the Sub-Terahertz Region," *J Infrared Millim Terahertz Waves*, vol. 36, no. 10, pp. 947–960, Oct. 2015, doi: 10.1007/s10762-015-0184-2.

[19] T. Otsuji, "Trends in the Research of Modern Terahertz Detectors: Plasmon Detectors," *IEEE Transactions on Terahertz Science and Technology* , vol. 5, no. 6, pp. 1110–1120, 2015.

[20] L. Minkevičius *et al.*, "Terahertz heterodyne imaging with InGaAs-based bow-tie diodes," *Appl Phys Lett*, vol. 99, no. 13, p. 131101, Sep. 2011, doi: 10.1063/1.3641907.

[21] Y. Yang, B. Zhang, X. Zhao, Y. Fan, and X. Chen, "220 GHz wideband integrated receiver front end based on planar Schottky diodes," *Microw Opt Technol Lett*, vol. 62, no. 8, pp. 2737–2746, Aug. 2020, doi: 10.1002/mop.32300.

[22] L. Minkevičius *et al.*, "Terahertz multilevel phase Fresnel lenses fabricated by laser patterning of silicon," *Opt Lett*, vol. 42, no. 10, p. 1875, May 2017, doi: 10.1364/OL.42.001875.

[23] E. D. Walsby *et al.*, "Multilevel silicon diffractive optics for terahertz waves," *Journal of Vacuum Science & Technology B: Microelectronics and Nanometer Structures*, vol. 20, no. 6, p. 2780, 2002, doi: 10.1116/1.1518021.

[24] L. Minkevičius *et al.*, “Terahertz zone plates with integrated laser-ablated bandpass filters,” *Electron Lett*, vol. 49, no. 1, pp. 49–50, Jan. 2013, doi: 10.1049/el.2012.3509.

[25] X. You *et al.*, “Broadband terahertz transmissive quarter-wave metasurface,” *APL Photonics*, vol. 5, no. 9, p. 096108, Sep. 2020, doi: 10.1063/5.0017830.

[26] A. Siemion, “Terahertz Diffractive Optics—Smart Control over Radiation,” *J Infrared Millim Terahertz Waves*, vol. 40, no. 5, pp. 477–499, May 2019, doi: 10.1007/s10762-019-00581-5.

[27] E. D. Walsby *et al.*, “Multilevel silicon diffractive optics for terahertz waves,” *Journal of Vacuum Science & Technology B: Microelectronics and Nanometer Structures*, vol. 20, no. 6, p. 2780, 2002, doi: 10.1116/1.1518021.

[28] S. Yu-Lei, Z. Qing-Li, and Z. Cun-Lin, “Diffraction of terahertz waves after passing through a Fresnel lens,” *Chinese Physics B*, vol. 18, no. 12, pp. 5511–5517, Dec. 2009, doi: 10.1088/1674-1056/18/12/064.

[29] A. G. Michette, “Diffractive Optics II Zone Plates,” in *Optical Systems for Soft X Rays*, Boston, MA: Springer US, 1986, pp. 165–215. doi: 10.1007/978-1-4613-2223-8_8.

[30] F. J. Torcal-Milla and L. M. Sanchez-Brea, “Single-focus binary Fresnel zone plate,” *Opt Laser Technol*, vol. 97, pp. 316–320, Dec. 2017, doi: 10.1016/j.optlastec.2017.07.008.

[31] H. D. Hristov, “Terahertz Harmonic Operation of Microwave Fresnel Zone Plate Lens and Antenna: Frequency Filtering and Space Resolution Properties,” *Int J Antennas Propag*, vol. 2011, pp. 1–8, 2011, doi: 10.1155/2011/541734.

[32] W. Withayachumnankul and D. Abbott, “Metamaterials in the Terahertz Regime,” *IEEE Photonics J*, vol. 1, no. 2, pp. 99–118, Aug. 2009, doi: 10.1109/JPHOT.2009.2026288.

[33] J. Pendry, “Metamaterials in the sunshine,” *Nat Mater*, vol. 5, no. 8, pp. 599–600, Aug. 2006, doi: 10.1038/nmat1697.

[34] Q. Wang *et al.*, “Design, Fabrication, and Modulation of THz Bandpass Metamaterials,” *Laser Photon Rev*, vol. 13, no. 11, p. 1900071, Nov. 2019, doi: 10.1002/lpor.201900071.

[35] B. Voisiat, A. Bičiūnas, I. Kašalynas, and G. Račiukaitis, “Band-pass filters for THz spectral range fabricated by laser ablation,” *Applied Physics A*, vol. 104, no. 3, pp. 953–958, Sep. 2011, doi: 10.1007/s00339-011-6456-3.

[36] H. Shahounvand, A. Fard, and M. B. Tavakoli, “Design, simulation and fabrication of a new terahertz cross-shaped metamaterial bandpass

filter to obtain a narrow frequency bandwidth," *Opt Quantum Electron*, vol. 54, no. 2, p. 120, Feb. 2022, doi: 10.1007/s11082-021-03502-w.

[37] Y. Demirhan *et al.*, "Metal mesh filters based on Ti, ITO and Cu thin films for terahertz waves," *Opt Quantum Electron*, vol. 48, no. 2, p. 170, Feb. 2016, doi: 10.1007/s11082-016-0427-z.

[38] H. Cao and A. Nahata, "Influence of aperture shape on the transmission properties of a periodic array of subwavelength apertures," *Opt Express*, vol. 12, no. 16, p. 3664, Aug. 2004, doi: 10.1364/OPEX.12.003664.

[39] D. D. Nolte, A. E. Lange, and P. L. Richards, "Far-infrared dichroic bandpass filters," *Appl Opt*, vol. 24, no. 10, p. 1541, May 1985, doi: 10.1364/AO.24.001541.

[40] K. D. Möller, K. R. Farmer, D. V. P. Ivanov, O. Sternberg, K. P. Stewart, and P. Lalanne, "Thin and thick cross shaped metal grids," *Infrared Phys Technol*, vol. 40, no. 6, pp. 475–485, Dec. 1999, doi: 10.1016/S1350-4495(99)00031-6.

[41] K. D. Möller, J. B. Warren, J. B. Heaney, and C. Kotecki, "Cross-shaped bandpass filters for the near- and mid-infrared wavelength regions," *Appl Opt*, vol. 35, no. 31, p. 6210, Nov. 1996, doi: 10.1364/AO.35.006210.

[42] E. A. Sedykh, V. Y. Soboleva, and M. K. Khodzitsky, "Tunable narrowband filters with cross-shaped resonators for THz frequency band," *J Phys Conf Ser*, vol. 643, p. 012071, Nov. 2015, doi: 10.1088/1742-6596/643/1/012071.

[43] C. M. Watts, X. Liu, and W. J. Padilla, "Metamaterial Electromagnetic Wave Absorbers," *Advanced Materials*, vol. 24, no. 23, pp. OP98–OP120, Jun. 2012, doi: 10.1002/adma.201200674.

[44] H.-T. Chen, A. J. Taylor, and N. Yu, "A review of metasurfaces: physics and applications," *Reports on Progress in Physics*, vol. 79, no. 7, p. 076401, Jul. 2016, doi: 10.1088/0034-4885/79/7/076401.

[45] F. Capasso, "The future and promise of flat optics: a personal perspective," *Nanophotonics*, vol. 7, no. 6, pp. 953–957, Jun. 2018, doi: 10.1515/nanoph-2018-0004.

[46] L. Minkevičius *et al.*, "Focusing Performance of Terahertz Zone Plates with Integrated Cross-shape Apertures," *J Infrared Millim Terahertz Waves*, vol. 35, no. 9, pp. 699–702, 2014, doi: 10.1007/s10762-014-0086-8.

[47] F. Gan, X. Yang, Y. Zhou, and W. Li, "Wavelength-multiplexed varifocal and switchable metalens with all-metallic C-shaped

antennas," *Opt Laser Technol*, vol. 147, p. 107630, Mar. 2022, doi: 10.1016/j.optlastec.2021.107630.

[48] K. S. Novoselov, V. I. Fal′ko, L. Colombo, P. R. Gellert, M. G. Schwab, and K. Kim, "A roadmap for graphene," *Nature*, vol. 490, no. 7419, pp. 192–200, Oct. 2012, doi: 10.1038/nature11458.

[49] A. K. Geim and K. S. Novoselov, "The rise of graphene," *Nat Mater*, vol. 6, no. 3, pp. 183–191, Mar. 2007, doi: 10.1038/nmat1849.

[50] K. S. Novoselov *et al.*, "Electric Field Effect in Atomically Thin Carbon Films," *Science (1979)*, vol. 306, no. 5696, pp. 666–669, Oct. 2004, doi: 10.1126/science.1102896.

[51] C. Casiraghi, "Doping dependence of the Raman peaks intensity of graphene close to the Dirac point," *Phys Rev B*, vol. 80, no. 23, p. 233407, Dec. 2009, doi: 10.1103/PhysRevB.80.233407.

[52] I. Childres, L. A. Jauregui, W. Park, H. Cao, and Y. P. Chen, "Raman Spectroscopy of Graphene and Related Materials," *New developments in photon and materials research* , vol. 1, pp. 1–20, 2013.

[53] P. Bøggild *et al.*, "Mapping the electrical properties of large-area graphene," *2d Mater*, vol. 4, no. 4, p. 042003, Sep. 2017, doi: 10.1088/2053-1583/aa8683.

[54] H. A. Hafez, S. Kovalev, K. Tielrooij, M. Bonn, M. Gensch, and D. Turchinovich, "Terahertz Nonlinear Optics of Graphene: From Saturable Absorption to High-Harmonics Generation," *Adv Opt Mater*, vol. 8, no. 3, p. 1900771, Feb. 2020, doi: 10.1002/adom.201900771.

[55] D. R. Cooper *et al.*, "Experimental Review of Graphene," *ISRN Condensed Matter Physics*, vol. 2012, pp. 1–56, Apr. 2012, doi: 10.5402/2012/501686.

[56] P. Weis, J. L. Garcia-Pomar, M. Höh, B. Reinhard, A. Brodyanski, and M. Rahm, "Spectrally Wide-Band Terahertz Wave Modulator Based on Optically Tuned Graphene," *ACS Nano*, vol. 6, no. 10, pp. 9118–9124, Oct. 2012, doi: 10.1021/nn303392s.

[57] Q.-Y. Wen *et al.*, "Graphene based All-Optical Spatial Terahertz Modulator," *Sci Rep*, vol. 4, no. 1, p. 7409, Dec. 2014, doi: 10.1038/srep07409.

[58] J. B. Pendry, A. J. Holden, D. J. Robbins, and W. J. Stewart, "Magnetism from conductors and enhanced nonlinear phenomena," *IEEE Trans Microw Theory Tech*, vol. 47, no. 11, pp. 2075–2084, 1999, doi: 10.1109/22.798002.

[59] Z. Song, Z. Zhao, H. Zhao, W. Peng, X. He, and W. Shi, "Teeter-totter effect of terahertz dual modes in C-shaped complementary split-ring

resonators," *J Appl Phys*, vol. 118, no. 4, p. 043108, Jul. 2015, doi: 10.1063/1.4927845.

[60] O. Sydoruk, E. Tatartschuk, E. Shamonina, and L. Solymar, "Analytical formulation for the resonant frequency of split rings," *J Appl Phys*, vol. 105, no. 1, p. 014903, Jan. 2009, doi: 10.1063/1.3056052.

[61] J. D. Ortiz *et al.*, "Babinet's principle and saturation of the resonance frequency of scaled-down complementary metasurfaces," *Appl Phys Lett*, vol. 118, no. 22, p. 221901, May 2021, doi: 10.1063/5.0048960.

[62] H.-T. Chen *et al.*, "Complementary planar terahertz metamaterials," *Opt Express*, vol. 15, no. 3, p. 1084, 2007, doi: 10.1364/OE.15.001084.

[63] T. Zentgraf *et al.*, "Babinet's principle for optical frequency metamaterials and nanoantennas," *Phys Rev B*, vol. 76, no. 3, p. 033407, Jul. 2007, doi: 10.1103/PhysRevB.76.033407.

[64] F. Gan, X. Yang, Y. Zhou, and W. Li, "Wavelength-multiplexed varifocal and switchable metalens with all-metallic C-shaped antennas," *Opt Laser Technol*, vol. 147, p. 107630, Mar. 2022, doi: 10.1016/j.optlastec.2021.107630.

[65] Q. Wang *et al.*, "A Broadband Metasurface-Based Terahertz Flat-Lens Array," *Adv Opt Mater*, vol. 3, no. 6, pp. 779–785, Jun. 2015, doi: 10.1002/adom.201400557.

[66] J. Huang *et al.*, "Enhanced terahertz focusing for a graphene-enabled active metalens," *Opt Express*, vol. 28, no. 23, p. 35179, Nov. 2020, doi: 10.1364/OE.409746.

[67] Q. Cheng *et al.*, "Broadband achromatic metalens in terahertz regime," *Sci Bull (Beijing)*, vol. 64, no. 20, pp. 1525–1531, Oct. 2019, doi: 10.1016/j.scib.2019.08.004.

[68] M. Hashemi, A. Moazami, M. Naserpour, and C. J. Zapata-Rodríguez, "A broadband multifocal metalens in the terahertz frequency range," *Opt Commun*, vol. 370, pp. 306–310, Jul. 2016, doi: 10.1016/j.optcom.2016.03.031.

[69] G. Raciukaitis, "Ultra-Short Pulse Lasers for Microfabrication: A Review," *IEEE Journal of Selected Topics in Quantum Electronics*, vol. 27, no. 6, pp. 1–12, Nov. 2021, doi: 10.1109/JSTQE.2021.3097009.

[70] R. Verma, M. K. Sharma, P. Senthilkumaran, and V. Banerjee, "Analysis of Fibonacci gratings and their diffraction patterns," *Journal of the Optical Society of America A*, vol. 31, no. 7, p. 1473, Jul. 2014, doi: 10.1364/JOSAA.31.001473.

[71] J. A. Monsoriu, A. Calatayud, L. Remon, W. D. Furlan, G. Saavedra, and P. Andres, “Bifocal Fibonacci Diffractive Lenses,” *IEEE Photonics J*, vol. 5, no. 3, pp. 3400106–3400106, Jun. 2013, doi: 10.1109/JPHOT.2013.2248707.

[72] V. Ferrando, A. Calatayud, P. Andres, R. Torroba, W. D. Furlan, and J. A. Monsoriu, “Imaging Properties of Kinoform Fibonacci Lenses,” *IEEE Photonics J*, vol. 6, no. 1, pp. 1–6, Feb. 2014, doi: 10.1109/JPHOT.2014.2304560.

[73] R. Verma, V. Banerjee, and P. Senthilkumaran, “Fractal signatures in the aperiodic Fibonacci grating,” *Opt Lett*, vol. 39, no. 9, p. 2557, May 2014, doi: 10.1364/OL.39.002557.

[74] G. Milne, G. D. M. Jeffries, and D. T. Chiu, “Tunable generation of Bessel beams with a fluidic axicon,” *Appl Phys Lett*, vol. 92, no. 26, p. 261101, Jun. 2008, doi: 10.1063/1.2952833.

[75] J. Durnin, “Exact solutions for nondiffracting beams I The scalar theory,” *Journal of the Optical Society of America A*, vol. 4, no. 4, p. 651, Apr. 1987, doi: 10.1364/JOSAA.4.000651.

[76] S. N. Khonina, N. L. Kazanskiy, S. V. Karpeev, and M. A. Butt, “Bessel Beam: Significance and Applications—A Progressive Review,” *Micromachines (Basel)*, vol. 11, no. 11, p. 997, Nov. 2020, doi: 10.3390/mi11110997.

[77] J. Durnin, J. J. Miceli, and J. H. Eberly, “Diffraction-free beams,” *Phys Rev Lett*, vol. 58, no. 15, pp. 1499–1501, Apr. 1987, doi: 10.1103/PhysRevLett.58.1499.

[78] D. McGloin and K. Dholakia, “Bessel beams: Diffraction in a new light,” *Contemp Phys*, vol. 46, no. 1, pp. 15–28, Jan. 2005, doi: 10.1080/0010751042000275259.

[79] S. Monk, J. Arlt, D. A. Robertson, J. Courtial, and M. J. Padgett, “The generation of Bessel beams at millimetre-wave frequencies by use of an axicon,” *Opt Commun*, vol. 170, no. 4–6, pp. 213–215, Nov. 1999, doi: 10.1016/S0030-4018(99)00463-0.

[80] Y. Yu and W. Dou, “Generation of pseudo-Bessel beams at THz frequencies by use of binary axicons,” *Opt Express*, vol. 17, no. 2, p. 888, Jan. 2009, doi: 10.1364/OE.17.000888.

[81] L. Minkevicius, D. Jokubauskis, I. Kasalynas, S. Orlovas, A. Urbas, and G. Valusis, “Imaging of thick objects using silicon Bessel zone plates at 0.6 THz,” in *2019 44th International Conference on Infrared, Millimeter, and Terahertz Waves (IRMMW-THz)*, IEEE, Sep. 2019, pp. 1–2. doi: 10.1109/IRMMW-THz.2019.8874471.

[82] L. Minkevičius, D. Jokubauskis, I. Kašalynas, S. Orlov, A. Urbas, and G. Valušis, “Bessel terahertz imaging with enhanced contrast realized by silicon multi-phase diffractive optics,” *Opt Express*, vol. 27, no. 25, p. 36358, Dec. 2019, doi: 10.1364/OE.27.036358.

[83] M. V. Berry and N. L. Balazs, “Nonspreading wave packets,” *Am J Phys*, vol. 47, no. 3, pp. 264–267, Mar. 1979, doi: 10.1119/1.11855.

[84] Y. Zhang, H. Zhong, M. Belić, and Y. Zhang, “Guided Self-Accelerating Airy Beams—A Mini-Review,” *Applied Sciences*, vol. 7, no. 4, p. 341, Mar. 2017, doi: 10.3390/app7040341.

[85] G. A. Siviloglou, J. Broky, A. Dogariu, and D. N. Christodoulides, “Observation of Accelerating Airy Beams,” *Phys Rev Lett*, vol. 99, no. 21, p. 213901, Nov. 2007, doi: 10.1103/PhysRevLett.99.213901.

[86] D. GABOR, “A New Microscopic Principle,” *Nature*, vol. 161, no. 4098, pp. 777–778, May 1948, doi: 10.1038/161777a0.

[87] M. S. Heimbeck and H. O. Everitt, “Terahertz digital holographic imaging,” *Adv Opt Photonics*, vol. 12, no. 1, p. 1, Mar. 2020, doi: 10.1364/AOP.12.000001.

[88] R. K. Amineh, M. Ravan, A. Khalatpour, and N. K. Nikolova, “Three-Dimensional Near-Field Microwave Holography Using Reflected and Transmitted Signals,” *IEEE Trans Antennas Propag*, vol. 59, no. 12, pp. 4777–4789, Dec. 2011, doi: 10.1109/TAP.2011.2165496.

[89] K. Wu, Q. Cheng, Y. Shi, H. Wang, and G. P. Wang, “Hiding scattering layers for noninvasive imaging of hidden objects,” *Sci Rep*, vol. 5, no. 1, p. 8375, Feb. 2015, doi: 10.1038/srep08375.

[90] L. Valzania, P. Zolliker, and E. Hack, “Topography of hidden objects using THz digital holography with multi-beam interferences,” *Opt Express*, vol. 25, no. 10, p. 11038, May 2017, doi: 10.1364/OE.25.011038.

[91] M. Locatelli *et al.*, “Real-time terahertz digital holography with a quantum cascade laser,” *Sci Rep*, vol. 5, no. 1, p. 13566, Aug. 2015, doi: 10.1038/srep13566.

[92] L. Rong *et al.*, “Terahertz in-line digital holography of human hepatocellular carcinoma tissue,” *Sci Rep*, vol. 5, no. 1, p. 8445, Feb. 2015, doi: 10.1038/srep08445.

[93] T. Zhang and I. Yamaguchi, “Three-dimensional microscopy with phase-shifting digital holography,” *Opt Lett*, vol. 23, no. 15, p. 1221, Aug. 1998, doi: 10.1364/OL.23.001221.

[94] I. Yamaguchi, “Phase-Shifting Digital Holography,” in *Digital Holography and Three-Dimensional Display*, Springer US, pp. 145–171. doi: 10.1007/0-387-31397-4_5.

[95] D. W. Phillion, “General methods for generating phase-shifting interferometry algorithms,” *Appl Opt*, vol. 36, no. 31, p. 8098, Nov. 1997, doi: 10.1364/AO.36.008098.

[96] G. Lai and T. Yatagai, “Generalized phase-shifting interferometry,” *Journal of the Optical Society of America A*, vol. 8, no. 5, p. 822, May 1991, doi: 10.1364/JOSAA.8.000822.

[97] A. Siemion, L. Minkevičius, L. Qi, and G. Valušis, “Spatial filtering based terahertz imaging of low absorbing objects,” *Opt Lasers Eng*, vol. 139, p. 106476, Apr. 2021, doi: 10.1016/j.optlaseng.2020.106476.

[98] T.-C. Poon and J. Liu, *Introduction to Modern Digital Holography*, 1st ed. Cambridge University, 2014.

[99] B. Javidi *et al.*, “Roadmap on digital holography [Invited],” *Opt Express*, vol. 29, no. 22, p. 35078, Oct. 2021, doi: 10.1364/OE.435915.

[100] E. Javadi, D. B. But, K. Ikamas, J. Zdanevičius, W. Knap, and A. Lisauskas, “Sensitivity of Field-Effect Transistor-Based Terahertz Detectors,” *Sensors*, vol. 21, no. 9, p. 2909, Apr. 2021, doi: 10.3390/s21092909.

[101] J. Zdanevicius *et al.*, “Field-Effect Transistor Based Detectors for Power Monitoring of THz Quantum Cascade Lasers,” *IEEE Trans Terahertz Sci Technol*, vol. 8, no. 6, pp. 613–621, Nov. 2018, doi: 10.1109/TTHZ.2018.2871360.

# CURRICULUM VITAE

Rusnė Ivaškevičiūtė-Povilauskienė was born in 1992 in Kėdainiai, Lithuania.

**Education:**

| | |
|---|---|
| 2018-2023 | Center for Physical Sciences and Technology (FTMC)<br>*Ph.D. studies* |
| 2016-2018 | Vilnius University<br>Material Science and Semiconductor Physics<br>*Master's degree, Cum laude* |
| 2011-2015 | Vilnius University<br>Physics<br>*Bachelor's degree* |

**Work experience:**

| | |
|---|---|
| 2018-present | Center for Physical Sciences and Technology (FTMC)<br>*Junior researcher* |
| 2017 (August-December) | NASA Ames Research Center<br>*Intern* |
| 2016-2017 | The Applied Research Institute for Prospective Technologies<br>*Researcher* |
| 2015-2017 | Modern E-Technologies<br>*Researcher* |

# APIE AUTORĘ

Rusnė Ivaškevičiūtė-Povilauskienė gimė 1992 m. Kėdainiuose.

**Išsilavinimas:**

| | |
|---|---|
| 2018-2023 | Fizinių ir technologijos mokslų centras |
| | *Doktorantūros studijos* |
| 2016-2018 | Vilniaus universitetas |
| | Medžiagotyra ir puslaidininkių fizika |
| | *Magistro kvalifikacinis laipsnis, Cum laude* |
| 2011-2015 | Vilniaus universitetas |
| | Fizika |
| | *Bakalauro kvalifikacinis laipsnis* |

**Profesinė veikla:**

| | |
|---|---|
| 2018-dabar | Fizinių ir technologijos mokslų centras |
| | *Jaunesnioji mokslo darbuotoja* |
| 2017 (rugpjūtis-gruodis) | NASA Ames Research Center |
| | *Stažuotoja* |
| 2016-2017 | Perspektyvinių technologijų taikomųjų tyrimų institutas |
| | *Tyrėja* |
| 2015-2017 | Modernios E-Technologijos |
| | *Tyrėja* |

## REPRINTED PUBLICATIONS

P1

**FLEXIBLE MATERIALS FOR TERAHERTZ OPTICS: ADVANTAGES OF GRAPHITE-BASED STRUCTURES**

**R. Ivaškevičiūtė-Povilauskienė**, L. Minkevičius, D. Jokubauskis, A. Urbanowicz, S. Indrišiūnas, G. Valušis

*Optical Materials Express* **9**(11), 4438-4446 (2019)
DOI: 10.1364/OME.9.004438

# Flexible materials for terahertz optics: advantages of graphite-based structures

**Rusnė Ivaškevičiūtė-Povilauskienė,[1,*] Linas Minkevičius,[1,3] Domas Jokubauskis,[1] Andrzej Urbanowicz,[1] Simonas Indrišiūnas,[2] and Gintaras Valušis[1,3]**

[1]*Department of Optoelectronics, Center for Physical Sciences and Technology, Sauletekio Avenue 3, Vilnius, LT 10257, Lithuania*
[2]*Department of Laser Technologies, Center for Physical Sciences and Technology, Savanoriu Avenue 231, Vilnius, LT-02300, Lithuania*
[3]*Institute of Photonics and Nanotechnology, Department of Physics, Vilnius University, Sauletekio Avenue 3, Vilnius, LT 10257, Lithuania*
[*]*rusne.ivaskeviciute@ftmc.lt*

**Abstract:** Flexible materials for applications in terahertz (THz) range imaging systems are investigated in this study. THz time-domain spectroscopy and THz imaging at 0.6 THz frequency are used to analyze optical properties of zone plates (TZP) with integrated cross-shaped filters, which are fabricated using direct laser writing on thin graphite, HB pencil-shaded graphite on paper, as well as reference metal-based and pure paper zone plates. Spectral features and focusing power comparable to the best metal-based TZP is achieved with graphite-based TZP. The pure paper and paper with pencil-shaded graphite TZPs showed increase in focusing power by a factor of ~1.5, supporting numerical 3D finite-difference time-domain simulations. The findings show that graphite-based TZPs can serve as a flexible, compact, and inexpensive optics elements for emerging THz imaging systems.



## 1. Introduction

Rapid evolution in terahertz technology [1], in compact solid-state THz emitters [2] and detectors [3,4] necessitates the search for ways to reduce the size of passive optical components. It is also desirable that such components are easy to integrate and align, while maintaining the systems mechanical reliability as well as reasonable costs. Metamaterials are a promising avenue as they allow to redesign bulky optical elements into thin and planar components with a wide range of optical properties [5]. Many applications of THz imaging require that packaged materials can be resolved and recognised without performing a full spectroscopic imaging [6,7], which entails recording of images at fixed THz frequencies that are known or selected *a priori* [8,9].

Terahertz zone plates (TZP) designed with cross-shaped filters, which permit shaping and focusing of the THz beam for imaging at selected frequencies, were proposed by several groups earlier [10,11,12,13]. The TZPs are compact focusing elements for handling of THz radiation beams and can be used in THz imaging systems with broadband source in case of imaging when only one particular frequency related to the material's fingerprints is needed to record the image. Innovative structures adding tunability of optical properties into compact optical elements can be provided by microelectromechanical systems (MEMS). One such example is a MEMS switch placed across a slit of a split ring-resonator (SRR), which acts as a switchable metamaterial with tubable frequency [14]. Another proposed design is based on origami containing periodic patterns of SRRs placed on different surfaces [15]. When the folding parameter is varied in these systems, the gap between the rings and hence the capacitance of the resonators is altered inducing a shift of the resonance frequency. Mechanically tunable components can be also achieved via programmability platform based on nonflat-foldable origami by employing its

intrinsic self-locking and reconfiguration capabilities [16] or by combining nonlinear mechanical elements with a multimodal architecture enabling a sequence of topological reconfigurations [17].

In this work, we extend the family of mechanically tunable materials by adding optical metamaterials based on flexible thin films. The approach can be found amenable for on-chip designs in integrated photonics and useful in development of origami-principle based optical solutions for compact THz imaging systems. Its particular role can be attributed in biophotonic THz applications, where the mechanical flexibility can reduce strongly the elastic mismatch between biological tissues and photonic components, enabling their conformal integration on curvilinear tissue surfaces.

More specifically, we explore the optical properties of flexible materials shaped in zone plates with integrated filters and produced from three different materials: 10 μm thick graphite foil, thin graphite layer deposited by HB graphite pencil on 100 μm paper sheet, and a pure paper serving as a reference for the TZP fabrication technology. THz time-domain spectroscopy and THz imaging techniques performed at 0.6 THz frequency revealed distinctive spectral features and an excellent focusing performance indicating advantages of the graphite-based TZP. This provides an inexpensive and flexible compact THz focusing element alternative to the metal foil or metal evaporation-based technological approaches.

## 2. Designs of flexible terahertz zone plates and experimental set-ups

In order to investigate new flexible diffractive optical components, TZPs made of three different materials with integrated cross-shaped filters were tested and compared to a reference metal zone plate. The metal zone plate had an identical design as the other materials used for the 0.6 THz frequency imaging with focal length of 10 mm. The TZP geometry is displayed in Fig. 1(e). The metallic reference zone plate was made from 30 μm thick steel foil. The second zone plate was made from 10 μm thick graphite foil ($\varepsilon_r$=12), which was deposited on a 75 μm thick plastic polyester film ($\varepsilon_r$=2.6), since thin graphite is a soft and non-free-standing material. The graphite film was acquired from "Shenzhen Zhenxing Technology Co., Ltd". The third zone plate was made from a thin graphite layer produced by shading HB graphite pencil on a 100 μm thick paper sheet ($\varepsilon_r$=2.31) [18]. The fourth zone plate was made from a 100 μm thick paper sheet and also served as reference.

All the TZPs, shown in Fig. 1(a)–(d), were produced using a laser direct writing (LDW) system equipped with high precision polygon scanner (LSE170 from Next Scan Technology) and translation stage (PR0115 from Aerotech).

Zone plates on the pure paper and paper with a graphite layer were fabricated using the 3rd harmonic (355 nm) of picosecond laser Atlantic-60 (1 MHz, 1064 nm, 10 ps, *Ekspla*). Laser beam was scanned at 1 mm/s, with 0.2 μm pulse pitch using 10 μm diameter laser spot, and 12 J/cm$^2$ laser irradiation fluence. Each scan was repeated 5 times. Paper samples were placed on another paper sheet and held on the sample holder by a vacuum suction. Paper sheet below the sample helped to avoid excessive charring of the paper cut due to the ablation of the metal sample holder. The zone plate on a graphite layer on a plastic substrate was fabricated using 1 mm/s, 0.2 μm pulse pitch, 10 μm diameter laser spot, 12 J/cm$^2$ fluence, and 3 scans.

Figure 1(f) shows Raman spectroscopy of 10 μm thick graphite film (black line) and 75 μm plastic film (red line), which served for fabrication of the graphite TZP. In the Raman spectrum of the graphite film, the line at 1744cm$^{-1}$ can be attributed to –C = O vibration, while 3239 cm$^{-1}$ presents –N-H line. One can also see distinct lines in Raman spectrum of the polyester plastic film ascribed to –C = O (1721cm$^{-1}$), C = C (1608, 3075 cm$^{-1}$) and $CH_3$ (2959 cm$^{-1}$) vibrations.

Two different set-ups were employed to investigate spectral properties of all four different zone plates. The THz time-domain spectroscopic measurement was performed by the Teravil-Ekspla "T-SPEC" THz Time Domain Spectrometer (THz-TDS) *(set-up presented in Fig. 2(a)*.

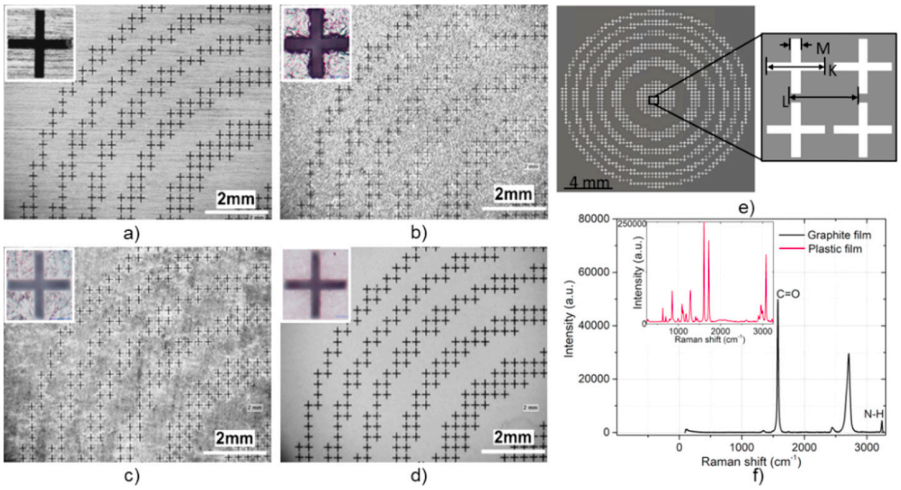


**Fig. 1.** Photos of the quarter of TZP made from different materials: a) metal; b) graphite foil; c) graphite on paper and d) paper. Inset depicts the shape of one cross-shaped aperture element. Photos were taken using "Hyrox KH-7700" digital microscope. e) Design of the graphite foil terahertz zone plate for 0.6 THz and geometry of cross-shaped filters (M = 40 μm, K = 260 μm, L = 290 μm). f) Raman spectroscopy of 10 μm graphite film and 75 μm polymer film. Most pronounced spectral signatures in plastic: -C = O (1721 $cm^{-1}$), C = C (1608, 3075 $cm^{-1}$) and $CH_3$ (2959 $cm^{-1}$). The N-H amine vibration line around 3300-3400 $cm^{-1}$, it is not prominent, likely due to overlapping with characteristic bands of absorbed water in the same region.

Femtosecond laser (Toptica, Femtofiber Pro) providing pulses of 780 nm wavelength, 90 fs pulse duration and 150 mW output power at 80 MHz pulse repetition rate was used for photoconductive antennas made from LT-GaAs excitation. The delay line was based on 10 times per second moving hollow retro-reflector with 120 ps time window what corresponds to ~8 GHz spectral resolution. A set of two parabolic mirrors was used to focus end effective collection of THz radiation. In the focus point diameter of THz beam was ~ 2 mm. THz signal was detected by the digital signal processing (DSP) card integrated into electronic module with analog-digital converter (ADC) [19].

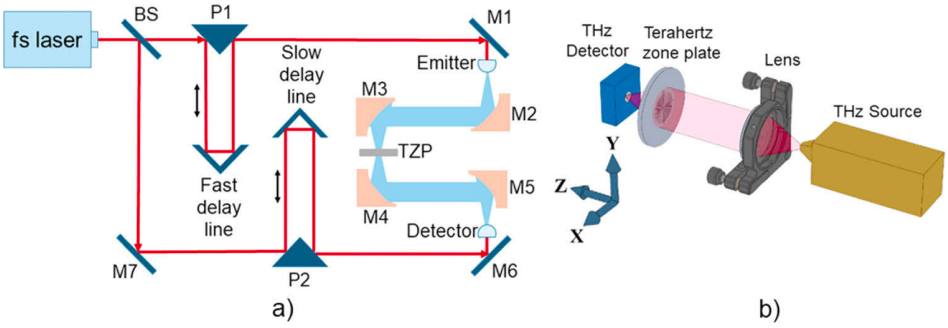


**Fig. 2.** a) THz-TDS set-up for evaluation of spectral properties of investigated zone plates [20], b) THz-CW set-up for evaluation of TZP focusing performance and THz beam profile measurements in the focal (*xy*) plane and along the *z*-axis, (*zy*) plane.

The second set-up was used to evaluate the focusing performance of zone plates and was based on a THz continuous wave (THz-CW) 0.6 THz electronic source (*Virginia Diodes*, VDI). It consisted of high-density polyethylene (HDPE) lens and a THz detector (titanium microbolometer [3]). The beam profile was recorded in both the focal plane and along the $z$-axis (set-up presented in Fig. 2(b)), modulating the source electronically at 1 kHz frequency and detecting the microbolometer-induced signal with a lock-in amplifier.

## 3. Results and discussion

Zone plates transmission spectra were obtained using THz-TDS (Fig. 3). All the spectra given in Fig. 3 are normalized to the unfocused beam values [21]. As the studied TZPs are based on very different materials, we introduced the following procedure to quantify the quality of their focusing performance. The transmittance of the radiation is divided into two zones: the first one (center zone) includes transmittance, which was calculated by integrating area of 2 mm radius from the TZP center. The second zone (peripheral zone) was defined from the average of the transmittance where it decreases two times, and was evaluated by integrating the remaining part of the TZP area. These zones are indicated by the red line (center zones, where the signal intensity is the highest), and the black line (peripheral zone). The choice of this approach is based on the consideration of the maximum contrast in the metal foil-based TZP.

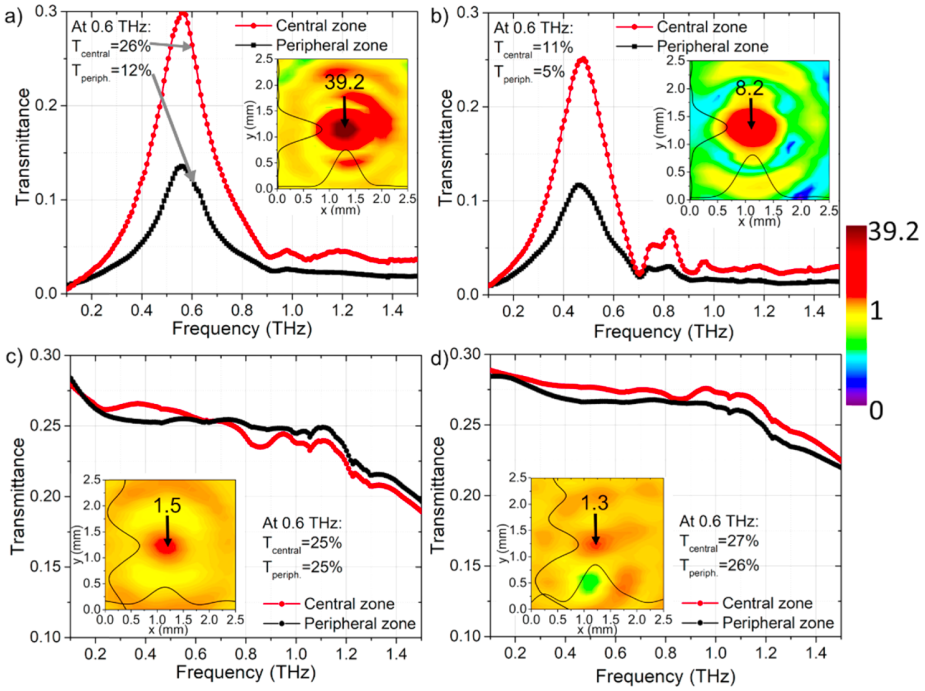


**Fig. 3.** THz-TDS transmittance spectra and insets depict THz-CW two-dimensional THz beam profiles focused with a) metal TZP; b) graphite foil TZP; c) graphite on paper TZP; d) pure paper TZP. The beam cross sections at the maximum intensity are presented in a linear scale as a solid black line for each case. Maximum signal amplitude of the TZPs is normalized to the maximum amplitude of the unfocused beam.

As one can see, spectra of metallic and graphite foil are quite similar in terms of the spectral shape, although the maximum amplitude in the latter is 18% smaller than the reference. A closer look at the resonance frequency shows that the graphite foil spectra is red-shifted to 0.48 THz,

in comparison to the metal one (Fig. 3(b)). Although the design of zone plates was the same, the dimensions of cross shaped filters were slightly smaller than designed (Table 1) due to the fact that the laser cutting parameters were kept constant in both cases, whilst the materials being processed were different. The smaller crosses induced blue-shift of the resonant frequency, $f_r = c/(1.8 \cdot K - 1.35 \cdot M + 0.2 \cdot L)$, which for graphite foil TZP amounts to 0.64 THz. However, the plastic film under the graphite layer red-shifts the resonant frequency due to its lower refractive index ($n$) of dielectric $r = \sqrt{2/(n^2 + 1)}$, which is in contact with the zone plate [22]. Taking into account that for plastic $n = 1.61$, the frequency shifting factor $r = 0.75$, and, as a consequence, the resonant frequency of graphite foil TZP is red-shifted to 0.48 THz. Spectra of the graphite on paper TZP and the pure paper TZP (Fig. 3(c, d)) reveal no resonances around expected 0.6 THz. Moreover, they are relatively smooth over the whole investigated range. The central part and peripheral parts do not keep constant transmission ratio due to the non-uniform coverage of the graphite by pencil. More details on the transmission properties can be found from the results of THz-TDS and THz-CW given in Table 2.

**Table 1. Dimensions of cross-shaped filters**

| Materials | \|Geometry | M (μm) | K (μm) | L (μm) |
|---|---|---|---|---|
| Design | | 40 | 260 | 290 |
| Metal TZP | | 39 | 258 | 298 |
| Graphite foil TZP | | 35 | 252 | 297 |
| Graphite on paper TZP | | 32 | 251 | 300 |
| Pure paper TZP | | 39 | 259 | 299 |

**Table 2. Transmittance of different zone plates measured using THz-TDS and THz-CW systems**

| Sample | Transmittance (%) | | | |
|---|---|---|---|---|
| | THz-TDS | | THz-CW | |
| | Central zone | Peripheral zone | Central zone | Peripheral zone |
| Metal TZP | 26 | 12 | 23 | 14 |
| Graphite foil TZP | 11 | 5 | 11 | 6 |
| Graphite on paper TZP | 25 | 25 | 25 | 24 |
| Pure paper TZP | 27 | 26 | 29 | 27 |

Insets of Fig. 3 present experimental two-dimensional THz beam profiles in the focal plane of THz-CW imaging system at 0.6 THz frequency. The intensities are calibrated to the unfocused beam intensity. Solid black lines represent the beam cross sections at the maximum intensity. As expected, the best operation is manifested by the metallic TZP. The flexible graphite foil TZP demonstrates focusing by increasing the signal by a factor of ~8, as compared to the unfocused one. Graphite on paper and pure paper zone plates exhibit poor focusing properties with enhancement factors of 1.5 and 1.3, respectively.

To complete the physical picture and evaluate operational performance, the beam profiles along $z$-axis were studied by comparing experimental beam profiles (symbol line) with theoretical simulations of the electric field $E_z/E_0$ ratio distribution (straight line), where $E_0$ is incident electric field taken to be equal to 1. Results are depicted in Fig. 4. All investigated TZPs reveal well expressed resonances at the focal point, i. e. at 10 cm from the zone plate, followed by Fabry–Perot oscillations due to interferences between the collimating lens and the studied TZPs. It is also evident that the experimental results are well reproduced by the simulation data. The most pronounced resonance is achieved with the metal TZP, while very similar performance can be attributed to the graphite foil-based TZP. To further analyse the profiles, a pure graphite sheet

of 10 µm thickness (without plastic foil as support) was modelled. It shows that the graphite foil operates more effectively than the graphite foil with plastic - the focusing effect is more than twice higher in the former.

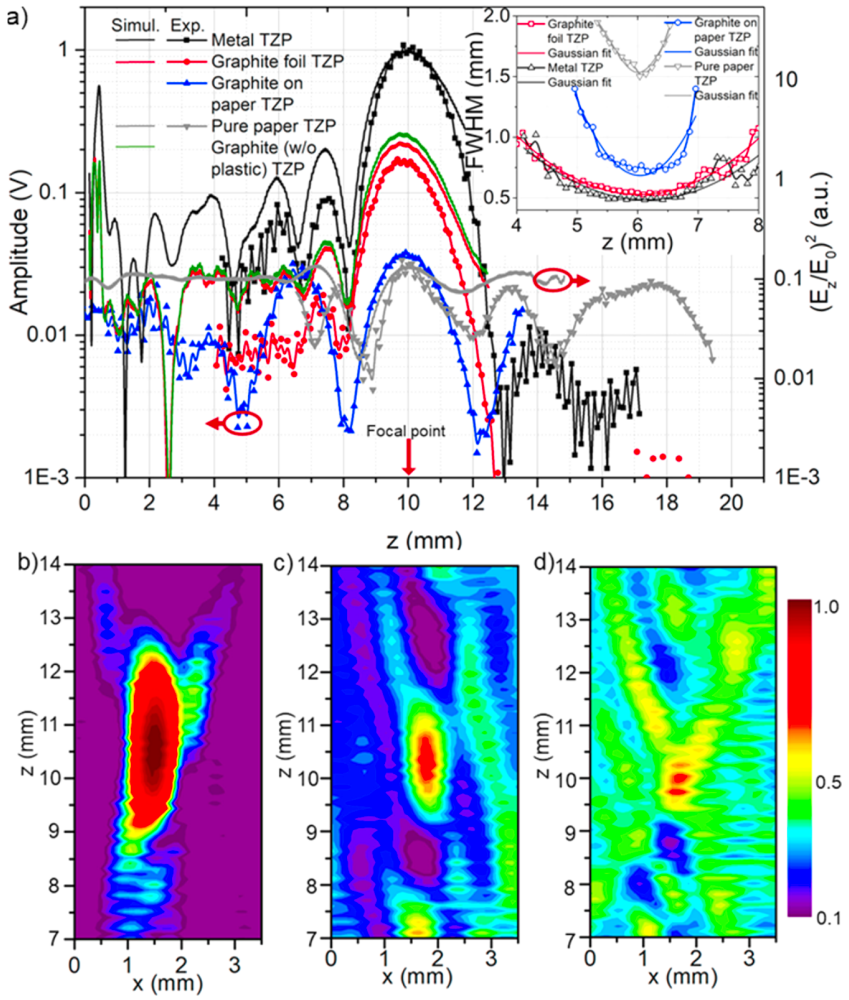


**Fig. 4.** a) Experimental results (symbols + lines) of the beam profile (left scale) and theoretical calculations (straight lines) of the normalized squared electric field (right scale) distribution along $z$-axes. Inset depicts FWHM variation along the $z$-axis for the beam focused with all investigated TZPs. (b-d) The beam profile along $z$-axes ($zx$-plane) focused with: b) graphite foil TZP, c) graphite on paper TZP, d) pure paper TZP.

It is interesting to note that the pure paper TZP also manifests some focusing performance. As it can be seen from Fig. 4(a), the signal in pure paper TZP increases by a factor of 1.3 in the focal plane, as compared to the unfocused beam, and the experimental data fits well with the modelling results. Graphite added on the paper by the HB pencil shading increases the focusing effect by about 15% with respect to the pure paper TZP. Thus, by adding the focusing TZP with integrated filters one can extend the range of paper applications to design and production of large scale inexpensive THz photonics components, such as paper THz wave plates [23] and aberration corrected paper-based lenses for low-frequency THz radiation [24,25].

Since the spatial beam quality is of particular importance [26], its Gaussian profile was checked recording 2D plot of the emitted beam. To estimate the focusing parameters, full width at half maximum (FWHM) of the Gaussian beam along the $z$-axis was measured for all TZPs by approximating them as Gaussians. The results are shown in inset of Fig. 4. It can be observed that FWHMs of the graphite foil and metal TZPs are relatively narrow and varies negligibly along the $z$-axis. In contrast, the FWHM of pure paper and graphite on paper TZPs suffer drastic spreading when moving away from the focal point.

Using experimentally obtained data, focusing parameters such as beam waist ($\omega_0$), Rayleigh range ($z_R$), focal depth ($b$), beam angular spread ($\theta$), and numerical aperture ($NA$) were evaluated. Estimates are given in Table 3. It is seen that the THz beam, focused with graphite foil zone plate displays only a 7% wider beam waist than the reference metal TZP. One can note that other parameters of both these TZPs also look quite similar. However, comparison of pure paper and graphite on paper based TZPs implies the important fact that the addition of only few microns of graphite strongly affects the parameters of the TZP: $\omega_0$, $\theta$ and $NA$ were estimated to be more than twice smaller for graphite on paper-based TZPs than the pure paper one. Concerning the Rayleigh range ($z_R$) and the focal depth ($b$), the difference is more than four times. Therefore, one can infer that even a few microns thick layer of graphite can significantly affect the TZPs focusing performance. This is also illustrated in Fig. 4(b–d), where the beam profiles of graphite foil TZP, graphite on paper TZP, and pure paper TZP are presented.

**Table 3. Gaussian beam parameters**

| | $\omega_0$ (mm) | $z_R$ (mm) | b (mm) | $\theta$ (°) | NA |
|---|---|---|---|---|---|
| Metal TZP | 0.48 | 1.4 | 2.8 | 20 | 0.343 |
| Graphite foil TZP | 0.52 | 1.64 | 3.28 | 18 | 0.316 |
| Graphite on paper TZP | 0.71 | 3.06 | 6.12 | 13 | 0.232 |
| Pure paper TZP | 1.51 | 13.9 | 27.8 | 6 | 0.109 |

To complete the picture, numerical 3D simulations were performed to elucidate the graphite foil, graphite on paper, pure paper-based TZPs, and the metal TZP (Fig. 5). Steel has been chosen as a perfect electrical conductor, paper as a material with permittivity of $\varepsilon_r$=2.31, graphite with electrical conductivity of $1{\cdot}10^5$ S/m and $\varepsilon_r$=12 and loss free polyester plastic with $\varepsilon_r$=3.5. To model the wave propagation through the cross-shaped apertures, 3D finite-difference time-domain (3D FDTD) method was employed. Simulation grid, corresponding to the $16.5 \times 16.5 \times 12$ mm$^3$ volume in $x$, $y$, $z$ directions respectively, was set-up with grid sizes $\Delta x = \Delta y = \Delta z = 38$ µm. In order to reduce the computational load, symmetry conditions of the structure were used to simulate only quarter of the zone plate, and absorbing boundary conditions were applied.

Figure 5 illustrates the calculated distribution of the electric field near the zone plates made of different materials. The transmitted plane wave is found focused in the focal spot of the TZP located at 10 mm.

Comparison of the plots in panels (a) and (b) in Fig. 5 indicates similar focusing abilities of graphite foil TZP and the metal one. Figure 5(c) displays the focusing performance of pure paper zone plate and the graphite on paper TZP. The focal points of both TZP overlap, thus, the focusing intensity is estimated theoretically. For pure paper and graphite on paper TZP the focusing intensity is increased by 1.3 and 1.5 times, respectively, as compared with the unfocused beam, and these values agree well with experimentally obtained data.

Therefore, one can presume that graphite-based THz zone plates can provide rational flexible and compact solutions for design of passive optical elements in THz imaging systems. Graphite is a unique material manifesting metal and non-metal properties, it is also disposable, eco-friendly and cheap, and these advantages forms a new dimension for production of diffractive optical components [27].

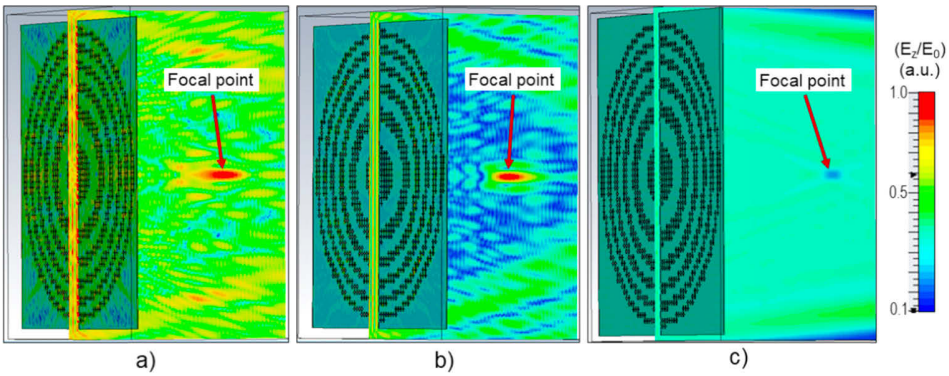


**Fig. 5.** Simulated distribution of electric field amplitude behind the a) metal TZP, b) graphite foil TZP, c) graphite on paper and paper TZPs – both focal points overlap; the increase in intensity of graphite on paper TZP is 15% higher than that of the paper alone.

## 4. Conclusions

Flexible graphite-based THz zone plates with integrated cross-shaped filters were demonstrated for compact optics in THz imaging systems. 3D finite-difference time domain method was employed to design the zone plates which were fabricated using direct laser writing technique. Flexible zone plates were produced from 10 μm thick graphite foil, thin graphite layer made by HB graphite pencil on a 100 μm thick paper sheet, and a pure paper sheet. The performance of zone plates was investigated using THz time-domain spectroscopy and THz imaging at 0.6 THz frequency. It was found that the graphite-based zone plate displays frequency features and focusing operation with a quality that nearly matches the metal-based zone plate. The graphite on paper and pure paper zone plates can increase the focusing by a factor of 1.5 and 1.3, respectively, as compared with the unfocused beam. The observed experimental data was supported by 3D finite-difference time domain method numerical calculations. The findings suggest that graphite-based THz zone plates can provide an inexpensive alternative to metal-based elements for design of passive optical elements in THz imaging systems.

## Acknowledgements

Authors are greatly indebted to Irmantas Kašalynas, Polina Kuzhir, Alesia Paddubskaya and Tadas Paulauskas for enlightening discussions, to Martynas Talaikis for Raman spectra measurements and to Jonas Zinkevičius for technical assistance in the manuscript preparation.

## References

1. S. S. Dhillon, M. S. Vitiello, E. H. Linfield, A. G. Davies, M. C. Hoffmann, J. Booske, C. Paoloni, M. Gensch, P. Weightman, G. P. Williams, E. Castro-Camus, D. R. S. Cumming, F. Simoens, I. Escorcia-Carranza, J. Grant, S. Lucyszyn, M. Kuwata-Gonokami, K. Konishi, M. Koch, C. A. Schmuttenmaer, T. L. Cocker, R. Huber, A. G. Markelz, Z. D. Taylor, V. P. Wallace, J. Axel Zeitler, J. Sibik, T. M. Korter, B. Ellison, S. Rea, P. Goldsmith, K. B. Cooper, R. Appleby, D. Pardo, P. G. Huggard, V. Krozer, H. Shams, M. Fice, C. Renaud, A. Seeds, A. Stöhr, M. Naftaly, N. Ridler, R. Clarke, J. E. Cunningham, and M. B. Johnston, "The 2017 terahertz science and technology roadmap," J. Phys. D: Appl. Phys. **50**(4), 043001 (2017).
2. G. Liang, T. Liu, and Q. J. Wang, "Recent Developments of Terahertz Quantum Cascade Lasers," IEEE J. Sel. Top. Quantum Electron. **23**(4), 1200118 (2017).
3. I. Kašalynas, R. Venckevičius, L. Minkevičius, A. Sešek, F. Wahaia, V. Tamošiūnas, B. Voisiat, D. Seliuta, G. Valušis, A. Švigelj, and J. Trontelj, "Spectroscopic terahertz imaging at room temperature employing microbolometer terahertz sensors and its application to the study of carcinoma tissues," Sensors **16**(4), 432 (2016).

4. K. Ikamas, D. Cibiraite, A. Lisauskas, M. Bauer, V. Krozer, and H. G. Roskos, "Broadband Terahertz Power Detectors Based on 90-nm Silicon CMOS Transistors with Flat Responsivity Up to 2.2 THz," IEEE Electron Device Lett. **39**(9), 1413–1416 (2018).
5. F. Capasso, "The future and promise of flat optics: a personal perspective," Nanophotonics **7**(6), 953–957 (2018).
6. M. Bauer, R. Venckevičius, I. Kašalynas, S. Boppel, M. Mundt, L. Minkevičius, A. Lisauskas, G. Valušis, V. Krozer, and H. G. Roskos, "Antenna-coupled field-effect transistors for multi-spectral terahertz imaging up to 425 THz," Opt. Express **22**(16), 19235–19241 (2014).
7. I. Kašalynas, R. Venckevičius, and G. Valušis, "Continuous Wave Spectroscopic Terahertz Imaging With InGaAs Bow-Tie Diodes at Room Temperature," IEEE Sens. J. **13**(1), 50–54 (2013).
8. U. Puc, A. Abina, A. Jeglič, A. Zidanšek, I. Kašalynas, R. Venckevičius, and G. Valušis, "Spectroscopic Analysis of Melatonin in the Terahertz Frequency Range," Sensors **18**(12), 4098 (2018).
9. U. Puc, A. Abina, M. Rutar, A. Zidanšek, A. Jeglič, and G. Valušis, "Terahertz spectroscopic identification of explosive and drug simulants concealed by various hiding techniques," Appl. Opt. **54**(14), 4495–4502 (2015).
10. M. E. MacDonald, A. Alexanian, R. A. York, Z. Popovic, and E. N. Grossman, "Spectral transmittance of lossy printed resonant-grid terahertz bandpass filters," IEEE Trans. Microwave Theory Tech. **48**(4), 712–718 (2000).
11. L. Minkevičius, B. Voisiat, A. Mekys, R. Venckevičius, I. Kašalynas, D. Seliuta, G. Valušis, G. Račiukaitis, and V. Tamošiūnas, "Terahertz zone plates with integrated laser-ablated bandpass filters," Electron. Lett. **49**(1), 49–50 (2013).
12. L. Minkevičius, K. Madeikis, B. Voisiat, I. Kašalynas, R. Venckevičius, G. Račiukaitis, V. Tamošiūnas, and G. Valušis, "Focusing Performance of Terahertz Zone Plates with Integrated Cross-shape Apertures," J. Infrared, Millimeter, Terahertz Waves **35**(9), 699–702 (2014).
13. A. Ferraro, D. C. Zografopoulos, R. Caputo, and R. Baccherelli, "Broad- and Narrow-Line Terahertz Filtering in Frequency-Selective Surfaces Patterned on Thin Low-Loss Polymer Substrates," IEEE J. Sel. Top. Quantum Electron. **23**(4), 8501308 (2017).
14. T. H. Hand and S. A. Cummer, "Frequency tunable electromagnetic metamaterial using ferroelectric loaded split rings," J. Appl. Phys. **103**(6), 066105 (2008).
15. K. Fuchi, A. R. Diaz, E. J. Rothwell, R. O. Ouedraogo, and J. Tang, "An origami tunable metamaterial," J. Appl. Phys. **111**(8), 084905 (2012).
16. H. Fang, S.-C. A. Chu, Y. Xia, and K.-W. Wang, "Programmable Self-Locking Origami Mechanical Metamaterials," Adv. Mater. **30**(15), 1706311 (2018).
17. C. Coulais, A. Sabbadini, F. Vink, and M. van Hecke, "Multi-step self-guided pathways for shape-changing metamaterials," Nature **561**(7724), 512–515 (2018).
18. D. Jokubauskis, L. Minkevičius, D. Seliuta, I. Kašalynas, and G. Valušis, "Terahertz homodyne spectroscopic imaging of concealed low-absorbing objects," Opt. Eng. **58**(02), 023104 (2019).
19. A. Urbanowicz, V. Pačebutas, A. Geižutis, S. Stanionyte, and A. Krotkus, "Terahertz time-domain-spectroscopy system based on 1.55 μm fiber laser and photoconductive antennas from dilute bismides," AIP Adv. **6**(2), 025218 (2016).
20. M. Karaliunas, K. E. Nasser, A. Urbanowicz, I. Kasalynas, D. Brazinskiene, S. Asadauskas, and G. Valusis, "Non-destructive inspection of food and technical oils by terahertz spectroscopy," Sci. Rep. **8**(1), 18025 (2018).
21. S. Tofani, D. C. Zografopoulos, M. Missori, R. Fastampa, and R. Beccherelli, "High-Resolution Binary Zone Plate in Double-Sided Configuration for Terahertz Radiation Focusing," IEEE Photonics Technol. Lett. **31**(2), 117–120 (2019).
22. B. Voisiat, A. Bičiūnas, I. Kašalynas, and G. Račiukaitis, "Band-pass filters for THz spectral range fabricated by laser ablation," Appl. Phys. A **104**(3), 953–958 (2011).
23. B. Scherger, M. Scheller, N. Vieweg, S. T. Cundiff, and M. Koch, "Paper terahertz wave plates," Opt. Express **19**(25), 24884–24889 (2011).
24. A. Siemion, A. Siemion, M. Makowski, J. Suszek, J. Bomba, A. Czerwinski, F. Garet, J. L. Coutaz, and M. Sypek, "Diffractive paper lens fot terahertz optics," Opt. Lett. **37**(20), 4320–4322 (2012).
25. A. Siemion, "Terahertz Diffractive Optics—Smart Control over Radiation," J. Infrared, Millimeter, Terahertz Waves **40**(5), 477–499 (2019).
26. S. Tofani, D. C. Zografopoulos, M. Missori, R. Fastampa, and R. Baccherelli, "Terahertz focusing properties of polymeric zone plates characterized by a modified knife-edge technique," J. Opt. Soc. Am. B **36**(5), D88–D96 (2019).
27. D. L. Chung, "Review Graphite," J. Mater. Sci. **37**(8), 1475–1489 (2002).

P2

**ADVANTAGES OF OPTICAL MODULATION IN TERAHERTZ IMAGING FOR STUDY OF GRAPHENE LAYERS**

**R. Ivaškevičiūtė-Povilauskienė**, A. Paddubskaya, D. Seliuta, D. Jokubauskis, L. Minkevičius, A. Urbanowicz, I. Matulaitienė, L. Mikoliūnaitė, P. Kuzhir, G. Valušis
*Journal of Applied Physics* **131**, 033101 (2022)
DOI: 10.1063/5.0074772

# Advantages of optical modulation in terahertz imaging for study of graphene layers

Cite as: J. Appl. Phys. **131**, 033101 (2022); doi: 10.1063/5.0074772
Submitted: 11 October 2021 · Accepted: 28 December 2021 ·
Published Online: 18 January 2022



R. Ivaškevičiūtė-Povilauskienė,[1,a)] A. Paddubskaya,[2] D. Seliuta,[1] D. Jokubauskis,[1] L. Minkevičius,[1] A. Urbanowicz,[1] I. Matulaitienė,[3] L. Mikoliūnaitė,[3] P. Kuzhir,[4] and G. Valušis[1]

## AFFILIATIONS

[1]Department of Optoelectronics, Center for Physical Sciences and Technology, Sauletekio av. 3, Vilnius 10257, Lithuania
[2]Laboratory of Nanoelectromagnetics, Institute for Nuclear Problems of Belarusian State University, Bobruiskaya Str. 11, Minsk 220006, Belarus
[3]Department of Organic Chemistry, Center for Physical Sciences and Technology, Sauletekio av. 3, Vilnius 10257, Lithuania
[4]Department of Physics and Mathematics, Institute of Photonics, University of Eastern Finland, Yliopistokatu 7, Joensuu 80101, Finland

**Note:** This paper is part of the Special Topic on Microwave Absorption by Carbon-Based Materials and Structures.
[a)]**Author to whom correspondence should be addressed:** rusne.ivaskeviciute@ftmc.lt

## ABSTRACT

It was demonstrated that optical modulation together with simultaneous terahertz (THz) imaging application enables an increase in contrast by an order of magnitude, thereby illustrating the technique as a convenient contactless tool for characterization of graphene deposited on high-resistivity silicon substrates. It was shown that the single- and double-layer graphene can be discriminated and characterized via variation of THz image contrast using a discrete frequency in a continuous wave mode. Modulation depth of 45% has been reached, and the contrast variation from 0.16 up to 0.23 is exposed under laser illumination for the single- and double-layer graphene, respectively. The technique was applied in the development and investigation of graphene-based optical diffractive elements for THz imaging systems.



## I. INTRODUCTION

Rapid evolution of terahertz (THz) technology and imaging evolving into a broad range spectrum of applications[1] stimulates an intensive search for new solutions in design and fabrication of convenient-in-use imaging systems. As a rule, preferences are given to compact or portable systems, preferably free of any optical alignment and containing only room temperature operating compact emitters and receivers coupled together with flat optical elements. The latter can be fabricated, for instance, using metamaterials,[2,3] either high-resistivity silicon-based diffractive optics[4] or 3D printed optical components.[5]

Due to its exceptional optical properties, graphene can be assumed as one of the most promising materials for THz and infrared passive optical components fabrication, i.e., modulators, transistors, etc.,[6,7] where contactless tuning is strongly preferred. However, for this kind of applications, high quality of the material is strongly preferred; therefore, contactless characterization gains particular attention.

Since pristine graphene is nearly transparent for THz radiation, it needs to be doped through any external force, i.e., either electrically driven or optically excited, aiming to make it effectively operating as a functional optical element. As a rule, such an approach of graphene modulation in a transmission mode requires substrate transparent for THz radiation; i.e., undoped silicon and germanium can be a suitable choice.[8–10] More detailedly, these studies were concentrated on single-layer graphene placement and investigation on these substrates under illumination of relatively high laser power reaching 400 mW in the case of germanium[10] and 40 mW in the case of silicon.[8] One can note that the modulation depth was estimated to be of 94% and about 70%, respectively. In the development of compact systems, preferences are given to small powers for modulation; therefore, the modulation depth

dependence on the laser power attains a special focus of exploration. It is worth noting that photomodulation depth vs the incident laser power was investigated, and the estimated values were found to be around 7% at 25 mW[9] and about 45% at the same power level.[8]

In this work, the potential of the graphene optical modulation technique was extended via its application in THz imaging, enabling thus characterization and discrimination of both the single- and double-layer graphene in a contactless way. It was shown that such a technique allows an increase in the contrast in an order of magnitude, indicating that it can serve as a convenient contactless tool for characterization of graphene deposited on high-resistivity silicon substrates. The optical excitation power was kept to 25 mW, and the modulation depth of 42% was reached for single-layer graphene and 45% for double-layer graphene. A strong increase in the THz image contrast, up to 0.16, for the single layer graphene and 0.23 for double-layer graphene under optical excitation demonstrates the ability of THz imaging in contactless characterization and discrimination of graphene layer quality. This technique can be found useful in fabrication of graphene-based diffractive optical elements for THz imaging systems and on-chip designs in integrated photonics.

## II. SAMPLE CHARACTERIZATION

To investigate optical modulation of graphene, two types of samples based on single-layer and double-layer graphene structures were fabricated on a high resistivity 460 $\mu$m thick Si substrate. Both samples—single- and double-layer graphene—were produced using commercially available CVD graphene ("Graphenea") grown on a copper substrate and covered with ≈60 nm thick PMMA. To place CVD graphene on an Si substrate, the "classical" wet transfer technique[11] was used. According to the standard procedure, after copper etching and washing with distilled water, the graphene/PMMA structure was transferred on an Si substrate and then annealed at 130 °C. To remove the PMMA layer, the chloroform solution was used. In order to fabricate the samples with a double-layer graphene structure, the same technique was repeated. A newly produced graphene/PMMA unit was deposited on top of the obtained graphene monolayer on the Si substrate. Then, the polymer was removed.

The quality of obtained samples was estimated by Raman spectroscopy. The measurements were carried out with a Renishaw inVia Raman spectrometer equipped with a thermoelectrically cooled (−70 °C) CCD camera. All the spectra were recorded using 532 nm laser excitation. To avoid laser-induced sample heating, the average power on the sample's surface was set below 2.3 mW. The OLYMPUS LCPlan N 50/0.65 NA objective was used to collect Raman spectra signals. The exposure time was 10 s, and each spectrum was collected per 10 scans, yielding total 100 s time accumulation. The Raman frequencies were calibrated using the polystyrene standard ASTM E 1840 spectrum. The relative intensities of the Raman signal (instrument response function) were calibrated by using luminescence of NIST Intensity Standard SRM 2241. For the imaging, the *xy* piezo stage was used.

The Raman spectra are shown in Fig. 1(a). As one can see, characteristic peaks of graphene are clearly visible. For single-layer graphene, the D peak is located at 1337 $cm^{-1}$, the G peak at 1583 $cm^{-1}$, and the 2D peak at 2673 $cm^{-1}$. The D mode is caused by a disordered structure of graphene. In this case, the intensity ratio of $I(D)/I(G) = 0.3$. The small ratio of D and G peaks indicates high order in the system and thus good quality of graphene. This also correlates well with higher carrier mobility.[12] For double-layer graphene, the D peak is visible at 1346 $cm^{-1}$, the G peak at 1581 $cm^{-1}$, and the 2D peak at 2686 $cm^{-1}$. The D peak is also very weak $I(D)/I(G) = 0.2$, which implies on a good quality of graphene. The G band position, intensity, and its shape are very sensitive to the doping level and the mechanical strain, which can be related to the interaction with the Si substrate. Since the G and 2D bands depend differently on graphene doping,[13] the evaluation of the $I(2D)/I(G)$ ratio is not suitable in our case.

Addition of the second graphene layer increases full width at half maximum (FWHM) of G and 2D peaks. For single-layer graphene, the FWHM of the G peak is 19.2 $cm^{-1}$, while FWHM of the 2D peak is 29.0 $cm^{-1}$. For double-layer graphene, the FWHMs of G and 2D peaks are 21.6 $cm^{-1}$ and 40.9 $cm^{-1}$, respectively. As expected, adding of the second layer of graphene causes the 2D band splitting into the overlapping modes. It also causes the FWHM of 2D peak widening by 41%.[14] In addition, the central position of the 2D peak shifts to a higher wave number. After deposition of the second graphene layer, it has shifted by 13 $cm^{-1}$ as with the increase of the number of layers, the 2D peak shifts to a higher wave number.[15]

Furthermore, from the comparison of Raman spectra collected from the areas corresponding to the single and double graphene (the measurements have been done on one sample), it can be concluded that the intensity of the G mode increased up to two times after transferring of the second graphene layer on top of the first one (data are not presented). This result is in a good agreement with the principle that the Raman intensity of the G mode increases almost linearly with the increasing graphene layer number until approximately ten layers.[16] In both Raman spectra, D +D″ bands are observed at 2450 $cm^{-1}$. These lines are associated with the emission of two phonons in the structure.[17] These results confirm that both samples display good graphene quality, and they show that additional layer of graphene gives expected Raman spectral properties of monolayer graphene.

To check the quality of the whole graphene layers, the Raman mapping has been performed. The measurements were carried out with a WITec alpha300 R Raman spectrometer equipped with a thermoelectrically cooled (−60 °C) CCD camera. All the spectra were recorded using 532 nm laser excitation. The average power on the sample's surface was set around 6 mW. The ZEISS EC Epiplan Neofluar 100×/0.9 NA objective was used to collect Raman mapping signals. The integration time was 0.5 s, and 50 spectra per line were collected. The Raman frequencies were calibrated using the polystyrene spectrum. For the imaging, the xy piezo stage was used.

Raman maps of the intensity of G and 2D modes for samples with single- and double-layer graphene, respectively, are shown in Figs. 1(c) and 1(d). A small variation in the intensity distribution of both modes and the absence of the D mode (data are not presented) indicate high uniformity of transferred CVD graphene. It was first demonstrated[18] that the effect of the mechanical strain and charge doping can be optically separated from each other by correlation

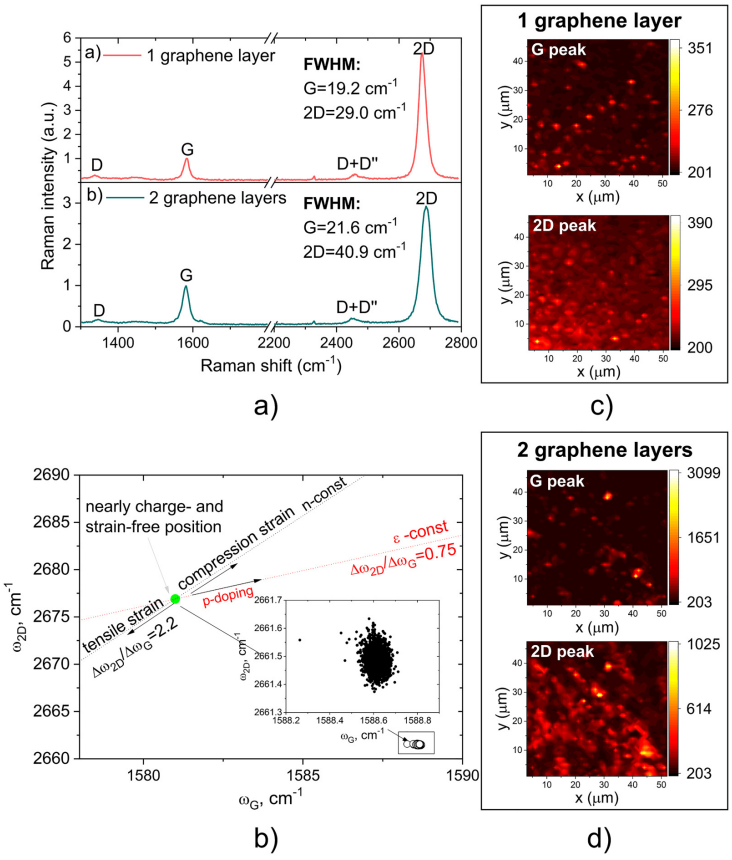


**FIG. 1.** (a) Raman spectra of single and double graphene layers. The intensity was normalized to G peaks for each sample. The spectra were excited by 532 nm laser limiting its power to 2.265 mW. (b) 2D and G peak frequency distribution for single-layer graphene. 2D and G peak mapping for (c) single-layer graphene and (d) double-layer graphene.

analysis of the frequency position of G and 2D modes. The plot demonstrates the distribution of $\omega_G$ and $\omega_{2D}$ obtained across a single graphene layer, as shown in Fig. 1(b). Red and black dashed lines corresponding to the directions in which the variation due to doping and mechanical strain are considered to be constant as well as zero point ($1581.6 \pm 0.2\,cm^{-1}$, $2676.9 \pm 0.7\,cm^{-1}$) were added for clarity. As one can see, due to interaction with oxygen environment, the single graphene layer on an Si substrate is affected by hole doping. On the other hand, the interaction with an Si substrate can explain the observed mechanical strain of the graphene layer.

## III. TERAHERTZ EXPERIMENTAL SETUPS

Three different setups were employed in the experiments. The continuous wave (CW) frequency-domain THz spectrometer (Toptica TeraScan 780) in transmission geometry used to

investigate properties of optically excited graphene in the THz frequency range is presented in Fig. 2(a). The emitted THz radiation is collimated by the first parabolic mirror (PM) and focused on the sample by the second PM. The beam spot diameter at the focal point of the second PM is 2 mm. Then, the transmitted beam again is collimated by the third PM and focused onto the detector by the fourth PM.

The THz mapping of graphene-based samples with and without optical excitation was recorded using a THz-CW imaging system [Fig. 2(b)], which provides additional information about the amplitude of the transmitted signal and its distribution along the sample surface. The THz-CW imaging system is based on a 0.3 THz electronic source (Virginia Diodes, VDI-175T) and includes the high-density polyethylene (HDPE) lenses and the antenna-coupled titanium microbolometer[19] as a THz detector

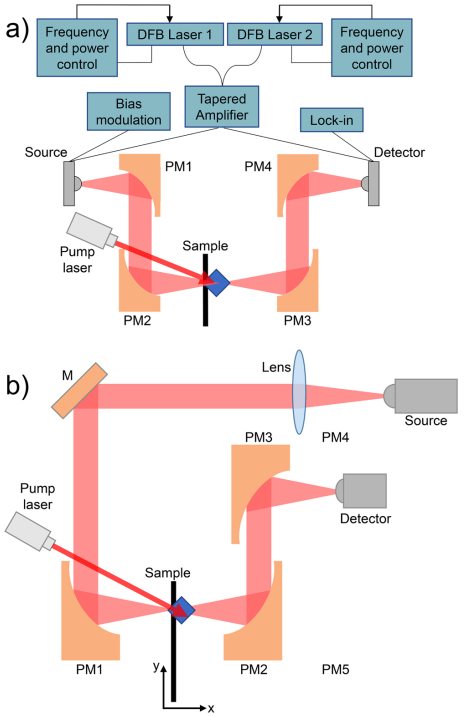


**FIG. 2.** (a) THz spectrometer setup (PM1–PM4—parabolic mirrors). (b) THz continuous wave THz imaging setup in transmission geometry (M, mirror; PM1–PM3, parabolic mirrors).

with an aperture of 2 mm. The imaging was recorded by electronically modulating the source at 1 kHz frequency and detecting the microbolometer-induced signal by a lock-in amplifier.[20] Two crossed motorized translation stages were used to move samples in the x–y directions perpendicular to the incident THz beam, where the diameter in the focal point is 3 mm.

To evaluate the variation of the dynamic graphene conductivity, spectroscopic measurements were performed using a Teravil-Ekspla T-SPEC THz time-domain spectroscopic (THz-TDS) system based on a femtosecond laser (Toptica TeraScan, Femtofiber Pro). The system provides pulses of 780 nm wavelength, 90 fs pulse duration, and 150 mW output power with a 80 MHz repetition rate. Photoconductive antennas based on low-temperature grown GaAs were used for the emission and detection. The fast delay line was based on 10 times per second moving hollow retro-reflector with a 120 ps time window corresponding to 8 GHz spectral resolution. The diameter of the focused beam was 2 mm. The THz signal was detected by the digital signal processing card integrated into the electronic module with an analog-digital converter.

During all the experiments, the optical modulation was driven by a 666 nm continuous wave laser with a power of 25 mW and a beam spot diameter on the sample surface of 3 mm. The principal scheme is presented in Fig. 3(a).

## IV. RESULTS AND DISCUSSION

It is known that pristine graphene has a cone-like band structure, where its Fermi level is at Dirac's point [Fig. 3(b)].[21] Control of the electric conductivity can be done via tuning the Fermi level by doping graphene chemically, electrically, or optically.[22] Because of this cone-like band structure, density of states (DOS) of graphene is zero; therefore, when charge carriers are generated on the surface of graphene, Fermi energy rapidly increases or decreases depending on the p- or n-type of doping [Fig. 3(b)]. For smaller energies (IR or THz ranges), Fermi energy determines the optical conductivity of graphene.[23,24]

In this work, we used optical modulation induced by a pump laser. Since graphene's band structure is linear, optical absorption is independent of the excitation wavelength.

Transmission spectra of all samples were obtained using a THz spectroscopy system, and for each sample, it was measured twice—with and without laser illumination [Fig. 4(a)]. As one can see, transmittance varies due to the Fabry–Pérot interference and decreases under photoexcitation. Moreover, for samples with graphene, transmittance reduction is higher than that for pure Si. It is supposed that the optical injection of carriers generated by light absorption in Si is responsible for this effect. In the case of free-standing graphene, this modulation effect can be inverse because of the optical pumping, which increases the number of carriers and, consequently, the Drude absorption.[25]

The optical excitation was done by the pumping laser with $\lambda = 666$ nm, and the penetration depth $\delta_p$ in Si for this particular wavelength is 8 $\mu$m. Since the total thickness of Si was 460 $\mu$m, $\delta_p$ is relatively shallow and indicates that carriers generated under photoexcitation can easily be transferred to the graphene layers. Since graphene exhibits higher carrier mobility than Si, it causes an

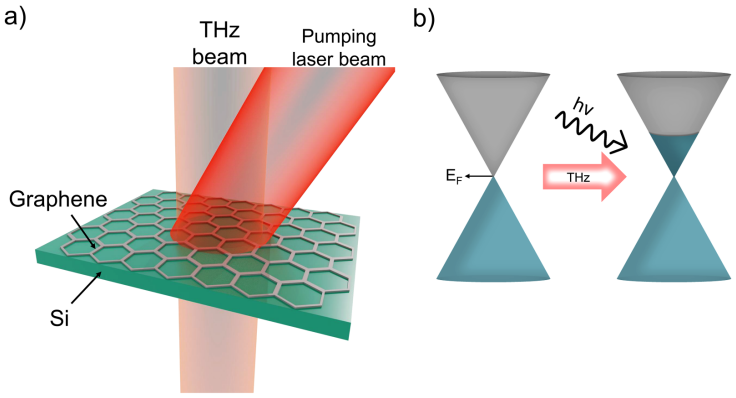


**FIG. 3.** (a) Principal scheme of the experiment. THz radiation and pumping laser beam overlapping at the sample surface. (b) Graphene band structure before and under laser illumination.

increase in electrical conductivity. According to (1) formula, higher conductivity results in reduced transmittance,[9]

$$\frac{T_{gr/Si}}{T_{Si}} = \frac{n+1}{n+1+Z_0\sigma(\omega)}; \tag{1}$$

here, $T_{gr/Si}$ is transmittance through graphene on an Si sample, $T_{Si}$ is transmittance through an Si substrate, $n = 3.42$ labels a refractive index of the substrate, $Z_0 = 377\,\Omega$ is impedance of free space, and $\sigma(\omega)$ denotes complex conductivity of graphene.

By adding the second layer of graphene, mobility of transferred free carriers increases, inducing thus a conductivity increase and, consequently, higher reduction in THz transmittance. Additionally, the modulation depth for all the samples was estimated by evaluating transmittance with and without photoexcitation using (2) and shown in the inset of Fig. 4(b),

$$M = \frac{T_{w/o} - T_{w/}}{T_{w/o}} \cdot 100\%; \tag{2}$$

here, $M$ is the modulation depth, $T_{w/o}$ labels transmittance without optical excitation, and $T_{w/}$ is transmittance with optical excitation.

As it was expected, the optical modulation is the weakest for pure Si and the maximum modulation depth is 14% at 0.43 THz frequency. Meanwhile, the maximum modulation depth reaches 42% for the single graphene layer and 45% for two graphene layers at 0.36 THz frequency.

Moreover, the modulation depth difference between single- and double-layer graphene is shown in Fig. 4(b). Shadows in the line indicate a 2% systematic error in the experiment. The maximum modulation depth difference between single and two graphene layers is well-resolved and reaches 12 ± 2% at 0.38 THz.

To evaluate a variation in electrical conductivity of graphene with and without optical excitation, THz time-domain spectroscopy (THz-TDS) measurements were carried out in two geometries—at the normal incidence of the THz beam and at the angle other than normal (as an example, at 43°). Such a rotation of the sample around the axis parallel to the component of the electric field of the incident THz beam is the simplest way to change pumping laser intensity (power/surface area) at the same point.

In contrast with the frequency-domain method, the THz-TDS technique is phase sensitive, which gives the possibility to evaluate the material parameters of the samples.[26,27] It was demonstrated[28] that for any thin conductive film deposited on a dielectric substrate, the transmittance can be defined using the following formula:

$$T_s = \frac{4 \cdot \alpha_s \cdot e^{ik_z} \cdot e^{-ik_z} \cdot e^{-ik_0}}{e^{ik_z} \cdot (1 + B_s - \alpha_s) \cdot (-1 + \alpha_s) + e^{-ik_z}(1 + \alpha_s) \cdot (1 + B_s + \alpha_s)}, \tag{3}$$

where for an $s$-polarized wave, $B_s = \sigma/\varepsilon_0 \cos[\theta]$, $k_0 = \omega/c$, $k_0 z = k_0 \cos[\theta]$, $k_z = k_0\sqrt{\varepsilon_s - (\sin[\theta])^2}$, and $\alpha_s = k_z/k_{0z}$. $\theta$ is the angle that is equal to 0° and 43° for considered cases.

Then electrical conductivity was calculated using Kubo's formula,

$$\begin{aligned}\sigma(\omega, \Gamma, \mu) = {} & \frac{i \cdot 2e^2 k_B T}{\pi\hbar^2(\omega i\Gamma)} \cdot \log\left(2\cosh\left[\frac{\mu}{2k_B T}\right]\right) \\ & + \frac{e^2}{4\hbar}\left[\frac{1}{2} + \frac{1}{\pi}\arctan\left(\frac{\hbar\omega - 2\mu}{2k_B T}\right)\right. \\ & \left. - \frac{i}{2\pi} \cdot \log\left(\frac{(\hbar\omega + 2\mu)^2}{\hbar\omega - 2\mu^2 + 4(k_B T)^2}\right)\right],\end{aligned} \tag{4}$$

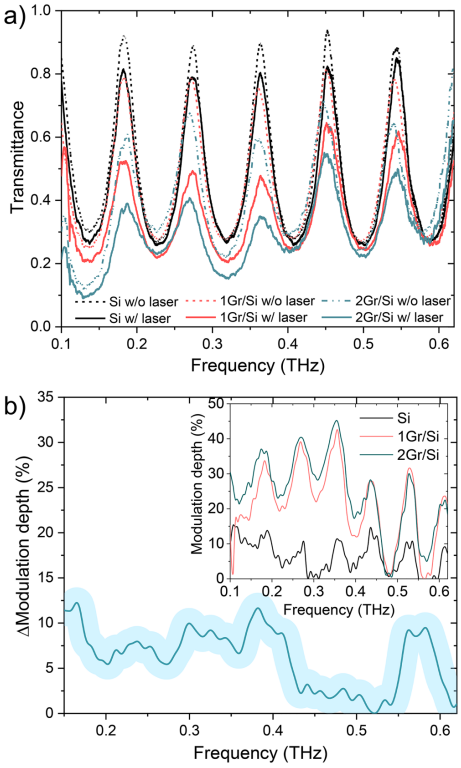


**FIG. 4.** (a) Transmittance spectra of the samples with and without photoexcitation. (b) Modulation depth difference between single- and double-layer graphene. Shadow of the line indicates a 2% systematic error in the experiment. The inset depicts the modulation depth of all investigated samples.

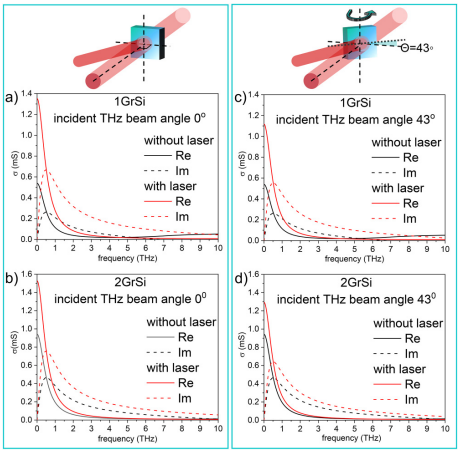


**FIG. 5.** *Re* and *Im* parts of (a) single- and (b) double-layer graphene conductivity when the incident THz radiation is perpendicular to the sample. *Re* and *Im* parts of (c) single-and (d) double-layer graphene conductivity when the THz radiation is at a 43° incident angle. The black line indicates results without photoexcitation and the red one with photoexcitation.

where $\omega$ is the angular frequency, $\Gamma = 1/\tau$, $\mu$ denotes the chemical potential, $k_B$ is the Boltzmann constant, $T = 293$ K depicts room temperature, and $\hbar$ indicates the reduced Planck constant.

It can be shown that formula (3) enables characterization of CVD graphene samples via parameter relaxation time $\tau = 50$ fs and chemical potential $\mu = 0.09$ eV. This technique allows one to evaluate the variation of the chemical potential of the single graphene layer from the value of 0.09–0.23 eV under photoexcitation at normal incidence and from 0.09 to 0.19 eV after sample rotation at 43°, which is in agreement with our predictions that the graphene doping level depends on the pumping laser intensity. The calculated *Re* and *Im* parts of the conductivity of the single graphene layer before and after excitation are presented in Figs. 5(a) and 5(c). In the case of the double graphene layers to have the best fit with the experimental data, it was necessary to take into account a weak interaction between the first and the second layers, which is in good agreement with our Raman results and a small difference in the doping level between the different graphene layers [Figs. 5(b) and 5(d)].

In order to evaluate the spatial distribution of transmittance changes under photoexcitation, THz imaging in transmission geometry was employed using the THz-CW imaging system operating at 0.3 THz. Results are presented in Fig. 6. Imaging results show that the single-layer graphene reduces THz transmittance by 5%, while the double-layer graphene reduces it up to 12%.

As it is illustrated in Fig. 4(a), the transmittance can be significantly modulated by photoexcitation. THz imaging results confirm that the transmittance change is minimal under photoexcitation for a pure Si substrate. However, the situation goes into sharp contrast when the single- and double-layer graphene is placed on the substrate and illuminated by the optical pumping laser. To qualitatively define the difference between the registered signal with and without laser illumination, contrast was defined as $C = |(T_{w/} - T_{w/o})/T_{w/}|$.[29] The contrast is 0.16 and 0.23 for single and double graphene layers, respectively. Meanwhile, the contrast value for pure Si is only 0.05.

These results point out that simultaneous application of a THz imaging technique with an optical excitation leads in well-

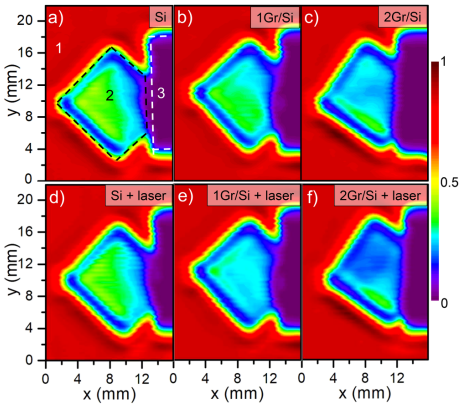


**FIG. 6.** 2D imaging of samples recorded at 0.3 THz in transmission geometry: without photoexcitation (a)–(c) and with photoexcitation (d)–(f). The transmittance scale is normalized to the maximum signal. Under photoexcitation, the resulting contrast is 0.16 for single-layer graphene and 0.23 for double-layer graphene. In (a), 1 marks the air, 2 the sample, and 3 the sample holder.

resolved changes in the image contrast; hence, the effect can successfully be used for contactless graphene characterization and evaluation of the different number of graphene layers in the investigated structure.

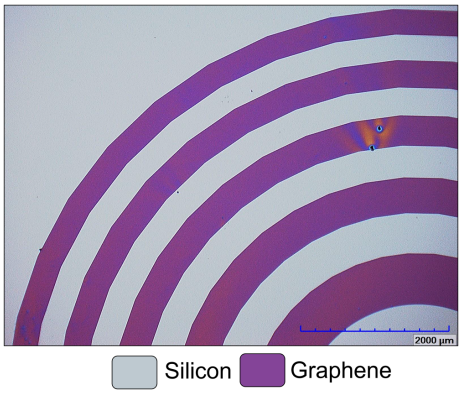


**FIG. 7.** Photo of the quarter of a graphene-based zone plate. The gray area indicates silicon, whereas the purple area depicts graphene parts.

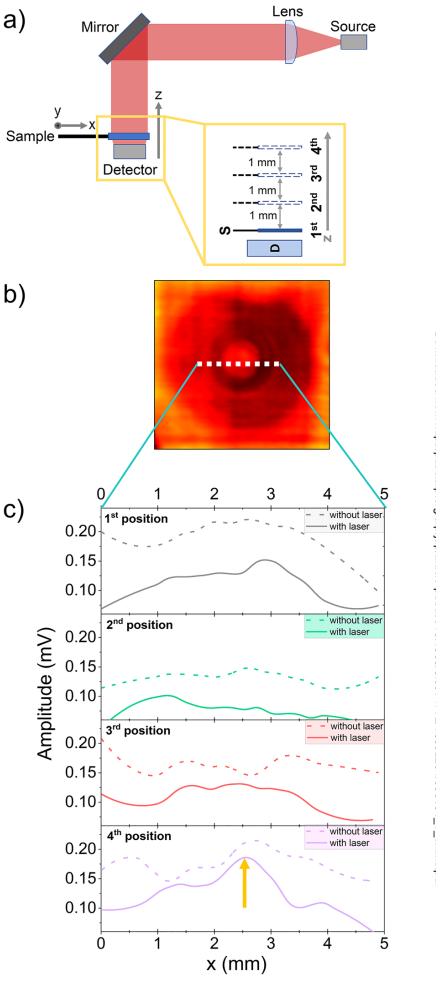


**FIG. 8.** (a) THz-CW system setup at 0.58 THz. The sample was shifted away from the detector, starting from the first position and moved further in a 1 mm step. (b) 2D imaging of investigated GZP. (c) Cross sections of transmitted THz radiation through GZP at first, second, third, and fourth positions indicated in panel (a). The evaluation is made from a 5 mm width part at the center depicted as a white dotted line in panel (b). The yellow arrow indicates pronounced focusing of the THz radiation.

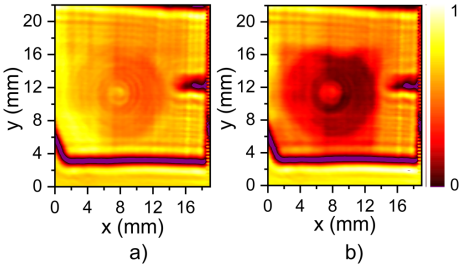


**FIG. 9.** Two-dimensional imaging of a graphene zone plate at 0.58 THz on an Si substrate (a) without and (b) with laser illumination. The colored scale indicates the transmitted signal normalized to the maximum value.

## V. GRAPHENE-BASED THz ZONE PLATE

THz zone plates as compact focusing elements can be useful in THz imaging systems with a broadband source when, e.g., for spectroscopic THz imaging aims, only one particularly selected frequency is needed to record the image.[20,30]

A graphene zone plate (GZP) (Fig. 7) was fabricated using a graphene patterning technique, where the single graphene layer was first transferred on the Si substrate in the same way as described in Sec. II. Then, the PMMA layer was coated on the top of graphene for protection. Subsequently, photolithography was performed after which patterned photoresist served as a mask for graphene. Later, step by step, each layer was removed until only patterned graphene in the shape of a zone plate was left on the Si substrate.

The zone plate was designed for 0.58 THz frequency; the diameter of the outer zone was 1 cm and the width of one stripe was $\approx 500\,\mu$m.

To examine GZP focusing abilities, THz imaging in the transmission geometry was recorded using a THz-CW system. The setup is shown in Fig. 8(a). Here, the same electronic THz source tuned to 0.58 THz as in Fig. 2(b) was used. The images were recorded moving GZP in $xy$ directions. Every full 2D scan was repeated by moving the GZP in the $z$ direction away from the detector, starting from the closest (first) position and then moving further in a 1 mm step.

Cross sections of the transmitted THz radiation were evaluated along the 5 mm line in the center of the beam, depicted as a white dotted line shown in Fig. 8(b). Cross sections at all four positions are shown in Fig. 8(c). As one can see at the first, second, and third positions, the mode cross section is smooth, about 4 mm wide with detection amplitudes of 0.15, 0.09, and 0.12 mV, respectively. At the fourth position, the profile exhibits peculiarities expressed as a higher peak with the reduced width to 1 mm and the increased amplitude to 0.19 mV (marked with a yellow arrow), indicating focused radiation at the center of the zone plate.

Two-dimensional imaging of a graphene zone plate at the fourth position with and without photoexcitation is displayed in Fig. 9. The colored scale indicates the amplitude of the transmitted signal normalized to the maximum value. As it is seen in Fig. 9(a), the transmitted signal is decreased in the zone patterned with graphene. The contrast at the center in the THz image without optical excitation is 0.44. Optical excitation changes the situation essentially in increasing the contrast up to 4.17 at 0.58 THz as it is presented in Fig. 9(b). Therefore, GZP can clearly be presented in THz imaging results. It implies that THz imaging combined simultaneously with optical modulation can serve as a convenient contactless tool for characterization and discrimination of graphene layers on silicon substrates.

## VI. CONCLUSIONS

Single- and double-layer graphene was deposited on the high-resistivity silicon substrates using a wet transfer technique. The measured Raman spectra indicated good quality of prepared layers. Optical modulation of single- and double-layer graphene is demonstrated with corresponding modulation depth values of 42% and 45%. THz time-domain spectroscopy enabled one to evaluate graphene conductivity before and under laser illumination, which exhibits an increase in its real part of $\approx$2.5 times for a single graphene layer and $\approx$1.6 times for a double graphene layer. Advantages of THz imaging with its simultaneous use of optical modulation were revealed. The pronounced change observed in contrast of 0.16 for single-layer graphene and 0.23 for double-layer graphene with and without laser illumination allowed one to infer that THz imaging can serve as a convenient contactless technique for characterization and discrimination of graphene layers on silicon substrates.

## ACKNOWLEDGMENTS

This work was supported by Horizon 2020 under Grant No. 823728 (DiSetCom). P.K. was supported by the Academy of Finland Flagship Programme "Photonics Research and Innovation (PREIN)" (Decision No. 320165).

## AUTHOR DECLARATIONS

### Conflict of Interest

The authors have no conflicts to disclose.

## DATA AVAILABILITY

The data that support the findings of this study are available from the corresponding author upon reasonable request.

## REFERENCES

[1]G. Valušis, A. Lisauskas, H. Yuan, W. Knap, and H. G. Roskos, Sensors **21**, 4092 (2021).
[2]P. Genevet, F. Capasso, F. Aieta, M. Khorasaninejad, and R. Devlin, Optica **4**, 139–152 (2017).
[3]W. T. Chen, A. Y. Zhu, and F. Capasso, Nat. Rev. Mater. **5**, 604–620 (2020).
[4]L. Minkevičius, S. Indrišiūnas, R. Šniaukas, B. Voisiat, V. Janonis, V. Tamošiūnas, I. Kašalynas, G. Račiukaitis, and G. Valušis, Opt. Lett. **42**, 1875 (2017).
[5]A. Siemion, Sensors **21**, 100 (2021).
[6]L. Ju, B. Geng, J. Horng, C. Girit, M. Martin, Z. Hao, H. A. Bechtel, X. Liang, A. Zettl, Y. Shen, and F. Wang, Nat. Nanotechnol. **6**, 630–634 (2011).
[7]J. Li, L. Niu, Z. Zheng, and F. Yan, Adv. Mater. **26**, 5239–5273 (2014).

[8]P. Weis, J. L. Garcia-Pomar, M. Hoh, B. Reinhard, A. Brodvanski, and M. Rahm, ACS Nano **6**, 9118–9124 (2014).
[9]M. Fu, X. Wang, S. Wang, Z. Xie, S. Feng, W. Sun, J. Ye, P. Han, and Y. Zhang, Opt. Mater. **66**, 381–385 (2017).
[10]Q. Y. Wen, W. Tian, Q. Mao, Z. Chen, W. W. Liu, Q. H. Yang, M. Sanderson, and H. W. Zhang, Sci. Rep. **4**, 7409 (2014).
[11]P. P. Kuzhir, A. G. Paddubskaya, N. I. Volynets, K. G. Batrakov, T. Kaplas, P. Lamberti, R. Kotsilkova, and P. Lambin, J. Nanophotonics **11**, 032504 (2017).
[12]P. Boggild, D. M. A. Mackenzie, P. R. Whelan, D. H. Petersen, J. D. Buron, A. Zurutuza, J. Gallop, L. Hao, and P. U. Jepsen, 2D Mater. **4**, 042003 (2017).
[13]C. Casiraghi, Phys. Rev. B **80**, 233407 (2009).
[14]A. C. Ferrari, J. C. Meyer, V. Scardaci, C. Casiraghi, M. Lazzeri, F. Mauri, S. Piscanec, D. Jiang, K. S. Novoselov, S. Roth, and A. K. Geim, Phys. Rev. Lett. **97**, 187401 (2006).
[15]C. N. R. Rao, K. Biswas, K. S. Subrahmanyam, and A. Govindaraj, J. Mater. Chem. **19**, 2457–2469 (2009).
[16]Y. Y. Wang, Z. H. Ni, and Z. X. Shen, Appl. Phys. Lett. **92**, 043121 (2008).
[17]P. Venezuela, M. Lazzeri, and F. Mauri, Phys. Rev. B **84**, 035433 (2011).
[18]J. E. Lee, G. Ahn, J. Shim, Y. S. Lee, and S. Ryu, Nat. Commun. **3**, 1024 (2012).
[19]I. Kašalynas, R. Venckevičius, L. Minkevičius, A. Sešek, F. Wahaia, V. Tamošiūnas, B. Voisiat, D. Seliuta, G. Valušis, A. Švigelj, and J. Trontelj, Sensors **16**, 432 (2016).
[20]R. Ivaškevičiūtė-Povilauskienė, L. Minkevičius, D. Jokubauskis, A. Urbanowicz, S. Indrišinas, and G. Valušis, Opt. Mater. Express **9**, 4438–4446 (2019).
[21]K. F. Mak, M. Y. Sfeir, J. A. Misewich, and T. F. Heinz, Proc. Natl. Acad. Sci. U.S.A. **107**, 14999–15004 (2010).
[22]R. Binder, *Optical Properties of Graphene* (University of Arizona, 2017).
[23]K. F. Mak, M. Y. Sfeir, Y. Wu, C. H. Lui, J. A. Misewich, and T. F. Heinz, Phys. Rev. Lett. **101**, 196405 (2008).
[24]K. F. Mak, J. Shan, and T. F. Heinz, Phys. Rev. Lett. **106**, 046401 (2011).
[25]M. Mittendorff, S. Winnerl, and T. E. Murphy, Adv. Opt. Mater. **9**, 2001500 (2020).
[26]H. Nemec, F. Kadlec, P. Kuzel, L. Duvillaret, and J.-L. Coutaz, Opt. Commun. **260**, 175–183 (2006).
[27]I. Pupeza, R. Wilk, and M. Koch, Opt. Express **15**, 4335–4350 (2007).
[28]K. Batrakov, P. Kuzhir, S. Maksimenko, N. Volynets, S. Voronovich, A. Paddubskaya, G. Valušis, T. Kaplas, Y. Svirko, and P. Lambin, Appl. Phys. Lett. **108**, 123101 (2016).
[29]A. Siemion, L. Minkevičius, L. Qi, and G. Valušis, Opt. Laser Eng. **139**, 106476 (2021).
[30]L. Minkevičius, K. Madeikis, B. Voisiat, I. Kašalynas, R. Venckevičius, G. Račiukaitis, V. Tamošiūnas, and G. Valušis, J. Infrared Millim. Terahertz Waves **35**, 699–702 (2014).

P3

## FLEXIBLE TERAHERTZ OPTICS: LIGHT BEAM PROFILE ENGINEERING VIA C-SHAPED METALLIC METASURFACE

**R. Ivaškevičiūtė-Povilauskienė**, V. Čižas, E. Nacius, I. Grigelionis, K. Redeckas, M. Bernatonis, S. Orlov, G. Valušis, L. Minkevičius

*Frontiers in Physics* **11**, 1196726 (2023).
DOI: 10.3389/fphy.2023.1196726



The article may be accessed online at https://doi.org/10.3389/fphy.2023.1196726

frontiers | Frontiers in Physics

TYPE Original Research
PUBLISHED 05 May 2023
DOI 10.3389/fphy.2023.1196726



OPEN ACCESS

EDITED BY
Li Li,
Harbin Institute of Technology, China

REVIEWED BY
Baptiste Fix,
Office National d'Études et de Recherches Aérospatiales, Palaiseau, France
Jinhui Shi,
Harbin Engineering University, China

*CORRESPONDENCE
Rusnė Ivaškevičiūtė-Povilauskienė,
rusne.ivaskeviciute@ftmc.lt

RECEIVED 30 March 2023
ACCEPTED 25 April 2023
PUBLISHED 05 May 2023

CITATION
Ivaškevičiūtė-Povilauskienė R, Čižas V, Nacius E, Grigelionis I, Redeckas K, Bernatonis M, Orlov S, Valušis G and Minkevičius L (2023), Flexible terahertz optics: light beam profile engineering via C-shaped metallic metasurface. *Front. Phys.* 11:1196726. doi: 10.3389/fphy.2023.1196726



# Flexible terahertz optics: light beam profile engineering via C-shaped metallic metasurface

Rusnė Ivaškevičiūtė-Povilauskienė[1]*, Vladislovas Čižas[1], Ernestas Nacius[2], Ignas Grigelionis[1], Karolis Redeckas[1], Matas Bernatonis[1], Sergej Orlov[2], Gintaras Valušis[1,3] and Linas Minkevičius[1,3]

[1]Department of Optoelectronics, Center for Physical Sciences and Technology, Vilnius, Lithuania, [2]Department of Fundamental Research, Center for Physical Sciences and Technology, Vilnius, Lithuania, [3]Department of Physics, Institute of Photonics and Nanotechnology, Vilnius University, Vilnius, Lithuania

The potential of terahertz (THz) imaging implementation in a large variety of applications requires compact, reliable, and relatively low-cost solutions in systems constituents. Here we focus on the development of passive optical elements and demonstrate flexible and reliable THz beam profile engineering for imaging aims via mechanical bending of a stainless steel-based C-shaped metasurface. The designed and laser-ablation technology fabricated metasurface provides compact THz focusing and enables THz light engineering as well as polarization control ability in THz imaging. Focusing, light profile engineering, and polarization control performances of the metasurfaces with different focal distances and C-shape designs are presented. Experimental data are well supported by simulations, using Finite Difference Time Domain (FDTD) method. THz images of different objects at ~ 94 GHz using InP Gunn diode, bow-tie sensors, and exclusively metasurfaces-based optics are exposed. Further routes in the development of low-cost multicolor and polarization-sensitive THz imaging are discussed.

KEYWORDS

**terahertz, imaging, metasurfaces, compact imaging systems, mechanical bending, light profile engineering**

## 1 Introduction

Terahertz (THz) imaging technique, due to its nondestructive origin, can serve as a powerful tool for a large variety of applications in material inspections, various security checks, or medical scanning [1, 2]. However, in the practical implementation of THz imaging systems, particular attention needs to be given to their miniaturization and optimization, enhanced functionality, reduced power consumption, and increased convenience in use [3]. It requires overcoming a number of significant obstacles related to the low power of THz emitters, the reliability of sensitive THz detectors, and effective solutions in the design and technology of passive optical components like mirrors, lenses, and beam splitters. As a rule, these elements are rather bulky, therefore, finding flat optics-based solutions can create a strong basis for the development of compact imaging systems and indicate routes for rational on-chip designs. It was demonstrated that metamaterials [4] provide unlimited rich freedom in the design of flat optical elements to manipulate features of electromagnetic waves starting from their propagation properties, polarization management, or control over the dispersion of refractive indexes of materials [5–7]. On the other hand, it was

revealed recently that THz light engineering having a strong effect on imaging properties and quality, in appropriate beam shaping schemes can outperform the conventional Gaussian illumination approach [8].

In the given work, flexible and reliable THz beam profile engineering via mechanical bending of a stainless steel-based C-shaped metasurface is presented. The designed metasurface provides compact THz focusing, light spatial profile engineering, as well as polarization control ability in THz imaging. To explore low-cost solutions in THz imaging, we have restricted ourselves to the ~ 94 GHz range relying the system on InP Gunn diode (Spacek Labs, model No: GQ-440KS), bow-tie sensors [9], and laser-ablation technology [10] fabricated metasurfaces. The study investigates the focusing, light profile engineering, and polarization control performances of metasurfaces with varying focal lengths (F = 10, 20, 30, and 40 mm) and different widths of split ring resonators SRRs (c = 30, 60, 75, and 90 μm). Experimental data are well supported by simulations using the Finite Difference Time Domain (FDTD) method. Terahertz images of different objects are exposed, and further routes in the development of low-cost multispectral and polarization-sensitive THz imaging systems are discussed.

## 2 Flexible optical elements and experimental setup

Any type of split ring resonator (SRR) relies on the principle of the electric field generated from the dipole or quadrupole appearing due to the charge carriers oscillating under the influence of external electromagnetic illumination [11]. In the case of the most popular type of SRRs, comprising conductive periodic structure deposited on transparent material, it can be illustrated via the dipole formation at the gap of the ring element [12]. During this study, the inverse SRR or complementary SRR (CSRR) structure, comprising periodic C-shaped openings in the conductive layer, is employed. The dipole in these structures is formed at the opening on the opposite side of the conductive gap [13]. One can note that the dipole itself can be generated due to charge carrier interaction with either separate magnetic or electric fields of the external radiation, or both, depending on how the incident radiation is applied [14]. In this study, the magnetic field vector was kept parallel to the metasurface layer, therefore, no resonance due to magnetic response can be expected, and the studied effects can be exclusively attributed to the electric resonance [15].

In any case, any SRR element can be treated as an LC circuit. Investigations dedicated to the derivation of the theoretical relations that estimate the LC parameters of any SRR structure [16, 17] allow not only to define a resonant frequency of the structure but also indicate a large variety of resonance-related phenomena, for instance, excitation of two resonance frequencies [18, 19] or frequencies shifts due to peculiarities of the meta element design [20]. The employment of the inverse (complementary) SRR structure may be of specific interest as the Babinet principle states that the diffraction pattern of the metasurface and its

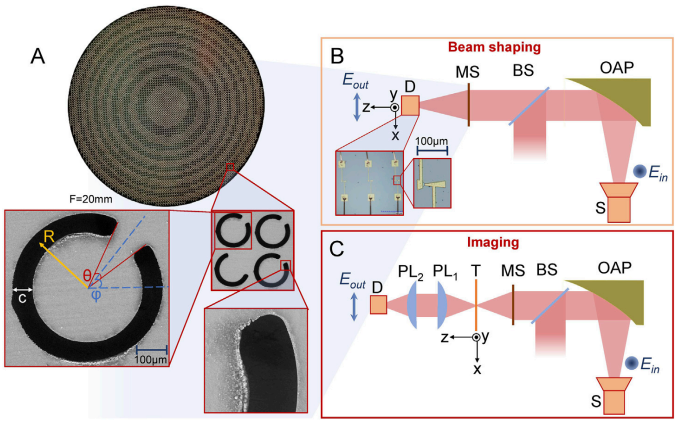


FIGURE 1
Metallic metasurface design and THz imaging setups. **(A)** Design of the metallic C-shaped complementary split-ring resonators metasurface, its geometry, and enlarged view of the metaelement depicting the parameters to be varied during this study: the letter *c* denotes the thickness of the opening, $\theta$ - the cutout angle, *R* is the radius, and $\varphi$ depicts the position of the gap. **(B)** Schematic layout of the THz beam engineering setup dedicated to the evaluation of metallic metasurface design effect on the polarized light. The radiation of power of around 40 mW with an electric field polarized along the Y-axis emitted from an adjustable frequency InP Gunn diode oscillator source (Spacek Labs, model No: GQ-440KS) (S) is collimated by F = 10 cm parabolic mirror (PM) as the beam diverges. The metasurface focuses the beam onto a focal point where a polarization-sensitive InGaAs-based bow-tie-shaped detector (D) is placed. The photo of the enlarged active part of the detector is depicted in the bottom inset. A high resistivity silicon beam splitter (BS) of 525 μm thickness is placed between a parabolic mirror and metallic metasurface in order to reduce the standing wave effects between the emitter and metallic metasurface. **(C)** THz imaging setup employing the THz beam engineering. The setup contains two additional paraffin lenses (PL1 and PL2) dedicated to collimate the THz beam after it passes through the target (T) and then focusing it into the detector.

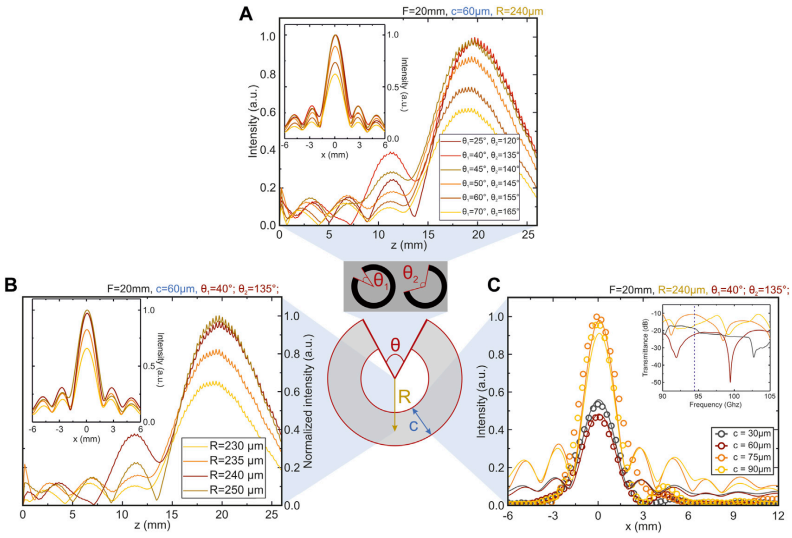


FIGURE 2
The dependence of CSRR metasurface focusing performance on different metacell geometrical parameters. **(A)** Simulation of the intensity distribution along the optical axis, obtained by varying cutout angles $\theta_1$ and $\theta_2$. Intensities along the $x$-axis at the focal plane are displayed in the inset. The optimal pair of angles $\theta_1$=40° and $\theta_2$=135° was selected for the following simulations. **(B)** Simulations of intensity distribution along the optical axis for the CSRRs metaelement radius $R$ ranging from 230 μm to 250 μm. Intensities along the $x$-axis at the focal plane are displayed in the inset. The optimal radius of $R$ =240 μm was selected for the following simulations. **(C)** Illustration of the experimentally measured (symbols) and simulated (solid line) intensities along $x$-axis at the focal plane for the varying opening widths of the metaelements, denoted by the letter $c$ at the central image. The inset denotes the simulated transmission spectra of the CSRR structure at the focal point, the blue dashed line represents the frequency used during the experiments. In all cases, fixed parameters are displayed in the insets of the relevant panels.

complementary metasurface is the same [21, 22]. This fact establishes the background for the development of the CSRR structure as a focusing element with the same focal length at the same resonant frequency as the conventional SRR [23]. Furthermore, this allows extending the beam shaping facilities using CSRR as metaelements employing experience of studies in more classic metasurfaces [24–27].

Investigated metasurface containing CSRRs was manufactured from a 25 μm thickness stainless steel foil employing laser-ablation technology, already successfully applied for compact THz optics fabrication aims [10, 28]. The ablation process was carried out by using Pharos SP (produced by Light Conversion Ltd.) laser, delivering ultrashort pulses of duration tunable from 158 fs to 10 ps at $\lambda$ = 1030 nm wavelength with a maximum average power of 6 W at 200 kHz repetition rate. The beam positioning system intelliSCAN (Scanlab), paired with the f-theta lens of effective focal length $f$ = 100 mm, was used to scan and focus the beam onto the surface of the foil. To keep the heat-affected zone as small as possible during the ablation, low pulse energy with a high scanning speed combination was used. Scanning was done with pulse density of 200 $mm^{-1}$ under peak fluence of $F$ = 9.4 J/$cm^2$ and repeating at least 250 times for a single feature to fully cut through the substrate. Such selection of parameters helped to maintain the flat surface of the foil unaffected by excess heat and to avoid oxidation. After the microfabrication, the sample was immersed in an ultrasonic bath in order clean off the built-up debris from its surface.

The complementary metasurface's openings were systematically placed in a recurring design based on the 5 zones and 4 subzones Fresnel equation [29] to act as a zone plate (top panel of Figure 1A) enabling a possibility to focus and manipulate the THz light beam. The CSRRs gap's position and cutout angle (described by $\varphi$ and $\theta$, respectively, in the bottom left part of Figure 1A) were adjusted relying on their location on the metasurface, aiming to achieve the required phase-shift for each CSRR. Each subzone of the zone plate was filled with identical CSRR metaelements, ensuring $\pi$/2 phase shift between the neighbouring zones. Furthermore, the radius of the openings ($R$) and their width ($c$) were varied for further optimization of the focusing element. It is deserved noting that the detected signal is due to radiation re-emission from the metasurface only. In this case, the ratio of exciting and re-emission powers is metasurface rotation angle-dependent and amounts to 6%–10%.

Figure 1B shows a schematic layout of the THz beam engineering setup, dedicated to investigating the designed metallic metasurfaces. The setup is based on an adjustable InP Gunn diode oscillator delivering tunable frequency radiation in

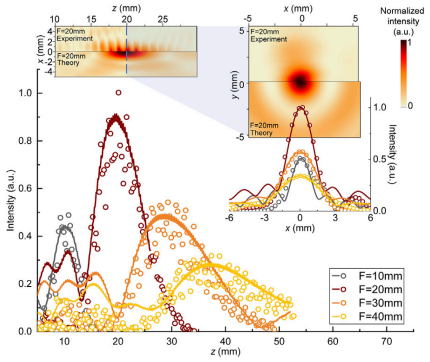


FIGURE 3
Focusing performances of the complementary C-shaped split ring resonators-based metasurface with different focal lengths ($F$ =10,20,30, and 40 mm) at ~ 94 GHz. The main graph–experimental results (symbols) and simulation results (solid lines) of the beam profile distribution along the optical axis for metasurfaces of the different focal lengths. Top left inset–the performance of the metasurface lens with the focal length of 20 mm: top half represents experimentally obtained and bottom half depicts simulated intensity distribution of THz beam along the optical axis. Note the standing wave effect occurring in the experimental part. The blue line indicates the focus position of the analyzed CSRR structure. The upper part of the top right inset–THz beam intensity distribution in the focal plane corresponding to the blue dashed line of the top left inset. The top half depicts experimental results and bottom half–theoretical simulations. The bottom part corresponds to the intensity beam profile along the $x$-axis at the focal point of the metasurfaces with different focal lengths, where the experimental results are marked as symbols and theoretical simulations are depicted as solid lines.

the interval of 93.8 GHz–94.1 GHz, passive optical elements, and bow-tie diode as the THz sensor, a photo of the detector is given in the left-bottom inset of Figure 1B. The latter device is based on the molecular-beam-epitaxy-grown InGaAs structure (sample I198:058 525 nm-thick $In_{0.46}Ga_{0.54}As$) and fabricated using procedures described in detail in Ref. [30]. The inherent feature of the device is the broadband operation with an almost flat response up to 0.8 THz [9]. As the sensor resembles a bow-tie antenna, it exhibits good coupling and nanoseconds duration response in free space at 94 GHz [31]. Figure 1C shows the schematic layout of the THz imaging setup, which contains two additional paraffin lenses, dedicated to collimating the THz beam after it passes through the target and then focusing it into the detector.

## 3 Experimental results and discussion

The primary objective was to determine the effect on the focusing abilities of the CSRR metasurface by variation of different CSRR metaelement parameters, depicted at the centre of Figure 2. The starting parameters, adapted for the desired frequency were taken from similar studies of another group [26]. Aiming to produce the most efficient focusing metasurfaces operating around ~94 GHz, numerical simulations, varying the cutout angle, were conducted with focal length $F$ = 20 mm, $R$ = 240 μm radius, and $c$ = 60 μm opening width (Figure 2A). The cutout angles of two different metaelements were varied keeping a constant relative phase shift of $\pi/2$. Additionally, employing the determined optimal cutout angle, the effect of different CSRR's metaelement radius ($R$) was simulated (Figure 2B). Finally, the variation of CSRRs width ($c$) as 30, 60, 75 and 90 μm was performed for the $F$ = 20 mm, $R$ = 240 μm and cutout angles of $\theta_1$ = 40° and $\theta_2$ = 135°. The metasurfaces with identical parameters were also investigated experimentally. The simulation-matching results, depicted in Figure 2C, reveal that the best focusing was achieved with the opening width of $c$ = 75 μm. The metasurfaces, containing metaelements with all three optimized parameters were used for the following studies of different focal length structures and the metasurface bending effect on the focusing performance.

Four metasurfaces with different focal lengths of $F$ = 10, 20, 30, and 40 mm have been fabricated, and their focusing performance was investigated both experimentally and theoretically. Experimentally obtained THz beam intensity distribution along the optical axis is depicted in the main graph of Figure 3 and is represented by symbols. The operation of metasurfaces as well as properties of propagating THz light was theoretically modeled using the FDTD method presented by straight lines. As one can see, the intensity of the beam, focused with $F$ = 20 mm focal length metasurface, expresses sharply increased intensity in comparison to other designs with $F$ = 10 mm, $F$ = 30 mm, and $F$ = 40 mm. Several aspects need to be taken into account analyzing these results. It is worth noting that the incident radiation excites dipole and quadrupole moments in the CSRR structure which signatures, as it will be shown later, become pronounced in angular dependencies of the re-emitted pattern [32]. The performance of a single metaelement can be explained using the concept of the numerical aperture (NA), which is NA = $\sin(\theta)$, where $\theta = \arctan(D/2f)$ is the largest meridional angle of the ray reaching the focal point ($f$ - focal length, $D$ - entrance pupil). The dipole wave radiation is not distributed isotropically in space. Like in a dipole antenna, the radiation directrix of the metacell obeys the squared cosine law in regard to the meridional angle (the direction at which rays arrive at the collective focus) [32]. Thus, the CSRR radiates around the directions lying perpendicular to the excited dipole moment because of the non-spherical electric and magnetic waves re-emitted from the structure. In the case of the zone plates with short focal distances (i.e., large NA) it means that the rays arriving at the focus have amplitudes modulated by the directrix function of the CSRR. The second effect which further decreases the intensity of the radiation in nonparaxial focal points is caused by the paraxial design of the zone plate. A variety of aberrations are introduced through, for example, the aplanatic factor - the rays arriving at the focal spot at larger spatial angles impinge the focus and are bent too much, therefore, their amplitudes are further modulated by the meridional angle.

As the focal distances increase, the NA decreases, thus, the aforementioned effects become less pronounced and the conventional behaviour of the Gaussian beam is observed. What is more, with an increase of the focal distance, the size of the Gaussian beam and its Rayleigh distance $z_r = k\omega_0^2/2$ also increases, therefore, the volume occupied by the beam is

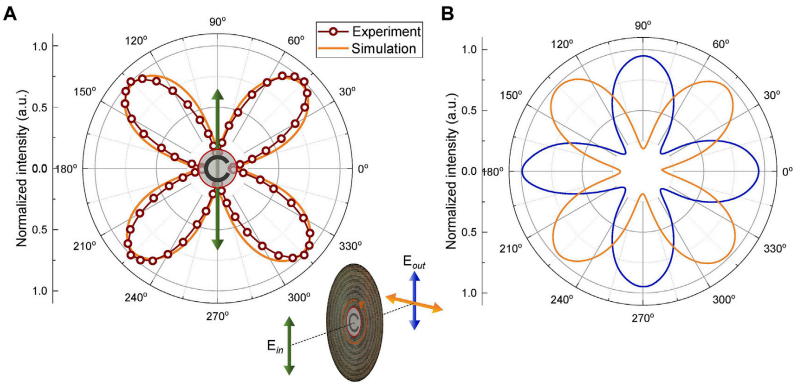


FIGURE 4
**(A)** Angular dependency of the recorded electric field component of the illumination on the rotation angle of the metasurface structure. Note that the polarization of the incident THz light is perpendicular to the recorded one (cf. orange arrow at the bottom right inset) as the rotation of the structure consequently changes the orientation of the dipole moment leading to the generation of the electric field component perpendicular to the direction of the incident electromagnetic field. The metaelement in the center of the graph depicts the 0° position of the central Fresnel subzone of the structure. The solid line with symbols represents experimental data while the thick solid line depicts simulation results. In the inset, the green arrow marked as $E_{in}$ corresponds to the polarization of the incident THz light, the orange arrow marks the recorded THz light, which is perpendicularly polarized to the incident light, and the blue arrow marks the recorded THz light, which is polarized in parallel to the incident light. **(B)** The simulated angular dependency of the electric field of two different polarizations on the angle corresponding to the position of the conductive gap of the metacell in the structure. The color of the solid line depicts the simulated polarization according to the inset of the panel (A). The differences in angular electric field dependencies allow employing polarization-resolved imaging.

$V = k\pi\omega_0^4/2$, and the maximal intensity decreases in the expected manner ($k = 2\pi/\lambda$ - wave number, $\omega_0$ is the beam waist). This effect is further intensified due to fixed-size 2-inch steel wafers used for the production, resulting that for the case of longer focal distance, the dimensions of the full 5 zones, 4 subzones Fresnel lens structure exceeds the 2-inch wafer size, therefore, it further decreases the intensity and the Rayleigh length.

The top left inset in Figure 3 shows the performance of the metasurface at the best operational focal point of $F = 20$ mm. The top half presents experimentally obtained and the bottom half depicts the simulated intensity distribution of THz beam along the optical axis. In contrast to the theoretical simulations, the experimental beam intensity distribution shows the presence of Fabry-Perot oscillations due to the formation of the standing waves. This discrepancy is due to different boundary conditions: in simulations, it is assumed that the waves, reflected from the metasurface, are absorbed, whereas in an experiment the waves experience the reflection from the beam splitter plate (cf. BS at Figure 1B) The top right inset depicts the THz beam profile in the focal plane ($xy$) of metasurfaces with different focal lengths. The best performance of $F = 20$ mm metasurface is compared with relevant simulations. The top half presents experimentally obtained results whereas the bottom half depicts numerical simulations. As it is seen, the theory describes the measurement data well.

As was aforesaid, the CSRR operation relies on dipole- and quadrupole-based re-emission of the incident THz radiation which is dependent on the angle between the $E$-field of the incident illumination and the CSRR gap, allowing thus the effect of polarization-sensitive focusing. To evidence it, we rotate CSRRs metasurface to measure the angular dependencies of the re-emitted THz radiation intensity. The angular dependency of the re-emitted electric field component, which is perpendicular-polarized to the incident THz radiation, is shown in Figure 4A. The intensity peaks are achieved when the angle between the CSRRs gap and incident electric field component is 45°, 135°, 225° and 315°. These observations, supported by FDTD simulations are consistent, taking into account the geometry of the above-described dipole formation in the CSRR metaelements. Consequently, such distribution enables a significant increase in signal-to-noise ratio for THz imaging systems operating in the transmission geometry. The bottom right inset depicts the polarization rotation features of the metasurface. The green arrow corresponds to the polarization of the incident THz radiation and the orange arrow indicates the polarization of the detected THz radiation. Considering angular dependency of the polarization, parallel to the incident THz radiation, depicted as a blue arrow in the inset of Figure 4A, one may note the 45° peak position shift, depicted as simulation results in Figure 4B. Typically, a single metacell would manifest a $\pi/2$ intensity symmetry for the perpendicular polarization (orange arrow) and $\pi$ intensity symmetry for the parallel one (blue arrow). However, as the metaelements in the subzones 3 and 4 of each Fresnel zone are 90° rotated copies of the subzones 1 and 2 respectively, the final angular dependency for both polarization expresses $\pi/2$ symmetry with 45° intensity shift between the polarizations (Figure 4B). Such

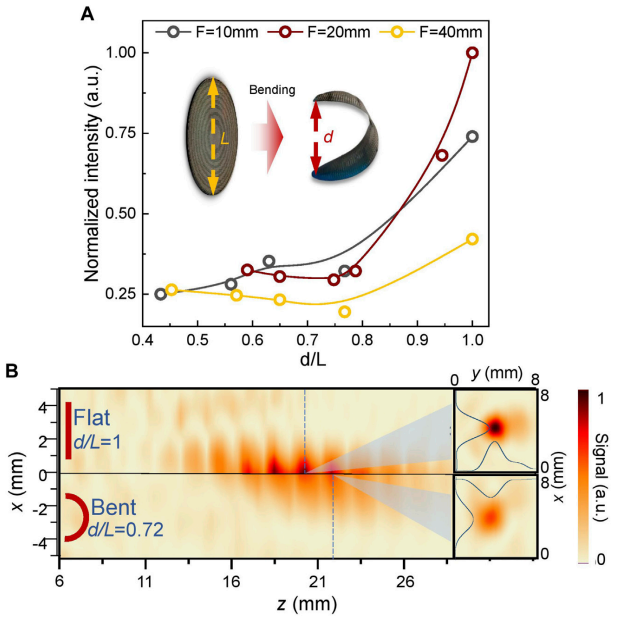


FIGURE 5
**(A)** Measured intensity dependence upon bending metasurfaces of different focal lengths. The inset depicts a visualization of the bent metasurface. Letter *L* denotes the diameter of the unbent metasurface and *d* is the distance between two opposite ends of the deformed plate. The bending level is represented as a ratio of *d*/*L*. **(B)** Intensity distribution of the THz beam along the optical axis (*xz*): the top half represents results when the metasurface was flat and the bottom half when the metasurface was bent. The dashed blue lines indicate the focus position. Note the change of the focal distance and intensity occurring due to bending, giving additional adjustment ability. Insets on the right side represent beam intensity distribution in the focal plane (*xy*) for the cases when the metasurface is flat and bent, respectively.

peculiarities of the structure allow for further enhanced imaging possibilities employing metasurfaces, as described below.

Another explored peculiarity of the CSRR structure, unavailable for the standard SRR, is structure bending ability. The flexibility of the metallic metasurface CSRRs not only allows them to maintain their functionality upon bending as an optical element but also provides tunability options for focusing and light manipulation under variations of mechanical deformation. To illustrate this, metasurfaces were investigated experimentally in a flat geometry and under variation of mechanical bending. The bending is represented by the *d*/*L* ratio, where *d* is the distance between the opposite ends of the deformed plate, and *L* is the diameter of the flat metasurface.

Signal dependency on the mechanical metasurface bending (*d*/*L*) is shown in Figure 5A. Three different metasurfaces designed for the focal lengths of ($F$ = 10, 20, and 40 mm) were investigated. As was discussed in Figure 3, without mechanical deformation, the metasurface with $F$ = 20 mm provides the highest signal. With the increase of mechanical bending, the recorded signal decreases in all the cases, however, the focusing ability of the structure remains. At the maximum bend, $d/L \approx 0.45$, all investigated structures reach similar signal values, amounting to $\approx 25\%$ of the maximum signal with respect to the best flat metasurface with focal length $F$ = 20 mm. Although the focal point changes its position due to the bending, the shape of the beam remains the same. It is evident from the plot depicted in Figure 5B, representing experimentally obtained flat and bent intensity distributions along the optical axis (*xz* plane), and right insets displaying experimental data of the intensity distribution in the focal (*xy*) plane. Therefore, the focusing abilities and focus tunability of CSRR-based optics elements via mechanical bending extend the area of different applications in the further development of compact THz imaging systems containing flexible optics.

## 4 THz imaging using C-shaped metasurface

THz imaging performance of the metasurface designed for $F$ = 20 mm is presented in Figure 6. Images were recorded using the setup, depicted in Figure 1C, where two non-transparent samples were raster-scanned during the THz illumination by the investigated metasurface. The first sample, comprising metallic target featuring cutout slits with varying widths (3 mm, 2 mm, and 1.5 mm) organized

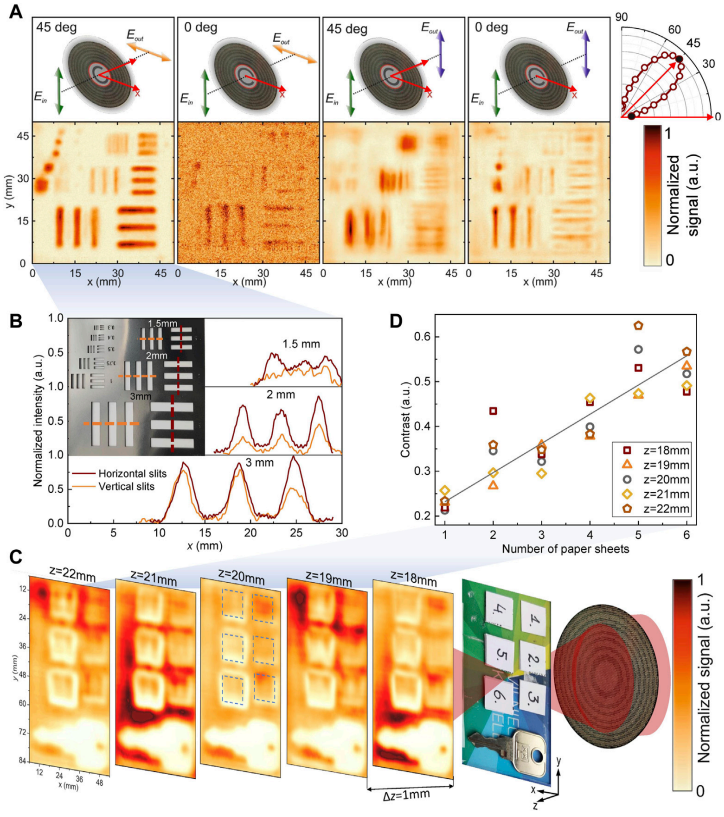


FIGURE 6
Demonstration of THz imaging using the focusing metasurface with the focal length of $F$ =20 mm. **(A)** Imaging of a metallic target with different period slits is achieved by recording different polarizations with the metasurface rotated either 0° or 45°. The color scale indicates the signal, normalized to its maximum value. Setups are depicted above each relevant imaging picture. The top right corner inset depicts the perpendicular-polarized electric field component dependence on the angle of the metasurface. The intensities, corresponding to the angle of the metasurface in this imaging experiment, are indicated by black dots. **(B)** Cross-sections of different period slits orientated vertically and horizontally at the positions denoted by the dashed lines for the case of the most left image of panel A. Inset shows a photograph of the imaged target. **(C)** Imaging of a special sample made of a plastic card containing a metal key and a different number (1–6) of paper sheets. During the imaging, the metasurface was used to focus the THz radiation onto the sample. Each image is obtained by moving the sample along the optical axis away from the focal plane of the metasurface with the step of 1 mm. The color scale indicates the signal normalized to its maximum value. **(D)** Contrast dependence on the number of paper sheets at different sample positions along the optical axis.

into groups according to their period, is depicted in the inset of Figure 6B. Each group of slits contains a 90° rotated duplicate so that the slits are oriented vertically and horizontally. Furthermore, as demonstrated later, the imaging of the target results in an object geometry that is responsive to variations in THz polarization on the other hand, it gives the possibility to determine the spatial resolution of the resulting images using the CSRR structure.

Figure 6A depicts the imaging results of the first sample, achieved by recording different polarizations with the metasurface rotated either 0° or 45°. The imaging setup is depicted above each relevant imaging picture, and the metasurface rotation angle is indicated on each top left angle of the setup. For the aim of convenience and clarity, the theoretical angular dependence of the perpendicularly polarized component is given in the right inset of panel (A). Perpendicular polarization-resolved imaging features can be seen from two left images of Figure 6A. In the left image, the metasurface is rotated by 45°, resulting in the peak of perpendicular polarization intensity (cf. Figure 4 and the right inset). One may note that horizontal lines are much more clearly

resolved in comparison to the vertical lines of the same period. This is because the perpendicular-polarized radiation is dominant in such setup geometry. The exception are the largest (3 mm) slits where almost no difference is visible between the different orientations as the slits are wide enough to resolve the parallel polarization. By rotating the metasurface by an additional 45° into 0° degree position, we get the minimal generation of the perpendicular-polarized radiation, therefore, nearly no imaging is possible as it is depicted on the second left imaging of Figure 6A. These results are further manifested by Figure 6B, where the intensity profiles of the most left image are taken for the different width slits at the lines depicted in the inset. The possibility to distinguish the slit at each profile for the case of perpendicular-polarized setup, results in 0.5$\lambda$ spatial resolution.

The situation becomes different in the case of parallel-polarized radiation (two right images of Figure 6A). For the case when metasurface is rotated by 45° degrees (the second right image), some blurred picture is visible, but no clear picture is resolved, as the intensity of the parallel-polarized component is very low, and the focal point of this polarization is more diffused compared to the perpendicular-polarized one. Still, by rotating the metasurface back to 0° (the case when the conductive gap is arranged along the $x$-axis) where the parallel-polarized radiation experiences a peak, we may achieve a parallel-polarized resolved image, manifested in highlighted vertical lines (most right image of Figure 6A). The target was additionally imaged by varying its distance from the metasurface focal plane by 1 mm steps. The spatial resolution was determined at each position, reaching 0.5$\lambda$ in all the cases, showing that the resolution remains the same regardless of the sample position within at least 5 mm range. This implies that such a metasurface enables high-quality images even if the imaged sample is not located precisely at the focal plane.

The second sample depicted in Figure 6C, was a plastic card with included a metal key and six areas containing a different number of paper sheets, varying from 1 to 6. In order to determine the effect of misalignment on imaging quality, the scanning process was repeated by moving the sample away from the metasurface focal plane with 1 mm step as in the previously described process of determination of spatial resolution. The contrast values are defined as $C = (I_B - I_S)/(I_B + I_S)$, where $I_S$ is the average intensity at the largest signal area and $I_B$ labels average intensity at the minimal signal area were calculated for each sample position in the optical axis and for different numbers of paper sheets. Contrast dependence on the number of paper sheets and the position of the sample presented in Figure 6D. The results show that the contrast remains very similar regardless of the out-of-focus distance for each number of paper sheets. This implies that good image quality can be obtained even if the metasurface-based imaging is significantly detuned from the focal point. This illustrates the operational flexibility of metasurfaces opening hence a possibility to deploy them in industrial THz imaging systems, where precise optical alignment and tunability of optical components is not possible or hard to achieve.

## 5 Conclusion

The proposed approach revealed promising features of mechanically deformable metasurfaces for THz light manipulation opening thus a new route for the implementation of flexibly reconfigurable metasurfaces into the further development of compact THz imaging systems. Metasurfaces based on C-shaped complementary split-ring resonators manufactured from a 25 µm thickness stainless steel foil employing laser-ablation technology were applied for compact THz optics aims. Mechanical bending as a tool to manipulate the intensity and focusing properties of THz illumination is investigated. Polarization control via complementary C-shaped metasurfaces was presented at 94 GHz, and polarization-resolved THz imaging was demonstrated with the spatial resolution of half of the wavelength. It is shown that mechanically deformable metasurfaces can provide a dimension of operational flexibility opening hence an optimistic option to implement them in industrial THz imaging systems, where precise optical alignment is hard to achieve.

The approach can successfully be extended for multispectral THz imaging [33] aims thus enabling the wider scale of more precise identification of packaged objects contents or for modulation and manipulation of THz wavefront via a proper selection of a relevant metasurface with a liquid crystal elastomer [34].

## Data availability statement

The original contribution presented in the study are included in the article, further inquiries can be directed to the corresponding author.

## Author contributions

Conceptualization of the research, GV, VČ, and LM; methodology, IG and VČ; software, VČ, IG, and SO; sample ablation, EN; sample preparation, KR and MB; investigation using THz imaging set up, RI-P, KR, MB, and LM; polarization theoretical and experimental investigation, VČ and IG; data acquisition, IG, LM, and RI-P; experimental data analysis, GV, IG, VČ, and LM; writing—original draft preparation, IG, RI-P, and VČ; writing—review and editing, RI-P, VČ, IG, SO, GV, and LM; visualization, VČ, RI-P, and KR; supervision and coordination, GV and LM; project administration, LM; All authors have read and agreed to the published version of the manuscript.

## Funding

This research has received funding from the Research Council of Lithuania (LMTLT), agreement No. (S-MIP-22-76).

## Acknowledgments

The authors are grateful to Prof. Vincas Tamošiūnas for illuminating discussions and Dr. Domas Jokubauskis for his kind technical assistance.

## Conflict of interest

The authors declare that the research was conducted in the absence of any commercial or financial relationships that could be construed as a potential conflict of interest.

## Publisher's note



## References

1. Mittleman DM. Twenty years of terahertz imaging [Invited]. *Opt Express* (2018) 26: 9417–31. doi:10.1364/oe.26.009417

2. Castro-Camus E, Koch M, Mittleman DM. Recent advances in terahertz imaging: 1999 to 2021. *Appl Phys B: Lasers Opt* (2022) 128:12. doi:10.1007/s00340-021-07732-4

3. Valušis G, Lisauskas A, Yuan H, Knap W, Roskos HG. Roadmap of terahertz imaging 2021. *Sensors* (2021) 21:4092. doi:10.3390/s21124092

4. Pendry J, Holden A, Robbins D, Stewart W. Magnetism from conductors and enhanced nonlinear phenomena. *IEEE Trans Microwave Theor Tech* (1999) 47: 2075–84. doi:10.1109/22.798002

5. Chen WT, Zhu AY, Capasso F. Flat optics with dispersion-engineered metasurfaces. *Nat Rev Mater* (2020) 5:604–20. doi:10.1038/s41578-020-0203-3

6. Dorrah AH, Rubin NA, Zaidi A, Tamagnone M, Capasso F. Metasurface optics for on-demand polarization transformations along the optical path. *Nat Photon* (2021) 15: 287–96. doi:10.1038/s41566-020-00750-2

7. Hu J, Bandyopadhyay S, Liu Y, Shao L. A review on metasurface: From principle to smart metadevices. *Front Phys* (2021) 8. doi:10.3389/fphy.2020.586087

8. Ivaškevičiūtė-Povilauskienė R, Kizevičius P, Nacius E, Jokubauskis D, Ikamas K, Lisauskas A, et al. Terahertz structured light: Nonparaxial airy imaging using silicon diffractive optics. *Light: Sci Appl* (2022) 11:326. doi:10.1038/s41377-022-01007-z

9. Seliuta D, Kašalynas I, Tamošiūnas V, Balakauskas S, Martūnas Z, Ašmontas S, et al. Silicon lens-coupled bow-tie InGaAs-based broadband terahertz sensor operating at room temperature. *Electro Lett* (2006) 42:825. doi:10.1049/el:20061224

10. Minkevičius L, Indrišiūnas S, Šniaukas R, Voisiat B, Janonis V, Tamošiūnas V, et al. Terahertz multilevel phase Fresnel lenses fabricated by laser patterning of silicon. *Opt Lett* (2017) 42:1875–8. doi:10.1364/OL.42.001875

11. Hein SM, Giessen H. Tailoring magnetic dipole emission with plasmonic split-ring resonators. *Phys Rev Lett* (2013) 111:026803. doi:10.1103/PhysRevLett.111.026803

12. Hesmer F, Tatartschuk E, Zhuromskyy O, Radkovskaya AA, Shamonin M, Hao T, et al. Coupling mechanisms for split ring resonators: Theory and experiment. *physica status solidi (b)* (2007) 244:1170–5. doi:10.1002/pssb.200674501

13. Song Z, Zhao Z, Zhao H, Peng W, He X, Shi W. Teeter-totter effect of terahertz dual modes in c-shaped complementary split-ring resonators. *J Appl Phys* (2015) 118: 043108. doi:10.1063/1.4927845

14. Gay-Balmaz P, Martin OJF. Electromagnetic resonances in individual and coupled split-ring resonators. *J Appl Phys* (2002) 92:2929–36. doi:10.1063/1.1497452

15. Schurig D, Mock JJ, Smith DR. Electric-field-coupled resonators for negative permittivity metamaterials. *Appl Phys Lett* (2006) 88:041109. doi:10.1063/1.2166681

16. Sydoruk O, Tatartschuk E, Shamonina E, Solymar L. Analytical formulation for the resonant frequency of split rings. *J Appl Phys* (2009) 105:014903. doi:10.1063/1.3056052

17. Wu G, Zhang Y, Huang C. Improved circuit model for plasmonic resonance of single split-ring resonators. *AIP Adv* (2022) 12:115304. doi:10.1063/5.0125608

18. Zahertar S, Yalcinkaya AD, Torun H. Rectangular split-ring resonators with single-split and two-splits under different excitations at microwave frequencies. *AIP Adv* (2015) 5:117220. doi:10.1063/1.4935910

19. Zheng X, Zhao Z, Song Z, Peng W, Zhao W, He X, et al. The influence of element deformation on terahertz mode interaction in split-ring resonator-based meta-atoms. *Plasmonics* (2017) 12:1391–8. doi:10.1007/s11468-016-0398-8

20. Hokmabadi M, Philip E, Kung RPE, Kim S. Plasmon-induced transparency by hybridizing concentric-twisted double split ring resonators. *Sci Rep* (2015) 5:15735. doi:10.1038/srep15735

21. Falcone F, Lopetegi T, Laso MAG, Baena JD, Bonache J, Beruete M, et al. Babinet principle applied to the design of metasurfaces and metamaterials. *Phys Rev Lett* (2004) 93:197401. doi:10.1103/PhysRevLett.93.197401

22. Jackson JD. *Classical electrodynamics*. Hoboken: John Wiley & Sons Inc. (1998).

23. Chen H, O'Hara J, Taylor A, Averitt R, Highstrete C, Lee M, et al. Complementary planar terahertz metamaterials. *Opt Express* (2007) 15:1084–95. doi:10.1364/oe.15.001084

24. Zhang X, Tian Z, Yue W, Gu J, Zhang S, Han J, et al. Broadband terahertz wave deflection based on c-shape complex metamaterials with phase discontinuities. *Adv Mater* (2013) 25:4567–72. doi:10.1002/adma.201204850

25. Liu L, Zhang X, Kenney M, Su X, Xu N, Ouyang C, et al. Broadband metasurfaces with simultaneous control of phase and amplitude. *Adv Mater* (2014) 26:5031–6. doi:10.1002/adma.201401484

26. He J, Ye J, Wang X, Kan Q, Zhang Y. A broadband terahertz ultrathin multi-focus lens. *Sci Rep* (2016) 6:28800. doi:10.1038/srep28800

27. Hashemi M, Moazami A, Naserpour M, Zapata-Rodríguez CJ. A broadband multifocal metalens in the terahertz frequency range. *Opt Commun* (2016) 370:306–10. doi:10.1016/j.optcom.2016.03.031

28. Minkevičius L, Jokubauskis D, Kašalynas I, Orlov S, Urbas A, Valušis G. Bessel terahertz imaging with enhanced contrast realized by silicon multi-phase diffractive optics. *Opt Express* (2019) 27:36358. doi:10.1364/oe.27.036358

29. Hristov HD, Rodriguez JM, Grote W. The grooved-dielectric Fresnel zone plate: An effective terahertz lens and antenna. *Microwave Opt Technol Lett* (2012) 54:1343–48. doi:10.1002/mop.26812

30. Minkevičius L, Tamošiūnas V, Kojelis M, Žąsinas E, Bukauskas V, Šetkus A, et al. Influence of field effects on the performance of InGaAs-based terahertz radiation detectors. *J Infrared, Millimeter, Terahertz Waves* (2017) 38:689–707. doi:10.1007/s10762-017-0382-1

31. Kašalynas I, Seliuta D, Simniškis R, Tamošiunas V, Köhler K, Valušis G. Terahertz imaging with bow-tie InGaAs-based diode with broken symmetry. *Electro Lett* (2009) 45:833–5. doi:10.1049/el.2009.0336

32. Stratton JA. *Electromagnetic theory*, 33. Hoboken: John Wiley & Sons (2007).

33. Kasalynas I, Venckevicius R, Valusis G. Continuous wave spectroscopic terahertz imaging with ingaas bow-tie diodes at room temperature. *IEEE Sensors J* (2013) 13:50–4. doi:10.1109/JSEN.2012.2223459

34. Zhuang X, Zhang W, Wang K, Gu Y, An Y, Zhang X, et al. Active terahertz beam steering based on mechanical deformation of liquid crystal elastomer metasurface. *Light: Sci Appl* (2023) 12:14. doi:10.1038/s41377-022-01046-6

P4

## TERAHERTZ STRUCTURED LIGHT: NONPARAXIAL AIRY IMAGING USING SILICON DIFFRACTIVE OPTICS

**R. Ivaškevičiūtė-Povilauskienė**, P. Kizevičius, E. Nacius, D. Jokubauskis, K. Ikamas, A. Lisauskas, N. Alexeeva, I. Matulaitienė, V. Jukna, S. Orlov, L. Minkevičius, G. Valušis

*Light: Science and applications* **11**, 326 (2022).
DOI: 10.1038/s41377-022-01007-z



The article may be accessed online at https://doi.org/10.1038/s41377-022-01007-z

Ivaškevičiūtė-Povilauskienė et al. *Light: Science & Applications* (2022)11:326
https://doi.org/10.1038/s41377-022-01007-z

Official journal of the CIOMP 2047-7538
www.nature.com/lsa

ARTICLE Open Access

# Terahertz structured light: nonparaxial Airy imaging using silicon diffractive optics

Rusnė Ivaškevičiūtė-Povilauskienė[1✉], Paulius Kizevičius[2], Ernestas Nacius[2], Domas Jokubauskis[1], Kęstutis Ikamas[3], Alvydas Lisauskas[3,4], Natalia Alexeeva[1], Ieva Matulaitienė[5], Vytautas Jukna[2], Sergej Orlov[2], Linas Minkevičius[1,6] and Gintaras Valušis[1,6]

**Abstract**

Structured light – electromagnetic waves with a strong spatial inhomogeneity of amplitude, phase, and polarization – has occupied far-reaching positions in both optical research and applications. Terahertz (THz) waves, due to recent innovations in photonics and nanotechnology, became so robust that it was not only implemented in a wide variety of applications such as communications, spectroscopic analysis, and non-destructive imaging, but also served as a low-cost and easily implementable experimental platform for novel concept illustration. In this work, we show that structured nonparaxial THz light in the form of Airy, Bessel, and Gaussian beams can be generated in a compact way using exclusively silicon diffractive optics prepared by femtosecond laser ablation technology. The accelerating nature of the generated structured light is demonstrated via THz imaging of objects partially obscured by an opaque beam block. Unlike conventional paraxial approaches, when a combination of a lens and a cubic phase (or amplitude) mask creates a nondiffracting Airy beam, we demonstrate simultaneous lensless nonparaxial THz Airy beam generation and its application in imaging system. Images of single objects, imaging with a controllable placed obstacle, and imaging of stacked graphene layers are presented, revealing hence potential of the approach to inspect quality of 2D materials. Structured nonparaxial THz illumination is investigated both theoretically and experimentally with appropriate extensive benchmarks. The structured THz illumination consistently outperforms the conventional one in resolution and contrast, thus opening new frontiers of structured light applications in imaging and inverse scattering problems, as it enables sophisticated estimates of optical properties of the investigated structures.

## Introduction

Structured electromagnetic fields have been shown to be viable in a variety of applications such as communication, metrology, and light-matter interactions[1,2]. Most advances are due to the rapid development of so-called nondiffracting electromagnetic beams[3] which nowadays are applicable for a broad selection of wavelengths extending from visible[4] to terahertz (THz) ranges[5]. Such popularity is caused by intriguing properties like diffraction and dispersion resistance[6], self-healing[7,8], self-acceleration[9–11], etc. The applicability of nondiffracting beams can be significantly increased when their vortical[12,13] and polarization properties[14] are introduced[15].

The family of nondiffracting beams has numerous relatives to the well-known Bessel beam. Elliptic Mathieu[16], parabolic Weber[17], Pearcey beams[18] and self-accelerating Airy beams[9,19] are less recognized, however, they can be found as more promising members in the family of nondiffracting illumination. The nondiffracting Airy beam manifests itself as a beam of a distinct parabolic propagation trajectory in the longitudinal plane[20]. The beam trajectory (or caustics) of nondiffracting electromagnetic fields can be shaped to any other form[21–23].

Correspondence: Rusnė. Ivaškevičiūtė-Povilauskienė (rusne.ivaskeviciute@ftmc.lt)
[1]Department of Optoelectronics, Center for Physical Sciences and Technology, Saulėtekio av. 3, Vilnius 10257, Lithuania
[2]Department of Fundamental Research, Center for Physical Sciences and Technology, Saulėtekio av. 3, Vilnius 10257, Lithuania
Full list of author information is available at the end of the article

These nonconventional states of light also can find their use also in imaging improvements[24–26], laser microfabrication[27,28], photonic communications[29,30], tomographic[31], light sheet[32], and sub-THz microscopy[33]. High resolution is one of the main objectives of the imaging theory, and it is usually achieved with Gaussian illumination in high numerical aperture systems. However, a high numerical aperture automatically leads to bulky imaging systems. The lenses and conical prisms become rather massive, and various aberrations can be induced.

The solution to this problem is flat optics[34–37], with Fresnel lenses[34,38] and axicons[4,26] being the most well-known examples. Flat optics elements can also enable efficient generation of Airy beams in both transmission and reflection geometries[39] in a wide range of wavelengths, from optical[19,40] to THz[41]. Flat optics reduces the thickness and weight of optical elements by exploiting diffraction. A spatial arrangement of sub or near wavelength thickness elements that locally phase-shifts a passing optical ray which leads to the constructive interference of the transmitted waves at the focal point. An implementation of this concept involves binary or multilevel diffractive elements where the phase delay is $(n-1)t$ for the material of refractive index $n$ and local thickness $t$ of the substructure[34]. Yet another implementation is based on the concept of metasurfaces using propagation or geometrical phase[37] For example, diffractive gratings were realized by local changes in the geometrical phase of the structure comprised of individual metaatoms[42,43]. We note that both approaches to flat optics can be equally effective; see ref. [34].

THz waves stand out among other sources and frequencies, as they not only serve as a flexible platform for scalable photonic experimentation, but also provide a strong background for a wide variety of applications in communications, spectroscopy, and imaging systems for nondestructive inspection in security, medicine, and materials research[44,45]. Recent progress in the development of compact and robust room temperature THz sources[46] stimulated strong demand for relevant flat optic advances with the aim of reducing the size of imaging or spectroscopic systems[37,42,43,47–49].

Its direct implementation requires convenience under real operational conditions, optimization, and miniaturization of THz imaging systems with reduced power consumption. Since silicon can be assumed to be one of the most promising materials for the development of compact THz systems containing solid-state-based emitters, room temperature detectors and their arrays, an important role must be attributed to the development of compact flat optics, in particular, considering their further integration into imaging setups[44,50]. Moreover, because of the relatively long THz wavelength, a large variety of high-quality compact metasurfaces, amplitude, and phase elements can be flexibly manufactured in a wide cost range. These circumstances display THz range as a flexible platform and promising toy model for fundamental research in scalable flat optics readily applicable for other wavelengths of electromagnetic radiation.

In this work, for the first time, we demonstrate a compact and nonparaxial solution based exclusively on flat silicon diffractive optics for structured THz light generation in the form of a configurable Airy beam. Second, we expose its accelerating nature via THz imaging of partially obscured objects using an opaque beam block. Third, in contrast to conventional approaches, when under paraxial conditions a combination of a lens and a cubic phase (or amplitude) mask creates a non-diffracting Airy beam, we also demonstrate simultaneous lensless nonparaxial Airy beam generation in the THz range. Fourth, the designed Airy lens performance in the conventional generation of the Airy beam, when a phase element creates the spatial spectra of the nonparaxial Airy beam, and in the non-conventional beam generation when the nonparaxial propagation itself performs focusing of the phase mask, are revealed and investigated.

Fifth, it is displayed that the self-accelerating properties of both Airy beams allow for recording of a THz image of an object behind an obstacle; also, high quality of THz Airy images of a single object and images over a controllable placed obstacle is exposed. Sixth, the ability to inspect the quality of 2D materials such as stacked graphene layers is affirmed and its correlation with Raman spectroscopy data is established.

Seventh, the distinct role of structured THz illumination on the quality of nonparaxial THz Airy imaging is illustratively benchmarked in mode profile measurements, numerical simulations, and their comparison with Bessel and Gaussian beams. Eighth, the THz imaging setup contains only flat optical elements manufactured from a high-resistivity silicon substrate ablated by femtosecond laser pulses[51].

## Results

### Design and fabrication of the nonparaxial flat optics elements

Our aim is to design a flat photonic element for imaging objects with THz illumination. Due to the rather long-wavelength $\lambda$ and characteristic dimensions of imaged objects, the element must be a nonparaxial object. Thus, its performance is described by the Rayleigh-Sommerfeld diffraction integral[52].

For our purpose, we devised a cubic phase profile

$$\Phi_{\mathrm{AI}}(\boldsymbol{r}) = a\left(x^3 - y^3\right) \tag{1}$$

($a = \pi \times 10^7\ \mathrm{m}^{-3}$) which we encoded in a flat element, where structural changes in the height of the elements

contribute to phase changes less than $2\pi$. The complex transmission function $T(\mathbf{r})$ of a multi-level phase mask is defined as

$$T(\boldsymbol{r}) = \exp\left(i\frac{2\pi}{N}\left[\frac{N\Phi(x,y)}{2\pi} - N\left\lfloor\frac{\Phi(x,y)}{2\pi}\right\rfloor\right]\right) \quad (2)$$

where $\Phi(x, y) = \Phi_{\mathrm{AI}}(\mathbf{r})$ and the brackets $\lfloor\rfloor$ represent a round-down operation and $N$ is the integer number of levels in the phase mask.

The spatial profile of the designed nonparaxial Airy phase mask with $a = \pi \times 10^7\ \mathrm{m}^{-3}$ and $N = 8$ is shown in Fig. 1a. This design represents a phase mask plate of eight levels ($N = 8$) of diameter 20 mm, which together with a zone plate ($f = 1$ cm) is dedicated to generate an Airy beam in the range of up to 10 mm.

To provide focusing abilities and additional management facilities for the engineered beam in the setup, we design and fabricate conventional zone plate with the phase of the transmission function being a quadratic phase function

$$\Phi_{\mathrm{ZP}}(\mathbf{r}) = \frac{k}{2f}\left(x^2 + y^2\right) \quad (3)$$

where $f = 1$ cm is the expected paraxial focus length. Similar designs and their performance were discussed in refs. [51,53,54].

Additionally, to generate Bessel THz beam a Fresnel axicon was designed with a linear phase function

$$\Phi_{\mathrm{B}}(\mathbf{r}) = \frac{2\pi\sin\beta}{\lambda}\sqrt{x^2 + y^2} \quad (4)$$

where $\beta = 0.4$ rad. In the end, we fabricated phase plates with linear, quadratic, and cubic phase profiles.

Fabrication was carried out on a high-resistivity silicon wafer with a refractive index of $n = 3.46$ and the wavelength of the electromagnetic radiation is $\lambda = 0.5$ mm corresponding to the frequency of 0.6 THz using the ultra-short pulsed laser ablation process[53,55]. Details can be found in the Materials and Methods Section.

The photographed spatial profile of the manufactured Airy lens, its cross section and the enlarged tilted photo of the Airy lens to visualize the levels, structural depth and quality of the surface of the fabricated element are depicted in Fig. 1b. For comparison, a picture of the 8-level laser ablated nonparaxial zone plate with a cross-section of the element as the inset is shown; see Fig. 1c.

One can note that no transverse distortions between the designed and fabricated elements are visible. However, only 7 phase levels can be resolved in the actual Airy element. For this reason, a phase difference of 0.6 rad (equal to 19.3 μm of height difference) between the designed and the fabricated elements was estimated. We have theoretically evaluated the influence of this phase mismatch and found it to be rather moderate, since it mostly causes a drop in the maximal intensity of about 40 percent, but it has almost no influence on the specifics of the spatial intensity distribution. Other elements were produced as intended.

As the devised elements are nonparaxial their performance is revealed using the Rayleigh-Sommerfeld integral with a spherical-point-source-based propagator. Details are given in the Materials and Methods Section. To illustrate the versatility of the operation of the designed flat optics for the 0.6 THz frequency, we studied the performance of the actual element with and without a nonparaxial zone plate.

Simulations were performed using an incident Gaussian beam of radius $w_0 = 10$ mm at the intensity level of $1/e^2$. The beam was collimated by the lens $L$ and directed onto the Airy phase mask to generate structured THz light, see Fig. 2. In Fig. 2a the distance between the Airy mask and the ZP was $f = 1$ cm. The simulation area is 8.5 mm × 20 mm in the longitudinal ($xz$) plane.

First, we calculate the electromagnetic fields generated using the Airy phase mask and a zone plate; see Fig. 2a. The design of the zone plate was based on the paraxial assesment of the focal spot at $z = 1$ cm. The actual nonparaxial focal point was formed at the distance $z = 0.85$ cm.

The analysis of the beam propagation revealed that the beam behaves as expected; the trajectory of the generated Airy beam is parabolic, although some deviations from the paraxial trajectory are observed. Due to the nonparaxiality (we remind that the propagator is spherical-point-source-based), the transverse profile is slightly distorted on the edges. This is a distinct effect caused by the highly nonparaxial zone plate – strictly speaking, the optical Fourier transform is valid only in the paraxial regime, consequently, the nonparaxial beam profile is not a product of two independent profiles as it is in the paraxial case, see Methods. It should be noted that the parabolically bending nonparaxial Airy beam focuses approximately 5% further as expected at $z = 1.05$ cm.

Subsequently, we looked into the performance of the nonparaxial Airy generating mask without a zone plate. Due to the choice of the parameter $b$, see Eq. (5), the reciprocal trajectories, following the law $x \sim 1/z$ can be revealed in the theoretical plot within the acceptable range of coordinates and are clearly observed experimentally, see Fig. 2b. Interestingly, the Airy profile is less distorted than in the previous case, compared with Fig. 2a, though the beam increases its dimensions as it propagates along the reciprocal trajectory proportionally to $z^2$, see Methods.

### Experimental verification of the nonparaxial designs

We start by benchmarking the fabricated THz phase element with experimental verification of its performance. Our aim here was to experimentally generate nonparaxial

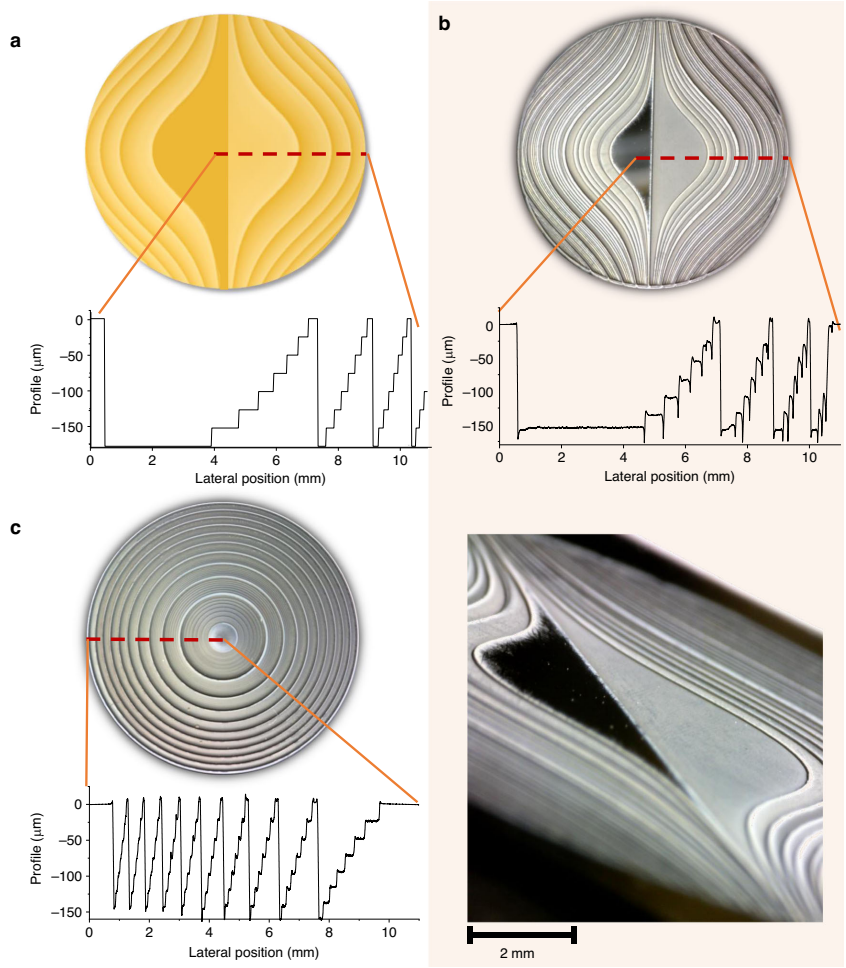


**Fig. 1 Designs of photonic elements under study.** Spatial distribution of **a** designed nonparaxial Airy mask and its lateral cross-section; **b** fabricated silicon nonparaxial Airy element and its cross-section with the enlarged surface structure (bottom panel); **c** fabricated nonparaxial silicon zone plate with quadratic phase profile and its cross-section

Airy beams with conventional parabolic and unconventional reciprocal trajectories. The principal optical schemes are shown in the top row of Fig. 2a, b.

The generation of the Airy beam was carried out experimentally using an electronic multiplier chain-based emitter (*Virginia Diodes, Inc*) to produce radiation of 0.6 THz frequency. Delivered through a converging lens ($L$, with $F = 12$ cm) it was collimated to illuminate the focusing elements arranged in different orders. The first setup is based on the Airy lens and zone plate combination and is shown in Fig. 2a, while the second setup uses only the cubic mask (Fig. 2b). The beam profiles along and perpendicular to the beam propagation direction were raster-scanned at a speed of 10 mm $s^{-1}$. Recording of a 100 $mm^2$ in $xy$ plane and 160 $mm^2$ in $xz$ plane-sized images of the focused Airy and Gaussian beam with a

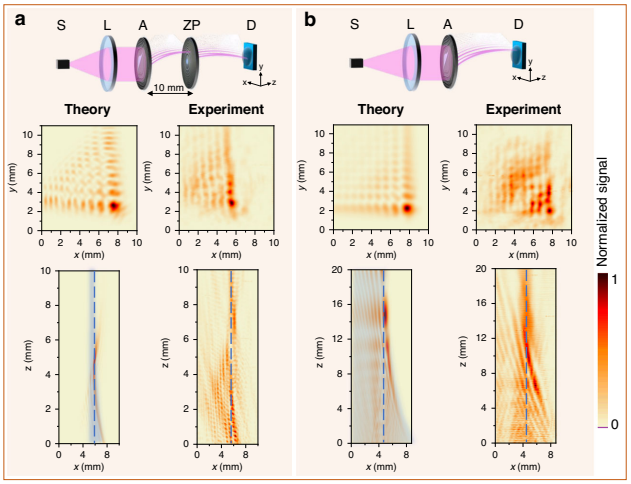


**Fig. 2 Numerically estimated and experimentally obtained intensity distributions of the nonparaxial Airy beam in the transverse (xy) (at the focal point) and in the longitudinal (xz) planes at 0.6 THz. S denotes a THz source, L is a lens, A stands for the Airy phase mask, ZP is a nonparaxial zone plate, D labels THz detector.** Panel **a** – using Airy phase mask with an additional zone plate. The distance between the Airy lens and the ZP is 10 mm, and for the transverse plane scan the detector is placed in 7 mm from the ZP. The starting scanning point along the *z*-axis is 1 mm away from the ZP; panel **b** – using the Airy lens only. The starting scanning point along the *z*-axis is 1 mm away from the Airy lens. Distributions are normalized to the maximum value of the signal. A dashed blue line in bottom panels – guide for an eye to accentuate Airy beam which exhibits parabolic trajectory. A light blue shaded area in theoretical plot enlightens the reciprocal trajectories. Note that in case of nonparaxial Airy generation with mask without zone plate (panel **b**), the Airy profile is not distorted as in the case with zone plate (panel **a**) although the beam increases its dimensions as it propagates along the optical axis proportionally to $z^2$. Reciprocal caustic trajectories following $x \sim 1/z$ law are also nicely pronounced both in theory and experiment. As it is seen the experiments fit well the modelling results (panel **b**)

pixel size of 0.1 $mm^2$ at a scanning speed of 10 mm $s^{-1}$ leads to a signal-to-noise ratio (*SNR*) of 570 for a setup with the single Airy lens and $SNR = 1180$ for the set-up containing the Airy lens and the zone plate.

Measurement was carried out in the area which was consistent with the simulation area. Typical experimental Airy beam profiles after the zone plate both in the transverse and longitudinal planes are presented in Fig. 2a. In general, the transverse intensity profile is skewed in the same way as expected due to the action of the nonparaxial focusing zone plate. The peak position in the transverse plane *xy* has a similar intensity distribution and is slightly shifted in the *y*-direction. In the transverse plane, we observe a parabolic trajectory, with small deviations from the design due to the fabrication. The main lobe of the generated Airy beam structure spans from 0 to 10 mm. Therefore, we can infer a good performance of the element.

Next, we remove the zone plate ZP and repeat the experiment. As one can see from Fig. 2b, the transverse distribution is now undistorted, with both arms of the structured THz radiation being perpendicular. Some minor deviations are observed, but they can be explained by the experimental implementation. The longitudinal profile shows the diffractive spreading of the Airy profile. Although it almost keeps its shape over a distance from 6 mm to 16 mm, the diameter of the beam increases proportionally to the square of the distance *z* from the element. It is worth noting that the Airy beam exhibits reciprocal self-bending during propagation in free space. Most importantly, we confirmed that the Airy phase mask can be used experimentally to create nonparaxial structured THz light with and without a zone plate. This becomes possible due to the nonparaxiality of the devised elements.

### Imaging of objects with nonparaxial structured illumination

For practical applications, it is important to benchmark the performance of the fabricated cubic nonparaxial phase mask in THz imaging applications using structured THz light illumination. Most notably, the nonparaxiality of the element allowed us to generate two versions of the Airy beams with different setups discussed above.

The first benchmark is a raster scan imaging of the nontransparent sample when the sample is illuminated by the nonparaxial Airy beam. As structured light illumination

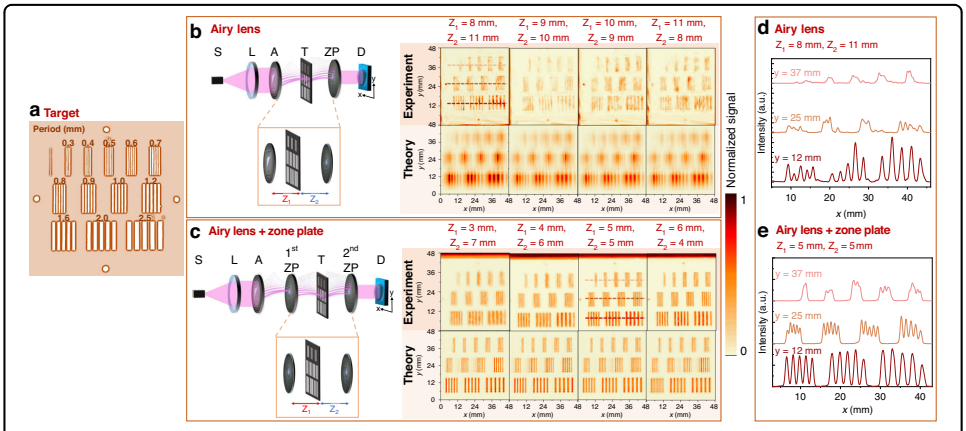


**Fig. 3 Imaging of non-transparent sample using nonparaxial Airy beam.** Image of the target with different period slits (**a**). Performance of the nonparaxial Airy phase mask in THz imaging in two setups: with a single nonparaxial zone plate (**b**) and two nonparaxial zone plates (**c**). T indicates the imaged target. The color bar is normalized to the maximal value of the signal. $Z_1$ and $Z_2$ indicate distances between optical elements and the object. The first row on the right and the second row on the right present comparison of the experimentally obtained and numerically calculated object pictures for both setups, respectively. Cross-sections of the imaged objects (at positions denoted by dashed lines) are depicted in graphs (**d**) for setup with an Airy lens and a single nonparaxial zone plate and (**e**) for an Airy lens and two nonparaxial zone plates. Cross-sections of the recorded image (**d**) proving the 3.2 $\lambda$ spacial resolution with more distorted target bars image; Cross-sections of the recorded image (**e**) with precise spatial frequency resolution reaching 1.6 $\lambda$ with the contrast of 2 (a.u.)

displays a self-accelerating bending structure, we studied its performance in THz imaging of the object behind an obstacle. The second case is related to THz transparent samples, where the observation of the object and the registration of its internal structure are a challenge due to low absorption, while the main attention needs to be focused on a phase change.

For benchmarks of structured illumination imaging of nontransparent targets, we employed a structure, which we routinely use in THz imaging experiments[26]. It contains a number (5) of bars of different widths arranged in groups of the same number of bars. The target has three rows of bars; the first row is 5 groups of the 5 smallest bars, the middle row contains 4 groups of larger bars, and the last row has 3 groups of the largest bars. Period and size are marked in Fig. 3a.

The fabricated photonic element enables us to generate two distinctly different nonparaxial versions of the structured THz illumination, so we investigated and benchmarked the performance of the imaging application in two set-ups. The first one contained the single Airy lens (Fig. 3a) while the second one consisted of the Airy lens in combination with the nonparaxial zone plate (Fig. 3b). In both experiments, the target was scanned in raster with a velocity of 20 mm $s^{-1}$ and a pixel size of 0.2 mm. The distance between the target and adjacent optical elements varied during the scanning process. In Fig. 3b panel, the red letter $Z_1$ marks the distance between the Airy lens and the target, while the blue letter $Z_2$ indicates the distance between the target and the zone plate. Accordingly, in Fig. 3c panel, the red letter $Z_1$ marks the distance between the first zone plate and the target, and the blue letter $Z_2$ indicates the distance between the target and the second zone plate. Since the Airy beam is nondiffractive, experimentation revealed that a similar image was recorded at all positions of the target object.

In the first case, the bar structure with the period of 1.2 mm is still distinguishable in the recorded images. Even the better spatial resolution and quality are achieved in the second setup with the Airy mask and the zone plate, see Fig. 3c, where the structure with the 0.8 mm period is still visible, and the contrast is 2 (*a.u.*).

A detailed comparison of spatial resolution and contrast is given in Fig. 3d, e, where the cross sections for each target bar (in places marked with red lines) are presented. It should be noted that a combination of the Airy mask with the zone plate provides spatial resolution reaching 1.6$\lambda$, while a simpler approach without the zone plate reaches only 3.2$\lambda$ spatial resolution with the recorded images being more distorted.

We numerically evaluated the expected performance of the structured illumination under the same conditions as in the experiment. The results are given in Fig. 3. In general, the conventionally generated Airy beam was

performed in a manner similar to that observed during the experiment. The resolution and contrast estimates agree well with the experimental observations.

However, we observed some discrepancies between the numerical estimate and the experiment when the non-paraxial Airy beam was generated non-conventionally. The experimental results demonstrate better contrast and resolution than the numerical estimation. Although the number of bars can be precisely estimated, the shape of bars looks slightly distorted in the numerics. It can be caused by the fact that the Airy beam with reciprocal trajectory spreads more in the numerical estimates than in the experiment and displays higher than experimental intensity. The reciprocal propagation and its direction were also the main cause of why in the virtual numerical experiment the shape of the bar is distorted, with one side of the bar looking more intense than the another one. The experimental realization can have some alignment imperfections; therefore, this effect is less pronounced in the recorded pictures.

Yet another intriguing feature of the self-accelerating structured THz illumination is the bending propagation trajectory. Results of the first imaging benchmarks induced an idea of a specific imaging experiment when an opaque obstacle is placed between the target and illumination.

In this set of experiments, we additionally employed a multilevel laser-ablated Fresnel axicon, which was previously benchmarked in THz imaging with the Bessel beam and allowed us to achieve a superresolution[26]. Given the nondiffractive nature of all contestants, this makes us wonder how those three set-ups can be compared under these rather unusual conditions.

Although the bending trajectory of the structured Airy illumination makes it easy to understand how the imaging behind the obstacle is possible, some additional comments are required in the case of nondiffracting Bessel beams. They can be represented as plane waves, whose wave vectors are located in the cone with angle $\alpha_B$[12,26]. For this reason, as we cover the target with an obstacle, we cover only a part of the plane wave components lying on the cone. The uncovered part of the spatial spectrum propagates at the cone angle $\alpha_B$ to the $z$-axis and reaches the region behind the obstacle. For this reason, we expect that part of the structured Bessel-type illumination is still able to reach the target. This property is observed many times in the literature under the moniker of the self-healing and self-recovery properties of the Bessel beam[8].

The experimental results of a sample imaging behind the obstacle are presented in Fig. 4. The obstacle was placed at the distance $z = 1$ mm behind the last element in the scheme before the object and other distances were selected optimally from the previous experimentation. A metal plate impermeable to THz radiation was used as an obstacle in three different setups. During the experimentation, an ever-increasing area of the optical element in front of the sample was shielded by this metal plate. The experimentation with structured THz illumination was repeated three times using different lens configurations in front of an obstacle: Airy lens only (Fig. 4a), the Airy lens in combination with the nonparaxial zone plate (Fig. 4b), and the Bessel lens (Fig. 4c).

As experimentation has revealed, see Fig. 4a, when a single Airy lens is employed, the image of the target is clear even when the optical element is almost completely covered by the metal obstacle. The smallest period of stripes, which is clearly resolved, is 1.2 mm. Our experimentation is in line with the numerical estimate presented in the same Figure. Some slight discrepancies might be caused by slight misadjustments in the system and slight imperfections in the position estimates. These results confirm the self-healing properties of the Airy beam and promise an opportunity to perform THz structured light imaging even when an opaque object is present.

The results are even more promising; see Fig. 4b when a combination of the nonparaxial cubic phase mask and the nonparaxial zone plate is employed. The slits of the target are still clearly visible, even if more than half of the illuminating element is covered. In this case, a surprisingly good resolution is still observed, indicating that the smallest period of stripes, which is clearly resolved, is 0.7 mm.

Lastly, we are curious how the Fresnel axicon will perform, as the structured THz illumination behind it is still nondiffracting and thus also self-recovering. During the experimentation with the Bessel lens (Fig. 4c), when small parts of the generating element are covered, the image of the target is still clearly recorded. In this case, the smallest period of stripes, which is clearly resolved, is 0.8 mm ($1.6\lambda$). Nevertheless, when a larger area of the element is covered, the image of the target is barely seen until only the noise is recorded. Numerical estimates demonstrate a similar behavior, although some images can be recognized in the background. This deviation is caused by some experimental uncertainties in the generated structured light illumination. Thus, the fabricated cubic phase plate shows better results in this benchmark than the Bessel generating element.

A summary of the performance benchmarks is given in Fig. 4d. First, we note that the performance of the single Airy phase mask decreases as we cover a larger part of the structured illumination, the spatial resolution changes up from $2\lambda$ to $3.2\lambda$ while the contrast fluctuates in the range of 30 (a.u.). Surprisingly, in the second experimentation, we did observe the even better performance of the Airy phase mask in conjunction with the zone plate - the spatial resolution does not depend on the covered percentage. It is $1.6\lambda$, and thus it is better than in the first experiment. The contrast was slightly less than for the

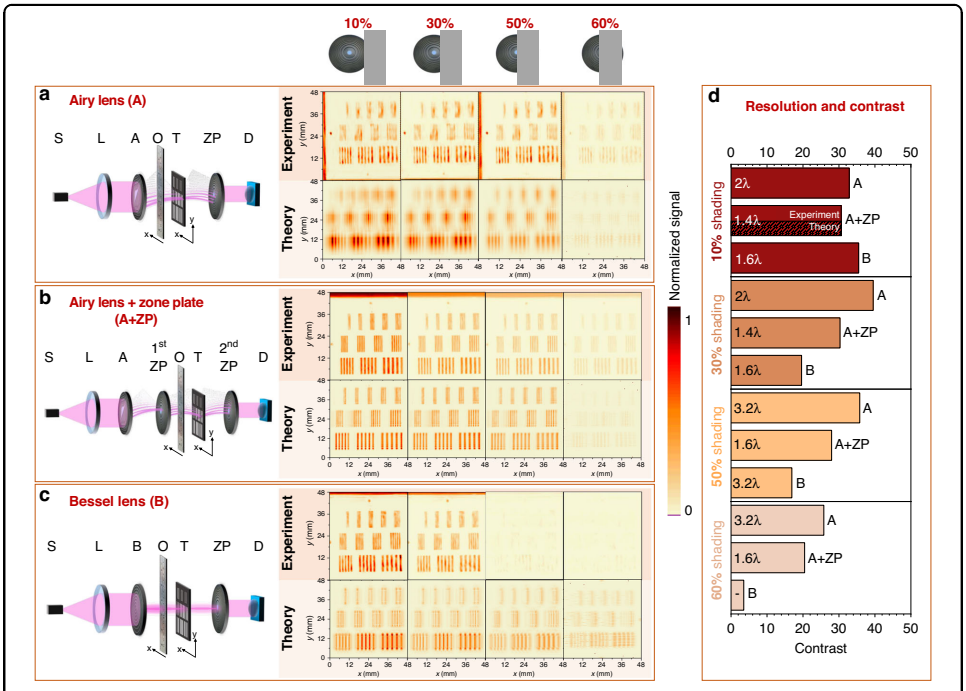


**Fig. 4 Benchmarking of structured nonparaxial illumination behind the obstacle.** Performance of the nonparaxial Airy phase mask in THz imaging behind the obstacle in two setups: with the single nonparaxial zone plate (**a**) and two nonparaxial zone plates (**b**), where O denotes an obstacle. Performance of the nonparaxial Bessel phase mask in the same THz imaging behind the obstacle setup (**c**). The color bar is normalized to the maximum value of the signal for each setup. The position of the obstacle is depicted on top of four columns on the right, starting from the almost uncovered object (middle, ~10% is covered) and ending with the most covered object (right, ~60% is covered). Results of resolution and contrast benchmarks for different coverage of the structured illumination percentage (**d**). Resolution values are marked inside the colored bars, the contrast is given on the x-axis. For the sake of brevity, the numerical estimate is given only for one particular case, since in all other cases the results between theory and experiments are well-coincident within 2 percent accuracy. The contrast is defined as the ratio of the maximal and minimal intensity values

case without the zone plate and did drop as we cover the illuminating element from 30 to 20. Lastly, the spatial resolution of the illumination of the Bessel beam decreased from 1.6λ to 3.2λ. Most noticeably, the contrast did drop drastically until no images were recorded for the largely covered illumination. An element covered by 30% results in a strongly reduced contrast for the case of the Bessel illumination, while the cases of the Airy and the Airy with the zone plate demonstrate the contrast less dependent on the block percentage.

Numerical estimates agree well with the experimental observations; for the sake of brevity, we present them only for one particular setup, where the agreement is the largest; see Fig. 4d. This is the second setup, see Fig. 4b, numerically obtained contrast does not deviate more than 5% from the experimental one.

Deviations are larger in the first set-up, though the dependence on the percentage of the covered part is similar. In the third case, see Fig. 4c, numerical contrast is smaller when 10% and 30% of the element are blocked, and it becomes equal to that in the experiment for the latter case indicating thus good agreement between the experiments and simulations.

### Inspection of thin 2D samples with nonparaxial THz structured light illumination

These promising results of our first two benchmarks have motivated us to study the performance of structured nonparaxial Airy THz illumination in the imaging of thin 2D samples. For this experimentation, we chose graphene as a highly interesting material for THz radiation. Graphene is one of the most popular and widely used two-dimensional

materials consisting of a single layer of carbon atoms arranged in a two-dimensional honeycomb lattice nanostructure of only 0.3 nm thickness. Graphene is distinguished from other materials due to its specific properties: good electrical and thermal conductivity etc. In this benchmark, we have investigated in total 5 different graphene samples, each containing 1, 2, 3, 4 and 5 graphene layers placed on a high resistivity silicon substrate. Bare Si was used as a reference sample.

All samples were investigated using the same setup, which we discussed earlier, with two different configurations of lenses: two-zone plates (Fig. 5a) and the Airy lens in combination with zone plates (Fig. 5b).

The results of the experiment and the numerical modeling for different numbers of graphene layers are given on the right side of the (a) and (b) parts of Fig. 5. The first setup does not generate the structured THz illumination, whereas the second one delivers the self-accelerating nonparaxial Airy beam.

In the first setup, under Gaussian illumination, the intensity decreases with an increase in the number of graphene layers. As expected, the drop is more or less linear for the first three graphene samples, while samples with 4 and 5 layers experience a weaker dependence; see Fig. 5c. Under structured THz Airy illumination, the situation becomes puzzling due to the pronounced nonmonotonic dependence: initially, the drop in transmission can be observed for the samples with 1 and 2 graphene layers, as expected; however, the unexpected increase in transmission is observed in the sample with 3 graphene layers. i. e., nonparaxial structured illumination is transmitted better through the sample than the conventional one. Regarding the sample with 4 graphene layers, the transmission drops well below that of the Gaussian illumination, and, more importantly, the sample with 5 graphene layers is now can clearly be distinguished from the sample with 4 layers which are in sharp contrast to the Gaussian case.

This issue can successfully be resolved taking into account the effects related to the light polarization, i. e., reasoning about the transmissivity of *s*- and *p* -polarized light (perpendicular and parallel) through a stratified medium (i. e., through a dielectric slab). First, the slab is a minuscule resonator with multiple reflections from the outer and inner surfaces that separate materials. Thus, any small deviation in the height of the sample or in the refractive indices of graphene or the Si wafer will have an imminent effect on the recorded transmissivity. For the paraxial illumination, there is no difference between the transmission of the incident polarization. However, the difference does appear for the nonparaxial illumination, as the transmission through the stratified medium behaves differently for plane wave components with large angles of incidence. Details are presented in the Supplementary Materials.

Therefore, one can assume that structured nonparaxial illumination not only ensures better spatial resolution but is also more sensitive to changes in the optical phase due to refractive indices and their variation in the stratified media. As the self-accelerating illumination has more spatial components with large transverse wave vectors, it distinguishes changes in optical parameters of the sample better than the conventional Gaussian illumination as given in Fig. 5a–c. Most importantly, a combination of these two signals together enables us to solve the inverse scattering problem[56]; i. e. we can make an educated and sophisticated guess to determine the height or effective dielectric constant of the sample.

To confirm the hypothesis, we have performed Raman spectroscopy of the graphene samples, of which two characteristic spectral bands, G and 2D, are plotted in Fig. 5d. It turns out that the samples contain distinct groups of graphene layers that behave differently. Due to graphene layer interaction with Si substrate or with other graphene layers, it can be mechanically strained. Second, graphene can experience electron depletion and other changes as a result of its deposition on the Si substrate. The existence of mechanical strain and doping can be exposed by performing the Raman mapping and examining the correlation analysis of the frequency position of the G and 2D bands; more details on Raman experiments can be found in the Supplementary Material. For the free-standing graphene sample, two characteristic bands, G and 2D, are located in the Raman spectra around 1580 $cm^{-1}$ and 2690 $cm^{-1}$, respectively. These values can vary depending on technological conditions in deposition processes or a number of the deposited layers as it is seen in distributions of $\omega_G$ and $\omega_{2D}$ of each sample depicted in Fig. 5d. Statistical dependency is accumulated from the single point data and a linear approximation as depicted on the plot. Zero-point indicates free-standing graphene and it is considered as reference ($\omega_G = 1581.6 \pm 0.2$ $cm^{-1}$; $\omega_{2D} = 2676.9 \pm 0.7$ $cm^{-1}$). The closer this $\omega_{2D}$ /$\omega_G$ distribution is to the zero point, the less this layer is affected by mechanical stress. As it is seen, the samples are strained differently. As can be seen, the 2D and G peak frequency distribution of the sample with 3 graphene layers is the farthest from the zero point, and its slope is $-0.66 \pm 0.5$, which can be associated with doping effects. Inclusion of these effects together with light polarization in the modeling allows them to fit well with the experimental data, as can be seen in Fig. 5c and enabling thus to explain the increase in transmittance in the structured THz light experiment; see the Supplementary Materials for details. Therefore, it can be

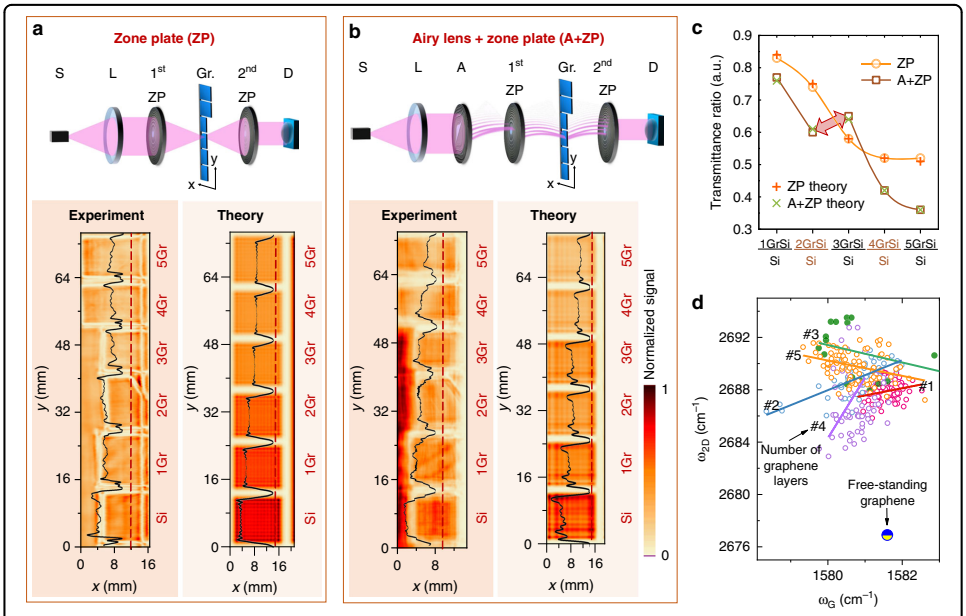


**Fig. 5 Imaging using nonparaxial THz structured light illumination.** The sample under test consists of different numbers of graphene layers denoted on the graph. The THz illumination is produced using different configurations of lenses: (**a**) two zone plates and (**b**) an Airy phase mask combined with two-zone plates. Setups are depicted at the top of segments (**a**) and (**b**). Gr denotes the imaged sample with graphene layers. Experimentally obtained and numerically calculated imaging results are presented below. The color bars are normalized to the maximum signal. The dashed red line indicates the position of cross-sections of the recorded and calculated intensities given in the left bottom corner. Transmittance ratio of all samples for two different configurations of lenses (**c**). Correlation between Raman 2D and G peak positions for 1–5 graphene layers (**d**). Blue/yellow point marks free-standing graphene

assumed that THz structured light can be assumed as a convenient and contactless tool for examining the properties of 2D materials and can also be extended to other materials systems or low-absorbing objects.

A good benchmark for the estimation of structured THz light illumination is *SNR*. For the conventional Gaussian-like illumination, we found the *SNR* to be around 118, meanwhile when the cubic phase mask creates a nonparaxial Airy beam the *SNR* is recorded to be almost three times higher $SNR = 326$. This is yet another indication that the structured illumination enables us to achieve significantly better resolution in the inspection of graphene layers.

## Discussion

It was demonstrated that the THz light can be shaped into structured self-accelerating and nonlinearly propagating nonparaxial radiation using high-resistance silicon diffractive optics prepared by femtosecond laser ablation technology.

It was shown that the designed element due to its nonparaxiality can simultaneously generate two distinct types of nonparaxial structured THz light – nondiffracting nonparaxial Airy beam with a parabolic trajectory and an expanding Airy beam with a reciprocal trajectory – in the same optical setup. Generation of these distinct three-dimensional field patterns was experimentally confirmed at 0.6 THz frequency and applied in THz imaging experiments.

Employing a sensitive, 90 nm CMOS technology-based THz detector signal-to-noise ratio has reached a value of 570 for the setup with the single Airy lens and that of 1180 for the setup with the Airy lens and the zone plate combination. Experiments indicated that, compared to only the Airy lens, the combination of the Airy lens and a nonparaxial zone plate results in twice better spatial resolution – 0.8 mm ($1.6\lambda$) period bars are visible.

THz imaging behind the obstacle was explored both numerically and experimentally in different obstacle geometries. It was validated that the Airy lens is superior

in comparison to other illuminating elements, even if the ~60% of the optical element was covered by an obstacle, the image of the target was still clear and exhibited a resolution of 3.2$\lambda$ and the contrast of around 26 (*a.u.*). Even better results were achieved for parabolically bending structured THz illumination: When the ~60% of the optical element was covered, the resolution did not decrease and was twice (1.6$\lambda$) as good as for the reciprocally bending structured THz illumination (3.2$\lambda$) with slightly lower contrast to 21 (*a.u.*).

With an increase in the blocked part, the contrast of the image experiences almost no changes in settings that contain bending illumination, while for the Bessel lens the contrast drops drastically from 35 (*a.u.*) to 3 (*a.u.*). Thus, although both Airy and Bessel illumination is nondiffractive, the bending propagation of the structured THz light provides an opportunity to image samples behind an obstacle with sufficient resolution and reasonable contrast.

To summarize, we presented the results of compact silicon flat optics-based THz structured light generation and its comprehensive benchmarks of various structured nonparaxial THz illumination-Bessel-like and self-accelerating along different paths. Our results indicate not only the good performance of the devised flat optics but also herald their potential in the applications of structured THz light in imaging and inspection of the quality of 2D materials e.g., stacked graphene layers. As the Raman spectroscopy indicates optical characteristics of the samples are different due to the strains, doping, depletion, etc., the structured Airy THz illumination gives an additional possibility to evaluate optical properties of stratified samples when combined with the conventional approach. It is in sharp contrast to the Gaussian illumination, where these features are indistinguishable. Extensive benchmarking allows to infer that the structured light consistently outperforms the classical Gaussian beam in THz imaging in such metrics as resolution and contrast allowing thus its expansion of applicability in rather complex investigation scenarios.

## Materials and methods

### Theoretical background

A distinct feature of the nondiffracting non-apertured paraxial Airy beam is its cubic spectral phase distribution $S(k_x, k_y)$[9,32]

$$S(k_x, k_y) = \exp\left[\frac{i}{3}(2\pi b)^3\left(k_x^3 + k_y^3\right)\right] \tag{5}$$

where $k_x$, $k_y$ are transverse components of spatial spectra, $x$, $y$ denote spatial coordinates, and $b$ is some characteristic acceleration value. A Fourier transform of the spatial spectrum results in the following expression for the electromagnetic field in the focus

$$\int_{-\infty}^{+\infty}\exp\left[\frac{i}{3}(2\pi b)^3\left(k_x^3 + k_y^3\right)\right]\exp[-2\pi i(k_x x + k_y y)]\mathrm{d}k_x\mathrm{d}k_y = \frac{1}{b^2}\mathrm{Ai}\left(-\frac{x}{b}\right)\mathrm{Ai}\left(-\frac{y}{b}\right) \tag{6}$$

Expression in Eq. (6) is a solution of a paraxial diffraction equation.

The propagation-dependent paraxial expression is given by

$$\begin{aligned} U(x,y,z) \quad &\approx \exp\left[-2\pi i\lambda z\left(\frac{1}{2\pi b}\right)^3\left(x - \frac{z^2}{4b^3k^2}\right)\right] \\ &\times \exp\left[-2\pi i\lambda z\left(\frac{1}{2\pi b}\right)^3\left(y - \frac{z^2}{4b^3k^2}\right)\right] \\ &\times \mathrm{Ai}\left[\left(\frac{x}{b} - \frac{z^2}{4b^4k^2}\right)\right]\mathrm{Ai}\left[\left(\frac{y}{b} - \frac{z^2}{4b^4k^2}\right)\right] \end{aligned} \tag{7}$$

It reveals the main feature of the nondiffracting Airy beam: the accelerating parabolic trajectory $4b^3k^2x = z^2$ of the dominant intensity peak. Most notably, the Airy cross-section is preserved during propagation.

Without loss of generality, a finite energy expression of the Airy beam is obtained by the introduction of the Gaussian envelope to the spatial spectra in Eq. (5). In other words, the cubic phase mask for the spatial spectra is essential in the engineering of the Airy beam.

We note that the designed element can also shape the incident radiation into a diffracting "caustic" beam when used without a lens[22,57]. In the paraxial regime, it is easily demonstrated by using the stationary phase method to evaluate the Fresnel integral[57]

$$U(x,y,z) \cong \mathrm{Ai}\left[\frac{\left(k + 2(2\pi b)^3 xz\right)^2}{2^{4/3}z^2(2\pi b)^4}\right]\mathrm{Ai}\left[\frac{\left(k + 2(2\pi b)^3 yz\right)^2}{2^{4/3}z^2(2\pi b)^4}\right] \tag{8}$$

leading to the reciprocal trajectory of the Airy beam $z = -k/(16\pi^3 b^3 x)$. There are two differences in comparison to the conventional realization, see Eq. (7): 1) the reciprocal trajectory of propagation and 2) the quadratic spreading with the propagation distance $z$ due to the presence of the factor $1/z^2$ in Eq. (8). Here, we note that in the paraxial regime the trajectories of the caustics produced with and without the lens do not overlap, as the coefficient $b$ enters equations for trajectories differently: $4b^3k^2x = z^2$ for the conventional case and for unconventional generation as $z = -k/(16\pi^3 b^3 x)$. It is important to underline that the selected parameters ensure a simultaneous generation of two different types of Airy beam.

### Numerical methods

In general, the choice of parameter $b$ in Eq. (5) usually describes paraxial masks. However, in our case, we choose $b = \sqrt[3]{3A}/(2\pi) = 50\ \mathrm{m}^{-1}$ therefore, numerical verification of its performance and validation of the trajectories of Eqs. (7, 8) was performed. We start by recalling the Rayleigh-Sommerfeld diffraction integral[52].

$$U(\mathbf{r}_1) = \frac{1}{i\lambda}\int_{S_A} U_{\mathrm{inc}}(\mathbf{r}_0)T(\mathbf{r}_0)\frac{\exp[ik|\mathbf{r}_{01}|]}{|\mathbf{r}_{01}|}\cos(r_{01},n)dS \tag{9}$$

where $U(\mathbf{r}_1)$ is the field in the observation plane, $U_{\mathrm{inc}}(\mathbf{r}_0)$ is the incident field in the diffraction plane, $T(\mathbf{r}_0)$ is the transmittance of the object. The coordinates of the observation plane are $\mathbf{r}_0 = (x_0, y_0, z = 0)$ and the coordinates of the observation plane are $\mathbf{r}_1 = (x_1, y_1, z = z_o)$, the vector $\mathbf{r}_{01}$ is the distance between two points in these planes, and n is normal to the surface of the object. Integration is performed over the surface of the element $S_A$. Based on this consideration we have employed a propagator using spherical point sources to numerically model propagation of the electromagnetic field within the system.

### Fabrication of silicon optics

The core material for production was 500 μm thick high-resistivity silicon wafer with a refractive index of $n = 3.46$. It was ablated employing a femtosecond pulse duration laser, which was a Pharos SP (Light Conversion Ltd.). It generated a maximum power of $P = 6$ W at $\lambda = 1030$ nm wavelength with a tunable repetition rate of 4–200 kHz and an output beam size of 9 mm at the intensity level $\exp(-2)$. For the optimal ablation process, the shortest pulse duration of $\tau = 156$ fs was employed keeping $P = 5$ W average power at 50 kHz repetition rate making thus $E = 100$ μJ energy per pulse. The pulse overlap density was established at 100 pulses per millimeter, while the spot size was approximately 20 μm. The amount of material removed in one pass was about 0.86 μm deep. Although the material ablation rate was not high – it was 1.257 $\mu\mathrm{m}^3\ \mathrm{s}^{-1}$ we used these optimal parameters to avoid excessive burning of the silicon substrate and to produce relatively smooth ablated surfaces with roughness less than 2 μm. In general, a recipe for technological quality of flat silicon optical elements production relies on a rational balance between the fabrication duration and optimal ablation rate aiming to minimize material roughness and avoid silicon oxidation.

### The detection scheme

In both benchmarks, the focused beam was registered with the raster scanning technique in the *xyz* directions using the Si-CMOS field effect transistor manufactured using 90 nm foundry technology and integrated with a 670 μm-diameter log-spiral THz antenna. An additional Si substrate lens with a diameter 12 mm and height 6.8 mm is used for efficient coupling between the antenna and the THz radiation, which is directed from the substrate side. Before the experiment, the THz sensor was investigated, and it was determined that it exhibits rather a flat responsivity over the 0.1–2 THz range with values of optical responsivity and noise equivalent power of around 40 mA $\mathrm{W}^{-1}$ and 42 pW $\mathrm{Hz}^{-0.5}$, respectively[58].

#### Acknowledgements

We thank Ignas Grigelionis, Dalius Seliuta, Pavel Gotovski, and Karolis Mundrys for useful discussions and enlightening remarks. This project has received funding from European Social Fund (project No. 09.3.3-LMT-K-712-01-0167) under a grant agreement with the Research Council of Lithuania (LMT). A. L. is thankful for the funding by the Foundation For Polish Science, grant number MAB/2018/9.

#### Author details

[1]Department of Optoelectronics, Center for Physical Sciences and Technology, Saulėtekio av. 3, Vilnius 10257, Lithuania. [2]Department of Fundamental Research, Center for Physical Sciences and Technology, Saulėtekio av. 3, Vilnius 10257, Lithuania. [3]Institute of Applied Electrodynamics & Telecommunications, Vilnius University, Saulėtekio av. 3, Vilnius 10257, Lithuania. [4]CENTERA Labs., Institute of High Pressure Physics PAS, ul. Sokolowska 29/37, Warsaw 01-142, Poland. [5]Department of Organic Chemistry, Center for Physical Sciences and Technology, Saulėtekio av. 3, Vilnius 10257, Lithuania. [6]Institute of Photonics and Nanotechnology, Department of Physics, Vilnius University, Saulėtekio av. 3, Vilnius 10257, Lithuania

#### Author contributions

L.M., S.O., and G.V. developed the concept of the study; R.I.-P., L.M., D.J. performed experiments; A.L. and K.I. developed the THz CMOS sensor; E.N. manufactured the silicon diffractive optics; V.J. has supervised the preparation of the silicon diffractive elements; R.I.-P. and N.A. fabricated graphene samples; I.M. performed Raman spectroscopy measurements of graphene samples; P.K., and S.O. performed theoretical investigation; numerical simulations were performed by P.K. (mostly) and S.O. (partially); experimental data were analyzed by S.O., P.K., L.M., R.I.-P., and G.V.; the manuscript was written and edited by S.O., R.I.-P., L.M., and G.V.; the project was initiated and coordinated by G.V. All authors discussed and commented on this work.

#### Conflict of interest

The authors declare no competing interests.

**Supplementary information** The online version contains supplementary material available at https://doi.org/10.1038/s41377-022-01007-z.

Received: 23 May 2022 Revised: 9 September 2022 Accepted: 8 October 2022
Published online: 17 November 2022

#### References

1. Rubinsztein-Dunlop, H. et al. Roadmap on structured light. *J. Opt.* **19**, 013001 (2017).
2. Angelsky, O. V. et al. Structured light: Ideas and concepts. *Front. Phys.* **8**, 114 (2020).
3. Ren, Y. X. et al. Non-diffracting light wave: Fundamentals and biomedical applications. *Front. Phys.* **9**, 698343, https://doi.org/10.3389/fphy.2021.698343 (2021).
4. Vasara, A., Turunen, J. & Friberg, A. T. Realization of general nondiffracting beams with computer-generated holograms. *J. Optical Soc. Am. A* **6**, 1748–1754 (1989).

5. Wei, X. L. et al. Generation of arbitrary order Bessel beams via 3D printed axicons at the terahertz frequency range. *Appl. Opt.* **54**, 10641–10649 (2015).
6. Orlov, S., Piskarskas, A. & Stabinis, A. Localized optical subcycle pulses in dispersive media. *Opt. Lett.* **27**, 2167–2169 (2002).
7. Broky, J. et al. Self-healing properties of optical airy beams. *Opt. Express* **16**, 12880–12891 (2008).
8. Vyas, S., Kozawa, Y. & Sato, S. Self-healing of tightly focused scalar and vector bessel–gauss beams at the focal plane. *J. Optical Soc. Am. A* **28**, 837–843 (2011).
9. Siviloglou, G. A. et al. Observation of accelerating airy beams. *Phys. Rev. Lett.* **99**, 213901 (2007).
10. Barwick, S. Accelerating regular polygon beams. *Opt. Lett.* **35**, 4118–4120 (2010).
11. Ruffato, G., Brunetta, S. & Kobayashi, H. A general conformal framework for regular cusp beams. *Opt. Commun.* **517**, 128325 (2022).
12. Orlov, S. et al. Propagation of Bessel beams carrying optical vortices. *Opt. Commun.* **209**, 155–165 (2002).
13. Vieira, T. A., Gesualdi, M. R. R. & Zamboni-Rached, M. Frozen waves: Experimental generation. *Opt. Lett.* **37**, 2034–2036 (2012).
14. Bouchal, Z. & Olivík, M. Non-diffractive vector Bessel beams. *J. Mod. Opt.* **42**, 1555–1566 (1995).
15. Forbes, A., De Oliveira, M. & Dennis, M. R. Structured light. *Nat. Photonics* **15**, 253–262 (2021).
16. Gutiérrez-Vega, J. C., Iturbe-Castillo, M. D. & Chávez-Cerda, S. Alternative formulation for invariant optical fields: Mathieu beams. *Opt. Lett.* **25**, 1493–1495 (2000).
17. Bandres, M. A., Gutiérrez-Vega, J. C. & Chávez-Cerda, S. Parabolic nondiffracting optical wave fields. *Opt. Lett.* **29**, 44–46 (2004).
18. Ring, J. D. et al. Auto-focusing and self-healing of pearcey beams. *Opt. Express* **20**, 18955–18966 (2012).
19. Fan, Q. B. et al. Broadband generation of photonic spin-controlled arbitrary accelerating light beams in the visible. *Nano Lett.* **19**, 1158–1165 (2019).
20. Efremidis, N. K. et al. Airy beams and accelerating waves: An overview of recent advances. *Optica* **6**, 686–701 (2019).
21. Guo, Y. H. et al. Polarization-controlled broadband accelerating beams generation by single catenary-shaped metasurface. *Adv. Optical Mater.* **7**, 1900503 (2019).
22. Zannotti, A. et al. Shaping caustics into propagation-invariant light. *Nat. Commun.* **11**, 1–73597 (2020).
23. Zhu, L. et al. Flexible rotation of transverse optical field for 2D self-accelerating beams with a designated trajectory. *Opto-Electron. Adv.* **4**, 200021 (2021).
24. Geng, J. Structured-light 3D surface imaging: A tutorial. *Adv. Opt. Photonics* **3**, 128–160 (2011).
25. Bitman, A., Moshe, I. & Zalevsky, Z. Improving depth-of field in broadband thz beams using nondiffractive Bessel beams. *Opt. Lett.* **37**, 4164–4166 (2012).
26. Minkevičius, L. et al. Bessel terahertz imaging with enhanced contrast realized by silicon multi-phase diffractive optics. *Opt. Express* **27**, 36358–36367 (2019).
27. Baltrukonis, J. et al. High-order vector bessel-gauss beams for laser micromachining of transparent materials. *Phys. Rev. Appl.* **16**, 034001 (2021).
28. Ševas, P. et al. Azimuthally modulated axicon vortical beams for laser microprocessing. *Opt. Commun.* **505**, 127509 (2022).
29. Yuan, Y. S. et al. Beam wander relieved orbital angular momentum communication in turbulent atmosphere using Bessel beams. *Sci. Rep.* **7**, 1–742276 (2017).
30. Zhu, L. et al. Airy beam for free-space photonic interconnection: Generation strategy and trajectory manipulation. *J. Lightwave Technol.* **38**, 6474–6480 (2020).
31. Wang, J. et al. Airy-beam tomographic microscopy. *Optica* **7**, 790–793 (2020).
32. Vettenburg, T. et al. Light-sheet microscopy using an airy beam. *Nat. Methods* **11**, 541–544 (2014).
33. Zhang, D. J. et al. Enhanced sub-terahertz microscopy based on broadband airy beam. *Adv. Mater. Technol.* **7**, 2100985 (2022).
34. Banerji, S. et al. Imaging with flat optics: Metalenses or diffractive lenses? *Optica* **6**, 805–810 (2019).
35. Engelberg, J. & Levy, U. The advantages of metalenses over diffractive lenses. *Nat. Commun.* **11**, 1–41991 (2020).
36. Reshef, O. et al. An optic to replace space and its application towards ultra-thin imaging systems. *Nat. Commun.* **12**, 1–83512 (2021).
37. Gao, H. et al. Recent advances in optical dynamic meta-holography. *Opto-Electron. Adv.* **4**, 210030 (2021).
38. Siemion, A. Terahertz diffractive optics—smart control over radiation. *J. Infrared, Millim., Terahertz Waves* **40**, 477–499 (2019).
39. Guo, W. L. et al. Airy beam generation: Approaching ideal efficiency and ultra wideband with reflective and transmissive metasurfaces. *Adv. Optical Mater.* **8**, 2000860 (2020).
40. Wen, J. et al. All-dielectric synthetic-phase metasurfaces generating practical airy beams. *ACS Nano* **15**, 1030–1038 (2021).
41. Cheng, Q. Q. et al. Achromatic terahertz airy beam generation with dielectric metasurfaces. *Nanophotonics* **10**, 1123–1131 (2020).
42. Deng, Z. L. et al. Full-visible transmissive metagratings with large angle/wavelength/polarization tolerance. *Nanoscale* **12**, 20604–20609 (2020).
43. Deng, Z. L. et al. Vectorial compound metapixels for arbitrary nonorthogonal polarization steganography. *Adv. Mater.* **33**, 2103472 (2021).
44. Valušis, G. et al. Roadmap of terahertz imaging 2021. *Sensors* **21**, 4092 (2021).
45. Castro-Camus, E., Koch, M. & Mittleman, D. M. Recent advances in terahertz imaging: 1999 to 2021. *Appl. Phys. B* **128**, 12 (2022).
46. Hillger, P. et al. Terahertz imaging and sensing applications with silicon-based technologies. *IEEE Trans. Terahertz Sci. Technol.* **9**, 1–19 (2019).
47. He, J. W. et al. Metasurfaces for terahertz wavefront modulation: A review. *J. Infrared, Millim., Terahertz Waves* **41**, 607–631 (2020).
48. Zang, X. F. et al. Metasurfaces for manipulating terahertz waves. *Light: Adv. Manuf.* **2**, 148–172 (2021).
49. Siemion, A. The magic of optics—an overview of recent advanced terahertz diffractive optical elements. *Sensors* **21**, 100 (2021).
50. Ikamas, K. et al. All-electronic emitter-detector pairs for 250 GHz in silicon. *Sensors* **21**, 5795 (2021).
51. Minkevičius, L. et al. Terahertz multilevel phase Fresnel lenses fabricated by laser patterning of silicon. *Opt. Lett.* **42**, 1875–1878 (2017).
52. Born, M. & Wolf, E. Principles of Optics: Electromagnetic Theory of Propagation, Interference and Diffraction of Light. (Elsevier, 2013).
53. Minkevičius, L. et al. Compact diffractive optics for THz imaging. *Lithuanian J. Phys.* **58**, 99–107 (2018).
54. Indrišiūnas, S. et al. Laser-processed diffractive lenses for the frequency range of 4. 7 THz. *Opt. Lett.* **44**, 1210–1213 (2019).
55. Jokubauskis, D. et al. Fibonacci terahertz imaging by silicon diffractive optics. *Opt. Lett.* **43**, 2795–2798 (2018).
56. Chadan, K. et al. An Introduction to Inverse Scattering and Inverse Spectral Problems. (SIAM, 1997).
57. Greenfield, E. et al. Accelerating light beams along arbitrary convex trajectories. *Phys. Rev. Lett.* **106**, 213902 (2011).
58. Čibiraitė-Lukenskienė, D. et al. Passive detection and imaging of human body radiation using an uncooled field-effect transistor-based THz detector. *Sensors* **20**, 4087 (2020).

Supplementary information for

# TERAHERTZ STRUCTURED LIGHT: NONPARAXIAL AIRY IMAGING USING SILICON DIFFRACTIVE OPTICS

**R. Ivaškevičiūtė-Povilauskienė**, P. Kizevičius, E. Nacius, D. Jokubauskis, K. Ikamas, A. Lisauskas, N. Alexeeva, I. Matulaitienė, V. Jukna, S. Orlov, L. Minkevičius, G. Valušis

*Light: Science and applications* **11**, 326 (2022).
DOI: 10.1038/s41377-022-01007-z

# Supplementary Information for Terahertz structured light: nonparaxial Airy imaging using silicon diffractive optics

Rusnė Ivaškevičiūtė-Povilauskienė[1*], Paulius Kizevičius[2], Ernestas Nacius[2], Domas Jokubauskis[1], Kęstutis Ikamas[3], Alvydas Lisauskas[3,4], Natalia Alexeeva[1], Ieva Matulaitienė[5], Vytautas Jukna[2], Sergej Orlov[2], Linas Minkevičius[1,6] and Gintaras Valušis[1,6]

[1*]Department of Optoelectronics, Center for Physical Sciences and Technology, Saulėtekio av. 3, Vilnius, 10257, Lithuania.
[2]Department of Fundamental Research, Center for Physical Sciences and Technology, Saulėtekio av. 3, Vilnius, 10257, Lithuania.
[3]Institute of Applied Electrodynamics & Telecommunications, Vilnius University, Saulėtekio av. 3, Vilnius, 10257, Lithuania.
[4]CENTERA Labs., Institute of High Pressure Physics PAS, ul. Sokolowska 29/37, Warsaw, 01-142, Poland.
[5]Department of Organic Chemistry, Center for Physical Sciences and Technology, Saulėtekio av. 3, Vilnius, 10257, Lithuania.
[6]Institute of Photonics and Nanotechnology, Department of Physics, Vilnius University, Saulėtekio av. 3, Vilnius, 10257, Lithuania.

*Corresponding author(s). E-mail(s): rusne.ivaskeviciute@ftmc.lt;

## 1 Theoretical background of analysis of Airy THz imaging in stratified medium samples

Puzzling behaviour of the sample with graphene layers did require some investigation. First of all, during the deposition on the Si wafer, the graphene layers

could be modified due to the interaction with the substrate. The presence of the substrate and the number of the accompanying layers have influence on the optical constant of the graphene [1–3]. Uniaxial or biaxial strain can also appear, which will lead to modulation of conductivity and refractive index [4]. However, the presence of graphene could modify the conductivity of the Si wafer; thus, its optical parameters could also be somewhat modified [5, 6]. Revealing possible reasons of the situation observed in the experiment is the main motivation of the text below.

Our considerations are based on the basics of propagation of electromagnetic waves through the stratified medium [7, 8]. The characteristic matrix $\boldsymbol{M}(z)$ is shown to be

$$\boldsymbol{M}(z) = \begin{bmatrix} \cos\beta & -\frac{\mathrm{i}}{p}\sin\beta \\ -\mathrm{i}p\sin\beta & \cos\beta \end{bmatrix}, \tag{1}$$

where $k_0$ is the wave vector in vacuum, $\beta = k_0 n z\cos\theta$, $n$ is the complex refractive index of the medium, $z$ is the distance between two surfaces of the dielectric film, and $\theta$ is the angle at which the plane wave propagates inside the film. For the TE ($s$-polarized) wave, the parameter $p$ is

$$p = \sqrt{\frac{\varepsilon}{\mu}}\cos\theta. \tag{2}$$

It should be replaced by the parameter $q$ if the incident polarization becomes TM ($p$-polarized)

$$q = \sqrt{\frac{\mu}{\varepsilon}}\cos\theta \tag{3}$$

The effective characteristic matrix of a three-phase system is given by

$$\boldsymbol{M}\left(z_2\right) = \boldsymbol{M}_1\left(z_1\right)\boldsymbol{M}_2\left(z_2 - z_1\right) = \begin{bmatrix} m'_{11} & m'_{12} \\ m'_{21} & m'_{22} \end{bmatrix}, \tag{4}$$

where phase 1 occupies space from $z = 0$ to $z = z_1$ and phase 2 extends from $z = 1$ to $z = z_2$. This procedure is repeated as many times as many strata are present in the sample.

The thickness of graphene layers is small; hence, for this situation, we get an approximation

$$\boldsymbol{M}_2 = \begin{bmatrix} 1 & -\frac{\mathrm{i}\beta_2}{p_2} \\ -\mathrm{i}p_2\beta_2, & 1 \end{bmatrix} = \begin{bmatrix} 1 & -\frac{\mathrm{i}}{p_2}k_0 n_2\delta z_2\cos\theta_2 \\ -\mathrm{i}p_2 k_0 n_2\delta z_2\cos\theta, & 1 \end{bmatrix}, \tag{5}$$

which can be generalized for $N$ graphene layers as

$$\boldsymbol{M}_{2,N} = \begin{bmatrix} 1 & -\mathrm{i}k_0\sum_{j=2}^{N}\frac{1}{p_j}n_j\delta z_j\cos\theta_j \\ -\mathrm{i}k_0\sum_{j=2}^{N}p_j n_j\delta z_j\cos\theta, & 1 \end{bmatrix}, \tag{6}$$

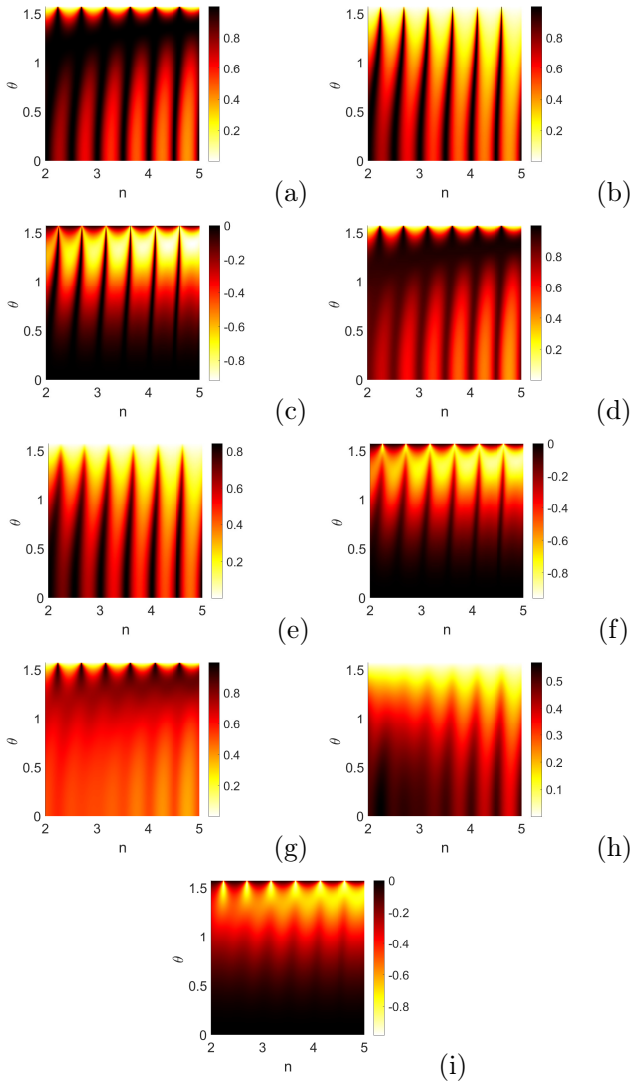


**Fig. S1** Transmittivity of the stratified layer on the refractive index $n$ of the substrate and angle of incidence $\theta$ for the (a,d,g) $p$-polarized and (b,e,h) $s$-polarized THz radiation of the frequency $\omega = 0.6$ THz, the thickness of the film is $d = 500$ µm. (c,f,i) Comparison of absolute numbers of the transmittivity between $s$ and $p$ polarizations. The graphene is (a-c) depleted and $n_{\mathrm{gr}} = 1.68$, (d-f) $n_{\mathrm{gr}} = 223 + 223i$, (g-i) $n_{\mathrm{gr}} = 500 + 500i$ .

Assuming homogeneity of individual graphene layers simplifies the expression and the characteristic matrix is

$$\boldsymbol{M} = \begin{bmatrix} \cos\beta_1 - \frac{p_2\beta_2}{p_1}\sin\beta_1 & -\frac{\mathrm{i}\beta_2}{p_2}\cos\beta_1 - \frac{\mathrm{i}}{p_1}\sin\beta_1 \\ -\mathrm{i}p_1\sin\beta_1 - \mathrm{i}p_2\beta_2\cos\beta_1 & \cos\beta_1 - \frac{p_1\beta_2}{p_2}\sin\beta_1 \end{bmatrix}. \tag{7}$$

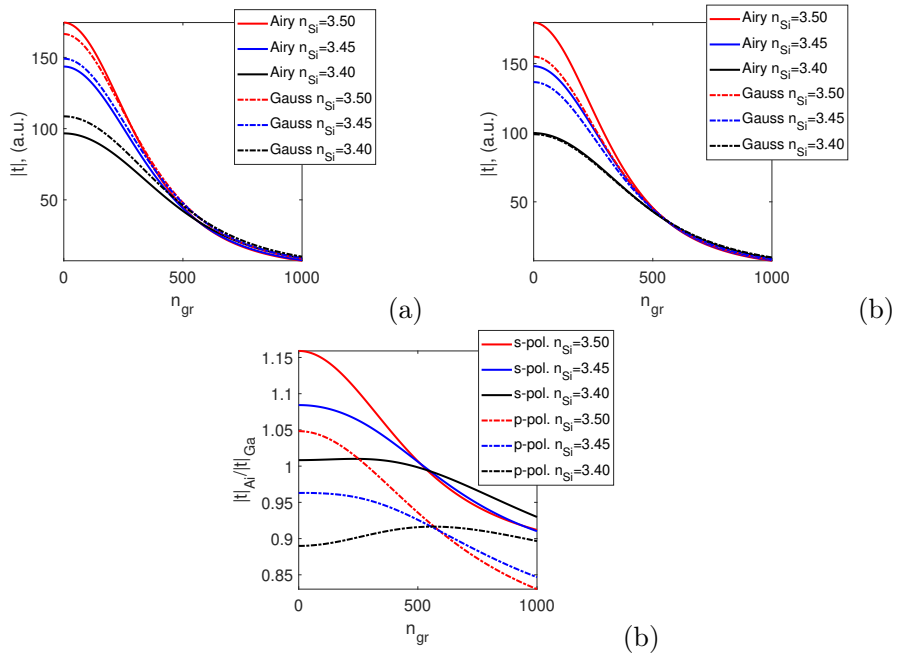


**Fig. S2** Transmission of the nonparaxial Gauss (dotted line) and Airy (continuous line) illumination through the stratified layer with graphene layer of refractive index $n_{\mathrm{gr}}$ for the (a) $s$-polarized and (b) $p$-polarized THz radiation of the frequency $\omega = 0.6$ THz, the thickness of the Si wafer is $d = 500$ µm, refractive index is (black) $n = 3.4$, (blue) $n = 3.45$ and (red) $n = 3.5$ . The thickness of a single graphene layer is $d_g = 0.3$ nm. (c) Ratio of the transmission of the nonparaxial Airy illumination normalized by the transmission of the nonparaxial Gauss illumination for the same case as previously, continuous line is $p$ polarization, $s$ polarization is dotted line.

The transmission coefficient of the stratified medium is given by

$$t = \frac{2p_1}{\left(m'_{11} + m'_{12}p_l\right)p_1 + \left(m'_{21} + m'_{22}p_l\right)}, \tag{8}$$

Once again, the expressions for the $p$ polarization are obtained by replacing $p$ with $q$. In particular, for thin 2D materials, the transmittivity depends on the thickness, number of layers, or absorption of the material only for very large values of the refractive index $n_{\mathrm{gr}}$.

The refractive index of the graphene changes in very wide range of values, the dielectric constant of the $N$ graphene layers is seen as

$$\varepsilon_r(\omega) = 2.5 + i\frac{\sigma(\omega)}{\varepsilon_0 \omega d}, \tag{9}$$

where $\sigma(\omega)$ is the conductivity of the graphene, $d$ is thickness and $\varepsilon_0$ is the permittivity of the vacuum. Some graphene samples can reach refractive indices up to $n_{\mathrm{gr}} = 1000 + 1000\mathrm{i}$ [1–3], on the contrary, the fully depleted graphene will reach values of only $n_{\mathrm{gr}} = 1.68$.

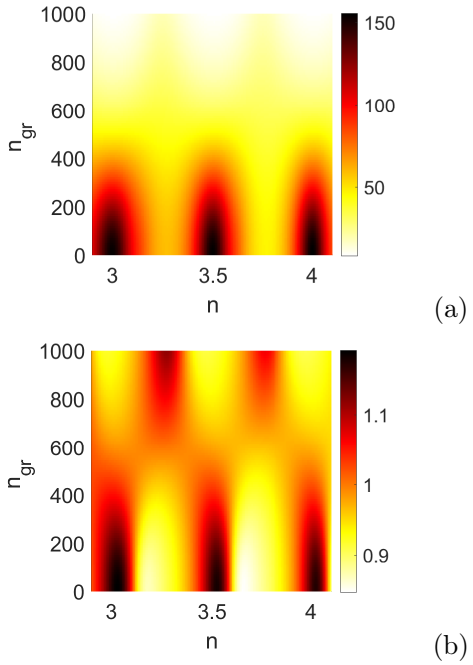


**Fig. S3** (a) Transmission distribution $T_s$ of the $s$ polarized Gaussian beam through the stratified medium on the effective refractive index $n$ of the Si substrate and on the normalized conductivity $\sigma/d$ of the graphene. (b) Distribution of the ratio $T_s^{\text{Airy}}/T_s^{\text{Gauss}}$ between transmissions of the $s$ polarized Gaussian $T_s^{\text{Gauss}}$ and Airy $T_s^{\text{Airy}}$ beams. The frequency is $\omega = 0.6$ THz, the thickness of the film is $d = 500$ µm.

.

First, we investigate the effect of graphene layers on transmittivity $t$, which is maximized when the denominator is maximized. The thickness of the graphene layers is very small and, as it turns out, the number of layers does not greatly influence transmittivity. For unusually high values of the refractive index $n_{\text{gr}} > 200$, a local maximum is observed that is angle dependent, and the transmittivity starts to depend on the number of layers $N$. These values are common in the THz regime for metal-like substances. Because of the very thin layers, absorption does not greatly influence the transmission of the sample. Thus, the metallic behavior results in an angle-dependent transmission. As the literature reveals such behaviour can be caused by a variety of reasons.

Next, we investigate how the optical properties of the substrate (wafer) in combination with the optical properties of the graphene affect transmittivity, see Fig. S1. We fixed the refractive index of graphene $n_{\text{gr}}$ to three distinct values: the value of a freestanding graphene (Fig. S1(a-c)), the semimetalic value (Fig. S1(e-f)) and the metallic value (Fig. S1(g-i)), and we changed the refractive index $n$ of the substrate in the stratified sample. The real part of the refractive index (as well as the thickness of the sample) causes oscillatory changes in the transmittivity because the effective optical path is directly affected by these variables. Second, for the paraxial illumination, the angle of

the incidence (angle in phase 1) $\theta_1 \approx 0$, therefore, the angles $\theta_2$ and $\theta_3$ for remaining two phases via the Snell's law are also small; consequently, both light polarizations are transmitted equally, see (Fig. S1 (c,f,i)). However, a situation for the nonparaxial case becomes nontrivial, as depending on the film thicknesses and the refractive indices, difference in phases and angles can clearly be resolved. Thus, from the transmission values of the wafer, we can deduce its thickness and/or refractive index. Second, although the graphene layers are thin, the refractive index of the graphene has a distinct effect on the polarization-dependent angle-resolved transmittivity of the sample. As the graphene becomes metallic, the $p$ polarization is transmitted better for larger values of incident angles $\theta$, while the $s$ polarization is transmitted better for smaller ones. This becomes even more pronounced, when the refractive index $n_{\mathrm{gr}}$ reaches values of $n_{\mathrm{gr}} = 1000 + 1000i$, see the Supplementary animations S1a and S1b.

Lastly, we numerically estimate the actual transmission of nonparaxial THz radiation. A numerical estimate was performed using an expression

$$U(\mathbf{r}_1) = \frac{1}{i\lambda} \int_{S_{\mathrm{A}}} U_{\mathrm{inc}}(\mathbf{r}_0) T(\mathbf{r}_0) \frac{\exp\left[\mathrm{i}k\left(\mathbf{r}_{01}\right)\right]}{\mathsf{r}_{01}} \cos\left(\mathbf{r}_{01}, \mathbf{n}\right) dS, \tag{10}$$

where $U(\mathbf{r}_1)$ is the field in the observation plane, $U_{\mathrm{inc}}(\mathbf{r}_0)$ is the incident field in the diffraction plane, $T(\mathbf{r}_0)$ is the transmittance of the object. The coordinates of the observation plane are $\mathbf{r}_0 = (x_0, y_0, z = 0)$ and the coordinates of the observation plane are $\mathbf{r}_1 = (x_1, y_1, z = z_o)$, the vector $\mathbf{r}_{01}$ is the distance between two points in these planes, and $\mathbf{n}$ is normal to the surface of the object. Integration is performed over the surface of the element $S_{\mathrm{A}}$.

We estimate the total transmission of the Gaussian and structured Airy THz illumination through a stratified sample with a Si wafer with refractive index $n$ and a graphene layer with normalized conductivity $\sigma/d$, leading to refractive index $n_{\mathrm{gr}}$. As the two-phase system is electrically connected, the depletion of graphene should lead to changes in the refractive index $n$ of the Si wafer. For this reason, the depletion of graphene changes not only the optical refractive index $n_{\mathrm{gr}}$ of graphene but also the optical properties of the second phase. As the volume of graphene is small compared to the volume of the Si wafer, large changes in the refractive index $n_{\mathrm{gr}}$ will lead to relatively small changes in the refractive index $n$ of the wafer. Transmission of the $p$ and $s$ polarized structured illumination through the stratified sample is depicted in Figure S2(a,b) for 3 different values of the refractive index of the substrate. We observe that, depending on the optical properties of the substrate, the transmission for the Airy beam can be larger than that of the Gaussian illumination.

Our main intention here is to explain the behavior that we observed in the experiment, so we investigate the ratio of two transmissions in Fig. S2(c). As the results indicate, for the $s$-polarization, the structured Airy illumination is mostly transmitted better than the Gaussian illumination as long as

the graphene is depleted. The optical properties of the wafer make this behavior less or more pronounced. Increasing conductivity diminishes this effect, and for refractive indices $n_{\mathrm{gr}} > 500$ the Gaussian illumination is transmitted better. We note that for $n_{\mathrm{gr}} > 200$ the number $N$ of graphene layers becomes relevant. The results are also valid for the $N$ layers if one keeps in mind that the optical path $l_{opt}$ for one and $N$ layers should be kept the same, i.e. $l_{opt} = n_N d_N = n_1 d_1$. The situation for $p$ polarization is more dependent on the optical properties of the Si wafer. For the refractive index of Si-wafer $n = 3.50$ the Airy structured illuminations is transmitted better, whereas the decrease in the refractive index results in the better transmission of the Gaussian illumination through the imaging system. More results are given in the animated sequence presented as a Supplementary video S2.

These results can be summarized as a 2D plot of the transmission of the $s$-polarized Gaussian beam $T_s^{\mathrm{Gauss}}$, see S3(a). As the $p$ polarized Airy beam is transmitted in a way very similar to the $s$ polarization, we present the difference caused by the structured illumination in Fig. S3(b) only for one case. Here we plot a ratio $T_s^{\mathrm{Airy}}/T_s^{\mathrm{Gauss}}$. In this way we observe that the difference in the behavior of the sample with 3 graphene layers can be caused either by inter-action of the graphene layer and the Si substrate, i. e. the changes in the graphene conductivity (meaning refractive index $n_{\mathrm{gr}}$) or by the changes in the refractive index of the substrate $n$.

As results reveal, the substrate has a similar effect on $s$ and $p$ polarized THz radiation created by a ZP. Changes in the real part of the refractive index $n$ cause an interferometric oscillation in the transmission for both polarizations. The difference between the $s$ and $p$ polarizations is not significant for the zone plate. However, for the structured bending THz illumination there is a distinct difference in comparison to the Gaussian signal. Thus, changes in the thickness of the wafer and in the optical properties of Si may also be the cause for the behavior we observed for the sample with 3 graphene layers.

The incident polarization in the experiment was $y$ polarized and can be decomposed into $s$ and $p$ polarized as

$$\mathbf{e}_y = \mathbf{e}_s \cos\phi + \mathbf{e}_p \sin\phi, \tag{11}$$

where $\phi$ is the azimuthal angle of the polar coordinates in the $xy$ plane. Therefore, the $s$ component of the spatial spectra is $S(k_x, k_y)k_x/k$ and the $p$ component is $S(k_x, k_y)k_y/k$. We were not fully certain how homogeneous the polarization state was; therefore, we have studied the $s$ and $p$ polarized components separately, and the transmission of the $y$ polarized radiation is a weighted sum of the $s$ and $p$ polarized beams.

This set of simulation results hint at the fact that a) the set of signals for the ZP illumination sets some limits on the dielectric constant of the graphene and Si substrates in the stratified medium, and b) a comparison of the Gaussian signal with the Airy signal enables a more precise polarization-dependent determination of the dielectric constant or other parameters of the sample.

## 2 Raman mapping of graphene layers

Raman spectroscopy serves as a convenient tool for characterization of the quality of graphene. The main role is played here by two spectroscopic peaks – so-called G and 2D bands – in graphene Raman spectra that are located around 1580 $cm^{-1}$ and 2690 $cm^{-1}$, respectively. The G band is associated with vibrations in the plane of carbon atoms bound to $SP2$. Its position, shape, and intensity are highly sensitive to the mechanical strain and doping. Mechanical stress may occur as a result of the interaction with the Si substrate on which graphene is transferred. The 2D band reflects a two phonon lattice vibrational process and it is always strong in graphene.

The Raman mapping was performed for the five samples studied that contained from 1 to 5 graphene layers. The mapping results of the G and 2D peaks are depicted on the left side of each section in Fig. S4(a-e). As one can see, the intensity of the G and 2D bands in the mapping of 3 layers of graphene is distinguished from others. Because the G band is strongly dependent of the mechanical strain, it can be assumed that during graphene transfer this sample was affected and thus experienced more strain between the layers in comparison to others, but not experiences carrier depletion. It also correlates with that seen in Fig.5(c) (in the main article): transmittance ratio in the sample consisting of 3 graphene layers increases in Airy lens experiment in comparison to the Gaussian one. It is related that the THz structured light is phase-sensitive, while the Gaussian THz illumination do not exhibits this feature. Therefore, the THz Airy imaging enables to reveal more precisely properties of single or several graphene layers placed on silicon substrates.

Moreover, existence of mechanical strain and doping can be exposed by correlation analysis of the frequency position of G and 2D bands in Raman spectra. The distribution of $\omega_G$ and $\omega_{2D}$ is shown on the right side of each segment in Fig. S4(a-e). The zero point indicates free graphene and is considered a constant ($\omega_G$=1581.6±0.2 $cm^{-1}$; $\omega_{2D}$=2676.9±0.7 $cm^{-1}$). Graphene interaction with Si substrate and each additional layer can cause a mechanical strain, while interaction with oxygen environment can affect graphene by hole doping.

In conclusion, the presence of mechanical strain and doping of graphene can be disclosed during inspection of the sample with structured THz light illumination.

A detailed study on the use of nonparaxial THz imaging and polarization-sensitive THz spectroscopy to characterize 2D materials is focus of a separate study to follow shortly.

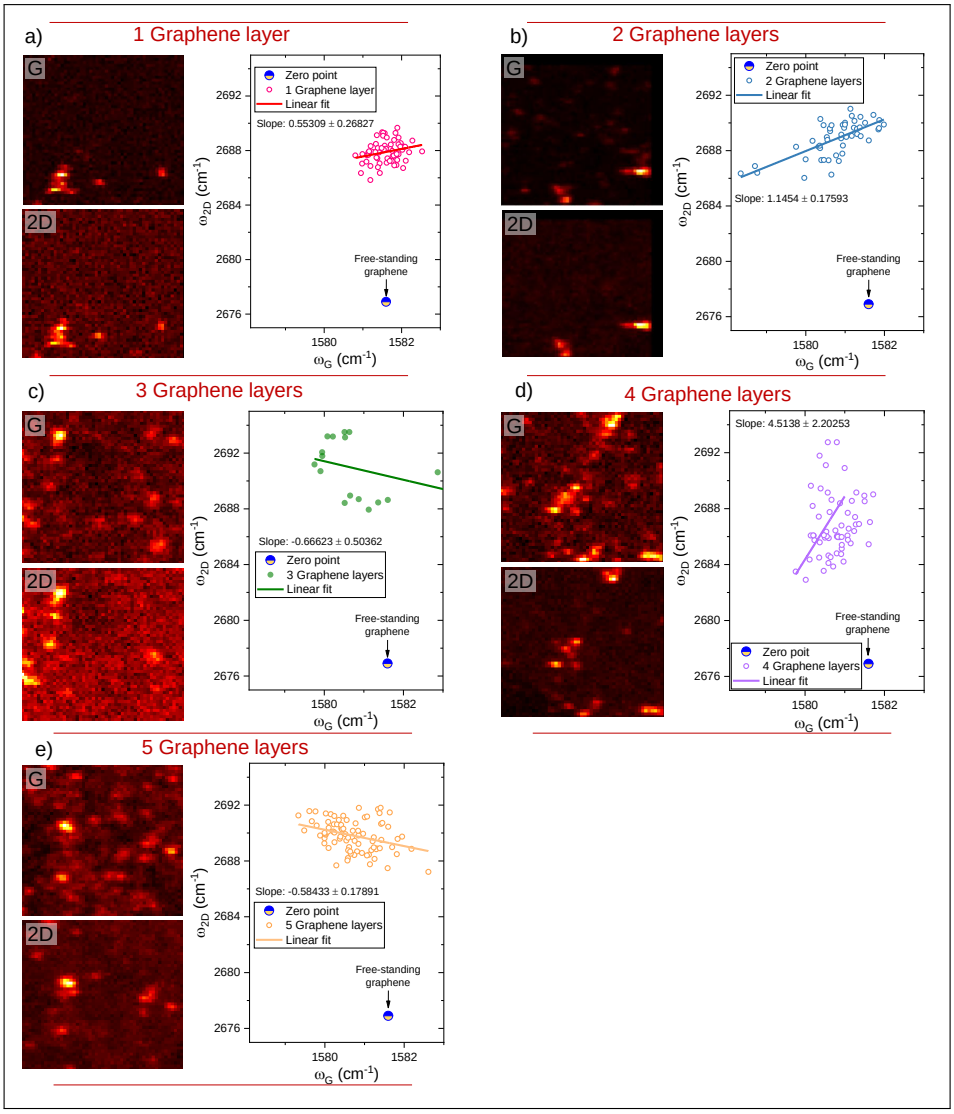


**Fig. S4 Left panels:** Results of the Raman mapping of G and 2D peaks for samples with different number of graphene layers. Note that for 1 and 2 graphene layers the map area displays low intensity intensity with only a few high intensity places. Sample containing 3 graphene layers expresses much higher intensity G and 2D peak mapping, meanwhile sample with 4 and 5 graphene layers intensity decreases, but still remaining higher than that of 1 and 2 graphene layers. **Right panels:** Distributions of $\omega_G$ and $\omega_{2D}$ peaks for each sample. Note that for the single graphene layer (a) distribution is relatively dense; for the sample containing 2 graphene layers (b) distribution of $\omega_G$ is wider indicating more strain. For 3 graphene layers sample (c), the slope changes its direction and frequency distribution of G and 2D peaks deviates stronger in comparison to other samples implying presence of a stronger mechanical strain. In case of 4 graphene layers (d), distribution of $\omega_{2D}$ gets wider meanwhile $\omega_G$ is dense, indicating, probably, presence of hole doping. The sample with 5 graphene layers (e), exhibits $\omega_G$ rather wide distribution implying mechanical strain between the layers.

# References


[1] Lin, I.-T.: Optical Properties of Graphene from the THz to the Visible Spectral Region. PhD thesis, University of California, Los Angeles (2012)

[2] Yang, Y., Kolesov, G., Kocia, L., Heller, E.J.: Graphene terahertz absorption. arXiv preprint arXiv:1705.06267 (2017)

[3] Batrakov, K., Kuzhir, P., Maksimenko, S., Volynets, N., Voronovich, S., Paddubskaya, A., Valusis, G., Kaplas, T., Svirko, Y., Lambin, P.: Enhanced microwave-to-terahertz absorption in graphene. Applied Physics Letters **108**(12), 123101 (2016)

[4] Naumis, G.G., Barraza-Lopez, S., Oliva-Leyva, M., Terrones, H.: Electronic and optical properties of strained graphene and other strained 2d materials: a review. Reports on Progress in Physics **80**(9), 096501 (2017)

[5] Nashima, S., Morikawa, O., Takata, K., Hangyo, M.: Measurement of optical properties of highly doped silicon by terahertz time domain reflection spectroscopy. Applied physics letters **79**(24), 3923–3925 (2001)

[6] Pejcinovic, B.: Examination of silicon material properties using thz time-domain spectroscopy. In: 2014 37th International Convention on Information and Communication Technology, Electronics and Microelectronics (MIPRO), pp. 22–26 (2014)

[7] Hansen, W.N.: Electric fields produced by the propagation of plane coherent electromagnetic radiation in a stratified medium. JOSA **58**(3), 380–390 (1968)

[8] Born, M., Wolf, E.: Principles of optics: electromagnetic theory of propagation, interference and diffraction of light. Elsevier (2013)

P5

## TERAHERTZ DIGITAL HOLOGRAPHY: TWO- AND FOUR-STEP PHASE SHIFTING TECHNIQUE IN TWO PLANE IMAGE RECORDING

A. Semion, L. Minkevičius, D. Jokubauskis, **R. Ivaškevičiūtė-Povilauskienė**, Valušis

*AIP Advances* **11**(10), 105212 (2021).
DOI: 10.1063/5.0062330

# Terahertz digital holography: Two- and four-step phase shifting technique in two plane image recording

Cite as: AIP Advances 11, 105212 (2021); doi: 10.1063/5.0062330
Submitted: 17 July 2021 • Accepted: 27 September 2021 •
Published Online: 8 October 2021



Agnieszka Siemion,[1,a)] Linas Minkevičius,[2] Domas Jokubauskis,[2] Rusnė Ivaškevičiūtė-Povilauskienė,[2] and Gintaras Valušis[2]

## AFFILIATIONS

[1] Faculty of Physics, Warsaw University of Technology, 75 Koszykowa, Warsaw, Poland
[2] Department of Optoelectronics, Center for Physical Sciences and Technology, Saulėtekėo Ave. 3, LT-10257 Vilnius, Lithuania

[a)] **Author to whom correspondence should be addressed:** agnieszka.siemion@pw.edu.pl

## ABSTRACT

A two- and four-step phase shifting (PS) technique in terahertz (THz) digital holography is proposed. Relying on the Mach–Zehnder interferometer-based setup, it was demonstrated that the two-step and four-step PS in Fresnel holograms can assist in a five times greater background subtraction. It allows us to improve the quality of the obtained holographic images, in particular when objects introduce phase changes. It was shown that the recording of holograms of an object consisting of two separated planes can enable qualitative reconstruction of 3D images. Here, the planes were separated by 30 mm, thus defining the longitudinal (depth) resolution in this experiment. It is shown that the PS can serve in distinguishing transparent objects and, by a proper selection of phase variation within the 0–2$\pi$ range, enable us to increase the quality of the reconstructed hologram. Finally, the advantages of the suggested holographic technique are illustrated by comparing the results with the data of weak absorbing objects obtained via point-to-point, plane-to-plane (4$f$ setup), and dark-field THz imaging approaches. Experiments were performed at frequencies of 0.3 and 0.6 THz recording THz images using resonance antenna-coupled titanium microbolometers.



## I. INTRODUCTION

Terahertz (THz) holography is a rapidly developing investigation technique stimulated by a large variety of possible applications, in particular in discriminating weakly absorbing or transparent materials due to its high sensitivity to phase shifts. These features make digital holography very attractive for biological and medical investigations;[1,2] they open possibilities to increase image resolution,[3] either with additional autofocusing techniques[4] or performing the Fourier transform digitally,[5] or multiplexing facilities.[6]

Holographic images can be registered and reconstructed using a large variety of methods.[7] The so-called Fresnel hologram is a classical example of hologram, where the beam, diffracted by or at the sample, propagates to the hologram plane and interferes with the reference beam. The collimated beams—object $U_{object}$ and reference $U_{reference}$—impinging the hologram plane from the same side are mostly recorded at some angle.[7] Due to the fact that the intensity of the interference pattern is registered, the reconstruction results in the formation of four components in the Fourier domain: two phase-independent terms form a DC term (a zero frequency component) and two terms with the phase dependence form virtual and real images. In the case of digital holography, only the real image can be reconstructed and observed. Therefore, three other components form the unwanted noise in the image reconstruction, reducing its quality. There are different methods to alleviate this situation. One way is to exploit the filtration in the Fourier spectrum:[7] if the angle is wide enough, the reconstruction in a large enough calculation matrix will separate the components. However, such a method requires more numerical capacity, and due to the filtration, only part of the recorded information is used.

An alternative route to tackle the unwanted noise issue is to engage phase shifting (PS) methods.[8–10] The PS techniques are commonly used in digital holography to increase the quality of reconstructed images by reducing noise in the reconstructed intensity

distribution introduced by the beams that do not form the image. The technique utilizes multiple exposures and a special reconstruction algorithm to remove the spurious components from the image of the registered object.[11] In more details, mostly between two and five exposures are performed by recording consecutive holograms with the changed phase value of each reference beam. These particular phase shifts introduced in the reference beam in each exposure allow us to reconstruct the image via a particular algorithm.[12]

In this work, we demonstrate a novel PS approach in THz holography—two- and four-step PS technique—which enables a reconstruction of 3D objects via the introduction of different phase shifts in the reference beam. Here, we used two types of objects—first introducing amplitude and phase changes and second consisting of two separated planes in a space. Relying on the Mach–Zehnder interferometer-based setup and applying two-step and four-step phase shifts with the corresponding values equal to 0 and $\pi$ for the two-step method and 0, $\frac{\pi}{2}$, $\pi$, and $\frac{3\pi}{2}$ for the four-step method, it was demonstrated that the PS in Fresnel holograms can assist in a comprehensive unwanted background subtraction, thus improving the essential quality of obtained holographic images in two color—300 and 600 GHz—experiments. The experimental results have shown the average increase in contrast ($K$) from 8.5 to 16.8 (Table I) and the decrease in the value of the background by a factor of 5 while reconstructing via a single hologram and the proposed two-step PS technique, respectively. In the case of four-step PS reconstruction, the contrast was not increased in relation to single hologram reconstruction and two-step PS; however, it should be noticed that all reconstructed parts of the image have a very similar contrast value. In other methods, they differ, while the object had uniform brightness.

The revealed improvement introduced by the usage of different phase-shifting techniques opens new possibilities to reconstruct the multi-plane images of recorded multi-plane weakly absorbing objects. It can be found well-suited for a large variety of applications, in particular in biology and biomedicine. Special attention should be given to the possibility to distinguish the phase levels of the investigated object that can be properly realized by the four-step PS method. The proposed in-line holographic systems with the phase-shifting technique allow us to increase the information capacity in the optical system. Moreover, we demonstrated the dual-wavelength recording of a two-plane object and its successful reconstruction in both planes.

## II. THEORETICAL FRAME FOR TWO- AND FOUR-STEP PS TECHNIQUES IN THz HOLOGRAPHY

Registering and reconstruction of digital holograms can be realized in many different ways[7] employing the features of optical setup geometry, properties of sources, or reconstruction techniques.

Interferometer principle-based setups are convenient for alignment and use; moreover, such a geometry allows us to reach a very small—close to 0°—angle between the interfering beams. However, in this case, the reconstructed components, corresponding to the DC term and real and virtual images, overlap,[13] which causes a reduction in the quality of the reconstructed image due to the increased background noise. This arises from the light field distribution in the real image plane coming from the virtual image and the DC term. Therefore, it is of a particular need to suppress this negative influence.

In what follows, we propose a step PS technique to resolve the issue of the noise subtraction and proper determination of phase distribution in the sample. More specifically, we introduce the two-step and four-step PS technique corresponding to the phase shifts in the reference beams equal to 0 and $\pi$ for the two-step technique and 0, $\frac{\pi}{2}$, $\pi$, and $\frac{3\pi}{2}$ for the four-step technique.

The intensity pattern recorded for a single hologram can be described as follows:

$$I_{hologram}(x,y) = |U_{object}(x,y) + U_{reference}(x,y)|^2, \tag{1}$$

where $U_{object}$ describes the light field distribution in the hologram plane $(x,y)$ coming from the object beam and $U_{reference}$ is the reference beam in the hologram plane (with or without a phase shift).

In the four-step case, four different holograms are recorded (each with different phase shifts introduced in the reference beam). The calculated complex transmittance reconstructing the light field distribution propagating back to the real image plane can be described using the following equation:

$$T_{hologram-PS4}(x,y) = \sum_{j=1}^{j=4} I_j(x,y) U_{reference\_j}(x,y), \tag{2}$$

where $I_j$ is the intensity of the hologram recorded for each exposure and $j$ is the consecutive number corresponding to different phase shifts introduced in each reference beam $U_{reference\_j}$ and is equal to 0, $\frac{\pi}{2}$, $\pi$, and $\frac{3\pi}{2}$ for $j = 1, 2, 3,$ and 4, respectively. The complex

**TABLE I.** Contrast values for simulation results and experimentally reconstructed image (calculated from the intensity distribution) for two areas of the "E" letter in one plane—with constant phase distribution (right letter) and various phase levels inside (left letter).

| Contrast | | Single hologram | PS2 | PS4 |
|---|---|---|---|---|
| Simulations (large aperture) (Fig. 2) | Right "E" | 8.85 | 25.00 | 14.85 |
| | Left "E" | 4.17 | 25.06 | 16.80 |
| Simulations (small aperture) (Fig. 3) | Right "E" | 3.60 | 1.07 | 5.55 |
| | Left "E" | 3.02 | 13.86 | 7.69 |
| Experiment (Fig. 7) | Right "E" | 8.54 | 16.76 | 6.03 |
| | Left "E" | 10.66 | 11.33 | 6.51 |

reference beam is a plane wave for each hologram having a different phase value. Thus, the term $U_{reference\_j}(x,y)$ can be simplified to $1, i, -1$, and $-i$ in the summation. Therefore, Eq. (2) can be rewritten as follows:

$$T_{hologram-PS4}(x,y) = I_1(x,y) - I_3(x,y) + i[I_2(x,y) - I_4(x,y)]. \quad (3)$$

We must recall that each $I_i(x,y)$ distribution consists of four components. Two of these components form a DC term that is not phase-sensitive, and the other two are real and virtual images. Furthermore, all these 4 exposures are multiplied by the value corresponding to the phase shift of the reference beam, and we obtain 16 components that can be simplified as follows:

$$T_{hologram-PS4}(x,y) = 4U_{object}(x,y), \quad (4)$$

which, after the back propagation (to the real image plane), will reconstruct only the light field distribution related to the real image.

In the case of the two-step technique, only two exposures are registered for the phase shift of the reference beam equal to 0 and $\pi$, and the resulting transmittance can be written as follows:

$$T_{hologram-PS2}(x,y) = I_1(x,y) - I_3(x,y). \quad (5)$$

In this case, there are eight different components, and after the multiplication with the corresponding phase shifts of the reference beams, we obtain

$$T_{hologram-PS2}(x,y) = 2U_{object}(x,y) + 2U^*_{object}(x,y), \quad (6)$$

where $^*$ is the complex coupling operation, and thus, $U^*_{object}$ describes the light field distribution forming the virtual image. As it is seen, the unwanted $U^*_{object}$ component is not removed in this technique. However, it should be mentioned that the transmittance $T_{hologram-PS2}(x,y)$ is propagated to the real image plane where the real image is sharp and well defined, while the light field distribution corresponding to the virtual image forms a divergent beam that only slightly affects the background. The background is lighter; however, it introduces noise. Nevertheless, in comparison with the noise introduced by the DC term component, the noise introduced by $U^*_{object}$ is hardly noticeable. It is worth noting that the two-step technique is two times faster due to the fact that it requires only two exposures instead of four used in a previous approach.

To illustrate the proposed approach, a special sample, consisting of two "E" letters of different types, was constructed. The sample design is shown and commented in Fig. 1. It should be noticed that the opening thickness in "E" letters is equal to 7 mm, which corresponds only to 7 wavelengths in the case of using the 300 GHz beam and 14 wavelengths for the 600 GHz beam.

The comparison between the different recording and reconstructing methods is illustrated in Fig. 2. One can note that in these simulations, the single "E" letter forming the object was 90 mm in height and 60 mm in width, i.e., two times larger than in the experiment (to additionally reduce possible large diffraction effects on the letters). It was assumed that two beams interfere in the hologram plane at an angle of 0°. The simulation parameters were as follows: the distance between the object and the hologram plane was equal to 85 mm, and the recording and reconstructing wavelength was chosen to be 0.5 mm (equivalent to the experimental frequency of

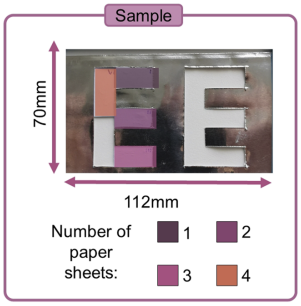


**FIG. 1.** Specially designed sample to illustrate the two- and four-step PS techniques in THz holography. The sample was fabricated from the aluminum foil of dimensions of 70 × 112 mm$^2$ with cut-out "EE" shape elements inside. The left "E" letter consisted of five areas dedicated to produce different phase shifts 0, $\frac{\pi}{4}$, $\frac{\pi}{2}$, $\frac{3\pi}{4}$, and $\pi$ for 600 GHz corresponding to 0, 1, 2, 3, and 4 paper sheets that are indicated by different colors. The right "E" letter was "empty" and served as a reference. This sample was illuminated with a quasi-plane wave and formed the object beam.

600 GHz). The calculation matrix was 2048 × 2048 pixels with the sampling equal to 0.3 mm that corresponded to a square area of 614.4 mm. Such a relatively large calculation matrix was chosen to diminish the edge effects and limited aperture influence.

As a reference, the intensity and phase distributions of the image reconstructed by the classic back propagation method (Angular Spectrum of Plane Waves—ASoPW) were calculated. The results are shown in Figs. 2(a) and 2(d). The light field corresponding to the

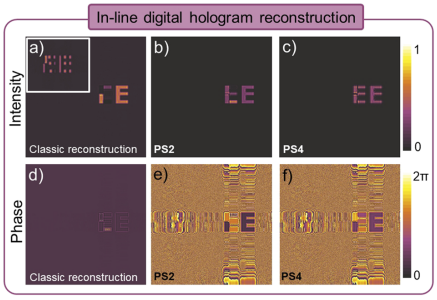


**FIG. 2.** Numerical simulations illustrating the differences between the reconstruction of the THz Fresnel hologram using different methods: (a) and (d) classic back propagation (using the angular spectrum of plane waves method), (b) and (e) two-step PS method, and (c) and (f) four-step PS method. (a)–(c) depict the intensity distributions, while (d)–(f) depict the corresponding phase distributions. The intensity pattern of the reconstructed image in the case of a small (1°) angle between the interfering beams is presented in the inset of (a) for illustration. Note the expressed characteristic sine-like interference pattern here.

DC term component is clearly visible, forming a uniform and noticeable background, which is not observed in other cases [see Figs. 2(b), 2(c), 2(e), and 2(f)]. As it is seen from the hologram reconstruction in Fig. 2(a), the reconstructed image is formed by two reconstructed beams corresponding to the object and reference. They propagate numerically along the same optical axis and overlap in the real image plane, making the reconstructed image not reliable. Inside the left "E" letter, bright and dark regions can be seen instead of uniform distribution as it was in the object. The intensity distribution is changed due to the different phase values of the object, and such an intensity distribution corresponds to the interference pattern. To illustrate this fact more thoroughly, an additional simulation was created with an angle of 1° between the beams, and in the inset of Fig. 2(a), the characteristic sine-like interference pattern is present.

In the THz range, many objects can be transparent and thus introduce a particular phase shift. Such features of the object result in the reconstructed interference pattern of two beams. It can also be clearly seen in the inset of Fig. 2(a) where an additional interference pattern appears even when an angle of 1° between the recorded beams is introduced. The numerical reconstruction does not take into account the presence of a beam splitter; thus, we observe such an effect. For visible light, most of the objects are diffusive, which means that their phase distribution is random. Therefore, the components (DC term and real and virtual images) would overlap, but there would be no interference fringes as it is visible in Fig. 2(a). As it was already mentioned, the two-step PS technique [Fig. 2(b)] removes only the influence of the DC term. As a result, an interference of real image reconstruction with the light field distribution formed as the divergent beam resulting from the virtual image creates an interference pattern in the left "E" letter. The background is significantly smaller than for classic reconstruction and is similar to that for the four-step PS technique [Fig. 2(c)].

One can note that the four-step PS technique ideally reconstructs the information about the intensity [Fig. 2(c)] and phase [Fig. 2(f)] of the object. Note the visible diffraction effects on the edges of the object. It must be underlined that in the case of phase retrieval methods, the four-step PS technique is preferable regardless of two times larger registering time. However, in the case of absorbing and not transparent objects, the two-step technique can give reasonable enough results, and it is two times faster. To remove the unwanted background, it is enough to apply the two-step PS algorithm; however, to reconstruct proper information about phase shifts introduced by the object, the four-step PS algorithm needs to be used. Thus, the two-step PS technique is beneficial in the case of absorbing objects, i.e., mainly intensity change related images, while the four-step technique is more preferable in the studies of low-absorbing or transparent objects relying on the phase changes.

After the illustration of the technique, a set of simulations was conducted corresponding to the real experimental conditions. The real object was smaller in comparison to that used in illustrating simulations given in Fig. 2—in the experiment, "E" letters were of 45 mm height and 30 mm width. The calculation matrix was 1024 × 1024 pixels (each having a size of 150 × 150 $\mu m^2$, resulting in the area of 153.6 mm-edge-size-square). Moreover, the left "E" letter was divided into five different areas to induce different phase shifts: 0, $\frac{\pi}{4}$, $\frac{\pi}{2}$, $\frac{3\pi}{4}$, and $\pi$ corresponding to 0, 1, 2, 3, and 4 paper sheets (for 600 GHz radiation). It was also assumed that two beams interfere in the hologram plane at an angle of 0° [for classic reconstruction

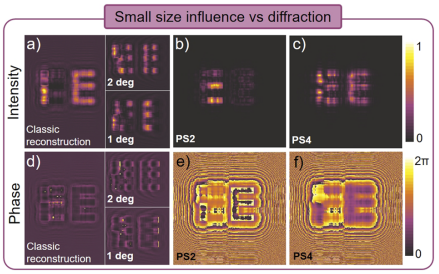


**FIG. 3.** Numerical simulations illustrating diffraction effects resulting from a small size of the object in comparison with the wavelength. Simulation parameters correspond to real experimental conditions. Reconstruction of the THz Fresnel hologram using different methods: (a) and (d) classic back propagation (using Angular Spectrum of Plane Waves—ASoPW), (b) and (e) two-step PS technique, and (c) and (f) four-step PS technique. (a)–(c) show the intensity distributions. (d)–(f) depict the corresponding phase distributions. The intensity and phase patterns of the reconstructed image in the case when small (1° and 2°) angles between the interfering beams are introduced are shown in the insets of (a) and (d). Note the pronounced characteristic interference pattern.

also at 1° and 2°, showing the influence of misalignment—insets of Figs. 3(a) and 3(d)]. The simulation parameters correspond to the values in the experiment. The distance between the object and the hologram plane was kept equal to 85 mm, and the recording and reconstructing wavelength was of 0.5 mm (600 GHz).

As it is seen from Fig. 3, a strong influence of diffraction effects is clearly noticeable.[14] The interference of two reconstructed beams in classic [Figs. 3(a) and 3(d)] and two-step PS [Figs. 3(b) and 3(e)] methods is evident. Moreover, misalignment-induced effects in the experimental setup are illustrated in the insets of Figs. 3(a) and 3(d). They manifest themselves as a characteristic stripe-like pattern resulting from the interference of two beams.

The resolved difference can be observed in the reconstructed phase distributions. The classic hologram approach does not give a proper mapping of the phase values introduced by the object. In the case of classic in-line digital holography, two beams—object and reference—are simultaneously reconstructed and overlap in the image plane, forming an interference pattern. Thus, the reconstructed light field distribution is not the exact amplitude and phase distribution introduced only by the object, which can be seen as dark areas in the reconstructed intensity distribution in the image of "EE" letters in Figs. 2(a), 2(b), 3(a), and 3(b). Hence, the best solution is to use the four-step PS technique illustrated in Figs. 2(c) and 2(f), which allows us to remove all unwanted reconstruction components, according to Eqs. (3) and (4). Using multiple exposures with different phase shifts of the reference beam allows us to reconstruct (from the numerically changed hologram) only the information about the object without additional components, forming noise. This approach allows us to properly reconstruct phase values introduced by the object. The two-step PS method [Figs. 2(b) and 2(e)] introduces the additional piston-like phase value resulting from the divergent field that shifts all phase values. Nevertheless, all differences introduced as the object phase shifts are distinguishable. The

intensity pattern suffers from the effect of interference of two reconstructed beams, forming the real and virtual images; however, the phase distribution is reconstructed properly.

The two-step and four-step PS techniques require an interferometric registering optical setup and give good quality reconstructed images. One can note that the two-step PS is faster, while the four-step provides better image quality, especially in the case of imaging phase objects. To quantitatively compare the obtained results, contrast values ($K$) defined as $K = \frac{I_{av}(s) - I_{av}(n)}{I_{av}(n)}$ were calculated. Here, $I_{av}(s)$ and $I_{av}(n)$ are the average intensity values corresponding to the signal area and the background noise area. The contrast values calculated from simulations and experimental results for object introducing phase changes characterized by variable intensity values are given in Table I and are strongly dependent on the phase level introduced by the object. It should be underlined that comparing parameters related to the intensity distribution (like contrast $K$) of the hologram of the phase object can be misleading while relating to the single areas. It is obvious that for two uniformly illuminated areas with introduced phase shifts of 0 and $\pi$, maximal and minimal intensity values, corresponding to positive and negative interferences, respectively, will be observed. The values of $K$ in the case of the experimental four-step PS technique are smaller than those for the two-step PS technique. Moreover, it should be underlined that the contrast of left and right "E" letters has the same values only for the four-step PS technique. Hence, only this technique (totally reducing all other hologram components) gives the assumed intensity distribution of the transparent object with introduced phase shifts. However, the phase values obtained only from the four-step PS technique correspond well to those introduced by the object; hence, this approach can successfully be used to map the phase objects properly. This illustrates also better fidelity of the intensity imaging in the case when the object introduces phase changes.

One of the essential points is the background subtraction by introducing PS techniques. The noise level was calculated as the average intensity value in the background area of reconstructed images. It is enough to use the two-step PS technique to reduce the noise level from 0.051 (calculated from single hologram reconstruction; Fig. 3) to 0.010 in simulations and from 0.034 to 0.017 in the experiment.

## III. EXPERIMENTAL SETUP

The experimental optical setup based on the Mach–Zehnder interferometer is presented in Fig. 4. It is based on Schottky diode-based frequency multiplier chains delivering the THz radiation of 0.3 and 0.6 THz frequencies.

The delivered coherent radiation is collimated by passing the converging lens (L1, with $f$ = 12 cm). Then, after the reflection by gold-coated mirror M1, the collimated THz beam is divided into two parts by beam splitter BS1 with a ratio of 1:1 and enters into the interferometric part. One part of the beam is reflected from mirror M2, and then, it is phase shifted by the introduced element PS and reaches beam splitter BS2 (thus forming the reference beam). The other part of the beam is reflected by mirror M3, passes through the object (sample), and reaches BS2 (forming the object beam). Then, both beams reunite, and from that time, they propagate along the same optical axis, reaching the detector. The intensity of the interference pattern is registered using a high performance antenna-coupled

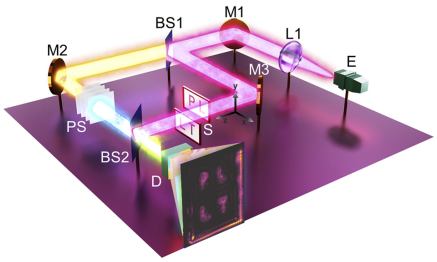


**FIG. 4.** Principal scheme of the optical setup used to record a THz digital hologram at 0.3 and 0.6 THz. Letter "E" denotes the electronic THz emitter; L1 is the high-density polyethylene (HDPE) lens with $f$ = 12 cm; M1, M2, and M3 are gold-coated flat mirrors with a diameter of 50 mm; BS1 and BS2 label high resistivity silicon beam splitters (525 $\mu$m thickness, with both sides polished); S (sample) is the object with "LT" and "PL" shape apertures in the aluminum sheet; PS is a phase shifter—different amounts of paper sheets introducing particular phase shifts in the reference beam; and D is a titanium-based microbolometric detector. The example of the image reconstructed from the registered hologram of "PL" and "LT" samples is shown behind the detector.

titanium microbolometer[15] working at room temperature. To alleviate the influence of the small-aperture-size optical elements, the detector was placed in the main optical axis, and the object was shifted by a computer controlled motorized $xyz$ axis stage. Such a solution allowed us to record the interference pattern resulting from two overlapping beams in the middle of the optical setup where the diffraction effects are not critical. Moreover, in such a case, the phase value in the reference beam remains constant for the whole hologram and is free from diffraction effects.

## IV. TWO-PLANE-OBJECT RECONSTRUCTION FOR TWO DIFFERENT FREQUENCIES

There are several propagation techniques that can be employed in the reconstruction process of THz holograms. One can use the Fresnel diffraction method,[7,16] or if the recording is made in different conditions, the Fourier transform method can be suitable.[5,7]

We preferred, however, the ASoPW method as it contains no approximations and assures proper sampling conditions; moreover, it is relatively free of numerical errors.[17] This technique allows us to access and modify the hologram digitally in its complex distribution, and also, it enables us to introduce changes in its spatial frequency domain (Fourier spectrum). The angular spectrum method relies on the assumption that any light field distribution can be decomposed into individual plane waves traveling at different directions. These plane waves combine to create a complex light field distribution, such as a diffractive element, a hologram. After decomposition into individual plane waves, these plane waves can be digitally propagated at a distance $z$ to recover the complex light field at any other location in space.[7] The propagation of the plane wave is simple as it has uniform amplitude and phase value changing as the sine function together with the propagation distance.

In this section, a reconstruction of two 2D objects separated by some distance was conducted. The hologram of the object composed of two planes was recorded and formed a single hologram that was

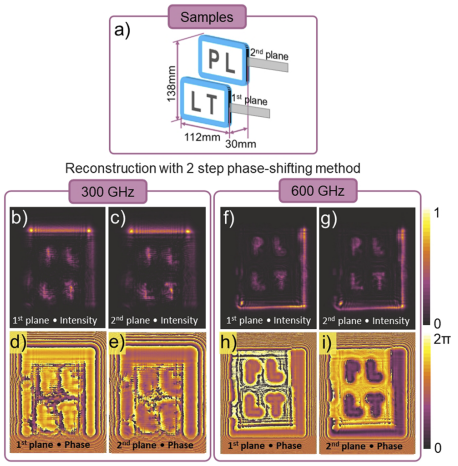


**FIG. 5.** Two 2D object reconstruction for two different frequencies using the PS technique and ASoPW propagation method. (a) Scheme of the object that consists of two 70 × 112 mm$^2$ aluminum foil sheets. The first sample has a cut-out "LT" shape element and was placed in the first plane (85 mm from the hologram plane), which is closer to BS2. The second sample has a cut-out "PL" shape element and was placed in the second plane (115 mm from the hologram plane). Samples are separated by a gap of 30 mm and are shifted vertically, so they do not overlap (such geometry results from the small size of the letters with respect to the used wavelength and the absence of the diffuser in the recording process). The intensity distributions of the reconstructed images in the first and second planes are shown in (b) and (c) for 300 GHz and (f) and (g) for 600 GHz. The corresponding phase distributions in the mentioned planes are shown in (d) and (e) for 300 GHz and (h) and (i) for 600 GHz.

reconstructed later. Figure 5 shows two-plane-object reconstruction for two different frequencies using the two-step PS technique and ASoPW propagation method.

Thus, two sets of transparent letters—"LT" and "PL"—were mounted at two different distances—85 and 115 mm—from the hologram plane. In the case of the two-step PS technique, two holograms were recorded for two different phase shifts of the reference beam, 0 and $\pi$, respectively. Moreover, such a set of holograms was recorded for the frequencies 300 and 600 GHz, which also enables heterodyne reconstruction.[18]

The better image resolution and reconstruction are obtained for higher frequency as expected. However, one needs to note that the width of the slits in "LT-PL" letters was equal to 5 mm (the height of the letter is equal to 30 mm), which corresponds to only five and ten wavelengths for each frequency, respectively. In 300 GHz reconstructed images, significant diffraction effects are visible. As one can see, numerical simulations that were conducted for the "EE" sample (presented in Fig. 3) should be free from any imperfections existing in real experimental conditions. The presented simulation data are characterized by a strong diffraction influence even though simulations are conducted at two times larger frequency.

The image was reconstructed at two distant planes using the phase-shifting technique (Fig. 5) and single hologram reconstruction given in Fig. 11 of the Appendix. The uniform phase distribution inside "LT-PL" letters is consistent with the theory and our predictions. In this experiment, no additional phase shifts were introduced inside the sample.

Single hologram reconstruction has almost no information about the phase, while in the PS technique, the contours of letters are visible and the inside of the letter has a uniform level of phase—the same in all letters but different in different image planes. Single hologram reconstruction can give similar intensity distribution as the phase-shifting technique, but in the case of the particular phase shift of the reference beam—here used for PS reconstruction—it can change the reconstructed image. As it can be seen in Fig. 11 (right), the letter area is darker than the background, which is caused by the $\pi$ shift in the reference beam. Such reconstruction is characterized by the negative values of contrast related to the contrast inversion. Thus, such reconstruction is not proper. In the case of using PS techniques, the intensity image is clear and has better contrast than the image reconstructed from the single hologram (in the case of normal and inverted images). The contrast values calculated for each letter area in two image planes are given in Table II. These values correspond to experimental data, and it can be seen that single hologram reconstruction is characterized by the decreased contrast value by ~90% in comparison to the PS technique for the first plane and 70% for the second plane at 300 GHz.

**TABLE II.** Contrast values for reconstructed images (calculated from the intensity distributions) for two planes (with "PL" and "LT" letters distant 30 mm from each other) and two frequencies—300 and 600 GHz. The minus sign corresponds to the inverted contrast—it means that the background is brighter than the letter area—see Fig. 11.

| | | 300 GHz | | | 600 GHz |
|---|---|---|---|---|---|
| | | One hologram | | | |
| Contrast | | No phase shift | $\pi$ phase shift | PS | PS |
| First plane | L | 3.63 | −0.66 | 37.37 | 13.85 |
| | T | 4.54 | −0.68 | 36.10 | 16.92 |
| Second plane | P | 4.25 | −0.79 | 14.86 | 8.16 |
| | L | 3.38 | −0.79 | 13.40 | 6.72 |

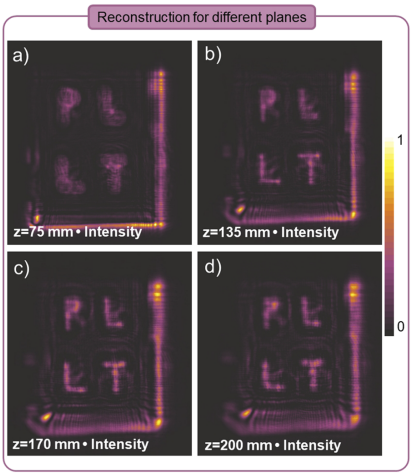


**FIG. 6.** Different reconstruction planes, equal to (a) 75, (b) 135, (c) 170 and (d) 200 mm, reconstructed from the hologram for 600 GHz. For such small hologram size, a large depth of field is observed under illumination with a parallel beam.

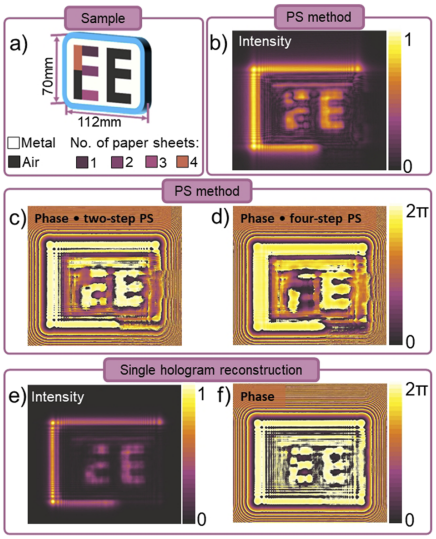


**FIG. 7.** Intensity and phase distributions of the reconstructed holograms. (a) Scheme of the object that consists of a 70 × 112 mm$^2$ aluminum foil with cut-out "EE" shape elements. Note that one of these elements contains areas corresponding to a different number of paper sheets (0, 1, 2, 3, and 4) indicated by different colors (particular phase values) in the image. The relevant intensity and phase distributions of the reconstructed image using the two-step phase-shifting technique are presented in (b) and (c). Additionally, a phase distribution for the four-step PS algorithm is given in (d). The intensity distribution for the four-step technique showed very similar intensity distribution to that of the two-step technique. To illustrate the importance of phase differences, two PS reconstruction algorithms are compared in (c) and (d). For better comparison, the intensity and phase distributions of the reconstructed image using a single hologram are presented in (e) and (f).

One can notice that the size of the recorded hologram is limited to 118 × 138 mm$^2$ for 0.5 and 1 mm wavelengths. The smaller the reconstruction area, the larger the depth of the field. This results in the appearance of the sharp image observed in a wide range of distances. Here, the reconstruction was conducted at distances from the hologram from 30 to 200 mm in 5 mm steps. The image is very similar to that illustrated in Fig. 5, which can be observed from the distance of 75 mm up to 200 mm (further propagation was not performed). This phenomenon can be seen in Fig. 6 where two exemplary more distant planes of the reconstructed hologram are shown. One can see that the letter shape can still be clearly distinguished. If strong inevitable diffraction effects (resulting from the object aperture size, propagation distance, and setup aperture) are not taken into account, the sharp image can be observed not only in one plane but also in the certain range of distances. However, it is difficult to evaluate them numerically even though the human eye sees the difference. Moreover, one needs to recall that in this THz experiment, a plane wave was used both as a reference beam and to illuminate the opaque-transparent object (without the diffuser making the phase random).

## V. RECONSTRUCTION OF THE PHASE SAMPLE (PHASE OBJECT)

A phase object (transparent sample introducing phase changes only) is analyzed by reconstruction with the PS algorithm (both two- and four-step). This is illustrated through a series of measurements of the sample with different numbers of phase shift areas at a frequency of 600 GHz. The reconstruction results using two-step and four-step PS algorithms in the form of the amplitude and phase distributions from the registered holograms are presented in Fig. 7.

The sample, described in Fig. 7(a), was used to illustrate the advantages of using the PS technique. Each additional paper sheet in the reference beam shifts the phase by $\frac{\pi}{4}$. First, the experiment was performed without any paper sheets between M2 and BS2 (Fig. 4), and second, it was repeated by adding 2, 4, and 6 paper sheets, which were intended to shift the phase of the reference THz beam by 0, $\frac{\pi}{2}$, $\pi$, and $\frac{3\pi}{2}$, respectively. The intensity and phase distributions were reconstructed using the two-step PS technique. The results are shown in Figs. 7(b) and 7(c). Additionally, the phase distribution was reconstructed using the four-step PS technique for all recorded holograms [Fig. 7(d)]. The intensity distribution for the four-step technique was very similar to the intensity distribution for the two-step one; thus, it was not plotted additionally here.

As one can see from the results, removing the DC term in the two-step PS technique is faster because it requires only two scans,

while the four-step technique does not give much better results when observing intensity distributions and requires two times longer time to record the holograms. The component corresponding to the virtual image forms only the divergent light field in the real image plane. Thus, it slightly increases the noise level in the background, which does not influence the quality of the reconstructed image significantly.[19] However, in the case of imaging (holography) phase objects, the four-step PS technique should be used due to the fact that it is characterized by better mapping of different phase level areas in the sample.

Figure 8 illustrates the phase levels reconstructed from the recorded holograms—both from simulations and experiment. The calculations show the average values of the phase for each area corresponding to the different numbers of the paper sheets in both "E" letters. Data were taken from simulations carried out in Sec. II for two different cases—with no aperture influence (Fig. 2) and with the small size of the hologram aperture (Fig. 3). These values are gathered on the same plot and compared with the experimental results. Three different techniques are shown—single hologram reconstruction (gray), two-step PS (yellow), and four-step PS (violet). It is worth noting that the particular value of the phase level is not essential; however, the most important item is the tendency between the different areas: As each area introduces different phase shifts, the relation between the following phase shifts should be properly mapped in both simulations and experiment. It can be easily noticed that for single hologram reconstruction (SH), the mapping between the phase shift (number of paper sheets) and the phase level is not linear. The two-step PS technique, both in the simulations and experiment, also does not fulfill the proper mapping between the phase shifts introduced by the object and the calculated phase level. In contrast, the four-step PS exhibits an advantage due to the proper phase mapping.

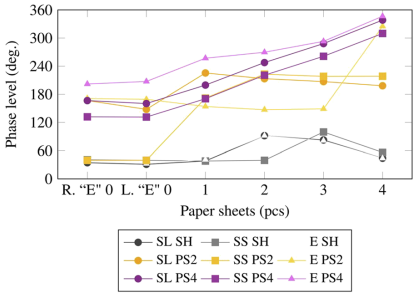


**FIG. 8.** Comparison of phase levels obtained in simulations for large and small apertures of the hologram (SL and SS, respectively) and in experimental evaluation (marked as E). Large aperture simulations correspond to Fig. 2, while phase levels for small apertures are calculated from simulation data illustrated in Fig. 3. Each category—SL, SS, and E—contains information about results obtained from single hologram reconstruction (SH, marked in gray), two-step PS techniques (PS2, marked in yellow), and four-step PS techniques (PS4, marked in red and shifted up by 50° for clarity). It can be seen that the mapping between the numbers of papers, and thus the phase shift introduced by the object, is linearly proportional to phase levels calculated from simulations and experiment only for the four-step PS technique (violet). In the horizontal axis, the numbers of paper sheets are given, which correspond to particular phase shifts introduced by the sample. 16 paper sheets correspond to $2\pi$. "R. "E" 0" and "L. "E" 0" stand for the empty region (0 paper sheet) inside the right and left "E" letter areas, respectively.

## VI. COMPARISON OF PHASE OBJECT IMAGES RECORDED BY DIFFERENT TECHNIQUES

One of the most illustrative ways to reveal the possibilities of phase-imaging applications is to compare the obtained results using different image recording techniques on the same sample. For this purpose, a special sample, i.e., phase object, constructed of differently transparent areas to introduce different phase shifts [Fig. 9(a)], already used in phase-contrast and dark-field imaging experiments,[20] was investigated in addition. Before proceeding to the detailed comparative analysis, it is worth noting the following: In the phase object, almost uniform intensity distribution in the object plane will result in almost uniform intensity distribution in the image plane. Such a problem exists in the $4f$ imaging setup shown in Fig. 9(c); however, this setup allows us to image the whole object plane instantly. To overcome problems with the imaging of phase objects, additional approaches, such as focused imaging [Fig. 9(b)], spatial filtering-based imaging [Fig. 9(d)],[20] or holography, need to be considered. Focused imaging requires raster scanning of the sample (object) plane point-by-point. The spatial filtering technique in the $4f$ setup or holographic approach enables instantaneous THz image formation, i.e., fast acquisition can be realized using a matrix of detectors.

A comparison of the results obtained via the PS technique with previously recorded images using point-to-point, plane-to-plane ($4f$), and dark-field techniques[20] is presented in Fig. 9. One can note the good quality of the intensity image registered using the point-to-point technique [Fig. 9(b)], revealing also some phase differences (edges) that can be registered using the focusing optics. The resolution of the obtained image is in the range of wavelengths. This results from the focal length and the diameter of the used mirror, which influences the Airy disk size in the focal spot. Thus, the smaller the focal spot, the better the resolution. However, in such a case, the point-to-point (raster) scanning is obligatory. To accelerate the imaging process, an array of detectors is needed, but at the same time, it imposes the requirement of different optical setup configurations. The influence of diffraction effects resulting from limited aperture size in comparison to the wavelength[14] forces us to use the large aperture optics to allow for plane-to-plane imaging (like in the $4f$ optical setup). This requirement can be alleviated in some application by using small aperture size optics and shifting the object with the detector placed on the optical axis. This solution can be quickly improved to the plane-to-plane imaging scheme by using large aperture lenses.[21] However, there is one significant drawback—spatial filtering techniques can be applied for objects introducing the phase shifts from the $0$–$\frac{\pi}{2}$ range. Such limitation results from the theoretical approximation and an assumption that the function describing the object can be expanded into Taylor series. Nevertheless, the holographic imaging can extract the phase values within the range of $0$–$2\pi$ or even more, but then it requires additional phase retrieval techniques. It should be underlined that using holographic techniques, a complex light field distribution (containing information about the amplitude and phase of the beam) can be extracted at

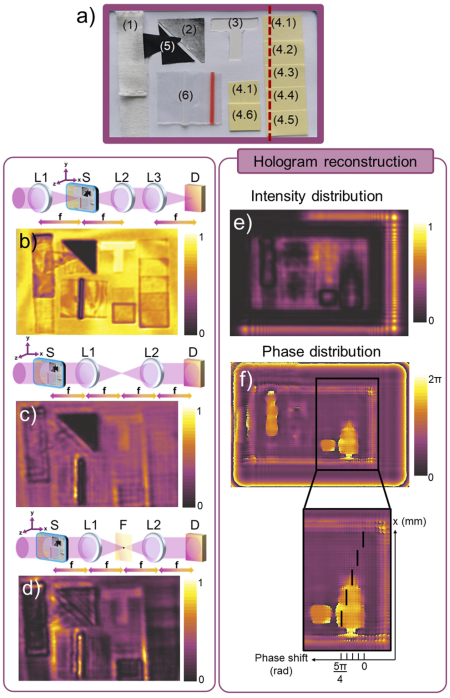


**FIG. 9.** (a) Photograph of the imaged sample consisting of (1) gauze cloth with different numbers of layers, (2) aluminum foil, (3) a T-shaped aperture, (4) paper (where the second number denotes the paper sheet number), (5) rubber glove, and (6) a low density polyethylene (LDPE) bag (two layers of the LDPE film). The comparison of images recorded at 300 GHz by setups described in Ref. 20 with different imaging techniques is shown: (b) direct THz image obtained with focusing THz radiation to the sample and detector—point-to-point technique; (c) direct THz image obtained without focusing THz radiation to the sample and detector—plane-to-plane technique—which is the 4 *f* imaging setup; and (d) THz image obtained using the dark-field filtering technique where the spatial filter is used to remove low frequency components from the spectrum, hence allowing us to form the image with a dark background around the sample. (e) and (f) show the intensity and phase distributions, respectively, reconstructed from the registered holograms using the PS technique. The sample part of paper sheets is enlarged in order to see the phase levels. The black lines are given as the guide the eye to indicate the phase change caused by each paper sheet. The hologram was registered and reconstructed for 600 GHz; thus, the phase shift introduced by the same number of paper sheets is two times larger. THz image pixel size: 0.3 × 0.3 mm$^2$; images are of 273 × 165 pixels.

different planes starting from the hologram plane; thus, a 3D light field distribution can be reconstructed.

In Figs. 9(e) and 9(f), the intensity and phase distributions of the reconstructed image are shown. As one can see, the intensity distribution indicates no total transparency in all areas, so the reconstructed intensity is not uniform [Fig. 9(e)]. It is worth to recall that in real experimental conditions, there are no ideally transparent materials; thus, the object under test will introduce some attenuation anyway. Nevertheless, the techniques enabling us to visualize the phase are more adequate due to the fact that they allow us to map different phase values from the object as different phase levels in the image plane. This can be illustrated via the dark-field technique [Fig. 9(d)] and the hologram in the form of reconstructed intensity and phase distributions [Figs. 9(e) and 9(f), respectively]. In Fig. 9(f), the phase distribution reconstructed from the hologram using PS is given with additional zoom in the inset. It can be noticed that in Fig. 9(f), the edges of different areas are visible, and also, the phase level inside the area is distinguishable.

In the case of imaging phase objects, special attention must be given to a proper phase mapping between the phase shift introduced by the object (sample) and the phase value calculated from the image. On the one hand, the average value of the intensity in the areas corresponding to the particular phase shifts was calculated for point-to-point, plane-to-plane, and dark-field techniques. On the other hand, the average value of the phase in the areas corresponding to the particular phase shifts was calculated from phase distribution in the reconstructed hologram. First three methods are supposed to visualize phase changes in the registered intensity pattern. In the fourth method–the hologram—a phase distribution (and amplitude) is reconstructed from the registered intensity interference pattern. These four sets of the data are plotted in Fig. 10, illustrating the dependence of the phase level to the introduced phase shift. It can be clearly seen that there is no proper mapping between the calculated phase level and the introduced phase shifts in the experimentally recorded intensity distributions in the point-to-point and plane-to-plane setups. The dark-field technique (using the amplitude spatial

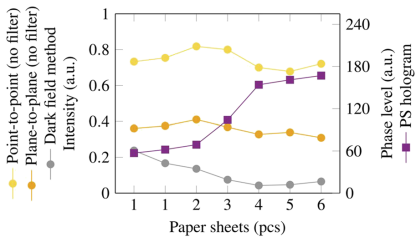


**FIG. 10.** Comparison of different phase level mapping obtained experimentally using different techniques. The intensity patterns are recorded for point-to-point, plane-to-plane, and dark-field techniques—left vertical axis—which are marked as circles in light yellow, dark yellow, and gray colors, respectively. The phase distribution is reconstructed from the hologram and is marked as squares (violet color)—right vertical axis. The dark-field (DF) technique follows the desired change in paper sheet numbers between 1 and 4 (inversely proportional), while the holographic reconstruction follows between paper sheet numbers 1 and 6 (proportionally). It must be underlined that intensity distributions (yellows and gray) were registered for 300 GHz (the $2\pi$ phase shift corresponds to introducing 16 paper sheets), while the hologram (violet) was registered for 600 GHz (the $2\pi$ phase shift corresponds to introducing 8 paper sheets), which give the proper phase mapping range $0–\frac{3\pi}{8}$ for the dark-field technique and $0–\frac{5\pi}{4}$ for the reconstructed hologram.

filter in the middle of the Fourier plane) forms the intensity image of the phase object. However, this object must introduce phase changes up to $\frac{\pi}{2}$, while the larger phase change results in a smaller intensity value in the image. In Fig. 10 (gray dots), the decrease in intensity can be noticed between 1 and 4 paper sheets, which agrees well with the theory and the applicability limits of the dark-field technique.

The hologram reconstruction of the "EE" sample (Fig. 8) revealed the possibility to properly map all introduced 4 paper sheets corresponding to the $0–\pi$ phase change. Here, the 5 paper sheet induced phase difference is properly mapped; however, one can note that the hologram was recorded and reconstructed for shorter wavelengths (higher frequency, 600 GHz). Therefore, the introduced phase shift is equal to $0–\frac{5\pi}{4}$ and is properly mapped with the phase shifts introduced by the sample. Each of the 6 different paper sheet areas (violet squares in Fig. 10) can be distinguished by the comparison of the average value in the reconstructed phase distribution.

## VII. CONCLUSIONS

A two- and four-step PS technique in THz holography is developed, and its ability to reconstruct 2D and 3D transparent objects is demonstrated. The two-step PS technique was found to be faster and easier for application; however, it leaves some divergent light field distribution propagating together with information about the object to the image plane. Therefore, this technique can still influence the phase pattern but cannot give precisely correct mapping between the phase shifts introduced by the sample and the phase levels calculated from the reconstructed hologram.

The four-step PS technique is preferable in the case of determining the exact phase values of the registered phase object. It requires more recording time; however, it exhibits the advantage of the proper phase mapping. For instance, in this article, we demonstrated that within the $0–\frac{5\pi}{4}$ range, the introduced phase changes and distributions can be reconstructed from the hologram using PS techniques.

A comparison of two-step and four-step PS approaches was demonstrated. Purely amplitude objects (not introducing phase variations in the sample plane) can be accurately holographed using the two-step technique, which is two times faster and is characterized with two times larger contrast than single hologram reconstruction. Moreover, the average value of the background in the case of single hologram reconstruction is reduced up to five times when using the two-step PS technique.

To highlight possibilities given by holographic registering of objects and their digital reconstruction, the comparison of the holographic imaging with other methods was given. Holographic imaging gives the information about amplitude and phase distributions in all planes after the hologram, i.e., the complex field can be reconstructed. Another interesting technique—spatial filtering (the dark-field method)—enables the mapping of phase values introduced by the sample into the intensity pattern in the image plane. Such image formation is possible due to the introduction of an amplitude filter in the Fourier plane of the $4f$ optical setup. This method is limited only to the mapping phase changes from the $0–\frac{\pi}{2}$ range. The holographic method can give a phase difference range of $0–2\pi$, and in the case of using additional phase retrieval methods, it is even higher.

The plane-to-plane and point-to-point methods are given as references. The former illustrates how the image is formed in a typical $4f$ setup by suppressing diffraction effects arising from the limited aperture of optical elements by placing the detector in the middle of the optical axis and shifting the sample in the object plane. This method does not provide proper information about the phase levels introduced by the sample. The latter describes the raster scanning method using a focused beam—on both the sample and the detector. This method displays good resolution resulting from the size of the focal spot illuminating the sample. It enhances edges and small changes in the sample. However, it does not provide proper mapping of the phase introduced by the sample with registered intensity values.

To summarize, the holographic methods of imaging give the whole variety of possibilities of forming reconstructed images and visualizing both amplitude and phase changes introduced by the sample. Only in the case of phase reconstruction from the in-line digital hologram using the four-step PS technique, the different phase level areas can be discriminated, indicating that the boundaries of THz imaging and digital holography[22] can be extended, in particular in the application of imaging of phase objects transparent for this particular range of radiation.


## ACKNOWLEDGMENTS

This study was funded by the FOTECH-1 project granted by the Warsaw University of Technology under the program Excellence Initiative: Research University (ID-UB).

The authors acknowledge Orteh Company for providing LS 6.0 software used here for the numerical reconstruction of the recorded holograms, which is accessible in the Laboratory of Optical Information Processing at the Faculty of Physics in the Warsaw University of Technology.


## AUTHOR DECLARATIONS

### Conflict of Interest

The authors have no conflicts to disclose.

## DATA AVAILABILITY

The data that support the findings of this study are available from the corresponding author upon reasonable request.

## APPENDIX: SINGLE HOLOGRAM RECONSTRUCTION

To compare the hologram reconstruction using the PS technique and the simple hologram reconstruction for 300 GHz, one needs to analyze the reconstructed images from the hologram recorded with no phase shift in the reference arm and with the $\pi$ phase shift. Such a phase shift was realized by four layers of paper, glued together, and introduced in the reference arm. It can be seen that reconstructed two-plane-images [Figs. 11(e) and 11(f)] for both holograms have inverted contrast (violet) in relation to those in Figs. 11(a) and 11(b) resulting from the recording with $\pi$-shifted reference beams. The phase distribution seems to be more uniform and thus less distinguishable than for the PS technique (illustrated in

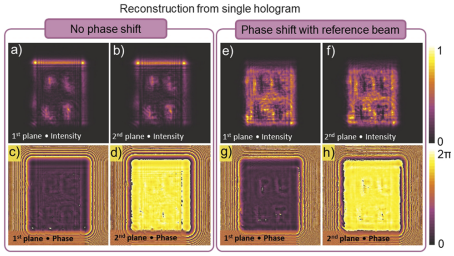


**FIG. 11.** Amplitude (a, b, e, and f) and phase (c, d, g, and h) distributions of reconstructed images for both planes for each hologram separately for 300 GHz (single hologram reconstructions). (a)–(d) Without the phase shift introduced in the reference arm and (e)–(h) with the $\pi$ phase shift introduced.

Fig. 5). The quantitative comparison of single hologram reconstructions with the one using the two-step PS technique is described in Sec. V.

## REFERENCES


[1]L. Guo, X. Wang, and Y. Zhang, "Terahertz digital holographic imaging of biological tissues," in *International Symposium on Ultrafast Phenomena and Terahertz Waves* (Optical Society of America, 2016), p. IW4B-3.

[2]L. Guo, X. Wang, P. Han, W. Sun, S. Feng, J. Ye, and Y. Zhang, "Observation of dehydration dynamics in biological tissues with terahertz digital holography," Appl. Opt. **56**, F173–F178 (2017).

[3]L. Rong, T. Latychevskaia, D. Wang, X. Zhou, H. Huang, Z. Li, and Y. Wang, "Terahertz in-line digital holography of dragonfly hindwing: Amplitude and phase reconstruction at enhanced resolution by extrapolation," Opt. Express **22**, 17236 (2014); arXiv:0911.0520.

[4]Z. Li, R. Zou, W. Kong, X. Wang, Q. Deng, Q. Yan, Y. Qin, W. Wu, and X. Zhou, "Terahertz synthetic aperture in-line holography with intensity correction and sparsity autofocusing reconstruction," Photonics Res. **7**, 1391 (2019).

[5]H. Yuan, A. Lisauskas, M. Wan, J. T. Sheridan, and H. G. Roskos, "Resolution enhancement of THz imaging based on Fourier-space spectrum detection," Proc. SPIE **11279**, 1127918 (2020).

[6]S. T. Thurman and A. Bratcher, "Multiplexed synthetic-aperture digital holography," Appl. Opt. **54**, 559 (2015).

[7]M. S. Heimbeck and H. O. Everitt, "Terahertz digital holographic imaging," Adv. Opt. Photonics **12**, 1–59 (2020).

[8]I. Yamaguchi and T. Zhang, "Phase-shifting digital holography," Opt. Lett. **22**, 1268–1270 (1997).

[9]T. Zhang and I. Yamaguchi, "Three-dimensional microscopy with phase-shifting digital holography," Opt. Lett. **23**, 1221–1223 (1998).

[10]C. Zuo, S. Feng, L. Huang, T. Tao, W. Yin, and Q. Chen, "Phase shifting algorithms for fringe projection profilometry: A review," Opt. Lasers Eng. **109**, 23–59 (2018).

[11]D. W. Phillion, "General methods for generating phase-shifting interferometry algorithms," Appl. Opt. **36**, 8098–8115 (1997).

[12]G. Lai and T. Yatagai, "Generalized phase-shifting interferometry," J. Opt. Soc. Am. A **8**, 822–827 (1991).

[13]L. Xu, J. Miao, and A. K. Asundi, "Properties of digital holography based on in-line configuration," Opt. Eng. **39**, 3214–3219 (2000).

[14]A. Siemion, "The magic of optics—An overview of recent advanced terahertz diffractive optical elements," Sensors **21**, 100 (2021).

[15]L. Minkevičius, L. Qi, A. Siemion, D. Jokubauskis, A. Sešek, A. Švigelj, J. Trontelj, D. Seliuta, I. Kašalynas, and G. Valušis, "Titanium-based microbolometers: Control of spatial profile of terahertz emission in weak power sources," Appl. Sci. **10**, 3400 (2020).

[16]G. Dwivedi, A. Sharma, S. Debnath, and Rajkumar, "Comparison of numerical reconstruction of digital holograms using angular spectrum method and Fresnel diffraction method," J. Opt. **2017**, 1–10 (2017).

[17]M. Sypek, "Light propagation in the Fresnel region. New numerical approach," Opt. Commun. **116**, 43–48 (1995).

[18]M. S. Heimbeck, W.-R. Ng, D. R. Golish, M. E. Gehm, and H. O. Everitt, "Terahertz digital holographic imaging of voids within visibly opaque dielectrics," IEEE Trans. Terahertz Sci. Technol. **5**, 110–116 (2014).

[19]A. Siemion, I. Ducin, K. Kakarenko, M. Makowski, A. Siemion, J. Suszek, M. Sypek, D. Wojnowski, and A. Kołodziejczyk, "Digital holography with self-imaging by a two-step phase element," Photonics Lett. Pol. **2**, 91–93 (2010).

[20]A. Siemion, L. Minkevičius, L. Qi, and G. Valušis, "Spatial filtering based terahertz imaging of low absorbing objects," Opt. Lasers Eng. **139**, 106476 (2021).

[21]M. Sypek, M. Makowski, E. Hérault, A. Siemion, A. Siemion, J. Suszek, F. Garet, and J.-L. Coutaz, "Highly efficient broadband double-sided Fresnel lens for THz range," Opt. Lett. **37**, 2214–2216 (2012).

[22]G. Valušis, A. Lisauskas, H. Yuan, W. Knap, and H. G. Roskos, "Roadmap of terahertz imaging 2021," Sensors **21**, 4092 (2021).

NOTES

NOTES

Vilniaus universiteto leidykla
Saulėtekio al. 9, III rūmai, LT-10222 Vilnius
El. p. info@leidykla.vu.lt, www.leidykla.vu.lt
bookshop.vu.lt, journals.vu.lt
Tiražas 25 egz.